UNIVERSITÉ DE MONTRÉAL

STUDIES ON METAL CATALYSTS AND CARBON MATERIALS

FOR FUEL CELL APPLICATIONS

GAIXIA ZHANG

DÉPARTEMENT DE GÉNIE PHYSIQUE

ÉCOLE POLYTECHNIQUE DE MONTRÉAL

THÈSE PRÉSENTÉE EN VUE DE L'OBTENTION

DU DIPLÔME DE PHILOSOPHIAE DOCTOR

(GÉNIE PHYSIQUE)

NOVEMBRE 2007

Canada

UNIVERSITÉ DE MONTRÉAL

ÉCOLE POLYTECHNIQUE DE MONTRÉAL

Cette thèse intitulée:

STUDIES ON METAL CATALYSTS AND CARBON MATERIALS

FOR FUEL CELL APPLICATIONS

présentée par: ZHANG Gaixia

en vue de l'obtention du diplôme de: Philosophiae Doctor

a été dûment acceptée par le jury d'examen constitué de:

M. SKOROBOGATIY Maksim, Ph.D., président

M. SACHER Edward, Ph.D., membre et directeur de recherche

M. DODELET Jean-Pol, Ph.D., membre et codirecteur de recherche

M. YELON Arthur, Ph.D., membre

M. PAYNTER Royston, Ph.D., membre

DEDICATION

To my parents.

To my sister.

To my husband.

ACKNOWLEDGEMENTS

I would first like to express my sincere and profound gratitude to my supervisor, Professor Edward Sacher, for providing me with the opportunity to study under his guidance. I am also very indebted to him for his patience, encouragement, financial support, and insightful advice. Without his extensive and comprehensive help, this thesis could not have been possible. Thank him so much for having given me so much help.

Next, I would like to thank my co-supervisor Professor Jean-Pol Dodelet, from INRS-EMT, for his kind guidance, helpful suggestions and much help in my study and life.

Further, I would like to thank Professor Authur Yelon for his many kindnesses and his encouragement, which meant so much to me.

Special thanks to Dr. Dequan Yang and Mrs. Suzie Poulin for introducing me to many surface analysis techniques, for many helpful discussions, as well as for their kindness, great help and good advice.

I also thank Ning Guo, Gang Li, Florina-Elena Truica-Marasescu, Stéphane Larouche, Pierre-Luc Girard-Lauriault, Marc Bostetter, Sarah Joyce-Ermolli, Pascale Bommersbach, Lyne Dénommée, Patricia Moraille, and many other friends, for their generous help, encouragement and friendship.

the "Bourse Complémentaire".

RÉSUMÉ

Les piles à combustibles utilisant la technologie «membrane à échange de protons» sont des candidats potentiels pour une production hautement efficace d'énergie électrique tout en préservant l'environnement. Ces piles, attirent aujourd'hui un grand intérêt pour diverses applications. L'un des défis pour la commercialisation des PEMFC est le coût élevé des métaux nobles utilisés comme catalyseur (ex. Pt). La diminution de la quantité de Pt utilisée dans les PEMFC, tout en augmentant l'efficacité de son utilisation, a été une préoccupation majeure au cours de la dernière décennie.

L'objectif principal de ce projet était de comprendre les interactions interfaciales des nanoparticules de Pt avec les substrats de carbone, de façon à déterminer les moyens d'optimiser l'électrode catalytique et d'augmenter son activité catalytique afin d'améliorer les performances des piles à combustible PEM.

Nous avons, tout d'abord, étudié les interactions interfaciales (conduisant à l'adhésion) de nanoparticules Pt évaporées sur les surfaces de graphite pyrolytique (HOPG) non traitées et traitées par faisceau Ar^+ qui sont respectivement à basse et à haute densité de défauts de surface. Le HOPG a été utilisé comme un modèle de nanotubes de carbone (CNT) et de fibres de carbone, car il a une structure bien définie, bien comprise, et de plus la structure de la surface est semblable à celles de fibres de carbone et CNT. Nous avons constaté que ces nanoparticules de Pt ont de faibles interactions avec leurs supports vierges de carbone et n'avons trouvé aucune preuve de formation de composés chimiques entre eux. Notre analyse a indiqué que l'adhésion de nanoparticules de Pt à leur support peut être améliorée, en utilisant des faisceaux d'ions, des plasmas, ou d'autres traitements visant à établir des défauts sur la surface du substrat de carbone. En outre, en utilisant l'analyse multicomposante XPS, nous étions capables d'attribuer les

composantes de formes symétriques formant l'enveloppe globale du pic de Pt à l'existence de pics d'oxydation surfacique, ainsi que des configurations électroniques de la surface et du volume. Nous avons utilisé les intensités de ces pics, en fonction du Pt déposé, pour expliquer l'évolution de la forme de l'enveloppe du Pt4f.

Une autre façon d'établir une forte adhérence entre eux est par la fonctionnalisation chimique du support. En utilisant un traitement d'acide mixte H_2SO_4/HNO_3, nous avons caractérisé chimiquement la surface de la fibre de papier de carbone fonctionnalisé par une combinaison des spectroscopies infrarouge, Raman et photoélectronique, ce qui nous a donné de nouvelles perspectives sur l'oxydation souvent utilisée pour les matériaux ayant la structure graphène. Nous avons, pour la première fois, démontré la présence de transitions des espèces contenant O, N et S durant le processus d'oxydation, ainsi que le fait que l'intensité de ces espèces varie de façon imprévisible lors de la durée du traitement, particulièrement au début, plutôt que de simplement croître en fonction du temps. Cette étude permet de mieux comprendre et de contrôler la fonctionnalisation, de manière à établir une forte adhésion des nanoparticules de Pt, ce qui améliore les performances des piles à combustible.

Même avec la fonctionnalisation des CNT dans le but d'augmenter la masse de catalyseur de l'activité, il y a toujours une fraction importante de Pt qui est isolée du circuit extérieur et/ou de la PEM, entraînant une faible utilisation du Pt. La croissance des CNT directement sur des fibres de papier de carbone, suivie par les dépôts de Pt, assure que toutes les nanoparticules de Pt soient en contact électrique avec le circuit électrique extérieur, améliorant l'utilisation du Pt, et pouvant ainsi potentiellement en diminuer l'utilisation. Afin de faire une synthèse contrôlée de CNT uniformes, il est nécessaire de gérer la taille et la densité des CNT lors du dépôt du catalyseur. Nous avons étudié les nanoparticules de Co/Ni, évaporées séparément ou conjointement sur

du carbone, en utilisant les techniques de spectroscopie photélectronique X (XPS), de spectroscopie de masse en temps de vol des ions secondaires (ToF-SIMS), de microscopie électronique à balayage (SEM) et de microscopie à force atomique (AFM). Nous avons constaté que les nanoparticules de Co/Ni sont très réactives, non seulement avec le substrat de carbone, mais aussi, avec le gaz résiduel, et ce même en ultravide, amenant à une couche surfacique d'oxydes et de carbures. Cette couche contaminée empêche la coalescence de nanoparticules et les aide à se stabiliser. L'AFM montre que la couche contribue à maintenir les dimensions de nanoparticules essentiellement indépendantes de la quantité de Co/Ni déposés. En outre, nous avons étudié le dépôt de nanoparticules de Co, et nous avons démontré qu'elles étaient plus réactives que les nanoparticules de Ni, étudiées précédemment par notre groupe. Tout cela nous a aidé à mieux comprendre le rôle du catalyseur dans la nucléation et la croissance des nanotubes de carbone sur des nanofibres de carbone, et aboutira à maîtriser leur croissance.

En plus d'améliorer l'adhérence des nanoparticules de Pt sur les supports de carbone, la synthèse des nanostructures de platine est devenue d'un grand intérêt, car l'efficacité et la sélectivité catalytique sont fortement tributaires de la taille et la forme du platine. Ici, nous avons démontré, pour la première fois, plusieurs moyens pour effectuer la synthèse des nanostructures, telles que les nanofleurs de Pt en 3D, et les hétérojonctions NW-CNT, via des réactions de réduction chimiques simples, à la température ambiante, sans gabarit ou agents tensioactifs. Les électrodes modifiées avec ces nouvelles nanostructures de Pt présentent des activités électrocatalytiques importantes, qui peuvent aboutir à des applications dans les piles à combustible PEM. En outre, nous sommes les premiers à démontrer la conséquence directe de la croissance de nanofils de Pt sur les matériaux en carbone. Nous avons montré que la densité surfacique des NW

de Pt sur le MWCNT peut être efficacement contrôlée par l'intermédiaire du bon choix du taux de concentration de MWCNT et du précurseur de Pt. Nous avons aussi obtenu des charges très élevées de Pt sur CNT, par rapport à l'évaporation des dépôts de nanoparticules de Pt sur les CNT. Les évaluations électrochimiques plus détaillées de ces nanostructures de Pt sont en cours. Les résultats préliminaires ont déjà montré une augmentation des activités électrocatalytiques. Nous pensons que ces nouvelles nanostructures de Pt, en particulier les hétérojunctions Pt-C, peuvent avoir de nombreuses applications, non seulement en tant qu'électrocatalyseurs pour les piles à combustible PEM, mais aussi en électronique, photonique, détection, etc., ou comme nanodispositifs électrochimiques pour d'autres applications.

ABSTRACT

As a potential candidate for an environmentally benign and highly efficient electric power generation technology, proton exchange membrane fuel cells (PEMFC) are now attracting great interest for various applications. One of the challenges in the commercialization of PEMFCs is the high cost of the noble metals used as catalyst (e.g., Pt). Decreasing the amount of Pt used in a PEMFC via the increase of its efficiency of utilization has been a major concern during the past decade.

The main objective of this project has been to investigate the interfacial interaction of Pt nanoparticles with their carbon supports, so as to determine ways to optimise the catalyst electrode and to increase its catalytic activity, thereby enhancing PEM fuel cell performance.

We first studied the interfacial interaction (leading to adhesion) of Pt nanoparticles evaporated onto untreated and Ar^+-treated highly oriented pyrolytic graphite surfaces, with, respectively, low and high surface defect densities; HOPG was used as a model for carbon nanotubes (CNTs) and carbon fibers. We found that those Pt nanoparticles have very weak interactions with their pristine carbon material supports, with no evidence of compound formation between them. Our analysis, however, indicated that the adhesion of Pt nanoparticles to their supports can be enhanced, using ion beams, plasmas, or other treatments to establish defects on the carbon substrate surface. In addition, by using multicomponent XPS analysis with symmetric lineshapes for each Pt4f spectral component ($4f_{7/2,5/2}$), we attributed the component peaks to the existence of (i) surface oxidation on the platinum nanoparticles, and different electronic configurations of (ii) surface and (iii) bulk Pt atoms. We used the varying intensities of

these component peaks, as a function of deposited Pt, to explain the changing shape of the Pt4f asymmetric envelope as a function of nanoparticle size.

One way of enhancing strong adhesion between them is by chemical functionalization of the support. Using mixed H_2SO_4/HNO_3 acid treatments, we have characterized the surface chemistry of functionalized carbon fiber paper by combining infrared, Raman and X-ray photoelectron spectroscopies, to give new insights into the often-used oxidation of graphene-containing materials. We have, for the first time, demonstrated the presence of transient O-, N- and S-containing species during the oxidation process, as well as the fact that the intensities of those species varied unpredictably with treatment time, especially in the early stages, rather than constantly increasing with time. This study helps to better understand and control the functionalization of carbon materials, so as to establish the strong adhesion of Pt nanoparticles, thereby enhancing fuel cell performance.

Even with the functionalization of the CNTs to increase the mass activity of the catalyst, there is still a significant fraction of Pt that is isolated from the external circuit and/or the PEM, resulting in low Pt utilization. Growing CNTs directly on carbon fiber paper, followed by Pt deposition, however, ensures that all the Pt nanoparticles are in electrical contact with the external electrical circuit, improves Pt utilization and could potentially decrease Pt usage. In order to synthesize controlled, uniform CNTs, it is necessary to manage the size and density of the deposited CNT growth catalyst. We have studied Co nanoparticles and Co-Ni alloy nanoparticles, deposited onto carbon material supports, using X-ray photoelectron spectroscopy (XPS), time-of-flight secondary ion mass spectrometry (ToF-SIMS), scanning electron microscopy (SEM) and atomic force microscopy (AFM). We found that these nanoparticles are quite

reactive, not only with the carbon substrate but, also, with residual gas, even in ultra-high vacuum, to form surface carbides and oxides. This surface contaminant layer prevents further nanoparticle coalescence and helps to stabilize them. AFM shows that the surface layer helps to maintain nanoparticle dimensions that are essentially independent of the amount of Co/Ni deposited. By analyzing the Co/Ni nanoparticles, we also demonstrated that Co is more reactive than Ni. All this has helped to better understand the role of the catalyst in the nucleation and growth of carbon nanotubes on carbon nanofibers, and will ultimately lead to control their growth.

In addition to enhancing the adhesion of the Pt nanoparticles to the carbon supports, the synthesis of specific platinum nanostructures has become an area of considerable interest, since catalytic efficiency and selectivity are highly dependent on the size and shape of the platinum material. Here, we have synthesized, for the first time, several novel nanostructures, such as 3D Pt nanoflowers and the single-crystalline Pt nanowire (NW)–CNT heterojunctions, via simple chemical reduction reactions, at room temperature, without templates or surfactants. Electrodes modified with these novel Pt nanostructures exhibit good electrocatalytic activities, which may ultimately lead to their adoption in PEM fuel cells. In addition, we were the first to demonstrate the direct growth of single-crystalline Pt nanowires on carbon materials. We showed that the surface density of Pt NWs on the MWCNTs can be effectively controlled through the proper choice of the concentration ratio of MWCNTs and the Pt precursor; we can also obtain very high Pt loadings on CNTs, compared to the evaporative deposition of Pt nanoparticles on CNTs. More detailed electrochemical evaluations of these Pt nanostructures are under way; preliminary results have already shown increased electrocatalytic activities. We believe that these novel Pt nanostructures, especially Pt-C heterojunctions, hold much potential application, not only as electrocatalysts for PEM

fuel cells, but also in electronic, photonic, sensing, etc., nanodevices for other electrochemical applications.

CONDENSÉ EN FRANÇAIS

Les piles à combustible à membrane polymérique (PEMFC) présentent de nombreux avantages : des rendements et des densités électriques élevées pour un fonctionnement à faible température. Ces piles connaissent un grand intérêt dans plusieurs applications comme les véhicules à faible émission de gaz (voire à émission nulle), les groupes électrogènes domestiques et les sources d'énergie pour les appareils électroniques portables. Parce qu'elles fonctionnent à une température relativement basse (80 °C), les piles à combustible PEM requièrent l'utilisation d'un catalyseur pour générer des courants appréciables. La totalité des piles commerciales récentes ou les prototypes utilisent, comme catalyseurs, des nanoparticules de platine (Pt) ou à base de Pt, aussi bien à l'anode qu'à la cathode, en raison de leur grande surface spécifique (grand rapport surface/volume) et de leur bonne électroactivité. Ainsi, l'un des défis majeurs pour la commercialisation des piles à combustible, est la réduction des coûts des catalyseurs. L'un des objectifs de ces dernières années a été la diminution de la quantité et l'amélioration du Pt utilisé dans les PEMFC.

L'objectif général de ce projet est de comprendre, de manière approfondie, l'interaction interfaciale des nanoparticules métalliques avec le carbone afin d'optimiser le catalyseur et d'accroître son électroactivité, et ainsi d'améliorer les performances des piles PEM. Les principaux objectifs de cette étude sont les suivants :

(1) L'étude de l'interaction entre les nanoparticules de Pt et le carbone, de manière à contrôler la morphologie des nanoparticules de Pt ainsi que la stabilité à long terme dans les conditions réelles d'utilisation des piles à combustible.

(2) l'étude de la fonctionnalisation des surfaces de carbone par greffage de manière à

obtenir une bonne adhérence des catalyseurs sur le carbone.

(3) l'étude de l'interaction des nanoparticules Co/Ni utilisées comme catalyseurs pour la croissance des nanotubes de carbone (CNT), ainsi que les papiers en fibres de carbone utilisés comme substrats pour la croissance des CNT pour le contrôle du diamètre et de la densité de surface des CNT. La croissance des CNT sur les fibres de carbone avec une bonne adhésion et exempt d'agrégats permettrait en effet une meilleure utilisation du platine dans les piles à combustible.

(4) la synthèse spécifique de nanostructures de Pt (différente de celles généralement utilisées avec les nanoparticules) possédant une grande surface spécifique de manière à augmenter l'activité catalytique et le rendement de l'utilisation, assurant ainsi de bonnes performances des PEMFC.

Ce projet de recherche est fondé sur les suivants :

(1) Notre groupe a mené depuis plusieurs années une étude approfondie de l'adhésion de nanoparticules à base de métaux de transition (Cu, Ni, Au, etc.) sur un substrat de graphite pyrolytique hautement orienté (HOPG). Le HOPG possède une structure similaire aux nanotubes de carbone, mais il est composé de feuilles de graphènes planaires. Par ailleurs, le HOPG a été largement utilisé dans l'étude de nanoparticules métalliques. Il possède en effet une structure bien définie avec une surface possédant beaucoup moins de défauts que les nanotubes de carbone à multi parois (MWCNT), une faible interaction avec le métal et une faible capacité de clivage. Ainsi, nos précédentes expériences sur HOPG peuvent constituer un modèle pour l'étude des interactions interfaciales nanoparticules-nanotubes.

(2) Une façon d'améliorer l'adhésion entre les nanoparticules métalliques et leur support en carbone, est de fonctionnaliser les matériaux. Jusqu'à présent, plusieurs méthodes différentes ont été expérimentées sur le traitement de fonctionnalisation : le traitement le plus utilisé consiste en un mélange d'acides sulfurique et nitrique (H_2SO_4/HNO_3), avec soit un reflux à haute température, soit une durée prolongée dans un bain à ultrasons, à basse température. Malgré la popularité de ce traitement, le mécanisme d'oxydation n'est pas connu. Nous avons dans un premier temps utilisé un bain à ultrasons et des traitements plasma pour fonctionnaliser les CNT et le HOPG; ces techniques induisent plusieurs types de carbone oxydé (–OH, –C=O, –COOH), et ce de façon reproductible. Ces résultats pourraient alors nous permettre d'étendre notre étude sur le traitement du mélange d'acide H_2SO_4/HNO_3 et proposer de nouvelles idées sur le mécanisme de ce traitement.

(3) Grâce à leurs uniques propriétés structurale, mécanique et électrique, les CNT ont récemment été proposés pour remplacer les traditionnelles poudres de carbone utilisées dans les PEMFC. Toutefois, les résultats obtenus en utilisant une poudre de nanotubes de carbone n'ont pas montré beaucoup d'avantages par rapport au noir de carbone parce que les problèmes d'utilisation du platine dans la couche catalytique sont restés inchangés en pile à combustible. Faire croître d'abord des CNT directement sur le papier de fibre de carbone, puis ensuite déposer le Pt sur les CNT, permet d'améliorer l'utilisation du Pt en assurant le contact électrique depuis les nanoparticules jusqu'au support de l'électrode. L'utilisation de la croissance *in-situ* des CNT garantit le passage électronique et élimine l'isolation du carbone dans l'électrode de Nafion. La taille et les propriétés des nanoparticules étant directement reliées au diamètre des CNT, il est important de comprendre la réaction interfaciale entre le catalyseur et le support de papier de fibre de carbone, sur lesquels les CNT

croissent directement.

(4) Il est généralement admis que le rendement et la sélectivité catalytiques dépendent fortement de la taille et de la forme du matériau du catalyseur de la pile (ex. Pt). C'est pourquoi, la synthèse de platine avec une nanostructure spécifique connaît un intérêt considérable. Pourtant, jusqu'à présent, la plupart des études ont été limitées aux nanoparticules métalliques; dans ce cas, malgré l'augmentation de la surface spécifique des nanoparticules par les supports de carbone, il y a toujours une fraction significative de Pt qui est isolée du circuit externe et/ou de la membrane, entraînant la faible utilisation du Pt. Ainsi, la maîtrise de la synthèse de nouvelles nanostructures de platine, telles les nanofleurs, les nanotubes, les nanofils, les couches minces de Pt nanoporeux ou encore les nanocristaux de Pt tétrahédriques, tous avec un indice de facettes et une activité électrooxydante élevés, présenteraient de forts avantages par rapport aux performances du catalyseur dans les applications des piles à combustible.

Cette thèse comporte deux chapitres en guise d'introduction, trois articles et une conclusion finale. Le premier chapitre introduit les piles à combustible, en particulier les piles à combustible à membrane échangeuse de protons (PEMFC) en plus des défis des catalyseurs. Ensuite, ce chapitre présente les objectifs et l'organisation de cette thèse.

Le deuxième chapitre présente les principes de base de plusieurs techniques expérimentales qui ont été utilisées pour étudier et comprendre complètement la composition chimique surfacique et la structure surfacique des échantillons. Ces techniques sont les suivantes: la spectroscopie photoélectronique par rayons-X (XPS), la spectrométrie de masse d'ions secondaires à temps de vol (ToF-SIMS), la

spectroscopie infrarouge à Transformée de Fourier (FTIR), la spectroscopie Raman, la microscopie électronique à balayage (SEM), la microscopie électronique à transmission (TEM) et la microscopie à force atomique (AFM).

Les chapitres 3 à 5 consistent en trois articles, présentant les principaux résultats de la thèse.

Le premier article (chapitre 3) présente l'étude par XPS de l'interaction interfaciale (adhésion) des nanoparticules de Pt évaporées sur HOPG non-traité et traité par Ar^{+}, possédant respectivement des densités de défauts faible ou importante. La technique XPS est spécifique aux surfaces. Elle a une profondeur de sonde de quelques nanomètres; celle-ci a été largement utilisée pour la caractérisation des propriétés structurales chimiques et électroniques des nanoparticules métalliques.

(1) Nous avons constaté que ces nanoparticules de Pt présentent de faibles interactions avec les supports de carbone non-traités, ne démontrant aucune formation de composés entre eux. C'est pourquoi, tout au long de la durée de vie du catalyseur, les nanoparticules diffusent facilement et coalescent en de plus gros agglomérats, entraînant la diminution de la surface catalytique disponible et l'activité de la particule.

(2) En comparant les surfaces traitées et non-traitées, nous avons également remarqué que plusieurs propriétés (ex. taille, distribution, etc...) de ces nanoparticules de Pt dépendent des défauts apparaissant sur les surfaces du substrat de carbone. L'utilisation de faisceaux d'ions, de plasmas, ou d'autres traitements a montré des défauts à la surface du carbone, améliorant ainsi l'adhésion des nanoparticules de Pt sur leurs supports.

(3) Les analyses XPS consistent à déconvoluer les pics par le biais de courbes symétriques. Pour chaque pic Pt 4f ($f_{7/2}$ et $f_{5/2}$), nous avons attribué les composantes dues à l'existence (i) d'une oxydation de surface des nanoparticules de Pt, (ii) aux différentes configurations électroniques des atomes de Pt en surface et (iii) en profondeur. Nous avons utilisé les diverses intensités de ces pics, en relation avec le Pt déposé pour expliquer le changement de l'asymétrie du spectre du Pt4f en fonction de la taille des nanoparticules. Ainsi, nous proposons une explication consistante sur le changement de la forme de l'enveloppe asymétrique de Pt4f avec la taille des nanoparticules: l'asymétrie du pic est due à l'existence de composantes identifiables de forme symétrique qui se superposent. Nous avons trouvé que la proposition faite par Doniach et Šunjić, acceptée depuis plus de 40 ans, pour expliquer l'asymétrie des composantes spectrales, montre des contradictions avec nos présents résultats.

Ces résultats sur l'interaction interfaciale entre les nanoparticules de Pt et leurs supports de carbone peuvent nous aider à mieux comprendre et à découvrir de bonnes voies pour changer et/ou contrôler les propriétés du catalyseur utilisé dans les PEMFC.

Etant donné que les nanoparticules de Pt présentent de très faibles interactions interfaciales avec le carbone, il est nécessaire de modifier la surface du support de carbone comme par exemple en introduisant des groupes fonctionnels capables de réagir avec le Pt déposé. La réaction interfaciale leur confère une meilleure adhésion à la surface et conduit à une plus grande densité de surface (nombre de nanoparticules par unité de surface) des nanoparticules plus petites et plus uniformes. Jusqu'à présent, plusieurs méthodes différentes ont été expérimentées sur le traitement de fonctionnalisation; le traitement le plus utilisé consiste en un mélange d'acides

sulfurique et nitrique (H_2SO_4/HNO_3), avec soit un reflux à haute température, soit une durée prolongée dans un bain à ultrasons à basse température. Malgré la popularité de ce traitement, le mécanisme d'oxydation n'est pas connu.

Le second article (chapitre 4) décrit notre étude du mécanisme de réaction du mélange d'acide H_2SO_4/HNO_3 avec les fibres de carbone que l'on veut fonctionaliser. Les mécanismes sont sensés être similaires à ceux des nanotubes de carbone, en se basant sur la combinaison des analyses infrarouge, Raman et XPS.

(1) En comparant trois méthodes utilisant un traitement H_2SO_4/HNO_3, avec ou sans bain à ultrasons, à températures ambiante ou élevée, nous avons obtenu un moyen efficace de fonctionnaliser les fibres de carbone : un mélange 3:1 en volume d'acides concentrés, avec passage au bain à ultrasons à 60 °C.

(2) En nous basant sur la méthode la plus efficace, nous présentons une nouvelle étude. Pour la première fois, nous avons démontré la présence non seulement d'espèces contenant de l'oxygène mais également de composés contenant des espèces amines et sulfures durant le processus d'oxydation. Il a également été démontré que la proportion de ces groupes fonctionnels varie en fonction de la durée du traitement, en particulier lors des premières étapes, plutôt qu'avec l'augmentation du temps. Nous avons démontré que les résultats antérieurs expliquant le processus d'oxydation sont en contradiction avec nos résultats actuels.

Cette étude permet de mieux comprendre et contrôler la fonctionnalisation du carbone permettant d'établir une forte adhésion des nanoparticules de Pt, améliorant ainsi les performances de la pile à combustible.

Comme nous l'avons mentionné auparavant, la croissance directe des nanotubes de carbone sur le papier de carbone assure un contact électrique depuis les nanoparticules métalliques jusqu'au collecteur de charges dans le support, puisque les nanotubes de carbones (ici les MWCNT) sont des conducteurs électriques. Par la suite, la structure relativement ouverte du papier de carbone ne permet pas le libre accès aux sites catalytiques, diminuant ainsi les surtensions du transport de masse qui sont particulièrement préjudiciables au niveau de l'anode. La méthode CVD a été largement utilisée comme une méthode pour la synthèse de ces CNT, car elle possède de nombreux avantages : faible coût, production à grande échelle, à basse température et présentant de faibles impuretés en carbone, comparativement avec les méthodes de décharge d'arc et d'ablation laser. Afin d'obtenir des CNT alignés ou contrôlés par l'utilisation de ces méthodes, il est nécessaire de se concentrer sur le contrôle de la taille et de la densité des catalyseurs à base de nanoparticules déposées. Pour synthétiser les CNT d'un diamètre uniforme, il est crucial de répartir uniformément le catalyseur à la surface du substrat. Jusqu'à présent, des catalyseurs à base de métaux de transition de la première série ont été utilisés, et en particulier les métaux non onéreux du groupe du fer tels le Co, Ni et leurs alliages.

Le troisième article (chapitres 5) présente nos études sur les nanoparticules de Co, évaporées sur les supports de carbone, en utilisant les analyses XPS et AFM; les analyses XPS apportent une information chimique, tandis que les analyses AFM montrent les morphologies des nanoparticules. Nous avons trouvé que les nanoparticules de Co sont plutôt réactives, non seulement avec les substrats de carbone, mais également avec les gaz résiduels même sous vide extrême, pour former sur la surface des oxydes et des carbures. Cette couche contaminée empêche la poursuite de coalescence des nanoparticules et contribue à les stabiliser. Les analyses AFM montrent

que la couche contribue à maintenir indépendamment la quantité déposée et les dimensions des nanoparticules de Co.

Nous avons aussi investigué les nanoparticules de Co/Ni (présentement étant analysées) co-évaporées sur des surfaces de HOPG, utilisant ToF-SIMS, XPS, SEM et AFM. ToF-SIMS détecte les fragments provenant de Co_xNi_y. Sous vide poussé, les nanoparticules réagissent avec les vapeurs résiduelles contenant C et O afin de former les carbures et oxydes de surface. Lors de l'exposition prolongée à l'atmosphère, le métal zérovalent ainsi que les carbures des deux composantes décroissent en fonction du temps, avec la formation de d'autres contaminants. Comme avec les métaux purs, la composante Co de l'alliage est la plus réactive.

Tout cela a aidé à mieux comprendre le rôle du catalyseur dans la nucléation et la croissance des nanotubes de carbone ou des nanofibres de carbone conduisant en définitive à maîtriser leur croissance.

En plus d'améliorer l'adhérence des nanoparticules de Pt aux supports de carbone, la synthèse de nanostructures spécifiques de Pt commence à présenter un intérêt considérable. En effet, l'efficacité et la sélectivité catalytiques dépendent fortement de la taille et de la forme du Pt. Toutefois, seules certaines méthodes ont été publiées; la plupart nécessite en général soit l'utilisation d'un surfactant ou d'un gabarit, soit une synthèse à températures élevées, mais quelquefois ces méthodes ont une limite d'application.

Ici, nous avons démontré (dans les Annexes B et C), pour la première fois, plusieurs voies de synthèse de nanostructures de Pt, telles les nanofleurs de Pt tridimensionnelles et les hétérojonctions Pt NW-CNT, à travers des réactions simples de réduction

chimique, à température ambiante, sans gabarit, ni surfactants.

(1) Ces superstructures tridimentionnelles de Pt, dans lesquelles l'assemblage à grande échelle de nanofleurs, composées de nanofils d'environ 4 nm de diamètre et de 10-30 nm de longueur, se produisent à température ambiante, sans aucun agent tensioactif, ni gabarit. Lorsque les nanofleurs adhèrent au papier de carbone, cela conduit à une plus grande surface électroactive, comparable à celle d'une électrode de Pt/C commerciale.

(2) De plus, nous avons été les premiers à réaliser la croissance directe de nanofils de Pt cristallin sur des matériaux carbonés. Nous avons montré que la densité de surface de NW de Pt sur MWCNT peut être contrôlée de manière efficace par le bon rapport de concentration de MWCNT et de précurseur du Pt; nous pouvons également obtenir des charges de Pt très élevées, du même ordre de grandeur que les nanoparticules de Pt sur CNT.

Des évaluations électrochimiques plus détaillées de ces nanostructures de Pt sont en cours d'étude, dans le but d'optimiser ces catalyseurs. Des résultats préliminaires indiquent leurs bonnes activités électrochimiques. Nous pensons que ces nouvelles nanostructures de Pt connaîtront de nombreuses applications potentielles, non seulement pour l'électrocatalyse des piles à combustible PEM, mais également pour d'autres applications électrochimiques dans les domaines de l'électronique, de la photonique et des senseurs.

En conclusion, en analysant l'interaction interfaciale entre les matériaux Pt et carbone, nous avons trouvé que les nanoparticules de Pt présentaient de très faibles interactions avec leurs supports de carbone non-traité. Pour obtenir une forte adhérence

entre eux, il existe deux principales manières d'optimiser les catalyseurs. La première méthode consiste à fonctionnaliser les supports de carbone par faisceaux d'ions, plasmas ou traitements chimiques (ex. H_2SO_4/HNO_3). Pour la deuxième méthode nous avons également étudié les catalyseurs (ex. Co/Ni) pour des croissances directes sur papier de fibre de carbone, pour lesquels le composite Pt/CNT/CP garantit le contact électronique et élimine l'isolation du support de carbone de l'électrode en Nafion, améliorant ainsi l'utilisation du Pt. La troisième méthode est de synthétiser des nouvelles structures spécifiques de Pt, telles les nanofleurs et les hétérojonctions de Pt NW-CNT, avec des surfaces spécifiques actives relativement élevées et d' importantes charges de Pt. Nous sommes convaincus que toutes ces études auront un impact considérable sur les catalyseurs pour les applications de piles à combustible PEM.

TABLE OF CONTENTS

LIST OF TABLES

LIST OF FIGURES

LIST OF ABBREVIATIONS AND SYMBOLS

Abbreviations

AES	Auger electron spectroscopy
AFC	alkaline fuel cell
AFM	atomic force microscopy
ARXPS	angle-resolved X-ray photoelectron spectroscopy
ATR-FTIR	attenuated total reflectance FTIR
BF	bright-field
BSE	backscattered electron
CCD	charge coupled device
CNTs	carbon nanotubes
CP	carbon paper
CNFs	carbon nanofibers
CVD	chemical vapor deposition
DF	dark-field
DMFC	direct methanol fuel cell
EDS	energy-dispersive X-ray spectroscopy
EELS	electron energy loss spectroscopy
ESCA	electron spectroscopy for chemical analysis
EXAFS	extended X-ray absorption fine structure
FC	fuel cell
FCC	face-centered cubic
FESEM	field emission scanning electron microscopy
HOPG	highly oriented pyrolytic graphite

FWHM	full width at half maximum
FTIR	Fourier transform infrared spectroscopy
HRTEM	high resolution transmission electron microscopy
IMFP	inelastic mean free path
IR	infrared
LEED	low energy electron diffraction
MEA	membrane electrode assembly
MCFC	molten carbonate fuel cell
MWCNTs	multiwalled CNTs
NPs	nanoparticles
NWs	nanowires
NW–CNT	nanowire–CNT
PA-FTIR	photoacoustic FTIR
PEM	proton exchange membrane
PEMFC	proton exchange membrane fuel cell
PAFC	phosphoric acid fuel cell
SAED	selected-area electron diffraction
SEM	scanning electron microscopy
SIMS	secondary ion mass spectrometry
SOFC	solid oxide fuel cell
STM	scanning tunneling microscopy
SWCNTs	single-walled CNTs
TEM	transmission electron microscopy
ToF-SIMS	time-of-flight SIMS
XRD	X-ray diffraction
VLS	vapor-liquid-solid

WDS	wavelength dispersive X-ray spectroscopy
XPS	X-ray photoelectron spectroscopy
UHV	ultra-high vacuum

Symbols

E_B	binding energy
E_K	kinetic energy
$\hbar\omega$	energy of the exciting X-ray photon
I	radiation intensity the sample surface (Wm^{-2})
l	orbital quantum number
s	the differential photoemission cross section
S_A	relative sensitivity factor of A
Φ	work function
λ_{AL}	attenuation length
θ	take-off angle
σ	spin quantum number

LIST OF APPENDICES

Chapter 1. Introduction

1.1 Research context

1.1.1 Fuel cells, with specific reference to proton exchange membrane fuel cells

With the increased demands of modern society, conventional energy sources, such as coal and petroleum, cannot satisfy our continually growing need for energy. For this reason, finding new energy sources, with higher efficiency, has become increasingly urgent. As a potential candidate for an environmentally benign and highly efficient electric power generation technology, fuel cells (FC), especially proton exchange membrane fuel cells (PEMFC), are now attracting great interest for various applications, such as low/zero-emission vehicles, distributed home power generators, and power sources for small portable electronics [1-3].

A fuel cell is an electrochemical device that can, with the help of catalysts, convert the chemical energies of the continuously supplied fuel and oxidant to electrical energy, as shown in Figure 1.1 [4]. Generically, most fuel cells consume hydrogen (or hydrogen-rich fuels) and oxygen (or air) to produce electricity, following a simply chemical process:

$$2H_2 + O_2 \rightarrow 2H_2O \tag{1.1}$$

Since the only by-products of the reaction are heat and water, fuel cells are very environmental-friendly.
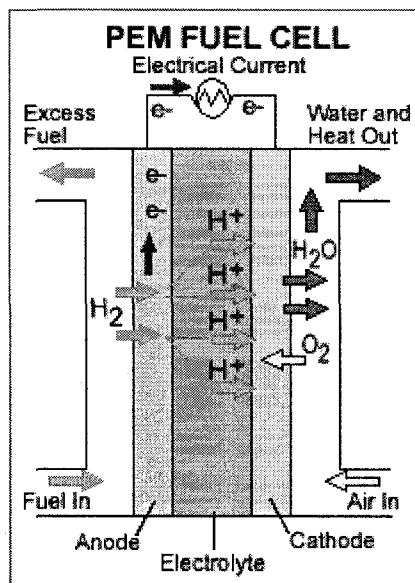
Figure 1.1. Schematic of a fuel cell.

Another selling point of fuel cell technology is its high energy-conversion efficiency [5]. Under favorable circumstances, this efficiency can be almost 60%. While this seems not to be a high value for the ''green economy'', it is much higher than that of car engines using fossil fuels (say 30% of a rated maximum). In addition, the engines will only be more efficient at high power loads while fuel cells are more efficient at low power loads. This is because fuel cells convert chemical energy directly to electrical energy, and this process does not involve conversion of heat or mechanical energy. Therefore, fuel cell efficiencies can exceed the Carnot limit even when operating at relatively low temperatures, for example, 80 °C. Figure 1.2, is a graphical illustration of energy conversion processes from chemical energy in fuels to electrical energy.
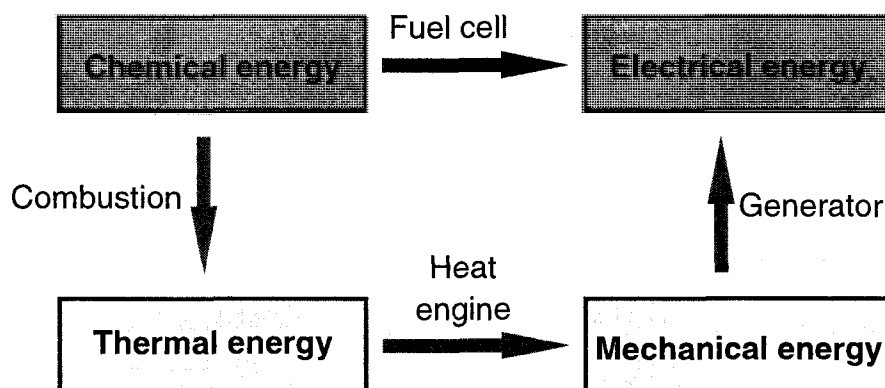
Figure 1.2. A graphical illustration of energy conversion processes.

In a word, fuel cells are promising energy conversion systems and can be used in many kinds of situations, from portable devices to large-scale power stations, as shown in Figure 1.3, because of their cleanliness (zero-emissions) and high efficiency (almost 60%) by comparison to the fossil fuels.

Traditionally, there are five types of fuel cells defined by electrolytes: Alkaline Fuel Cells (AFC), Phosphoric Acid Fuel Cells (PAFC), Molten Carbonate Fuel Cells (MCFC), Solid Oxide Fuel Cells (SOFC), and Proton Exchange Membrane Fuel Cells (PEMFC). Direct Methanol Fuel Cells (DMFC) have also been developed recently, but they can be classified as PEMFCs since they, too, use proton exchange membranes (PEM). Generally, almost all fuel cells (with the exception of DMFCs) consume hydrogen and oxygen to produce electrical current, as mentioned above; however, different fuel cell types have their strengths and weaknesses and, as a result, they have their application niches.
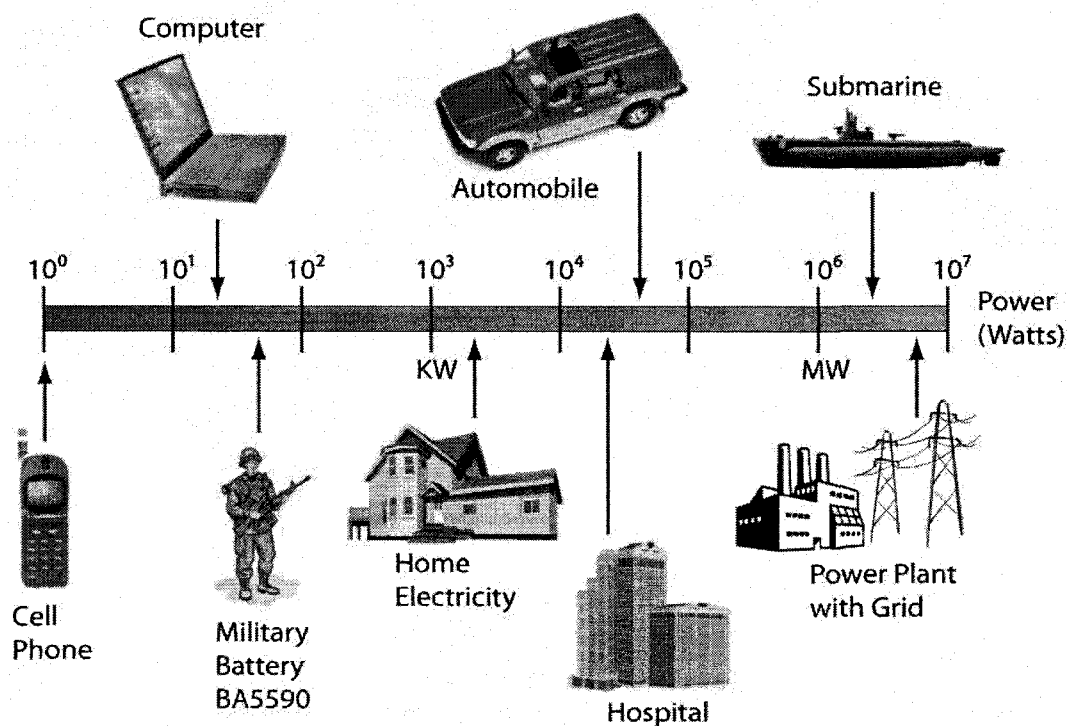
Figure 1.3. Fuel cell power spectrum.

At present, PEMFCs are attracting much more attention, and may, eventually, become a choice for power production due to their many advantages over the others. First, they work at lower temperatures and, as such, are very easy to start up; second, they are all solid-state and compact, and can thus provide high power density. Therefore, they have a wide range of applications, especially for vehicles.

A PEMFC consists of two electrodes and an electrolyte, as shown in Figure 1.4 [6]. At the anode, H_2 is fed in and split into protons and electrons with the help of catalysts. The protons are conducted through the membrane to the cathode, while the electrons

travel in an external circuit, supplying power. At the cathode, O_2 reacts with the protons and electrons to form water and heat.

Electric Circuit
(40%-60% efficiency)

Fuel input
(humidified
hydrogen gas)

Oxygen gas
(from air) input

Anode

Heat (85 °C)

Unused hydrogen gas
output recirculated

Air + Water output

Oxygen
cathode

| Gas diffusion backing | Catalyst electrode layer | PEM membrane | Catalyst electrode layer | Gas diffusion backing |

H_2 gas from serpentine flow field finds a pathway to catalyst layer

O_2 from air in serpentine flow field finds a pathway to catalyst layer

Pathway of H^+ conduction

Pathway of H_2O from catalyst layer

Carbon nanoparticles   Pt catalyst

Pathways of electron conduction

Figure 1.4. Schematic of the working mechanism for fuel cells.

1.1.2   Challenges of catalyst electrodes

While fuel cell technology is, by itself, very simple in principle, and there are huge advantages in many aspects of its implementation, it may still be considered in its infancy for applications in the wide consumer market since there are numerous reasons for the relatively slow development in "market-ready" fuel cells, such as high cost, membrane electrode assemblies (MEA), and hydrogen fuel problems.

In this thesis, we are specifically interested in catalyst electrodes since one of the challenges in the commercialization of PEMFCs is the high cost of noble metals used as catalysts (e.g., Pt). Decreasing the amount of Pt used in a PEMFC via an increase of its utilization efficiency has been a major concern during the past decade.
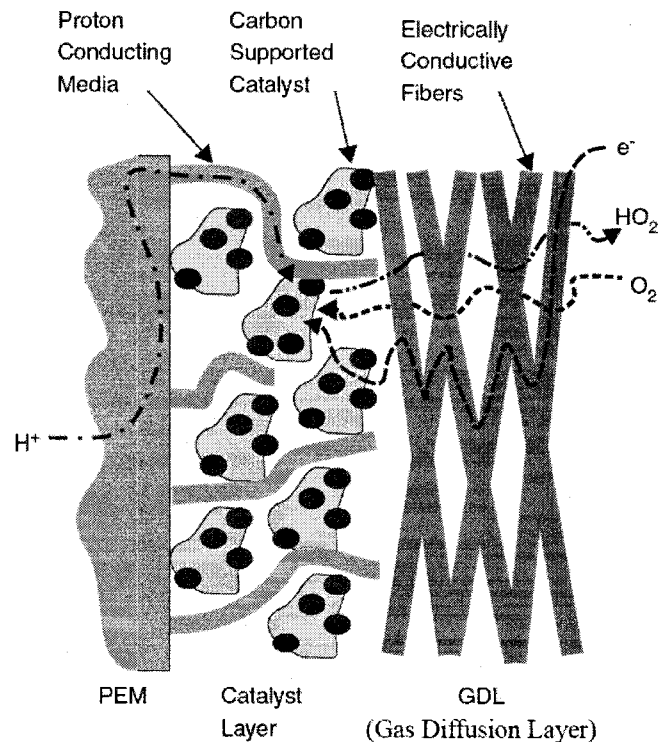
Figure 1.5. Illustration of the catalyst layer for PEM fuel cells.

To effectively utilize the Pt catalyst, it must have simultaneous access to the gas, and the electron-conducting and the proton-conducting media, as shown in Figure 1.5 [7]. In the catalyst layer of one Pt-based conventional (ink-process) fuel cell, the simultaneous access of the Pt particle to the electron-conducting and the proton-conducting media is achieved via a skillful blending of Pt-supporting carbon particles and Nafion. The carbon particles conduct electrons and the Nafion conducts protons. However, even with the most advanced conventional electrodes, there is still a significant portion of Pt that is isolated from the external circuit and/or the PEM, resulting in low Pt utilization. Efforts directed at improving the utilization efficiency of the Pt catalyst have focused on finding optimum material configurations while minimizing the Pt loading and satisfying the requirements of gas, and proton access, and electrical continuity. In the conventional ink-process, a common problem has been that the necessary addition of Nafion for proton transport tends to isolate carbon particles in the catalyst layer, leading to poor electron transport.

Due to their unique structural, mechanical, and electrical properties, carbon nanotubes (CNTs) have been proposed to replace traditional carbon powders in PEMFCs, and have been demonstrated by making MEAs using a carbon nanotube powder, through the conventional ink process [8,9]. However, these results did not show many advantages over carbon black (Vulcan XC-72) because the Pt utilization within the PEMFC catalyst layer remained unaddressed.

Growing carbon nanotubes directly on the carbon paper [10], and subsequently electrodepositing the Pt selectively on the carbon nanotubes, promises to improve the Pt utilization by securing the electron route from Pt to the supporting electrode in a PEMFC. The use of carbon nanotubes, and the resulting guaranteed electronic pathway,

eliminates the previously mentioned problem with conventional PEMFC strategies where the Nafion isolates the carbon particles from the electrode support, thereby improving the utilization rate of Pt. Further, the rather open structure of carbon paper enables free access of reactant gases to the catalytic sites (see Figure 1.6), thus decreasing mass transport overvoltages, which are especially detrimental at the anode. Preliminary studies have already shown the possibility of depositing metal particles onto carbon nanotubes by using a grafted silane to fix Pt ions, which are readily reduced to metal by heat treatment in a reducing atmosphere [11]. High Resolution Transmission Electron Microscopy (HRTEM) has shown that it is feasible to produce very small Pt nanocrystals with high surface areas, on multiwalled CNTs (MWCNTs), which were themselves grown on carbon papers.
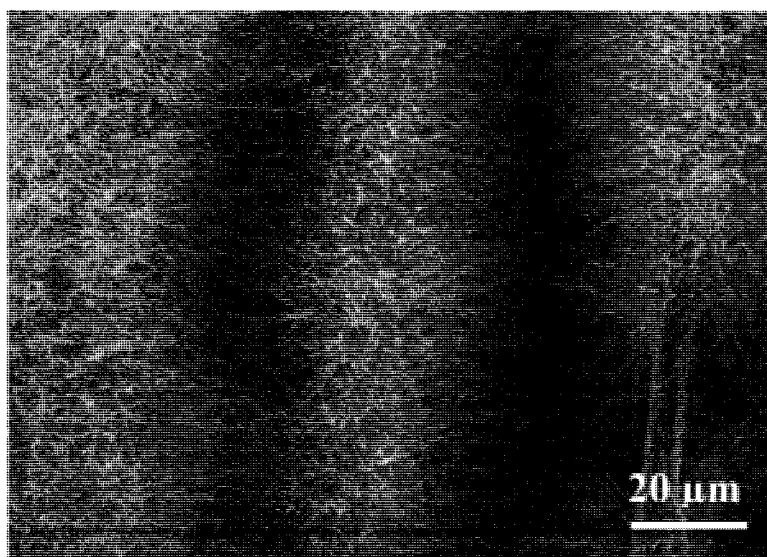
Figure 1.6. Carbon nanotubes grown on carbon fiber synthesized by chemical vapor deposition (CVD).

However, there are still some problems that need to be resolved to improve the Pt utilization. One may accomplish this in the following ways:

(1) To enhance the interfacial interaction between Pt nanoparticles and their carbon support, to avoid metal nanoparticle diffusion on the support, and coalescence into larger agglomerates, which would decrease both the available catalytic surface and the particle activity.

(2) To obtain controlled or aligned CNTs with a uniform diameter, grown directly on the carbon fiber papers.

(3) To find superior methods to increase Pt loading and their utilization, since it is generally acknowledged that both catalytic efficiency and selectivity are highly dependent on the size and shape of the catalyst material.

1.2   Objectives of the thesis

The general objective of this project is to understand, in greater depth, the interfacial interaction of metal nanoparticles with their carbon material supports and, using this, to determine methods to optimise the catalyst electrode and to increase its catalyst activity, enhancing the performances of PEM fuel cells. Specific goals are as follows:

(1) To study the interaction between Pt nanoparticles and their carbon supports, so as to achieve well-controlled Pt nanoparticle surface densities and sizes, as well as long-time nanoparticle stability at the operating conditions of the fuel cell.

(2) To study the functionalization of carbon materials by grafting or depositing functional groups, in order to determine the best methods of firmly adhering the

catalyst nanoparticles to the carbon material supports.

(3) To study the interaction of Co/Ni nanoparticles, used as catalysts to grow carbon nanotubes, and the carbon fiber papers used as CNT growth substrates, in order to control the diameter and surface density of the CNTs. Growing CNTs directly on the carbon fiber paper, with good adhesion and no bundling, followed by Pt deposition, promises to improve the Pt utilization for fuel cells.

(4) To synthesize specific Pt nanostructures (other than normally used nanoparticles, such as nanowires or nanotubes), with high surface areas for increased catalytic activity and utilization efficiency, thereby much increasing PEM fuel cell performances.

1.3   Organization of the thesis

This thesis consists of two introductory chapters, six articles (three are in the text, and the others are in the appendices) and one final chapter. The first chapter gives an introduction to fuel cells, especially proton exchange membrane fuel cells (PEMFCs), as well as challenges of the catalyst electrodes. It then provides the objectives and organization of the thesis. The second chapter presents the basic principles of several experimental analytical techniques, which were used to study and characterize the samples. The principal results of this thesis are presented in the chapters 3-5 and appendices, and their interrelationships are shown in Figure 1.7.

platinum ⟺ carbon materials

(Pt nanoparticles ⟺ HOPG)
weak interaction

novel Pt
nanostructures

functionalization
of carbon materials

Pt
nanoflowers

Pt nanowire-CNT
heterojunctions

Co/Ni for
growing CNTs
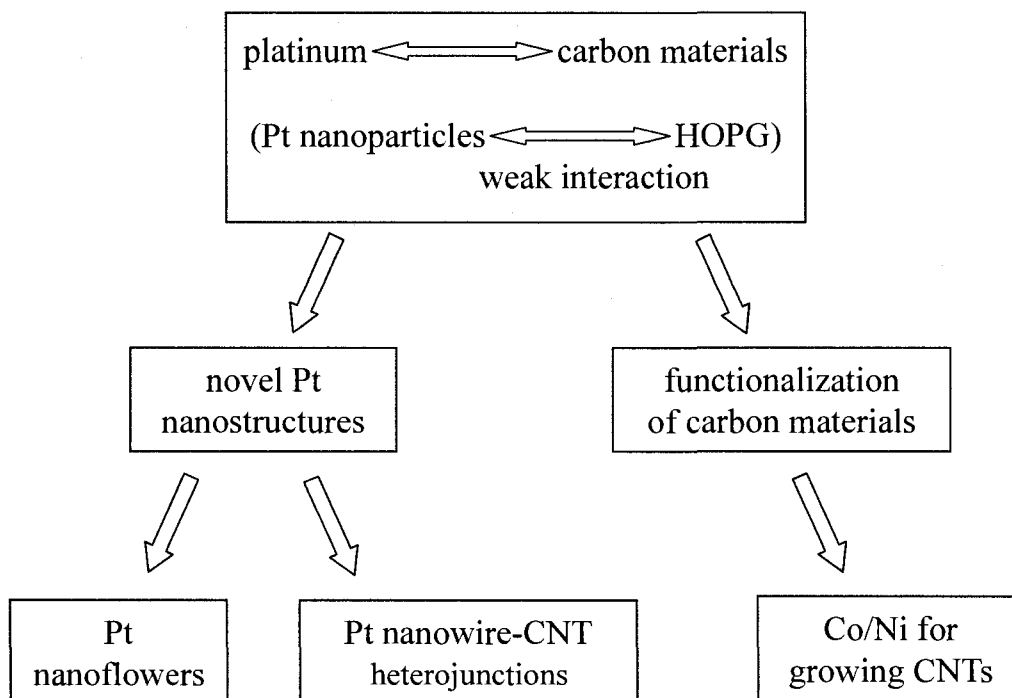
Figure 1.7. The interrelationships among the principal results of the thesis. The interfacial interaction of Pt nanoparticles and pristine HOPG surfaces was found to be weak. In order to enhance their adhesion, as well as for the purpose of increasing Pt utilization efficiency, several approaches were considered for optimising the catalyst electrode and for increasing its catalytic activity: (1) the study of carbon substrate functionalization, and the properties of Co/Ni nanoparticles as catalysts for growing CNTs directly on carbon fiber paper and (2) the study of the synthesis of specific Pt nanostructures, such as Pt nanoflowers (Appendix B) and single-crystalline Pt NW–CNT heterojunctions (Appendix C).

Chapter 3 (X-ray photoelectron spectroscopic analysis of Pt nanoparticles on highly

oriented pyrolytic graphite) describes the XPS characterizations of Pt nanoparticles evaporated onto untreated and Ar^+-treated highly oriented pyrolytic graphite surfaces, with, respectively, low and high surface defect densities. We wished to understand the interfacial interactions controlling the adhesion of Pt nanoparticles deposited onto such surfaces, since determining the adhesion of Pt nanoparticles to carbon-based materials is a key feature in the determination of catalyst activity for fuel cell applications. HOPG was used as a model for carbon nanotubes because it has a planar structure that is well characterized and understood.

Chapter 4 (The surface analytical characterization of carbon fibers functionalized by H_2SO_4/HNO_3 treatment) describes a systematic, time-dependent, surface-sensitive study, which has, for the first time, given new insights into the mechanism of the often-used, but unexplained, sulfuric/nitric acid oxidation of graphene-containing materials, such as carbon fibers and carbon nanotubes. This study helps us to better understand and control the functionalization of carbon materials by this method. The functionalization can establish the strong adhesion of Pt nanoparticles to their carbon material supports, and to maintain it over the field-use lifetime of the catalyst, thereby enhancing fuel cell performance.

Chapter 5 (The structure and morphology of Co nanoparticles deposited onto highly oriented pyrolytic graphite) studied the Co nanoparticles evaporated on carbon materials. The deposition of Ni nanoparticles was previously studied by our group [12]. Co/Ni nanoparticles can be used as efficient catalysts for growing CNTs, and it is important to understand the interfacial interaction between them and their carbon support, since it is known that the size and the properties of the catalyst nanoparticles are directly related to the diameter of the CNTs.

Concerning the novel Pt nanostructures, we reported, for the first time, their syntheses and characterization: 3D Pt nanoflowers (Appendix B) and the single-crystalline Pt nanowire–CNT heterojunctions (Appendix C). Electrodes, modified with these novel Pt nanostructures, exhibit good electrocatalytic activities, which implies their potential adoption in PEM fuel cells.

Chapter 6 presents a discussion of the results of the work, as well as our conclusions and suggestions of new avenues for future work.

1.4   Publications and conferences

● **Publications**

1. Yang, D. Q., **Zhang, G. X.**, Sacher, E. *Evidence of the Interaction of Evaporated Pt Nanoparticles with Variously Treated Surfaces of Highly Oriented pyrolytic Graphite*. **J. Phys. Chem. B**, 2006, 110, 8348.

2. **Zhang, G. X.**, Yang, D. Q., Sacher, E. *The interaction of evaporated Pt nanoparticles with variously treated surfaces of highly oriented pyrolytic graphite.* **J. Phys. Chem. C,** 2007, 111, 565.

3. **Zhang, G. X.**, Sun, S. H., Yang, D. Q., Dodelet, J. P., Sacher, E. *The surface analytical characterization of carbon fibers functionalized by H_2SO_4/HNO_3 treatment.* **Carbon**, in course of publication.

4. **Zhang, G. X.**, Yang, D. Q., Sacher, E. *The structure and morphology of Co nanoparticles deposited onto highly oriented pyrolytic graphite*. **J. Phys. Chem. C**, **2007**, 111, 17200.

5. **Zhang, G. X.**, Sun, S. H., Bostetter M., Poulin S., Sacher, E. *Chemical and morphological characterizations of Ni/Co alloy nanoparticles, co-evaporated onto highly oriented pyrolytic graphite*, to be submitted.

6.   Sun, S. H., Yang, D. Q., **Zhang, G. X.**, Sacher, E., Dodelet, J. P. *Synthesis and Characterization of Carbon Nanotube–Platinum Nanowire Heterostructures*. **Chem. Mater.**, in course of publication.

7.   Sun, S. H., Yang, D. Q., Villers, D., **Zhang, G. X.**, Sacher, E., Dodelet, J. P. *Template-free, Surfactant-free Room Temperature Synthesis of Self-Assembled 3D Pt Nanoflowers from Single-Crystal Nanowires*. **Adv. Mater.**, in course of publication.

● **Conferences**

1.   Sun, S. H., Yang, D. Q., **Zhang, G. X.**, Sacher, E., Dodelet, J. P. *Template-Free Synthesis of Self-Assembled 3D Pt Nanoflowers from Single-Crystal Nanowires and Their Electrocatalyst Properties*. **The 212th Meeting of the Electrochemical Society.** 2007, Washington DC, USA.

2.   **Zhang, G. X.**, Yang, D. Q., Poulin, S., Sacher, E. *An Example of the Use of Surface Analytical Techniques to Assess Nanoscale Interactions*. **Proceedings of the 30th Annual Meeting of the Adhesion Society**, Adhesion Society, Inc., Blacksburg, VA, USA. 2007, pp. 367-369.

3.   Yang, D. Q., **Zhang, G. X.**, Sacher, E. *XPS characterization of the interaction between Pt nanoparticles and highly oriented Pyrolytic Graphite*, Annual Meeting, Regroupement Québécois sur les Matériaux de Pointe, QC, Canada, 2007.

Chapter 2. Experimental techniques

A variety of analytical techniques have been used in this thesis to study the surface chemical composition and surface structure of the samples, such as metal nanoparticles on HOPG, carbon fibers, and CNTs. To fully understand physical and chemical properties of such samples required the combination of several analytical techniques, such as X-ray photoelectron spectroscopy (XPS), time-of-flight secondary ion mass spectrometry (ToF-SIMS), Fourier transform infrared spectroscopy (FTIR), Raman spectroscopy, scanning electron microscopy (SEM), transmission electron microscopy (TEM) and atomic force microscopy (AFM). This chapter presents the basic principles of these experimental techniques.

2.1 X-ray photoelectron spectroscopy (XPS)
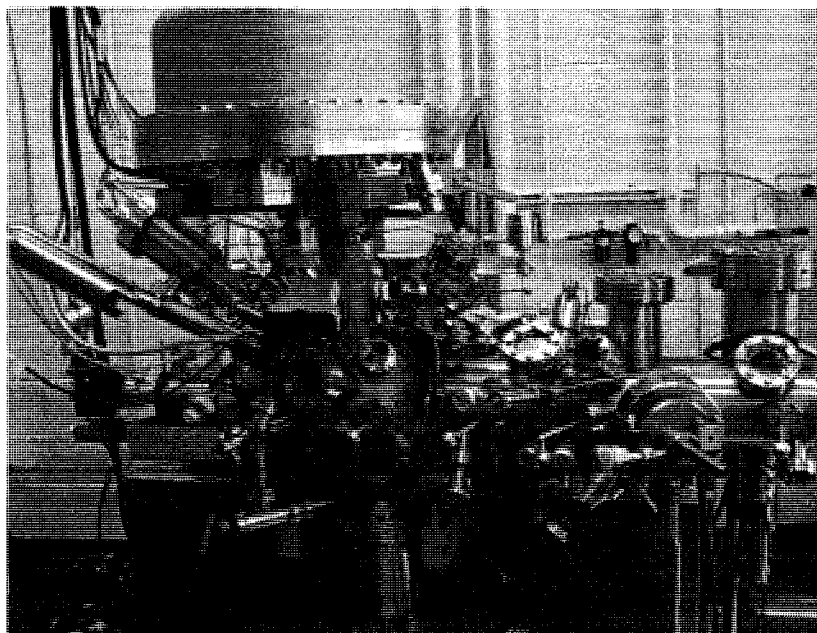
Figure 2.1. A photo of our VG ESCALAB 3 MARK II XPS.

X-ray photoelectron spectroscopy (XPS), also known as ESCA (Electron Spectroscopy for Chemical Analysis), is an extremely surface-sensitive, non-destructive analytical technique, which is widely used to determine the elemental composition and chemical states of the surface and near surface regions of various materials [13-15]. Figure 2.1 shows a photo of the XPS of our VG ESCALAB 3 MARK II (Thermo VG Scientific).

2.1.1 The basic principles of XPS

In XPS, a sample material is irradiated with mono-energetic soft X-rays, causing core level electrons to be ejected [16]. It is based on the photoelectric effect: when an x-ray beam irradiates the sample surface, the energy of the x-ray photon $\hbar\omega$, if larger than that of a core level of an atom, is adsorbed completely by the electron level. The core electron will then be photoemitted from the atom with a certain kinetic energy E_K. The binding energy of the core electron in the conducting solid, relative to the Fermi level, is given by the Einstein relationship, as shown in Equation 2.1 and schematically, in Figure. 2.2:

$$E_B = \hbar\omega - E_K - \Phi \tag{2.1}$$

where $\hbar\omega$ is the energy of the exciting X-ray photon; E_K is the kinetic energy of photoelectron measured by the energy analyzer; and Φ is the work function of the spectrometer (about 5 eV) [16]; its relation to that of the sample is shown in Figure 2.2 [17]. As the exciting photon energy of the X-ray ($\hbar\omega$) and Φ are known and E_K is determined experimentally, the binding energy of the core electron can be calculated from Eq. 2.1.
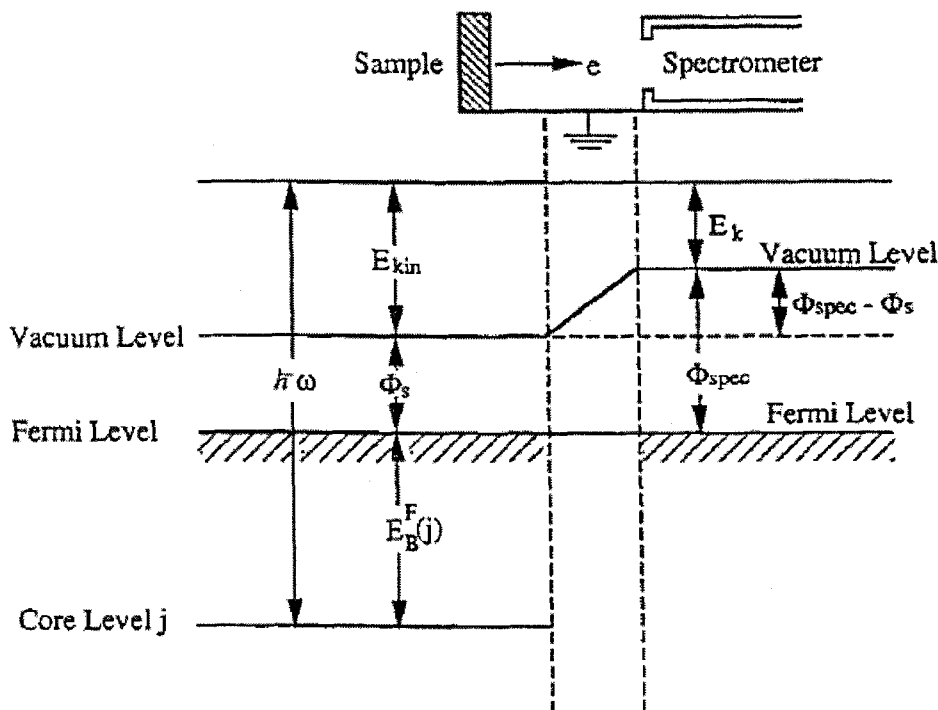
Figure 2.2. Schematic of the relevant energy levels for XPS binding energy measurement.

For insulating samples, once the photoelectrons are emitted out of the sample surface, a positive charge zone will be established quickly at the sample surface. As a result, the sample surface acquires a positive potential (varying typically from several volts to tens of volts) and the kinetic energies of core electrons are reduced by the same amount, C [18]:

$$E_B = h\upsilon - (E_K - C) - \phi \tag{2.2}$$

It can be seen that the surface charging results in the shift of the XPS peaks to higher binding energy. In this case, the binding energy has to be calibrated by correcting the

position of a known peak to a standard position. There are many approaches to charge correction; in this thesis, we chose the simplest and most widely used method: to shift the principal C1s line to 284.6 eV.

Since the core electron of an element has a unique binding energy, which is like a "fingerprint", almost all elements, except for hydrogen and helium, which have no core electrons, can be identified *via* measuring the core electron binding energy.

2.1.2 Instrumentation for XPS

A basic XPS instrument is schematically shown in Figure 2.3. The main components are a primary source of X-rays, an electron analyzer and a detector, all contained within an ultra-high vacuum (UHV) enclosure and controlled by a dedicated computer.
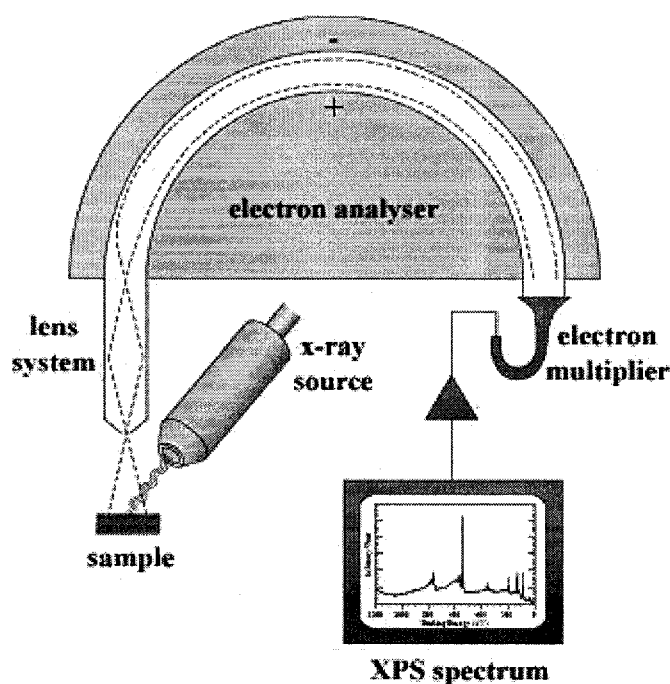
Figure. 2.3. Schematic of a typical XPS instrument.
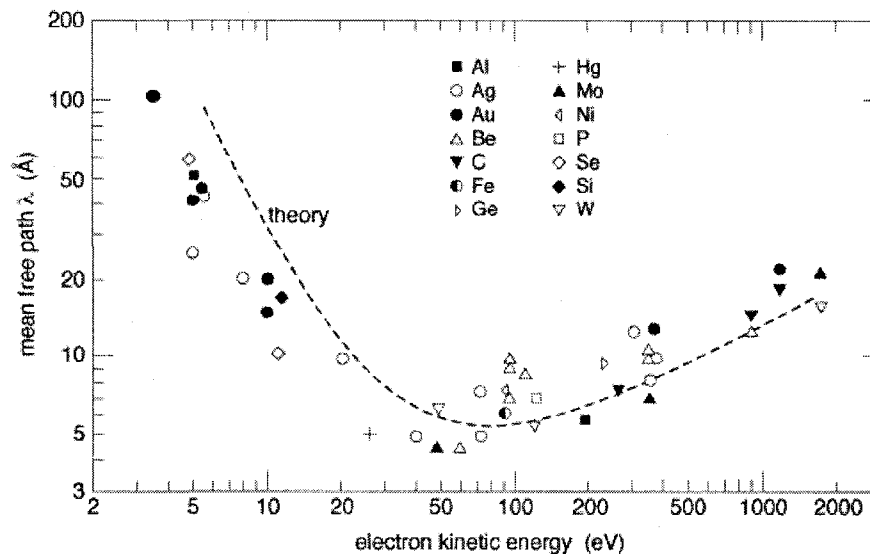
Figure. 2.4. Escape depth (mean free path) of electrons in solids as a function of their

kinetic energy.

Due to the X-ray source energy, the emitted photoelectrons will therefore have kinetic energies in the range of $\sim 0 - 1250$ eV (Mg K_α) or $\sim 0 - 1480$ eV (Al K_α); thus, the Inelastic Mean Free Path (IMFP) of the electron may be estimated by universal curves, as shown in Figure. 2.4 [19], and is typically $4 - 20$ Å. It is defined as the distance, normal to the surface, at which the number of electrons escaping without significant energy loss drops to e^{-1} (36.8 %) of its original value. The detail for clarifying these terms is found in reference [16].

Since 95% of the signal detected comes from within a depth of three times the escape depth, the sampling depth d, shown as Figure 2.5, is given by

$$d = 3\lambda_{AL} \sin\theta \qquad (2.3)$$

where λ_{AL} is the attenuation length and θ is the take-off angle. Therefore, the XPS technique has high surface sensitivity, with an analysis depth less than 10 nm. In addition, the variation of the vertical sampling depth with photoelectron take-off angle, can be used to perform non-destructive analysis of the variation of the surface composition with depth. This technique is often referred to as angle-resolved XPS (ARXPS) [16].
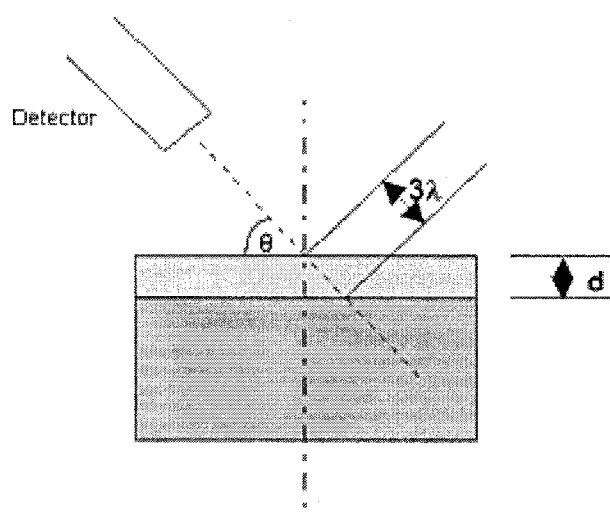
Figure 2.5. Schematic of the sampling depth for XPS.

2.1.3 Information from XPS spectra

A typical X-ray photoelectron spectrum is illustrated in Figure 2.6, and the various components that contribute to it are clearly evident. In that spectrum, the peaks can be grouped into three classes: those due to photoemission from core levels, those due to photoemission from valence levels and those due to X-ray excited Auger emission (Auger series). Note that, sometimes, satellite peaks can be seen due to the sudden approximation, where the relaxation of the valence electrons in response to photoemission of a core-electron is such that the final state may involve an electron in an

excited bound state (shake-up), or in an unbound state above the vacuum level (shake-off), as shown in the inset of Figure 2.7.
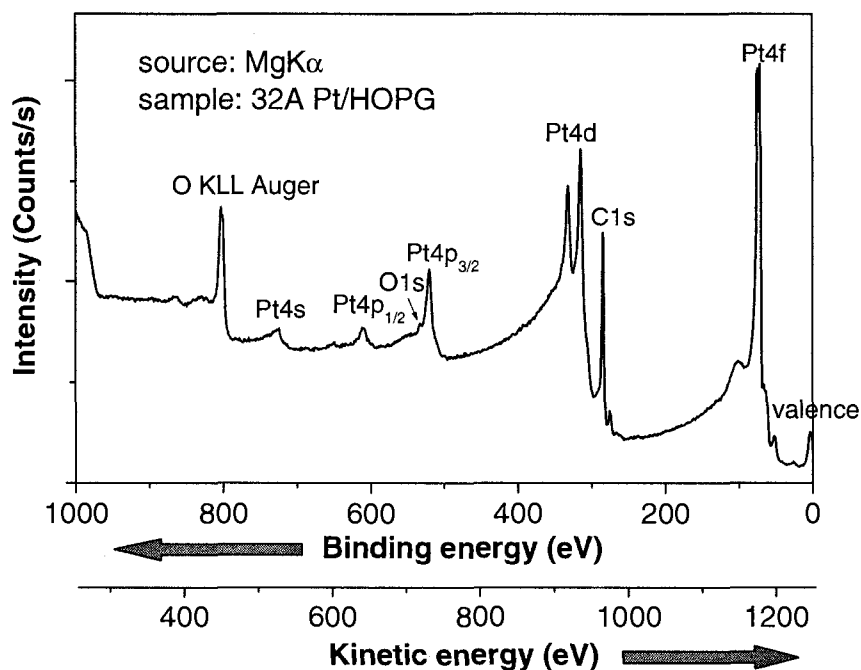
Figure 2.6. XPS survey spectrum of Pt nanoparticles evaporated onto HOPG, excited by MgKα.

Another important feature in XPS spectra is that non-s levels are doublets due to spin-orbit coupling, as shown in Figure 2.8. The doublets arise through the fact that an electron is a charged particle, and its orbit (with the characteristic quantum number l, l = *0, 1, 2, 3,* ...) around a nucleus induces a magnetic field, which will interact with the inherent magnetic field of the electron, produced by the spin (with spin quantum number s, s = ± 1/2) [16]. Under the j-j coupling scheme, the interaction energy E_j can be expressed as

$$E_j = \frac{1}{4m^2c^2}\left(\frac{1}{r}\cdot\frac{dU(r)}{dr}\right)\cdot\left[j\cdot(j+1)-l(l+1)-\frac{3}{4}\right] \tag{2.4}$$
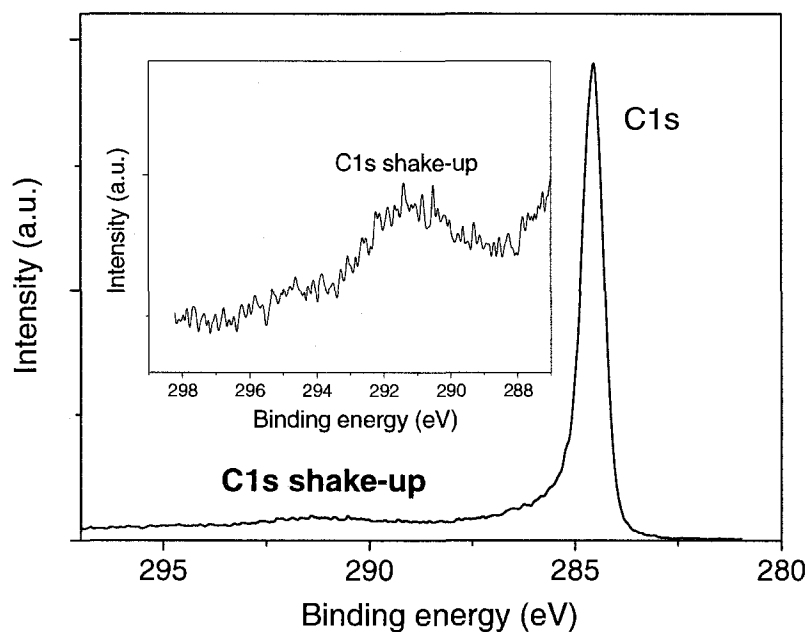
Figure 2.7. C1s XPS spectrum of carbon fiber paper excited by Al$K\alpha$; inset is the C1s $\pi^*\leftarrow\pi$ shake-up with binding energy at about 291 eV.

where m is the electron mass, c is the speed of light, r is the orbit radius, U(r) is the central force potential, and $j = l \pm 1/2$. Two possible states arise when l > 0. The spin-orbit splitting ΔE_j, the difference in energy of two states reflects the "parallel" or "anti-parallel" nature of the spin and orbital angular momentum vectors of the remaining electron.
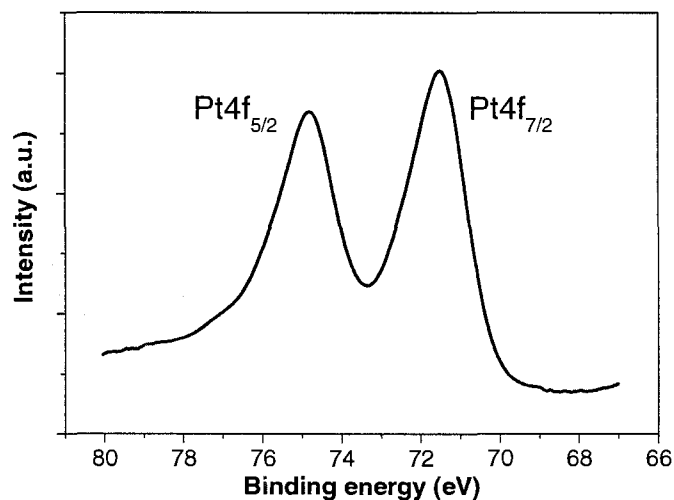
Figure 2.8. A typical example of non-s level XPS spectrum.

The spin-orbit splitting, ΔE_j, and relative intensity of the doublet peaks are important parameters in the curve-fitting of XPS spectra. The relative intensities of the doublet peaks are given by the ratios of their respective degeneracies (2j+1). The intensity ratios and designations (n, l, j) of spin-orbit doublets are given in table 2.1.

Table 2.1. Spin-orbit splitting parameters.

Subshell	l	j values	Area ratio
s	0	1/2	–
p	1	1/2, 3/2	1:2
d	2	3/2, 5/2	2:3
f	3	5/2, 7/2	3:4
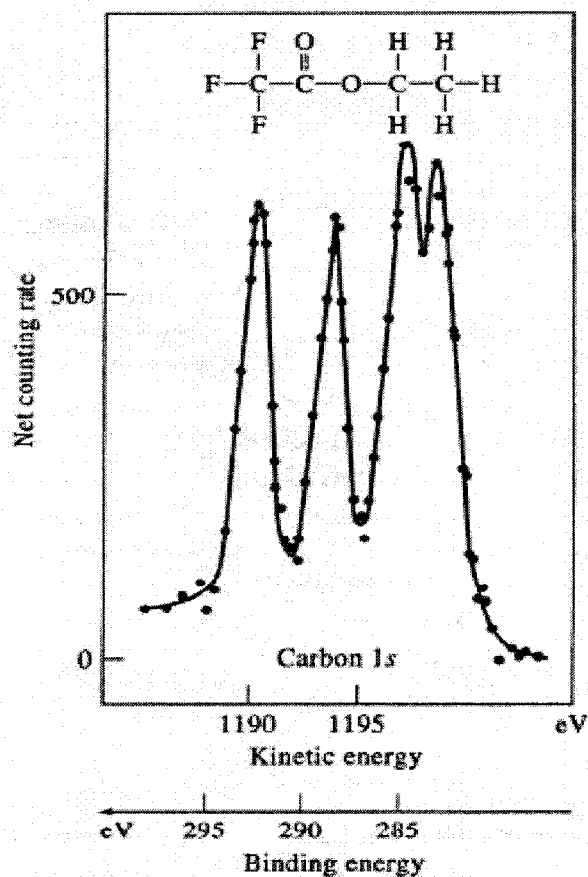
Figure 2.9. C1s chemical shifts in ethyl trifluoroacetate. Note that the four carbon peaks correspond to the four carbon atoms within one molecule.

Since the core electron of an element has a unique binding energy, which seems like a "fingerprint", almost all elements except for hydrogen and helium can be identified *via* measuring the binding energy of their core electrons. Furthermore, the binding energy of a core electron is very sensitive to the chemical environment of element. The same atom may be bonded to the different chemical species, leading to changes in the binding energy of its core electron. The variation of binding energy results in the shift of the

corresponding XPS peak, ranging from 0.1eV to 10eV. This effect is termed a "chemical shift", which can be applied to studying the chemical states of elements in the surface. Therefore, XPS is also known as electron spectroscopy for chemical analysis (ESCA). A good illustration of the chemical shifts as a function of the chemical environment or valence state is demonstrated in the spectrum of the C1s levels in ethyl trifluoroacetate, found in Figure 2.9 [20]. In this molecule, each carbon atom is in a different chemical environment and yields a slightly different XPS line. The binding energies of C1s cover a range of about 8 eV.

Since the number of photoelectrons of an element is dependent upon the atomic concentration of that element in the sample, XPS is used to not only identify the elements but also quantify the chemical composition. Quantitative analysis can be achieved through the use of relative sensitivity factors, with one elemental peak taken as the standard to which other peaks are referred (usually F1s, or C1s).

The intensity of a core level j from element A, I_{jA}, can be expressed by the following relationship:

$$I_{jA} = K_A \cdot \sigma_{jA} \cdot N_A \cdot \lambda_A \cos(\alpha) \qquad (2.5)$$

where I_{jA} is the intensity of the XPS peak generated by the orbital j of the element A, which can be determined by the area under the peak envelope after background subtraction; K is an experimental parameter often referred to as the instrument transmission function; σ is the differential photoemission cross section; N is the atom density of the sample surface; λ is the inelastic mean free pass; α is the take-off angle, namely the one between the collection detection of the analyzer and the normal to

the sample surface. Thus, the intensity ratio of the two different peaks (one is element A and the other one is the standard element) is

$$\frac{I_A}{I_S} = \frac{K_A \cdot \sigma_A \cdot N_A \cdot \lambda_A \cos(\alpha)}{K_S \cdot \sigma_S \cdot N_S \cdot \lambda_S \cos(\alpha)} \qquad (2.6)$$

Defining $I_S = 1.00$ gives

$$I_A = \frac{K_A \cdot \sigma_A \cdot \lambda_A \cos(\alpha)}{K_S \cdot \sigma_S \cdot N_S \cdot \lambda_S \cos(\alpha)} N_A = S_A N_A \qquad (2.7)$$

where S_A is the relative sensitivity factor of A. The relative sensitivity factors can be calculated or determined empirically. However, it is believed that the quantification is more accurate when empirical relative sensitivity factors are employed as compared with the calculated values; this is mainly because of the fact that the measured intensity omits shake-up and shake-off events. Since the relative sensitivity factors are related to the instrument, it may be most expedient to determine them under the particular instrument conditions routinely used.

With these relative sensitivity factors (S_n), the relative atomic concentration of any chosen element, A, is then simply obtained from

$$C_A = \frac{I_A/S_A}{\sum_n (I_n/S_n)} \times 100\% \qquad (2.8)$$

where C_A is usually expressed as atomic% (of all elements determined, hydrogen excluded).

2.2 Time-of-flight secondary ion mass spectrometry (ToF-SIMS)

Time-of-Flight Secondary Ion Mass Spectrometry (ToF-SIMS) is the mass spectrometry of ionized particles (positive and negative) which are emitted from a surface when an energetic primary ion beam, typically liquid metal ions such as Ga^+ and Cs^+, as well as O^-, with an energy of 1-25 keV, bombards the surface. A schematic diagram of a ToF-SIMS instrument is shown in Figure 2.10 [21]. It consists of a vacuum vessel, a primary ion source, a mass spectrometer and a secondary ion detection system; in addition, an electron flood gun is necessary to overcome surface charging effects.
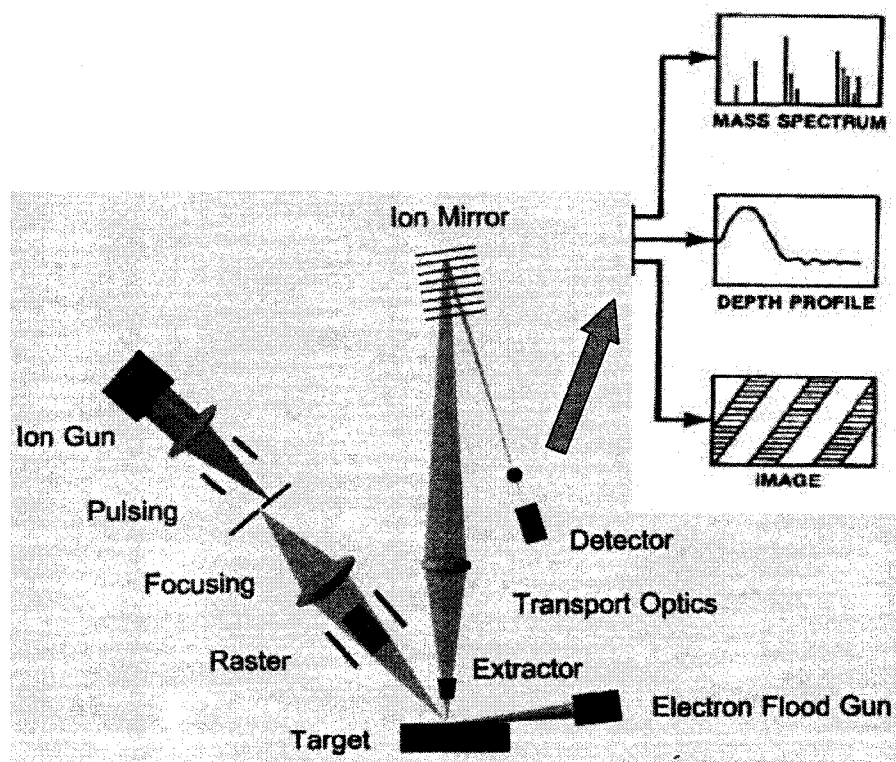
Figure 2.10. Schematic of a ToF-SIMS instrument.

The secondary ions from the sample surface are electrostatically accelerated into a field-free drift region with a nominal kinetic energy of [16]:

$$E_k = eV_0 = \frac{1}{2}mv^2 \tag{2.9}$$

where V_0 is the accelerating voltage, m the mass of ion, v the flight velocity of ion, e its charge. Therefore, the ion with lower mass has higher flight velocity than one with higher mass, and reaches the secondary ion detector earlier. As a result, the mass separation is obtained in the flight time t from the sample to the detector. The flight time t is expressed by:

$$t = \frac{L}{\sqrt{2eV_0/m}} \tag{2.10}$$

where L is the effective length of the mass spectrometer. Thus, the resulting secondary ions are accelerated into a mass spectrometer, where they are mass-analyzed by measuring their time-of-flight from the sample surface to the detector.

There are three different modes of analysis in ToF-SIMS: 1) mass spectra are acquired to determine the elemental and molecular species on a surface; 2) images are acquired to visualize the distribution of individual species on the surface; and 3) depth profiles are used to determine the distribution of different chemical species as a function of depth from the surface. That is, SIMS can be use to analyze not only the elemental composition but also the chemical structure of the surface.

Generally, ToF-SIMS has several attractive capabilities [18]:

(1)   Identifying the elemental composition and the chemical status (fragments) near the surface (~ 5 Å) with high sensitivity (~ 1 ppm) and high mass resolution (~ 9000).

(2)   Distinguishing the different isotopes of the same element.

(3)   Imaging the topography of surface using the secondary electrons.

(4)   Line-scanning of chemical species.

(5)   Mapping chemical species on the submicron scale.

(6)   Ultra-thin depth profiling.

(7)   Database of compound spectra.

(8)   Identifying automatically peaks with the database of fragments.

However, we should note two aspects of ToF-SIMS:

(1) Only semi-quantitative analysis, since the sputtering and ionization rates depend not only on the types of primary and secondary particles, but also on the chemical environment from which the ions are sputtered (the so called *matrix effect*) [16].

(2) It is inherently destructive, because of the processes leading to secondary ion formation and the surface will be progressively damaged as the bombardment continues. For this reason, it has been reported that 10^{13} ions cm^{-2} is likely to represent a damaging dose, if the minimum requirement for SIMS is that the same spectrum can be obtained from a given area of sample in successive experiments [16].

Sections 2.1 and 2.2 describe the information of XPS and ToF-SIMS. The two techniques are highly complementary, having certain shared attributes but differing markedly in other aspects, as shown in table 2.2. Therefore, combining information from the two techniques will be beneficial.

Table 2.2. Comparison of XPS and ToF-SIMS.

	XPS	ToF-SIMS
Detected elements	all elements except H	all elements with isotopic specificity
Limited sensitivity	0.2 atomic %	ppm of one monolayer
	quantitative	qualitative
Structural information	dominated by functionality and limited by the poor dynamic range of chemical shifts	with high level of molecular specificity
Sampling depth	1~5 nm	less than 1 nm, i.e. outmost monolayer
Spatial resolution	~ 10 μm	~ 1 μm

2.3 Fourier Transform infrared spectroscopy (FTIR)

Infrared (IR) spectroscopy is a chemical analytical technique that detects the vibration characteristics of chemical functional groups in a sample, by measuring the sample absorption of the infrared intensity as a function of wavelength or wavenumber. When infrared light interacts with matter, chemical bonds will stretch, deform and bend. As a result, a chemical functional group tends to absorb infrared radiation in a specific wavenumber range regardless of the structure of the rest of the molecule. Hence, the correlation of the band wavenumber position with the chemical structure is used to identify a functional group in a sample. The wavenumber positions where functional groups adsorb are consistent, despite the effect of temperature, pressure, sampling, or change in the structure in other parts of the molecule [18].

The infrared spectral region extends from 14,000 cm^{-1} to 10 cm^{-1}. The region of most interest for chemical analysis is the mid-infrared region (400 ~ 4,000 cm^{-1}) which corresponds to changes in vibrational energies within molecules; the lower region (below 1500 cm^{-1}), which contains many peaks of varying intensities, is known as the "fingerprint region", because almost every organic compound produces a unique pattern in this area, and identity can often be confirmed by comparison of this region to a known spectrum [22].
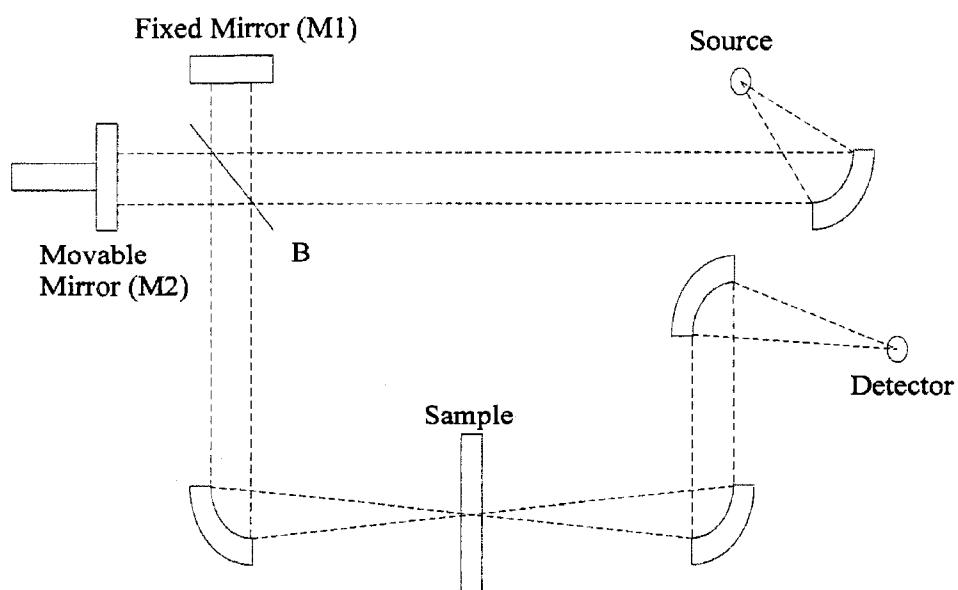
Figure 2.11. Schematic diagram of a typical FTIR spectrometer.

The early-stage IR instrument was of the dispersive type, which used a prism or a grating monochromator, with a slow scanning speed. The Fourier transform infrared (FTIR) system mostly used today measures all of infrared frequencies simultaneously, by first collecting an interferogram of a sample signal with an interferometer. A typical schematic of a FTIR instrument is demonstrated in Figure 2.11 [23]. The key

components of an FTIR instrument are a moveable mirror and a beam splitter. The beam splitter splits the IR beam 50/50 to the fixed and moveable mirrors, and then recombines the beams after being reflected at each mirror to form the interferogram. As we can see, the Fourier transform spectrometer is just a Michelson interferometer, with one of the two fully-reflecting mirrors movable, allowing a variable delay (in the travel-time of the light) to be included in one of the beams. Therefore, the moveable mirror is responsible for the quality of the interferogram, which has every infrared frequency "encoded" into it. When the interferogram signal is transmitted through or reflected off of the sample surface, specific frequencies of energy are adsorbed by the sample due to the excited vibration of function groups in the molecules. The beam finally arrives at the detector, and the detected interferogram is "decoded" by the well-known Fourier transformation, to obtain the infrared spectrum.

2.4 Raman spectroscopy
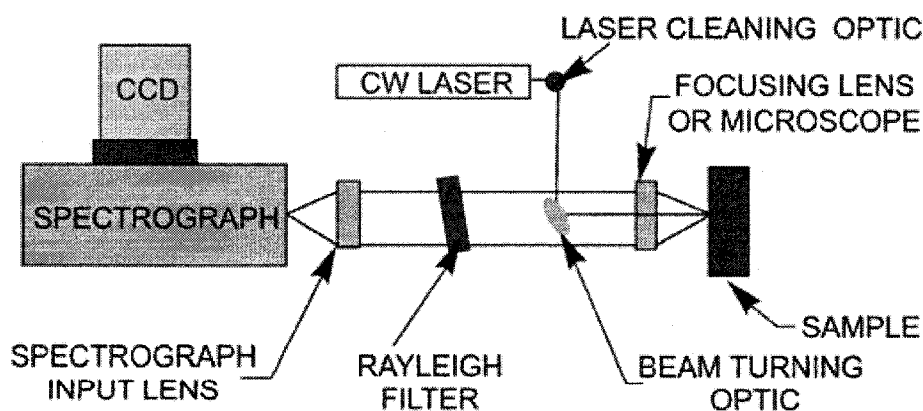
Figure 2.12. Schematic diagram of Raman set-up.

Raman spectroscopy is the measurement of the wavelength and intensity of inelastically scattered light from molecules of the material. It differs from infrared spectroscopy in that it is concerned with the scattering of radiation by the sample, rather than an absorption process. A typical schematic of Raman instrument is illustrated in Figure 2.12 [24].

When light is scattered from a molecule, most photons are elastically scattered with a same frequency as the incident photons; this is known as Rayleigh scattering. Meanwhile, a small fraction of light (approximately 1 in 10^7 photons) is scattered at optical frequencies lower (Stokes) or higher (anti-Stokes), than the frequency of the incident photons, as shown in Figure 2.13 [24]. The process leading to this inelastic scatter is termed the Raman effect. The scattered radiation occurs in all directions and may also have observable changes in its polarization along with its wavelength. It is the shift in wavelength of the inelastically scattered radiation that provides the chemical and structural information.

VIRTUAL STATE

STOKES   RAYLEIGH   ANTI STOKES

VIBRATIONAL
LEVELS

GROUND ELECTRONIC STATE
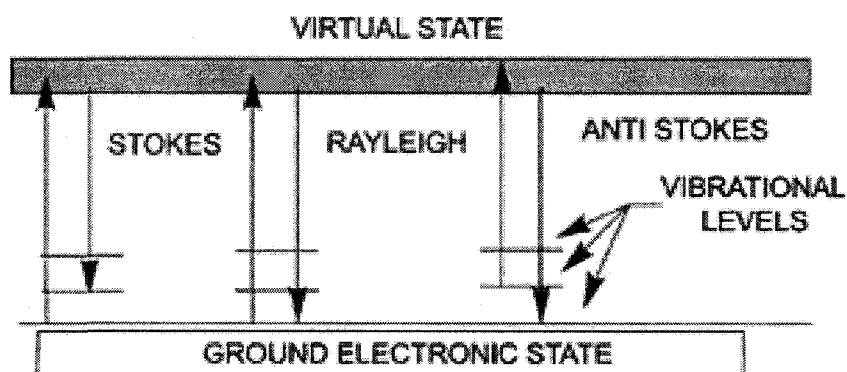
Figure 2.13. Simplified energy diagram of Raman scattering.

The Raman scattered light occurs at wavelengths that are shifted from the incident light by the energies of molecular vibrations and therefore the wavenumbers of the Stokes and anti-Stokes lines are a direct measure of the vibrational energies of the molecule. A schematic Raman spectrum may appear, as shown in Figure 2.14 [24]. One should note that the Stokes and anti-Stokes lines are equally displaced from the Rayleigh line. This occurs because in either case one vibrational quantum of energy is gained or lost. One must also note that the anti-Stokes line is much less intense than the Stokes line. This occurs because only molecules that are vibrationally excited prior to irradiation can give rise to the anti-Stokes line. Hence, in Raman spectroscopy, only the more intense Stokes line is normally measured.
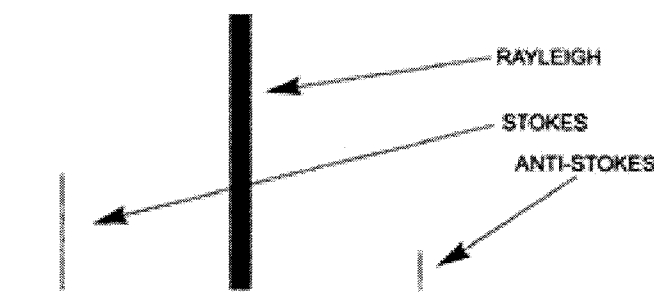
Figure 2.14. Schematic of Raman spectrum.

Infrared and Raman spectroscopy both measure the vibrational energies of molecules but these methods rely only different selection rules: 1) For a vibrational motion to be IR-active, the dipole moment of the molecule must change. Therefore, an asymmetric stretch is IR active, while the symmetric stretch may not be. 2) For a vibration to be Raman-active, the polarizability of the molecule must change with the vibrational motion. Thus, Raman spectroscopy complements IR spectroscopy.

2.5 Scanning electron microscopy (SEM)

The scanning electron microscope (SEM) is capable of producing high-resolution images of a sample surface, using electrons rather than light. Because seeing is believing and understanding, the SEM is perhaps the most widely employed instrument for directly studying solid surface structures. A schematic of the typical SEM is shown in Figure 2.15 [25].
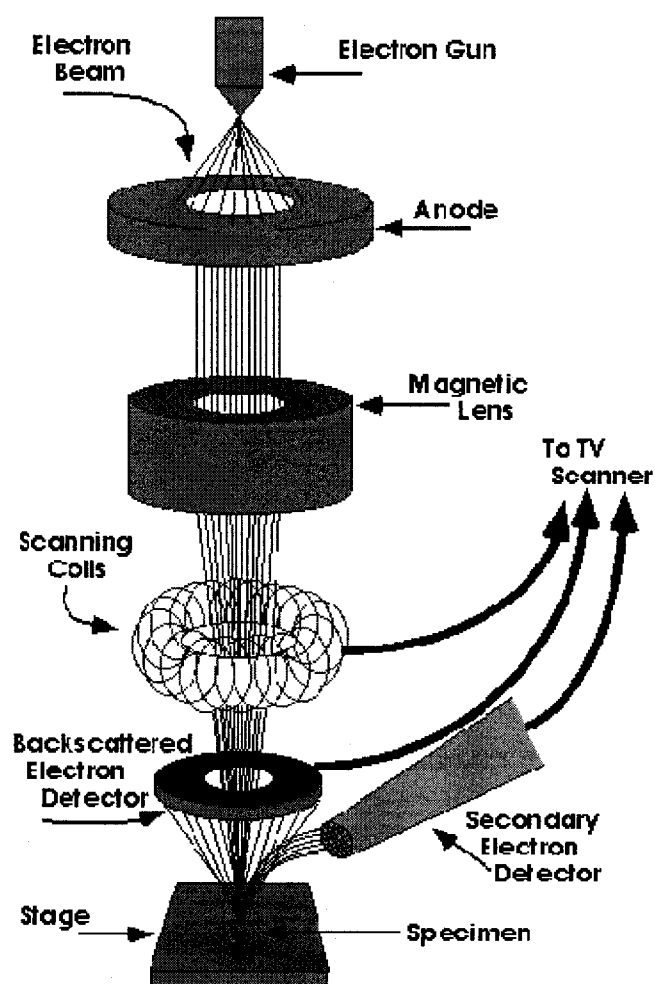
Figure 2.15. Schematic of the scanning electron microscope.

In a SEM instrument, electrons are thermionically emitted from a tungsten or lanthanum hexaboride (LaB_6) cathode and are accelerated toward an anode; alternatively, electrons can be emitted via field emission (FE); the comparison of those cathodes is shown in Table 2.3. The electron beam follows a vertical path through the column of the microscope, making its way through electromagnetic lenses which focus and direct it down toward the sample. Once it strikes the sample, other electrons (backscattered or secondary) are ejected. Detectors collect the secondary or backscattered electrons, and convert them to a signal that is sent to a viewing screen similar to the one in an ordinary television set, producing an image.

Table 2.3. SEM Cathode Comparison.

	Tungsten filament	LaB_6	Schottky (TF)	Field Emission
Apparent Source Size	100 μm	5 μm	<100 Å	<100 Å
Brightness	1 A/cm²-steradian	20-50 A/cm²-steradian	100-500 A/cm²-steradian	100-1000 A/cm²-steradian
Vacuum Required	10^{-5} Torr	10^{-6} Torr	10^{-8} Torr	10^{-9} Torr

The most common imaging mode monitors low energy (<50 eV) secondary electrons; because of their low energy, these electrons originate within a few nanometers of the surface. Backscattered electrons consist of high-energy electrons originating in the electron beam, which are back-scattered out of the specimen interaction volume. Backscattered electrons may be used to detect contrast between areas with different chemical compositions, especially when the average atomic numbers of the various regions are different, since the brightness of the backscattered electron (BSE) image tends to increase with the atomic number. X-rays, which are also produced by the

interaction of electrons with the sample, may also be detected in an SEM equipped for energy-dispersive X-ray spectroscopy (EDS or EDX) or wavelength dispersive X-ray spectroscopy (WDS or WDX) [26].

There are many advantages to using an SEM:

(1) The SEM has a large depth of field, which allows a large amount of the sample to be in focus at one time and, thus, can produce an image representing a three-dimensional surface of the sample.

(2) The SEM produces images of high resolution, which means that closely spaced features can be examined at a high magnification.

(3) Preparation of the samples is relatively easy since most SEMs only require the sample to be conductive.

Therefore, the combination of higher magnification, larger depth of focus, greater resolution, and ease of sample observation makes the SEM one of the most heavily used instruments in research today.

2.6 Transmission electron microscopy (TEM)

TEM is an imaging technique in which a beam of electrons is focused onto a specimen, causing an enlarged version to appear on a fluorescent screen or layer of photographic film, or to be detected by a CCD camera, as shown in Fig. 2.16 [27]. In comparison, the resolution of the SEM is about an order of magnitude poorer. As its name implies, the TEM is used to obtain structural information from specimens thin enough to transmit electrons. Modern research TEMs may include aberration correctors, to reduce the amount of distortion in the image, allowing information on features on the scale of 0.1 nm or less to be obtained. Monochromators may also be used, which reduce

the energy spread of the incident electron beam to less than 0.15 eV.
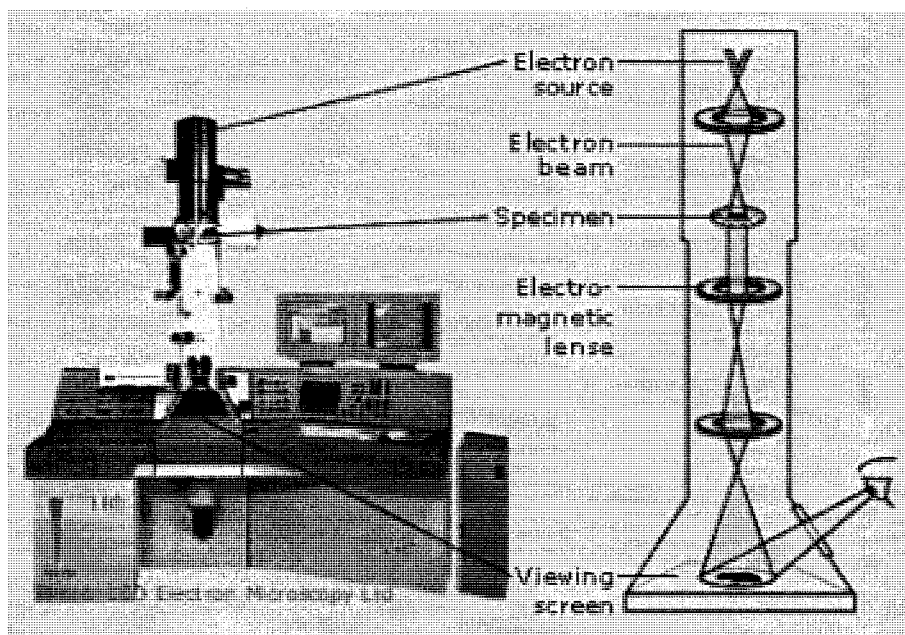
Figure 2.16. Transmission electron microscopy.

There are two very broad techniques of TEM operation: imaging and analytical [26]. In the former, structural images ranging from low magnification to atomic resolution are directly revealed whereas, in the latter, structural information is indirectly revealed through the analysis of diffracted beam geometries and energies. Each of the techniques is briefly described in turn below.

(1) Bright-field imaging (BF). Also known as conventional TEM, bright field imaging intentionally excludes all diffracted beams and only allows the central beam through.

(2) Dark-field imaging (DF). Dark-field images are also formed by magnifying a single beam; this time one of the diffracted beams is chosen by means of aperture which blocks both the central beam and the other diffracted beams.

(3) Lattice imaging. In this now-popular method of imaging periodic structures with atomic resolution, the primary transmitted and one or more of the diffracted beams are made to recombine, thus preserving both beam amplitudes and phases.

(4) Diffraction. Diffraction yields both crystallographic and orientational information on structural features, defects, and phases. Convergent-beam electron diffraction enables detection of less than ± 0.001 Å variations in lattice parameter with high precision. This sensitivity makes it possible, for example, to measure deviations in textural orientations and strains in individual grains of polycrystalline films.

(5) X-ray spectroscopy. This analytical capability, otherwise known as X-ray energy dispersive analysis (EDX), allows elemental identification through the measurement of characteristic X-ray energies.

(6) Electron energy loss spectroscopy (EELS). Through energy analysis of the transmitted electron beam, compositional analysis is possible. EELS is particular useful for detecting low-Z elements.

In addition, by applying a field-emission (FE) gun to the TEM, more detailed information related to the surface structure can be acquired. The FE electron beam has a small energy spread and high coherency, as discussed in section 2.5, so that it enables high resolution, high contrast TEM imaging and high energy resolution chemical analysis with EELS. A high current nanometric probe is best for the elemental analysis

of small particles with high spatial resolution with EDS. Since UHV provides a clean environment for semiconductor surface observation, a new ultrahigh vacuum field-emission transmission electron microscope (UHV-FE-TEM) has been developed for the *in situ* evaluation of the structures and electrical properties of semiconductor surfaces and nanostructures or metal particles. In this thesis, all the TEM images were obtained by field-emission TEM, using a JEOL 2100F.

2.7 Atomic force microscopy (AFM)

The atomic force microscope (AFM) is a very high resolution type of scanning probe microscope, with demonstrated resolution of fractions of a nanometer. It is one of the foremost tools for imaging, measuring and manipulating matter at the nanoscale.
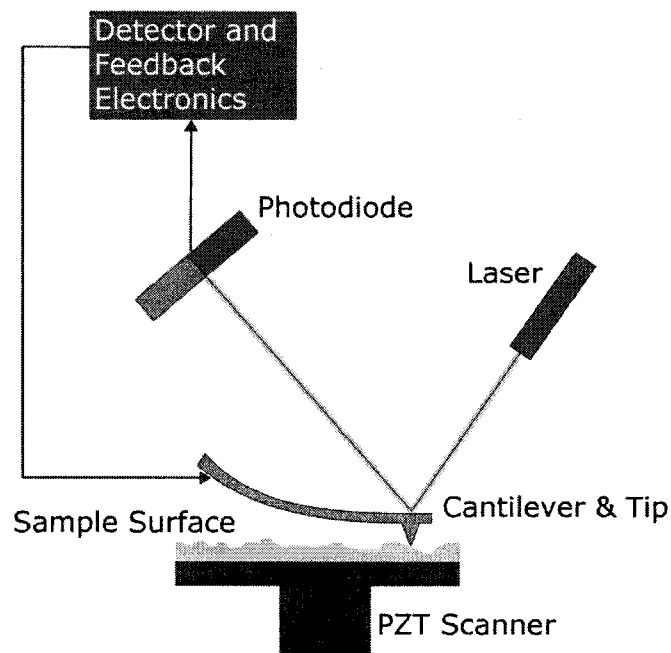
Figure 2.17. Schematic diagram of atomic force microscope.

An Atomic Force Microscope (AFM) consists of an extremely sharp tip (Si_3N_4 or Si) mounted or integrated on the end of a tiny cantilever spring, which is moved by a mechanical scanner over the surface to be observed. A schematic diagram of AFM is illustrated in Figure 2.17 [28]. Every variation of the surface height varies the force acting on the tip and, therefore, varies the bending of the cantilever. This bending is measured by an integrated stress sensor at the base of the cantilever spring and recorded line by line in the electronic memory. If the tip were scanned at a constant height, there would be a risk that the tip would collide with the surface, causing damage. Hence, in most cases a feedback mechanism is employed to adjust the tip-to-sample distance between the tip and the sample. The AFM therefore can be operated in a number of modes, depending on the application. In general, possible imaging modes are divided into the static (also called Contact) mode and a variety of dynamic modes. In the static mode, as explained above, the tip is in contact with the surface and the force between the tip and the surface maintains constant while, in a dynamic mode, such as non-contact and tapping modes, it is not in contact with the surface and the cantilever spring is oscillated at its resonance frequency, which is influenced by changing forces from the sample, where the frequency deviation is used to make an image of the sample.

Comparing to other imaging techniques, there are some advantages of using AFM:

(1) Even though, in some cases, the resolution of scanning tunneling microscopy (STM) is better than AFM, STM is generally applicable only to conducting samples while AFM is applied to both conductors and insulators.

(2) Compared with Scanning Electron Microscopes (SEM), AFM provides extraordinary topographical contrast, direct height measurements and unobscured views of surface features (no coating is necessary)

(3) Compared with Transmission Electron Microscopes (TEM), three-dimensional AFM images are obtained without expensive sample preparation (e.g., one need not use UHV; ambient air or even liquid environments may be used) and yield far more complete information than the two dimensional profiles available from cross-sectioned samples.

On the other hand, we should note that there are also several disadvantages for the AFM, such as the small image size and slow image scanning compared with the electron microscopes, as well as the limited image maximum height; but the greatest inconvenience is that, at high resolutions, the quality of an image is limited by the radius of curvature of the probe tip, and an incorrect choice of tip for the required resolution can lead to image artifacts, which are also known as "tip effects" [29-31].

Therefore, the complementarity of AFM and other techniques (such as SEM and TEM) investigation will benefit the precise and reliable characterization of the sample topography and structure.

Chapter 3. Article 1: X-ray photoelectron spectroscopic analysis of Pt nanoparticles on highly oriented pyrolytic graphite, using symmetric component line shapes

Gaixia Zhang, Dequan Yang and Edward Sacher

Regroupement Québécois de Matériaux de Pointe, Département de Génie Physique, École Polytechnique, C.P. 6079, succursale Centre-Ville, Montréal, Québec H3C 3A7, Canada

PEM fuel cells produce electricity through the electrochemical oxidation of hydrogen and the reduction of oxygen at the catalyst nanoparticle surfaces; at present, carbon-supported Pt nanoparticles are widely used as electrocatalysts, especially in low-temperature fuel cells. Therefore, it is very important to assure the strong adhesion of Pt nanoparticles to their carbon material supports, and to maintain it over the field-use lifetime of the catalyst. If this adhesion is not strong enough, the metal nanoparticles will diffuse on the support and coalesce into larger agglomerates, thereby decreasing both available catalytic surface and particle activity. For these reasons, we have studied the interfacial interactions controlling the adhesion of Pt nanoparticles deposited onto such surfaces.

First, we studied Pt nanoparticles evaporated onto three different highly oriented pyrolytic graphite (HOPG) surfaces: one of very low defect density (untreated), one having a high defect density (Ar^+-treated), and one having a surface containing a high defect density of oxidized C structures (Ar^+ treatment, followed by air exposure); we

used XPS core-level line shape analysis (see Appendix A), with HOPG as a model for carbon nanotubes because it has a well-defined, well understood, conducting surface structure similar to that of CNTs. The C1s and Pt4f$_{7/2}$ peaks were each considered to be composed of one asymmetric peak, and changes in their asymmetry parameters were used to study their interfacial interactions. In addition to these changes, strong signal intensity changes with time were found for both the C1s and Pt4f peaks, indicating an initial crystalline orientational instability of the Pt nanoparticles, which was supported by time-dependent high resolution electron microscope studies at elevated temperatures.

In addition, our group has reported that, in the case of many materials such as HOPG and CNTs, as well as Cu, Ni, Co, Pt and other transition metals, the asymmetry of the XPS lineshape is due to the existence of identifiable, overlapping component species having symmetric line-shapes. Therefore, we also analyzed the Pt4f peaks using multiple symmetric components; it was our purpose to study spectral evolution as a function of deposition, as well as to learn what these changes can tell us about Pt nanoparticle/substrate interactions and how they influence the Pt4f peak shape asymmetry. We used two HOPG surfaces, pristine (untreated) and Ar$^+$-treated, with, respectively, low and high surface defect densities of -C=O, -C-OH, -COOH and free radicals. Each Pt4f spectral component (f$_{7/2}$ and f$_{5/2}$) was found to be separable into three symmetric peaks. On analyzing the relationships among the Pt4f, C1s and O1s spectra, we attributed these peaks to the existence of (i) surface oxidation on the platinum nanoparticles, and to the different electronic configurations of (ii) surface and (iii) bulk Pt atoms; we found no evidence of compound formation between Pt nanoparticles and the HOPG surface. We used the varying intensities of these component peaks, as a function of deposited Pt, to explain the changing shape of the Pt4f asymmetric envelope with nanoparticle size.

3.1. Introduction

Pristine highly oriented pyrolytic graphite (HOPG), a model for carbon nanotubes, has a well-defined, well understood, conducting surface structure that interacts weakly with metals. Because carbon-supported Pt nanoparticles are widely used as electrocatalysts, especially in low-temperature fuel cells [32-35], we wish to understand the interfacial interactions controlling the adhesion of Pt nanoparticles deposited onto such surfaces. Determining the adhesion of Pt nanoparticles to carbon-based materials is very important because it is a key feature in the determination of catalyst activity.

X-ray photoelectron spectroscopy (XPS) is a highly surface-specific technique, with a probe depth of a few nanometers, that has been widely used in characterizing the chemical and electronic structural properties of metallic nanoparticles [36-39]. While symmetric component lineshapes are normally used for the spectral deconvolution of nonmetals [40-42], metals are generally understood to be composed of single peaks with asymmetric lineshapes [43-45].

Such lineshape asymmetry has a long history. In 1967, Mahan proposed that the scattering of an electron at the Fermi level of a metal is a singularity [46]. Subsequently, Nozières and de Domenicis (ND) showed that this singularity arose because of the competition between the scattering resonance and deep-level broadening [47]. Doniach and Šunjić applied the Mahan and ND theory to XPS core level electrons, deriving a line shape with an asymmetric tail at the high binding energy side of the peak [48]. Citrin et al. [49], Gadzuk and Šunjić [50], and others [51,52] carried out further developments. The commonly accepted view is that the asymmetry is caused by a potential created between the hole formed by the photoemission and the remaining electrons, permitting the promotion of electrons near the Fermi level to empty states just above it. As in a

shake-up process, this promotion occurs simultaneously with photoemission, and it has been referred to as the Mahan shake-up [50].

However, it has been demonstrated that, in the cases of HOPG, Cu, Ni, Co and Pt, the asymmetry of the XPS lineshape is due to the existence of identifiable, overlapping component species having symmetric line-shapes [53-55]. For example, the C1s XPS lineshapes in graphite and vitreous carbon are highly asymmetric [52,56,57]; we have shown, for both HOPG [53] and carbon nanotubes [58], that this asymmetry is due to the presence of definable, quantifiable symmetric component peaks. Further, in a study of the C1s XPS spectra of variously treated HOPG surfaces, comparing multicomponent symmetric and single-component asymmetric peak-fitting procedures [59], we found that, the single-peak asymmetry parameter is directly related to the extent of damage to the alternant hydrocarbon structure of the HOPG surface; this was demonstrated by the correlation of the single-peak asymmetry parameter with the symmetric C1s component due to the damaged structure.

Several workers have, in fact, attributed the asymmetry of the Pt4f XPS spectrum to the presence of ubiquitous surface platinum oxide [55,60,61], represented as PtO_x. Kim et al. [55] reported that, on etching platinum foil, followed by reduction, platinum oxide was still found by XPS analysis; this has also been observed for platinum after vapor deposition at 10^{-5} Torr [55]. Our present results confirm that PtO_x is, indeed, a component of the asymmetry but not the only one.

We previously reported (see Appendix A) the use of a single asymmetric peak to fit the 4f XPS spectrum of evaporated Pt [62]. Here, we use multiple symmetric components, as we previously did for HOPG and CNTs [53,58], and several First Transition Series elements [54], our purpose being to ascertain what information can be

extracted from such a procedure. We use two HOPG surfaces, pristine (untreated) and Ar$^+$-treated, with, respectively, low and high surface defect densities of -C=O, -C-OH, -COOH and free radicals [53,58]. Chemical characterization was carried out by examining (1) peak intensities, (2) binding energies, (3) full widths at half maxima (FWHM) of the XPS peak components, and (4) peak area ratios as a function of Pt evaporation thickness. Our purpose is to study spectral evolution as a function of deposition, as well as to learn what these changes can tell us about Pt nanoparticle/substrate interactions and how they influence the Pt4f peak shape asymmetry.

3.2. Experimental

HOPG, grade ZYA, 1 cm × 1 cm × 2 mm, was obtained from Advanced Ceramics. Inc. It was cleaved with adhesive tape immediately prior to each experiment and inserted into the X-ray photoelectron spectrometer. Ar$^+$ treatment of the HOPG surface was performed in the UHV preparation chamber of the XPS instrument at a pressure of ~ 5×10^{-6} Torr, using a 3 keV Ar$^+$ beam having a flux of ~ 1×10^{13} ions/cm^2/sec, for 4 min, at an angle of ~ 60° from the surface normal. We have found that this treatment condition provides a uniform, repeatable surface defect density of free radicals [37,53,54].

Pt evaporation, subsequent to Ar$^+$ treatment, used an ultra-pure Pt rod purchased from SPI, Inc. It, too, was carried out in the preparation chamber, at a pressure of < 3 × 10^{-8} Torr, using a Quad-EVC evaporator (Mantis Deposition, Ltd.), at a rate of ~ 0.15 nm/min. The thickness was monitored by a quartz crystal microbalance placed near the sample.

After transfer through a gate valve, without atmospheric exposure, XPS was performed in the analysis chamber of our VG ESCALAB 3 MARK II (Thermo VG Scientific), using a non-monochromated Mg Kα X-ray source (1253.6 eV), at a base pressure of < 2 × 10^{-9} Torr. High resolution spectra were obtained at a perpendicular take-off angle, using a pass energy of 20 eV (step size: 0.05 eV; step dwell time: 200 ms). The instrument resolution was ~ 0.7 eV. After Shirley background removal, the component peaks were separated by the VG Avantage V1.62 program (Thermo VG Scientific), using mixed Gaussian-Lorenzian functions. The peak energies were calibrated by placing the C1s peak at 284.6 eV [37,53].

3.3. Results

3.3.1. Symmetric component analysis of the interaction between Pt nanoparticles and the HOPG substrate

3.3.1.1. The relationship between Pt4f and C1s

Five peaks are required in order to properly deconvolute the C1s envelope [53]. Figure 3.1a shows an exemplary spectrum of Ar^+-treated HOPG with 32 Å Pt deposition, where the four symmetric components, labeled 1, 2, 3 and 4, are attributed as follows[53,54,58,59]: *C1* (284.6, undamaged alternant hydrocarbon structure), *C2* (285.6, damaged alternant hydrocarbon structure), *C3* (286.5, sp^3 free radical defects), and *C4* (287.8, the *C2* π*←π shake-up satellite); peak 5, the *C1* π*←π shake-up, at 291.4 eV, is omitted. The C1s spectra do not change significantly on the deposition of many metals [63,64], and no new peaks appear in the 282-284 eV region that signal carbide formation. In contrast, in XPS studies of Al and Fe films, the presence of a

carbide is immediately obvious from the change in C1s lineshape signaling carbide

formation [65].
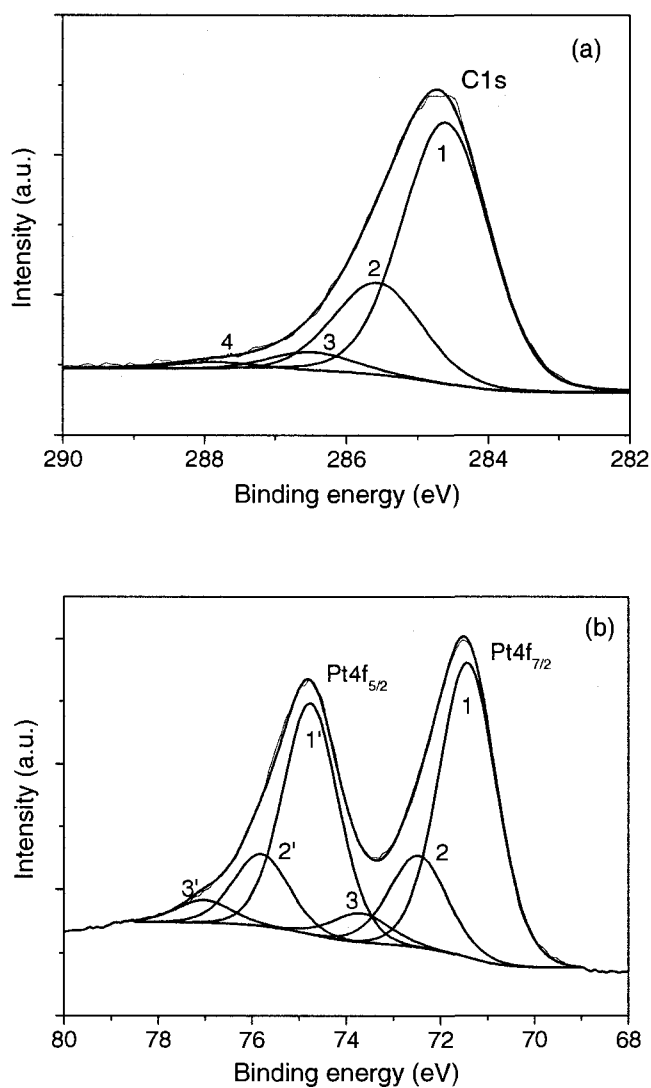
Figure 3.1. Exemplary XPS peak separations of 32 Å Pt evaporated onto the Ar$^+$-treated

HOPG surface: (a) C1s and (b) Pt4f.

The Pt4f spectrum was deconvoluted into doublets labeled 1, 2 and 3 ($4f_{7/2}$), and 1', 2'

and 3' ($4f_{5/2}$), shown in Figure 3.1b. For 32 Å of Pt deposition, for example, the $Pt4f_{7/2}$

binding energies are about 71.4, 72.5 and 73.7 eV for the Ar^+-treated HOPG, which are ~ 0.3 eV higher than those for untreated HOPG. Figure 3.2a shows their variation with Pt
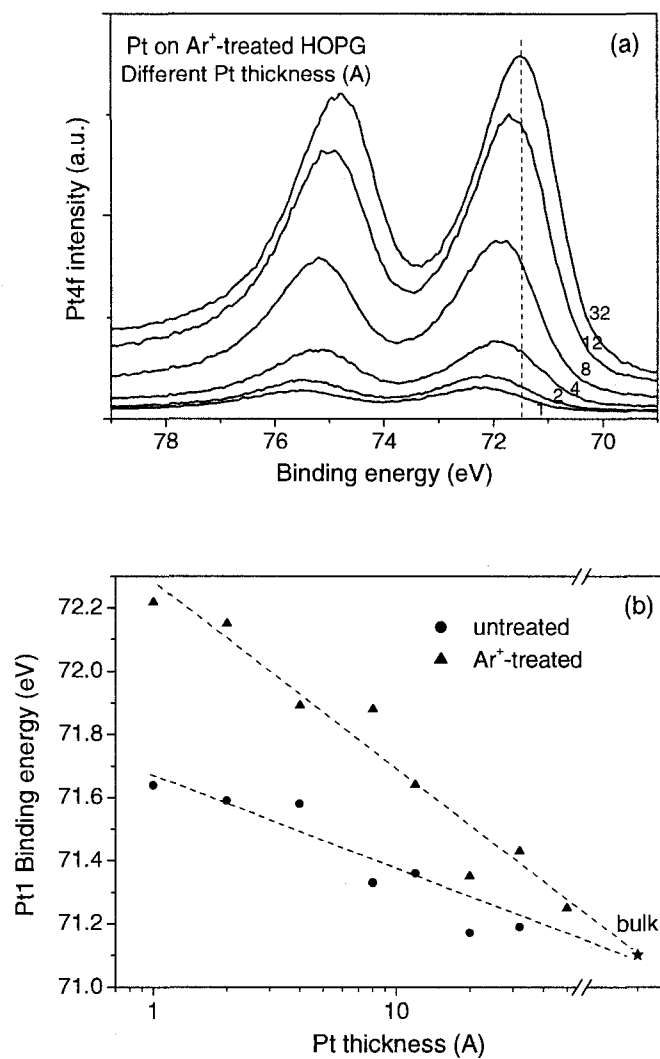
Figure 3.2. (a) Pt4f spectral evolution on the Ar^+-treated HOPG surface, and (b) the binding energies of $Pt4f_{7/2}$ peaks for both untreated and Ar^+-treated HOPG surfaces, as a function of nominal Pt deposition.

thickness. The binding energy of the thickest Pt deposition (32 Å) is marked in the figure. A major feature observed is the shift to lower binding energy with increasing particle size [36,62], as plotted semi-logarithmically in Figure 3.2b. Note that, with increasing Pt thickness, the binding energy trends to the bulk value, 71.3 eV [66]. This indicates the formation of a contiguous Pt film thick enough to mask the substrate so that XPS can not detect it. Since the principal binding energy of $Pt4f_{7/2}$ decreases almost 1 eV with increasing Pt thickness, it is clear that the binding energy is influenced by nanoparticle size. In addition, since the binding energy increases $\sim$ 0.3 eV on Ar^+ treatment, the nanoparticles interact more strongly with the defects produced.

The FWHM values for both the $Pt4f_{7/2}$ and C1s spectra in Figure 3.3, manifest different developments with Pt deposition: $Pt4f_{7/2}$ shows a continual decrease while C1s shows a continual increase. This has been attributed to charge transfer from Pt nanoparticles to HOPG surface [67], as well as to cluster size effects [68].

Comparing these two sample treatments, after normalizing the Pt atom flux (32 Å), we find that the Pt coverage of the Ar^+-treated sample is about 45% greater, and the binding energies, as noted earlier, about 0.3 eV higher; these are consistent with the results of Howells [69] et al. The Ar^+-treated sample has a noticeably broader C1s spectrum and, possibly, a slightly broader Pt4f spectrum (Figure 3.3), due to stronger interaction with the HOPG, as well as to the smaller Pt nanoparticles deposited on Ar^+ treatment [62]. As already mentioned, this is because there are more defects (free radicals and oxidized carbon species) on the Ar^+-treated surface, and these defects are the preferred sites for Pt nanoparticle nucleation [70-72]. The stronger interaction impedes nanoparticle diffusion and coalescence, as was also found for Cu and Ni nanoparticles [54,73].
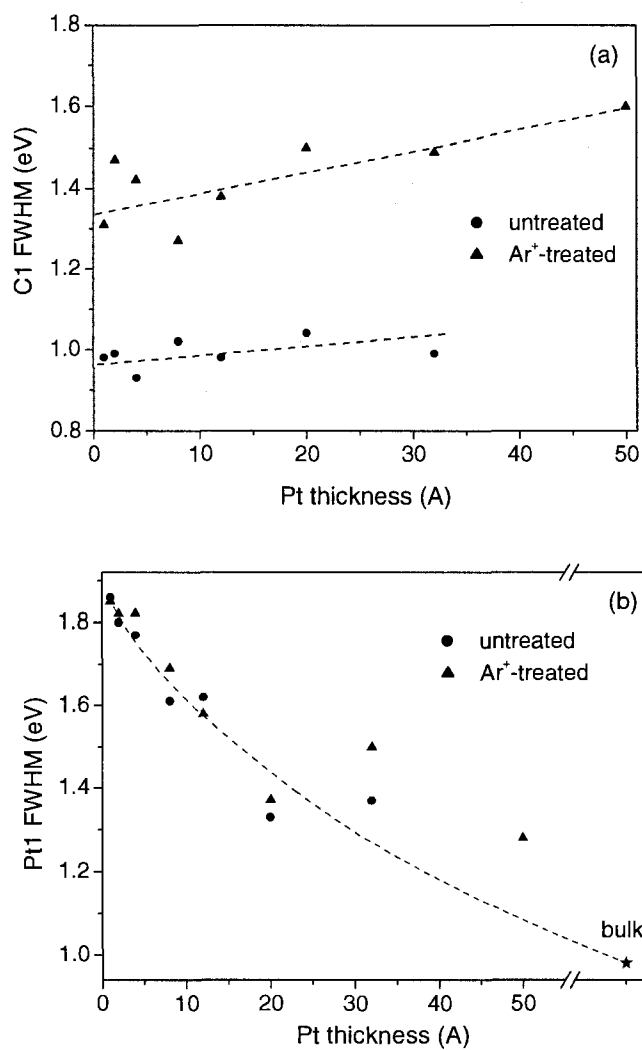
Figure 3.3. FWHM changes of the (a) C1 and (b) Pt1 components as a function of

nominal Pt deposition onto untreated and Ar^+-treated HOPG surfaces.

3.3.1.2   The relationship between Pt4f and O1s

HOPG surfaces, freshly peeled in air, exhibit steps whose edges are formed by layers

cleaved during peeling. On atmospheric exposure for a short time, some of these free

radical defects react with atmospheric O_2 and H_2O to form oxidized carbon species; the

O1s spectrum in Figure 3.4a exhibits a small peak with two components (*O2*, 532.1 eV, and *O3*, 533.5 eV, attributed, respectively, to –C=O/C–OH and –COOH [74]). On Pt deposition, a new peak (*O1* in Figure 3.4b), appears. Simultaneously, symmetric Pt4f components (*Pt3,3'* in Figure 3.1b) also appear; both O1 and *Pt3,3'* increase with
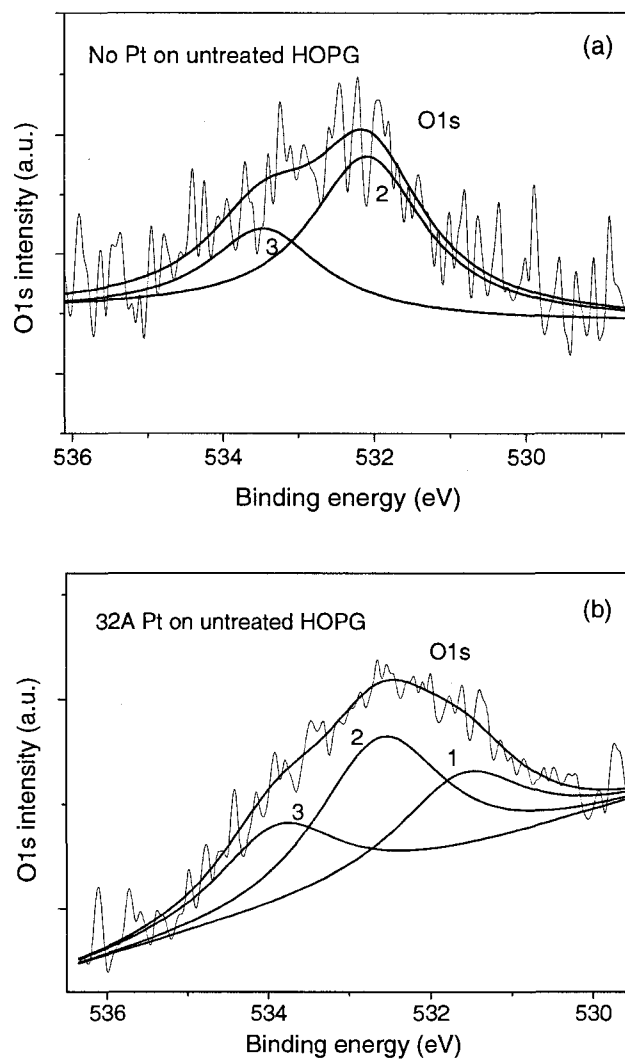
Figure 3.4. The O1s XPS peak separations (a) before and (b) after Pt deposition.

deposition, although neither is easily detected below 1-2 Å. Further, Parkinson et al. have reported oxygen adsorption on a Pt substrate during oxygen dosing at pressures between 10^{-7} and 10^{-8} mbar [75]. A shoulder, representing Pt-O formation, was found, even at room temperature, at a Pt4f binding energy of 76.8 eV, which is nearly the same position as our *Pt3'* peak. Their angle-resolved XPS analysis showed that the intensity of the shoulder peak increases with decreasing taking-off angle, indicating its location at the surface. This confirms our association of *Pt3,3'* with *O1*. Based on this, we attribute the appearances of *O1* and *Pt3,3'* to the onset of Pt nanoparticle surface oxidation.
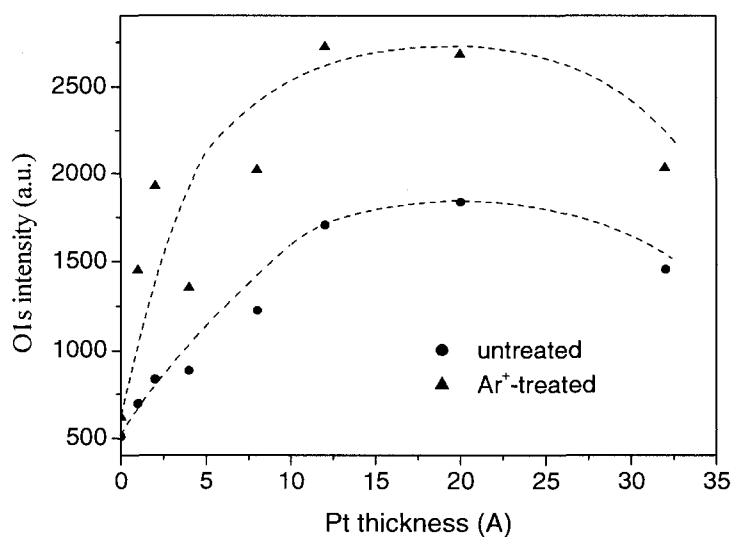
Figure 3.5. The total O1s areal intensities for both untreated and Ar^{+}-treated HOPG surfaces, as a function of nominal Pt deposition.

Figure 3.5 presents the total O1s areal intensity increase with increasing Pt deposition, showing the Ar^{+}-treated surface to be 1.5 times that of the pristine surface before eventually decreasing toward a value nearly that of the latter. This appears to indicate the

onset of a contiguous film of Pt nanoparticles, beginning at ~ 25 Å [76], that masks the oxygen at the HOPG defect sites until XPS can no longer detect it.

Because Pt deposition took place in vacuum ($< 3 \times 10^{-8}$ Torr), peak *O1* must occur by one or more of the following pathways: (1) the Pt target (oxygen adsorption occurs on platinum surfaces) [75,77]; (2) during specimen transfer between treatment and analysis chambers; (3) residual oxygen (water vapor or molecular oxygen) adsorbed on the inner walls of the spectrometer; (4) chemical reaction with the oxidized HOPG defects (Pt has a condensation energy > 5.52 eV [78], so that enough heat is released on condensation to cause reaction of the -OH/C=O/COOH groups, especially -OH, whose bond energy is 3.73 eV while that of the C=O bond is 8.32 eV [79]).

As already mentioned, Figure 3.5 shows that the total O1s areal intensity on Ar^+ treatment is 1.5 times that of the untreated material. This is true for the individual components, as well (not shown). This almost two-fold increase on Ar^+ treatment is due to the fact that the free radicals produced on bond scission react with residual oxygen to create oxidized carbon species; that this holds for *O1*, as well as *O2* and *O3*, suggests a relationship among them, implying that pathway (4) is favored for the production of *O1*.

The *O1:Pt3* atomic ratios, as determined from XPS component areas and relative sensitivity factors, are plotted against the deposited Pt thickness in Figure 3.6. While the scatter is large, at least partly due to the uncertainties of the deconvolution process, it is clear that the *O1:Pt3* ratio on Ar^+ treatment is significantly larger than that in the absence of treatment, just as was found for the *O1* component intensity, above. The implications of this finding will be discussed later.
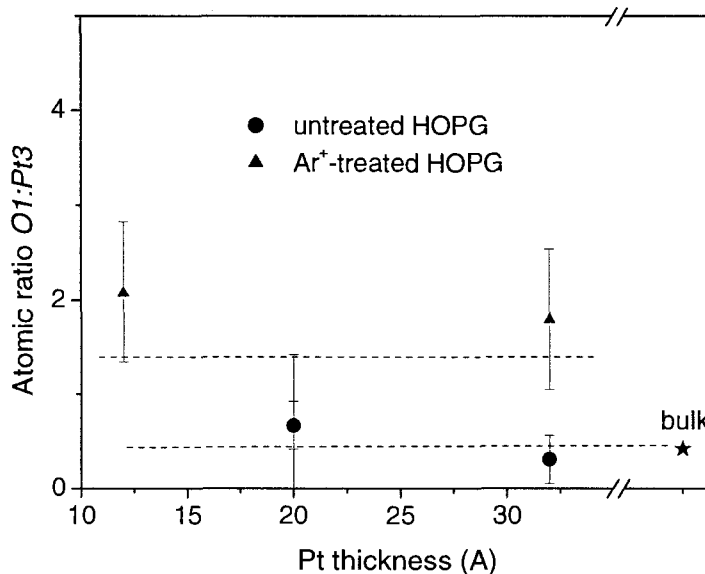
Figure 3.6. The atomic ratio *O1:Pt3* as a function of nominal Pt deposition onto untreated and Ar⁺-treated HOPG surfaces.

Several authors [60,61] have attributed the total Pt asymmetry to oxide formation. However, as we have just shown, only the *Pt3* component is so related.

3.3.2. The relationships among *Pt1*, *Pt2* and *Pt3*

The Pt4f envelope asymmetry is found to increase with increasing nanoparticle size [36,62] which is different than the behavior of First Transition Series metals, such as Ni, Mn, Cr, V, and Cu [54,80]; there are several public domain programs, such as XPSPeak 4.1 [81] and Fitt [82], which may be used to fit single asymmetric peaks to the spectrum.

Our use of symmetric components to analyze the Pt4f spectrum is based on our success in using such components to analyze several First Transition Series elements

[54], as well as HOPG and CNTs [53,58]. Using FWHM values, previously determined in our laboratory, we established that three symmetric peaks were needed for each of our Pt4f doublets ($f_{7/2}$: 1, 2, and 3, and $f_{5/2}$: 1', 2' and 3'); the $f_{7/2}$-$f_{5/2}$ energy separations used were identical for each pair of peaks, and the $f_{7/2}$-$f_{5/2}$ peak area ratios were 4:3, values expected for an f orbital spin-orbit doublet. Our first inkling of success came with the finding that *Pt3* correlated with *O1*, as already described.

As noted in the Introduction, the asymmetric lineshape has generally been attributed to the Mahan shakeup satellite, which is due to the promotion of electrons near the Fermi level to empty states just above it. However, this seems unlikely here since, as seen in Figure 3.1, the proposed shakeup satellite, *Pt2*, has a FWHM equal to those of *Pt1* and *Pt3*, while the FWHM of a true shakeup, which is composed of several overlapping transitions, is much broader than that of a regular peak [83].

The *Pt2:Pt1* and *Pt3:Pt1* component area ratios, for both untreated and Ar^{+}-treated HOPG, are plotted in Figure 3.7; no obvious difference is seen with treatment. The *Pt2:Pt1* area ratio (Figure 3.7a) increases nearly linearly with Pt deposition to ~ 20 nm, where it appears to go through a small maximum before reaching the ratio found for bulk material, while the *Pt3:Pt1* area ratio remains constant (Figure 3.7b); the maximum in Figure 3.7a may be due to attenuation effects [84-86]. It is these intensity variations that cause the asymmetry changes seen in the Pt4f spectra, as shown in Figure 3.2a.
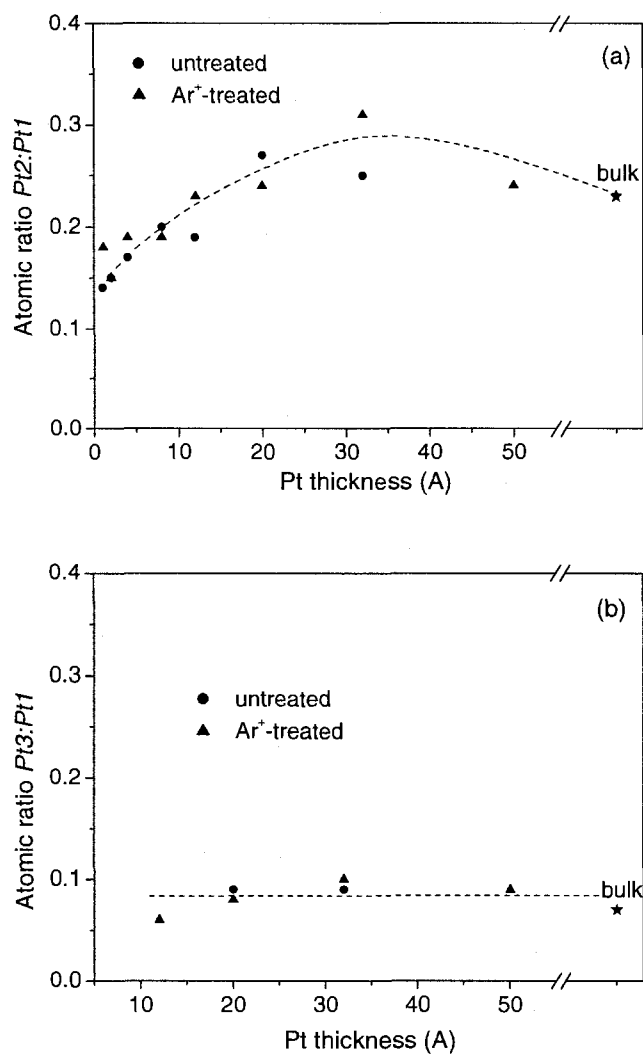
Figure 3.7. The atomic ratios (a) *Pt2:Pt1* and (b) *Pt3:Pt1* as a function of nominal Pt deposition onto untreated and Ar$^+$-treated HOPG surfaces.

Changes in electronic configuration with particle size have been predicted theoretically and often found experimentally [63,87-94]. They have been used as the basis for interpreting the photoemission spectra of rare earth and Platinum-group metal clusters, in which surface and bulk atoms have different electronic configurations. Mason et al. reported the first definitive example of a change in electronic configuration

with Sm particle size [63], using both XPS and UPS spectral analyses. They showed an initial predominance of the atom-like divalent (i.e., $(4f^6)(sd)^2$) electronic configuration at small particle size. With increasing size, the bulk-like trivalent (i.e., $(4f^5)(sd)^3$) electronic configuration is formed, although a large divalent contribution from surface atoms remains. Theoretical calculations on Pt nanoparticles [87,89,93] support a similar interpretation in the present case: Kua and Goddard [93] used non-local density functional methods, based on the interstitial electron model, and found that bulk Pt has a $5d^8 6s^2$ electronic configuration, while the surface atoms at the Pt(111) face have a $5d^9 6s^1$ configuration.

As has already been found for Sm [63], we propose that *Pt1* is due to surface platinum atoms, and *Pt2* represents bulk atoms. This is consistent with our results in Figure 3.7a: with increasing Pt deposition, *Pt2* increases faster than *Pt1*, as the bulk-like content of the nanoparticle increases, before attaining the bulk value.

Our present results are supported by the work of Mason [88], who reported that, for less interactive substrates such as carbon, the metal-support interaction is weak and electronic configuration shifts, from atom-like to bulk-like, are expected with increasing cluster size. Further, Yang and co-workers [92] reported that Pt_{13}, with a diameter less than 1 nm, exhibits an amorphous, atom-like structure, and beyond a certain size (not mentioned), the fcc structure becomes favorable, which dominantly exhibits a bulk-like fcc structure.

By combining the results of Mason et al. [63,88] and Yang et al. [92] with our previous studies by contact-mode atomic force microscopy (C-AFM) [74], as well as by XPS and high resolution electron photomicrographic analyses [62], it is clear that the nanoparticle diameter increases from ~ 1 to 5 nm as our deposition thickness increases

from ~ 1 to 32 Å, and the number of atoms contained in these nanoparticles increases from tens to thousands. It is, therefore, to be expected that our smaller nanoparticles are almost entirely composed of surface atoms and, with the increasing nanoparticle diameter, the bulk is able to form nanocrystals [62].

3.4. Discussion

3.4.1. Interfacial interaction between Pt nanoparticles and the HOPG surface

Although no significant changes were found in the C1s peak shape on Pt evaporation (Figure 3.1a), the Pt4f binding energy shifts to lower values (Figure 3.2b), the FWHM of the Pt4f spectrum narrows (Figure 3.3b) and the FWHM of the C1s spectrum broadens (Figure 3.3a) with increasing Pt deposition for both treatments. Because the nanoparticle size increases with the amount of deposition, these changes illustrate the effect of nanoparticle size.

Comparing the untreated and Ar^+-treated substrates, the Pt4f spectrum of the Ar^+-treated sample is seen to have a higher binding energy (Figure 3.2b) and a narrower FWHM (Figure 3.3b), as well as a broader C1s spectral FWHM (Figure 3.3a). These changes are due to the introduction of defects on Ar^+ treatment, resulting in a greater density of nanoparticles of smaller size and stronger Pt interaction [62].

3.4.2. Symmetric peak components of the Pt4f spectrum

As shown in Figure 3.4b, a new O1s peak, *O1*, appears on Pt deposition, correlated with *Pt3* in Figure 3.1b, indicating Pt oxidation; the constancy of the *Pt3:Pt1* area (atomic) ratio in Figure 3.7b indicates the relationship between the surface oxide (*Pt3*) and the component we have identified as representing the nanoparticle surface (*Pt1*).

The existence of surface PtO_x has already been demonstrated in numerous studies [77,95-98] that showed that, in ultrahigh vacuum, molecular oxygen dissociates and chemisorbs onto Pt, even at cryogenic temperatures. In particular, Gouérec et al. [99] have shown, by *in situ* reduction in fuel cells, that oxidized Pt occurs exclusively at the nanoparticle surface. There are no reports of the true *O:Pt* atomic ratios. However, Hull et al. [100] reported Pt coordination with oxygen (in the form of PtO_x) at the outermost perimeter of the Pt cluster while the majority of the bulk was in the metallic form.

The *O1:Pt3* atomic ratios, for both untreated and Ar^{+}-treated substrates, are found in Figure 3.6. The atomic ratio for the Ar^{+}-treated substrate extends to 2:1 (for the highest oxidized Pt state, PtO_2); we believe that this may be an artifact, resulting in an artificially high value. A similar phenomenon was found for our XPS study of oxidized nanoporous Si thin films, where Si:O atomic ratios greater than 1:2 were found [85]. As with the oxidized Si, we believe that there are at least four reasons for such obviously erroneous ratios: (1) the oxygen resides on the nanoparticle surface, and its photoelectrons are not attenuated, as are those emitted by the Pt in the nanoparticle bulk; (2) the much lower intensity of *O1* means that the signal-to-noise ratio is not sufficiently high; (3) the closely spaced, overlapping components of both the O1s and $Pt4p_{3/2}$ spectra may cause some uncertainty during peak separation; (4) photoemission intensities and relative sensitivity factors of nanoparticles differ from those of bulk solids, following a size-dependent law [86,101]. Thus, although x, in PtO_x, is probably smaller in the case of the untreated substrate, these factors introduce an uncertainty that makes it impossible to use the present ratios to specify their true values.

Another method often used to specify valence is the chemical shift. Because Pt[IV] has a greater binding energy than Pt[II], one may consider the use of chemical shifts to estimate

the valence of the Pt species contributing to *Pt3*. Indeed, the chemical shift between Pt^0 and Pt^{II} (in PtO) is ~ 3 eV and between Pt^0 and Pt^{IV} (in PtO_2) is ~ 4 eV [102]. Our data indicate a chemical shift of ~ 2 eV between *Pt1* and *Pt3* for both untreated and Ar^+-treated HOPG, strongly implying that no true compound has been formed, and the surface oxide layer is incomplete (no monovalent Pt compounds are known). The greater *O1:Pt3* ratio in the case of the Ar^+-treated HOPG may simply reflect the presence of $Pt(OH)_2$ rather than PtO, due to the greater concentrations of C–OH and COOH on Ar^+ treatment.

Combining the Mason theory [63] and the different electronic configurations of surface and bulk atoms [94] with our analyses on Pt deposition, we obtain a reasonable explanation for the three pairs of symmetric Pt4f components: (1) the lowest binding energy doublet (*Pt1,1'*; ~ 77% of the total above 30 Å) is due to surface Pt atoms in the $5d^9 6s^1$ electronic configuration; (2) the middle doublet (*Pt2,2'*; ~ 15.5%) is due to bulk atoms in the $5d^8 6s^2$ electronic configuration; (3) the highest binding energy components (*Pt3,3'*; ~ 7.5%) is due to surface PtO_x, where x is greater on Ar^+ treatment .

Figure 3.7 shows the initial increase of the *Pt2:Pt1* atomic ratio, before reaching a plateau near 20 nm, and the constancy of the *Pt3:Pt1* atomic ratio. This indicates why the Pt4f spectrum increases in asymmetry with increasing size [36,62], as opposed to First Transition Series metals, whose asymmetries decrease [54,80], as described in the next section.

3.4.3. Interfacial interaction in the Pt4f spectrum

Our previous work on First Transition Series metals showed that the asymmetry of, e.g., the Ni2p spectrum [54] was found to be due to an additional small peak, at a

binding energy higher than the Ni^0 peak, due to $Ni^{\delta+}$ that has undergone interfacial interaction with the HOPG substrate. Because Pt nanoparticle-HOPG interaction has been demonstrated to exist in the present case, such a Pt-HOPG interaction peak would be expected here, too, at about the positions of the *Pt2,2'* peaks. However, with increasing nanoparticle size, the contributions of the *Pt2,2'* increase at a rate greater than those of *Pt1,1'* while the interaction peaks decrease rapidly [63]. Thus, while a Pt-HOPG interaction component surely exists, it is masked by the increasing contributions of the *Pt2,2'* peaks.

3.5. Conclusions

We have used symmetric component XPS peak analysis to study the interfacial interaction of Pt nanoparticles with untreated and Ar^+-treated HOPG surfaces having low and high defect densities, respectively. Each Pt4f spectral doublet was deconvoluted into three peaks; we attribute the peaks, in order of increasing binding energy, to surface atoms in the $5d^9 6s^1$ electronic configuration, bulk atoms in the $5d^8 6s^2$ electronic configuration, and PtO_x at the nanoparticle surface. We have shown that the changes of binding energy and FWHM of the spectra contain information on nanoparticle size, substrate interactions and surface oxidation. We have also shown that the changes in symmetric component peak areal intensities, on Pt deposition, account fully for the changes in Pt4f peak asymmetry.

We have shown that Pt nanoparticle deposition onto HOPG involves interaction with defects, such as free radicals and oxidized carbon. The heat released on nanoparticle condensation causes some of the trace HOPG surface oxidation products to react with the Pt, to produce PtO_x.

Chapter 4. Article 2: The surface analytical characterization of carbon fibers functionalized by H_2SO_4/HNO_3 treatment

Gaixia Zhang,[a] Shuhui Sun,[b] Dequan Yang,[a] Jean-Pol Dodelet,[b] and Edward Sacher[a]

[a] Regroupement Québécois de Matériaux de Pointe, Département de Génie Physique, École Polytechnique, C.P. 6079, succursale Centre-Ville, Montréal, Québec H3C 3A7, Canada

[b] INRS, Énergie, Matériaux et Télécommunications, Varennes, Québec J3X 1S2, Canada

From the previous chapter, we know that the Pt nanoparticles have very weak interfacial interactions with pristine carbon materials, resulting in poor nanoparticle adhesion; as a result, surface diffusion of the nanoparticles leads to both increased nanoparticle size, through coalescence, and a lower particle number density. It is only by the intentional chemical functionalization of these support materials that groups are provided to which the Pt nanoparticles adhere. To date, many different treatments have been carried out to functionalize carbon materials; one of the most used treatments is mixed sulfuric/nitric acids (H_2SO_4/HNO_3), with either high temperature reflux or prolonged lower temperature sonication. Despite the popularity of this treatment, the oxidation mechanism is not known. Here, we describe our mechanistic study of the use of mixed H_2SO_4/HNO_3 acids to functionalize carbon fibers; because they, too, contain graphene layers, the mechanism is expected to be similar to that for CNTs. Our purpose was to better understand and control the functionalization of carbon materials for fuel cell applications.

In this chapter, a systematic, time-dependent, surface-sensitive study has, for the first time, given new insights into the mechanism of the often-used, but unexplained, sulfuric/nitric acid oxidation of graphene-containing materials, such as carbon fibers and carbon nanotubes. To do this, we have used X-ray photoelectron, photoacoustic FTIR and Raman spectroscopies to follow the evolution of the functionalization of carbon fibers sonicated in a 3:1 (v/v) mixture of concentrated sulfuric/nitric acids at 60°C. The study has revealed, for the first time, the presence of not only four O-containing species but, also, two N-containing species and two S-containing species, all strongly bonded to the fibers, during the oxidation process; the amounts of those species varied, in a discontinuous manner, with treatment time, especially in the early stages, rather than constantly increasing with time. Two of the O-containing species diminished in concentration with treatment time, eventually disappearing, as did all the S- and N-containing species. The only nontransitory oxidized carbon functionality was COOH, manifested by the two remaining O1s XPS peaks, which continued to form long after the disappearance of the N- and S-containing species. This slow production of carboxylic acid indicates that it is the rate controlling step of the functionalization process, occurring subsequent to the site preparation process initiated by the transitory species.

4.1. Introduction

Polymer electrolyte membrane fuel cells are presently attracting interest for power source applications, due to their high efficiency, high energy density, low operating temperatures, and low pollution [1-3,5,103,104]. One of the challenges to their commercialization is the high cost of noble metal nanoparticles, such as Pt, used as electrocatalysts. To enhance the utilization and cost-effectiveness of the catalyst, novel carbon materials, such as carbon black, carbon nanotubes (CNTs), and carbon fibers, possessing the required mechanical, thermal and electrical properties, as well as high surface areas, have been used as electrocatalyst supports [105-109]. These untreated carbon material surfaces, which must be chemically inert, manifest weak interfacial interactions, resulting in poor nanoparticle adhesion; as a result, surface diffusion of the nanoparticles leads to both increased nanoparticle size, through coalescence, and a lower particle number density. It is only by the intentional chemical functionalization of these support materials that functional groups are provided, to which the Pt nanoparticles adhere.

Carbon fiber paper (or carbon cloth) is presently used, both as an effective electrode substrate and as a catalyst support for the direct growth of carbon nanotubes or nanofibers in fuel cells [8,11,110-114]; this is not only because of its desirable properties, as mentioned above but, also, because of its network-like, highly porous structure. The paper is woven from carbon fibers, which are, themselves, made from graphitized poly(acrylonitrile), polysaccharide (e.g., cellulose) or pitch fibers [115,116]; they are cost-effective and have been extensively applied in fuel cells. Being graphitized, such fibers contain the same graphene sheets present in CNTs and highly oriented pyrolytic graphite (HOPG); in fibers, they are aligned, to some extent, along the fiber drawing

axis [115,116], creating a nematic structure often referred to as turbostratic. The edges of the graphene sheets are terminated by aliphatic chains that did not participate in the graphitization process.

Surface functionalization will be necessary for the deposition of high loadings of metal nanoparticles on the fibers because their surfaces are, as mentioned above, inert. To date, many studies have been carried out on the functionalization of carbon fibers, mostly by Sherwood [117]. We have chosen to expand on these studies because there is a commercial need for the functionalization of carbon fibers in fuel cell applications, as well as in fiber-reinforced composites; further, because of their graphene structures, the results on carbon fibers can be used as a model for a better understanding of the functional mechanism of other carbon materials, such as CNTs and highly oriented pyrolytic graphite (HOPG).

Notwithstanding the fact that the use of mixed sulfuric/nitric acids (H_2SO_4/HNO_3) to functionalize CNTs is widespread [118-124], using either high temperature reflux or prolonged lower temperature sonication, the oxidation mechanism is not known. This lack of understanding of the mechanism exists despite the fact that several authors have tried, over several decades, to understand it; one author, for example, has devoted over 20 papers in an effort to do so. One reason for this continued lack of understanding is that, although mixed H_2SO_4/HNO_3 is used in aromatic nitration [125], that reaction is a *nucleophilic substitution*, in which a ring proton is substituted by a nitro group. As used in CNT and carbon fiber functionalization, it is an *oxidative cleavage*. Textbooks generally do not mention such a reaction; when they do, it is presented without a mechanism.

An attempt had been made to explain this oxidation process, using the nitration of 2,4-dinitrotoluene to 2,4,6-trinitrotoluene as a model [126]. Among the byproducts formed are 2,4,6-trinitrobenzyl alcohol, 2,4,6-trinitrobenzaldehyde and 2,4,6-trinitrobenzoic acid. The explanation relied heavily on attacks by •NO₂ and •NO free radicals; in the proposed mechanism, the benzaldehyde and benzyl alcohol are the principal byproducts, and the benzaldehyde further reacts to form benzoic acid. We initially considered that the oxidation of the methyl group in 2,4-dinitrotoluene may be a model for the oxidation of the structure in carbon fibers because we thought that, in a fashion similar to what occurs in 2,4-dinitrotoluene, only the aliphatic groups that terminate the graphene sheets would be oxidized, while hydrogenated graphene terminations would be nitrated.

We previously reported the use of aqueous sonication [127] and plasma treatments [128] to functionalize CNTs and HOPG; such techniques introduce several oxidized carbon species (–OH, –C=O, –COOH) in a controllable, repeatable manner. Here, we describe our mechanistic study of the use of mixed H_2SO_4/HNO_3 acids to functionalize carbon fibers, whose mechanism is expected to be similar to that for CNTs. Comparing three methods using this mixed acid treatment, with and without sonication, at room and elevated temperatures, we have obtained an efficient means to functionalize carbon fibers. Using this method, we have characterized the surface chemistry of functionalized carbon fiber paper by combining infrared, Raman and X-ray photoelectron spectroscopies to give new insights into the often-used oxidation of graphene-containing materials. We have, for the first time, demonstrated the presence of not only O-containing, but also N- and S-containing species during the oxidation process, as well as the fact that the amounts of those functional groups varied with treatment time, especially in the early stages, rather than constantly increasing with time. We have found

that the previous attempt made to explain the oxidation process [126] is inconsistent with our present results.

4.2. Experimental

The carbon fiber substrate used was Spectracorp carbon paper, type B-3/2050A-0550, purchased from E-TEK. It has a typical thickness of 0.13 mm and a typical density of 0.5 g/cc. All the chemicals were purchased from Sigma–Aldrich.

Three methods were used for carbon fiber oxidation: Method 1 employed a 3:1 (v/v) mixture of concentrated H_2SO_4/HNO_3, with sonication at 60°C. In a typical reaction, several small pieces of carbon fiber paper were added to 60 ml of this mixture in a reaction flask. (**The acid mixture is highly corrosive. Extreme care should therefore be exercised during handling.**) The flask was placed in an ultrasonic water bath (Cole-Parmer Instrument Company), operating at 152 W and 47 kHz and maintained at 60°C. The treatment was carried out at various precisely controlled times, between 10 s and 240 min. The treated substrate was then placed in a beaker and washed twice in DI water. If the pH of the wash water was not ~ 7, it was again washed for 2 min, with sonication; this was repeated, without sonication, until the pH ~ 7. Washing removes all water-soluble N- and S-oxides, i.e., those O-bonded to the fiber, replacing them with hydroxyl groups through ion exchange; those directly N- and S-bonded are retained.

Method 2 employed a 1:1 (v/v) mixture of concentrated H_2SO_4/HNO_3, with sonication at 60°C. The treatment and washing were identical to those used in Method 1.

Method 3 employed a 1:1 (v/v) mixture of concentrated H_2SO_4/HNO_3, with storage at room temperature. The treatment did not include sonication, and took place only for a duration of 53 h; the washing was identical to that used in Method 1.

X-ray photoelectron spectroscopic (XPS) analysis was carried out in a VG ESCALAB 220i-XL, using a monochromated Al Kα source (1486.6 eV), at a base pressure of 2×10^{-9} mbar. High resolution spectra were obtained at a perpendicular take-off angle, using a pass energy of 20 eV and 0.05 eV energy steps. After Shirley background removal, the component peaks were separated using the public domain XPSPeak program, version 4.1 [129]. The binding energy was calibrated by placing the principal C1s peak at 284.6 eV.

Surface vibrational data were obtained in a Bio-Rad FTS 6000 spectrometer, using both attenuated total reflectance (ATR-FTIR) and photoacoustic Fourier Transform IR (PA-FTIR) spectroscopies. For both, the spectral resolution was set at 4 cm^{-1}, with 2000 spectral co-additions used to increase S/N. ATR-FTIR spectra were acquired using a trapezoidal Ge single-crystal prism ($50 \times 20 \times 2$ mm) with a $45°$ facet angle; the background was determined with the prism alone, and then subtracted from all the spectra. PA-FTIR spectra were acquired using a He-purged MTEC 300 photoacoustic cell.

Raman spectra were acquired using a Renishaw RM3000 Raman microscope equipped with a 1800 lines/mm grating and a motorized three-axis *XYZ* mapping stage. A 514.5 nm Ar$^+$ laser beam, with an incident power of $\sim$ 10 mW at the sample, served as the excitation source. It was focused, with a 50× magnification objective, onto a spot 1-2 μm in diameter. The optical power at the laser head position was maintained at 69.9 mW. Spectral calibration employed the 520.5 cm^{-1} transverse optical phonon-phonon mode

peak of a Si wafer reference. Confocal spectra, from the sample surface, were accumulated in the 100-3500 cm^{-1} range of the Stokes Raman shift region. Spectral acquisition used a detector integration time of 30 s/grating exposure position, with four accumulations to improve S/N.

4.3. Results

4.3.1. XPS

4.3.1.1 Comparison of the three carbon fiber oxidation methods

The C1s, O1s, S2p and N1s XPS spectra of four samples, illustrating the functionalization methods mentioned in Section 2, are found in Figures 4.1a-d. These include samples **A** (method 1, 3:1 v/v H_2SO_4/HNO_3, sonicated at 60°C for 15min), **B** (method 2, 1:1 v/v H_2SO_4/HNO_3, sonicated at 60°C for 15min), **C** (method 3, 1:1 v/v H_2SO_4/HNO_3, maintained at room temperature, without sonication, for 53h), and **D** (untreated carbon fiber paper). While there is little difference in the C1s spectra for the untreated and treated samples, there are substantial differences in the O1s, S2p and N1s spectra. This is most readily seen in Table 1, which contains the atomic percentages of the various elements, as determined from the spectral areas and relative sensitivity factors. We see that, compared to untreated carbon paper, which has a trace of O, obvious functionalization has occurred on samples treated by all three methods. Samples B and C have similar degrees of functionalization, with ~ 10% heteroatoms, despite substantially different treatment conditions, while sample A, with just the same 15 min treatment time as sample B, has double its concentration of heteroatoms. That is, method 1 is the most efficient in functionalizing the carbon fibers; although the increased functionalization efficiency with increased H_2SO_4 concentration has also been found in

past studies, we have not yet attempted to understand why. Nonetheless, because of this result, subsequent functionalization experiments were confined to method 1.
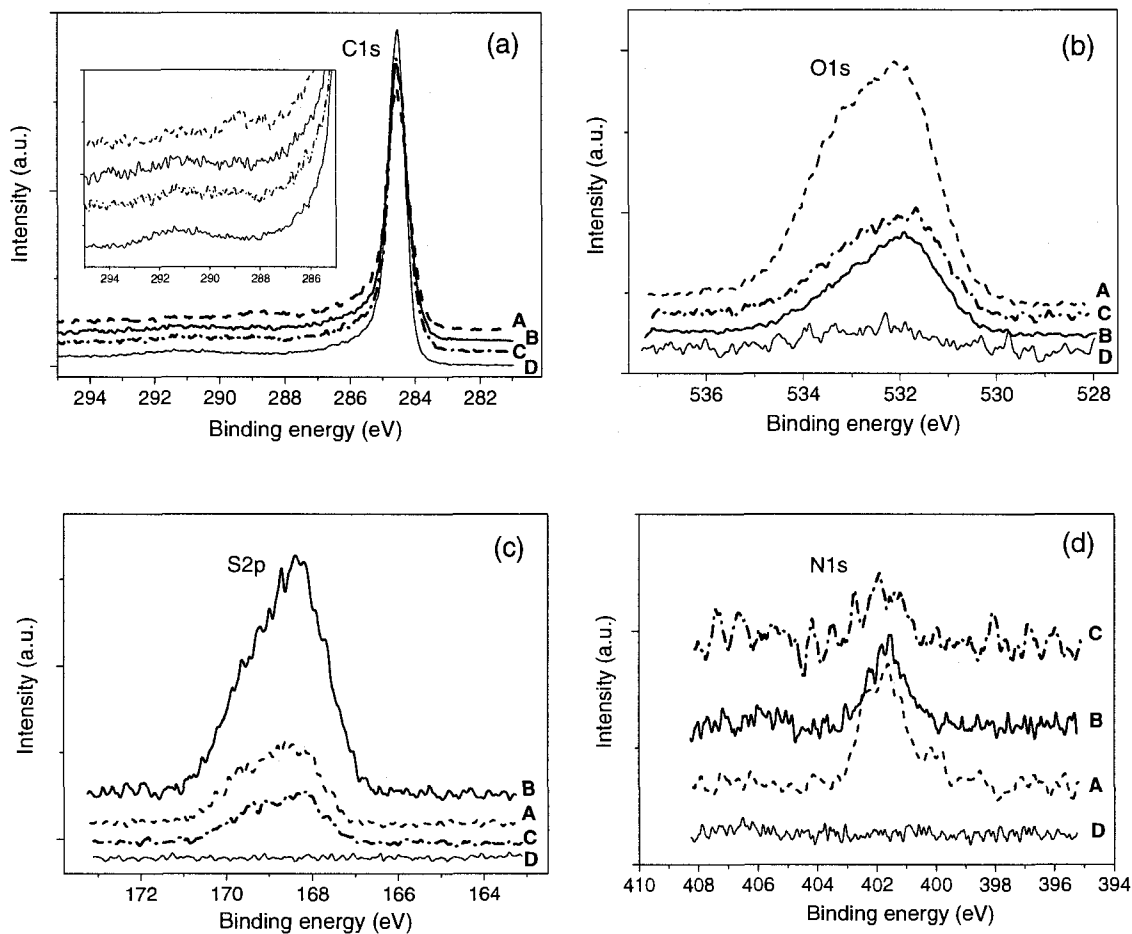
Figure 4.1. The high-resolution XPS spectra of (a) C1s, (b) O1s, (c) S2p and (d) N1s of four samples: **A** (method 1, 3:1 v/v of H_2SO_4/HNO_3, sonicated at 60°C, 15 min), **B** (method 2, 1:1 v/v of H_2SO_4/HNO_3, sonicated at 60°C, 15 min), **C** (method 3, 1:1 v/v of H_2SO_4/HNO_3, at room temperature, 53 h), and **D** (untreated carbon paper).

Table 4.1. The atomic percentages of the various elements at the sample surfaces.

Samples	H₂SO₄/HNO₃ treatments	Times	C%	O%	S%	N%
sample A	Method 1, 3:1 (v/v), 60°C	15 min	81.3	16.4	1.0	1.3
sample B	Method 2, 1:1 (v/v), 60°C	15 min	89.6	6.5	3.0	0.9
sample C	Method 3, 1:1 (v/v), RT	53 h	91.0	7.6	0.7	0.7
sample D	pristine	0 min	98.9	1.1	0	0

4.3.1.2 XPS analysis of carbon fibers, functionalized by method 1, as a function of sonication time

The variations of the C1s, O1s, S2p and N1s XPS spectra of treated carbon fibers, normalized to the same C1s areal intensity, are found in Figures 4.2a-d as a function of treatment time. The peak separations used for the various spectra are shown as insets.

As seen in Figure 4.2a, there is little change in the main peak of the C1s spectrum, at 284.6 eV, with sonication time; before treatment, five peaks were required to fit the spectrum of the nematic graphene structures created on fiber formation, as we previously found with HOPG [53] and CNTs [127]. However, with treatment, a new C1s peak appeared at ~289 eV, that evolved with increasing treatment time. The peak positions, including that of the new one that appeared on treatment, are found in Table 2.
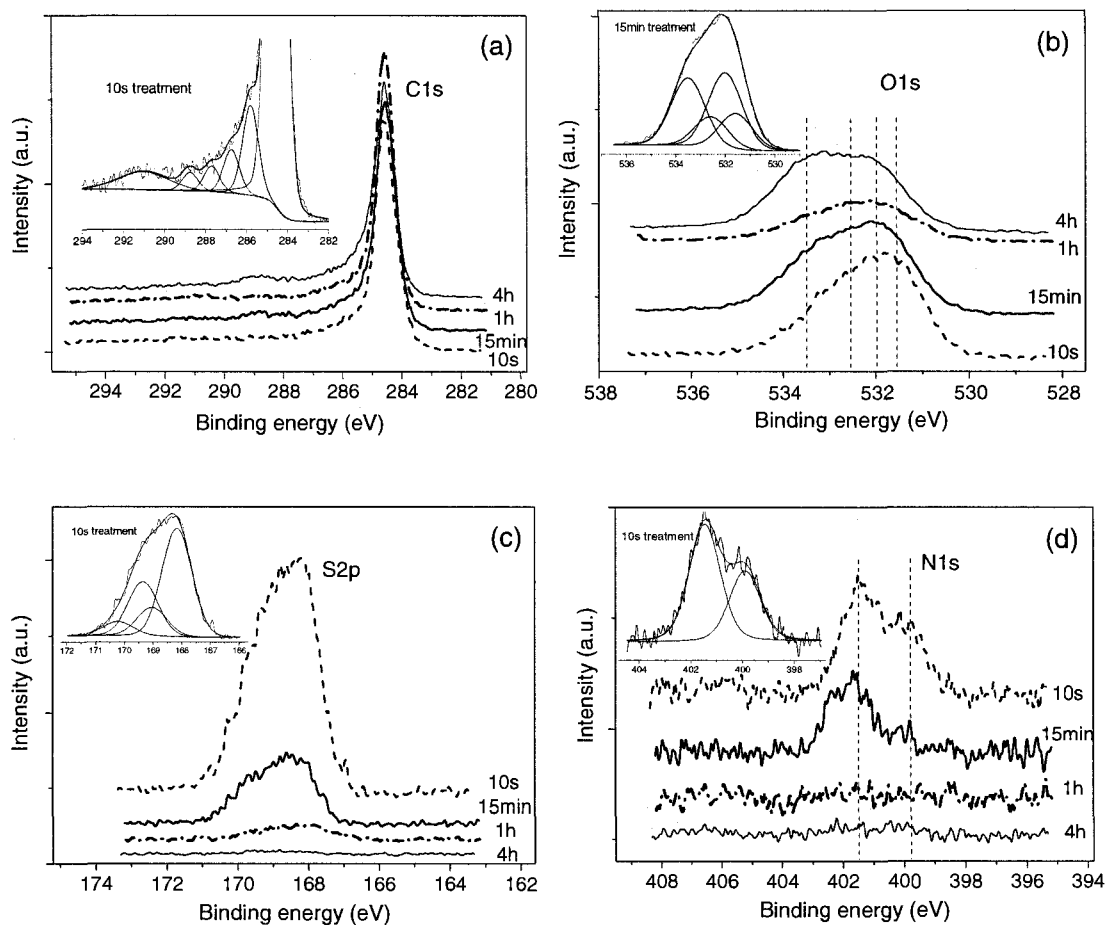
Figure 4.2. The variations of the (a) C1s, (b) O1s, (c) S2p and (d) N1s XPS spectra with treatment time. The peak separations used for the various spectra are shown as insets.

While the untreated fibers manifested only a bare trace of oxygen, an O1s spectrum developed immediately on treatment, which required 4 peaks: two new ones (531.6 and 532.6 eV) in addition to the two expected for oxidized carbon (532 and 533.5 eV) [130]. The spectral evolution may be seen in Figure 4.2b, where the vertical lines indicate the peak positions. The lack of residual oxygen in the pristine sample indicates that its

source is pitch, since poly(acrylonitrile) retains residual N, and polysaccharides, residual O.

Table 4.2. Component peaks and attributions of XPS spectra.

Peak No.		Binding energy (eV)	Attributions
C1s	C1	284.6	Extensively delocalized alternant hydrocarbon
	C2	285.6	Localized alternant hydrocarbon
	C3	286.6	Surface free radical sp^3 bonds, -OH, S-component
	C4	287.8	$\pi^* \longleftarrow \pi$ shake-up peak of C2, -C=O
	C5	288.9	COOH, N-component
	C6	290.8	$\pi^* \longleftarrow \pi$ shake-up peak of C1
O1s	O1	531.6	unattributed oxides of S
	O2	532.0	C=O
	O3	532.6	unattributed oxides of N
	O4	533.5	C–O
S2p	S1	168.2	unattributed oxide of S
	S2	169.1	unattributed oxide of S
N1s	N1	400.0	unattributed oxide of N
	N2	401.8	unattributed oxide of N

Treatment introduced two S2p doublets, found in Figure 4.2c, each having a 2:1 $p_{3/2}$:$p_{1/2}$ ratio, and 1.18 eV $p_{3/2}$-$p_{1/2}$ separation. Similarly, the N1s spectrum introduced on treatment, composed of two peaks, is found in Figure 4.2d. Interestingly, both the S2p and N1s spectral intensities decrease with treatment time, before disappearing.

4.3.2 Raman Spectroscopy

In graphene-containing structures, such as CNTs and carbon fibers, Raman spectroscopy can be a sensitive probe of both electronic structure and the presence of defects. The first-order Raman spectra of the pristine and acid-treated fibers (Figure 4.3a) contain two prominent peaks, located at about 1350 (D band) and 1580 (G band) cm^{-1}, with an additional weak feature, becoming more evident with treatment, at about 1610 cm^{-1} (D′ band). The G band corresponds to graphitic in-plane vibrations with E_{2g} symmetry; while several explanations have been proposed for the origins of the D and D′ bands [131-133], they are both generally believed to arise from the presence of defects and disorder, such as the presence of in-plane substitutional heteroatoms, grain boundaries, aliphatic chains, etc., which serve to lower the symmetry of the quasi-infinite lattice. The different behaviors of the D and D′ bands are attributed to the different Raman-allowed modes from which they are generated [134]. As confirmed in Figure 4.3a, where the spectra have been normalized to the intensity of the G band, both are related to the extent of disorder: treatment has caused large increases in the D and D′ band intensities.

Attempted peak separation has revealed a single D band component. The G-D′ separation is seen in Figure 4.3b, and the D/G and D′/G intensity ratios are found in Figure 4.3c. Peak Raman shifts are found in Figure 4.3d, and FWHM changes, in Figure 4.3e.
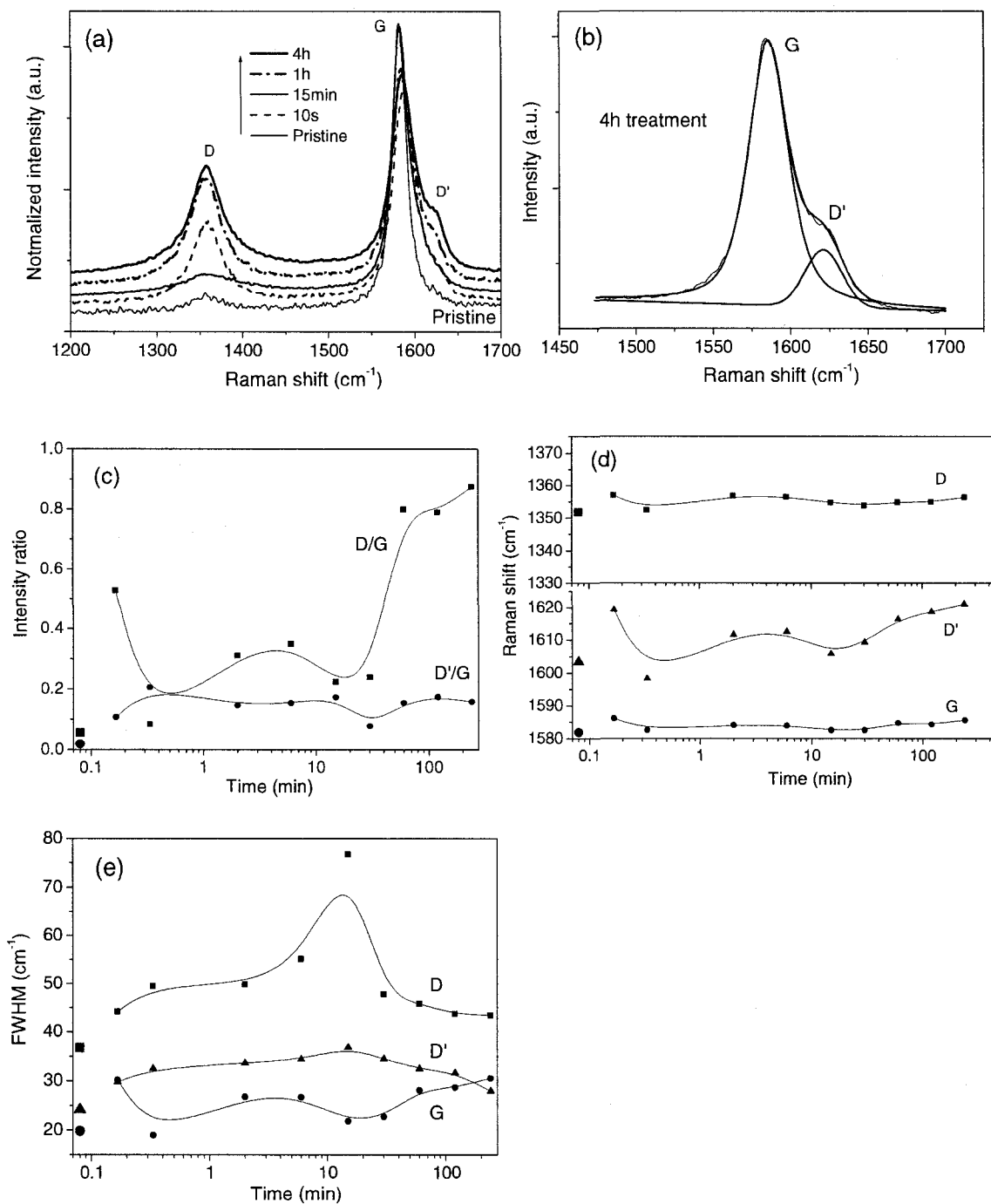
Figure 4.3. (a) The first-order Raman spectra (normalized to the G peak) of carbon fibers, (b) the G-D′ separation, (c) the D/G and D′/G intensity ratios, (d) the peak Raman shifts of D, D′ and G bands, and (e) their FWHMs, with treatment time. The points at the left border are those at t = 0.

4.3.3 Photoacoustic FTIR Spectroscopy
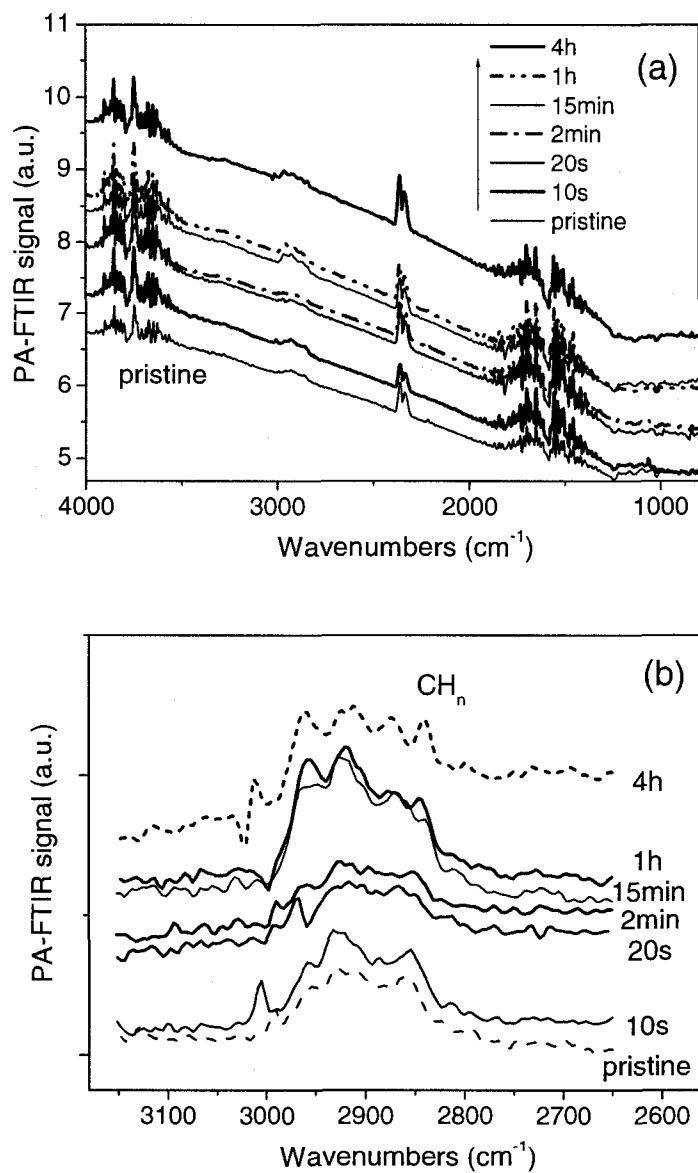
Figure 4.4. (a) The PA-FTIR spectra of carbon fibers with acid treatment time; (b) the high-resolution PA-FTIR spectra of the CH_n stretching peaks.

While FTIR spectroscopy has been successfully adapted by us to study CNT surfaces [127,135], the severe scattering of carbon fibers has made a similar analysis difficult here: both photoacoustic and ATR results were limited. Figure 4.4a shows the photoacoustic results. While ATR spectra are not shown, both suffered from the presence of strong skeletal in-plane vibrations (1450-1600 cm^{-1}) and aromatic substitution patterns (1660-2000 cm^{-1}) [136], effectively obscuring any oxidized C and N groups that might have been present.

In addition, despite the presence of an S2p XPS spectrum, in Figure 4.1c, no evidence is seen for S-containing groups in the 1150-1230 cm^{-1} range [136] in Figure 4.4a. The reason for this may be seen in Figure 4.4b, where, even with XPS evidence of oxidation, the CH_n stretching peaks, at 2800-3000 cm^{-1}, show nothing more than sample-to-sample variations. This is because, under the conditions used, photoacoustic FTIR probes the whole sample (2-3 μm probe depth) while oxidation occurs only in the nm range at the sample surface; such changes are more easily seen by XPS, which probes to a depth of several nm. One is led to suspect that, even in the absence of the interferences in the 1450-2000 cm^{-1} range, any oxidized C and N present would also have been undetected.

4.3.4 Carbon fiber morphologies

Carbon fiber morphologies, before and after acid treatment, were obtained by FESEM. They are found in Figure 4.5. Photomicrographs of pristine fibers are found at low magnification in Figure 4.5a and, at high magnification, in Figure 4.5b, where fiber orientation marks are evident. Acid treatment for 15 minutes (Figure 4.5c) and 4 hours (Figure 4.5d) serves only to accentuate the orientation marks, indicating the removal of some surface material.
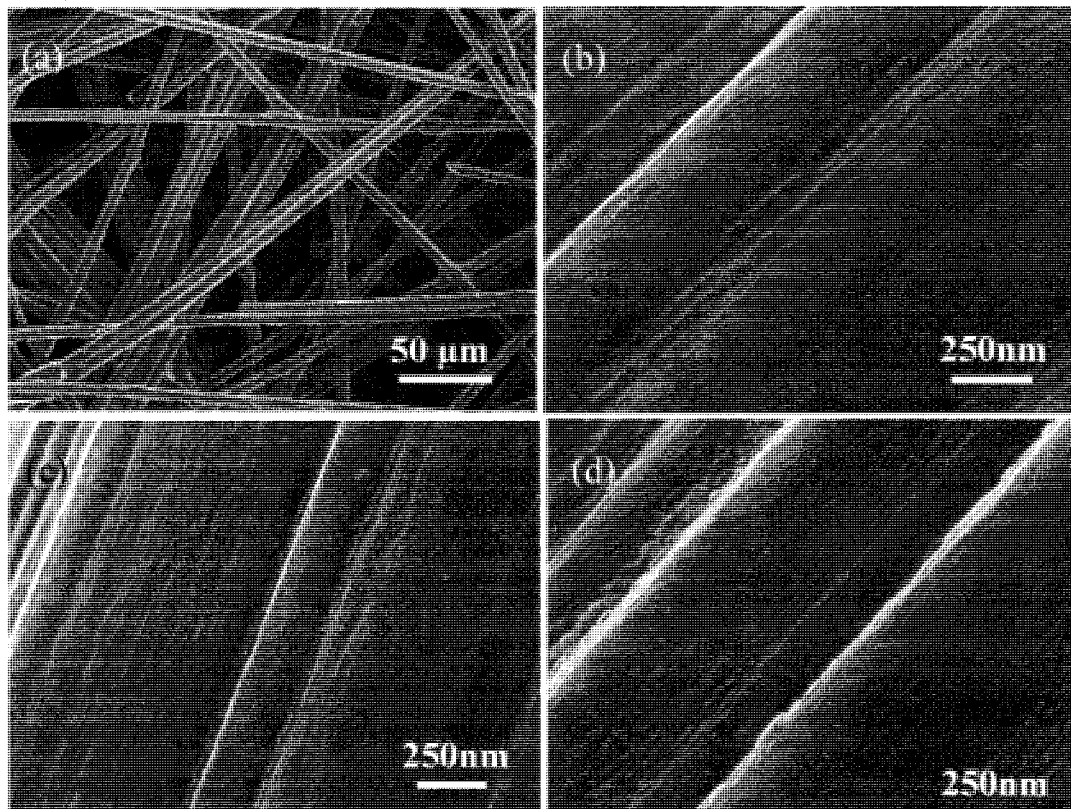
Figure 4.5. Pristine carbon fiber at (a) low and (b) high resolution, and after (c) 15 min and (d) 4 h of acid treatment.

4.4. Discussion

4.4.1 XPS Analysis

Peak separations were carried out based on our prior work on graphene-containing systems [53,137,138], and the five peaks in pristine carbon fibers are given in Table 2. The lack of oxygen in the pristine sample (Figure 4.1c) means that oxidized C species do not have to be taken into account in determining the pristine fiber peak positions. Table 1

and Figures 4.1 and 4.2 show that, on treatment, large amounts of heteroatoms are introduced; despite this, the five original peaks, plus an additional new peak at ~289 eV, are all that are needed to separate the C1s spectral components. This means that any additional peaks, due to oxidized C, S and N groups produced on treatment, and seen in Table 1 and Figures 4.1 and 4.2, add little to the C1s spectrum of the pristine sample; this indicates that only the outer surface of the fiber is attacked.

Since these spectra evolve with time, with species appearing and disappearing while the same C1s peaks are maintained, this signifies that several components may contribute to each of the peaks. For example, various compendia of peak attributions [130] show that peaks due to oxidized carbon species (e.g., –OH, –C=O, –COOH) exist in the 285.5-289.5 eV range, peaks due to carbon bonded to oxidized sulfur (e.g., sulfonyl, sulfonic acid) exist in the 284.5-287 eV range, and peaks due to carbon bonded to oxidized nitrogen (e.g., nitro) exist in the 287-289 eV range. Thus, in the present case, a peak at 286.6 eV might be due to the graphene structure and/or alcohol and/or sulfone formation. For this reason, it is difficult to precisely attribute the source of any evolving peak. Even the new peak formed at 289 eV may be due to COOH and/or nitryl formation. With treatment time, as Figures 4.2c and 4.2d show, the eventual disappearance of both S and N makes attribution more straight-forward.

The O1s spectra were found to be composed of four peaks (Figure 4.2b). A *single* peak at 532 eV is attributed to C-OH/C=O, which we have not tried to separate. The *simultaneous* appearance of a peak at 533.5 eV is attributed to the second oxygen present in COOH (the acid C=O appears at 532 eV, and the acid C-OH, at 533.5 eV). Those at 531.6 and 532.6 eV are attributed to S- and N-containing species[130], respectively, and, as the S and N contents, in Figures 4.2c and 4.2d, diminish and

disappear, so do they. The variations of all the peak intensities, over the total sonication treatment time, are found in Figures 4.6a-d, and the atomic fractions, in Figure 4.6e.

As noted earlier, attributions to oxidized carbon species may be made toward the end of the treatment time, when the S and N concentrations (Figure 4.6e) are essentially zero. Thus, the parallel rise in both O2 and O4 (Figure 4.6b), indicates the formation of COOH, even while the concentrations of S and N are decreasing (Figure 4.6e). This means that both S and N participate in the formation of some precursor site that only subsequently forms COOH.

The similar trends found for C3 (possibly C-OH), C4 (possibly C=O), and C5 (possibly COOH) in Figure 4.6a, after the first hour of treatment, indicating that all three oxidation products may, in fact, be produced This is mirrored by the apparently greater intensity of O2 over O4, in Figure 4.6b, until the final stages of treatment, where –OH and –C=O are apparently consumed. Indeed, assuming that C3, C4 and C5 relate to O2, and that C5 alone relates to O4, these contributions may be quasi-converted to O1s contributions by dividing by the C1s sensitivity factor and multiplying by the O1s sensitivity factor; this is done in Figure 4.6f, and the plots compare favorably with those of O2 and O4, in Figure 4.6b.
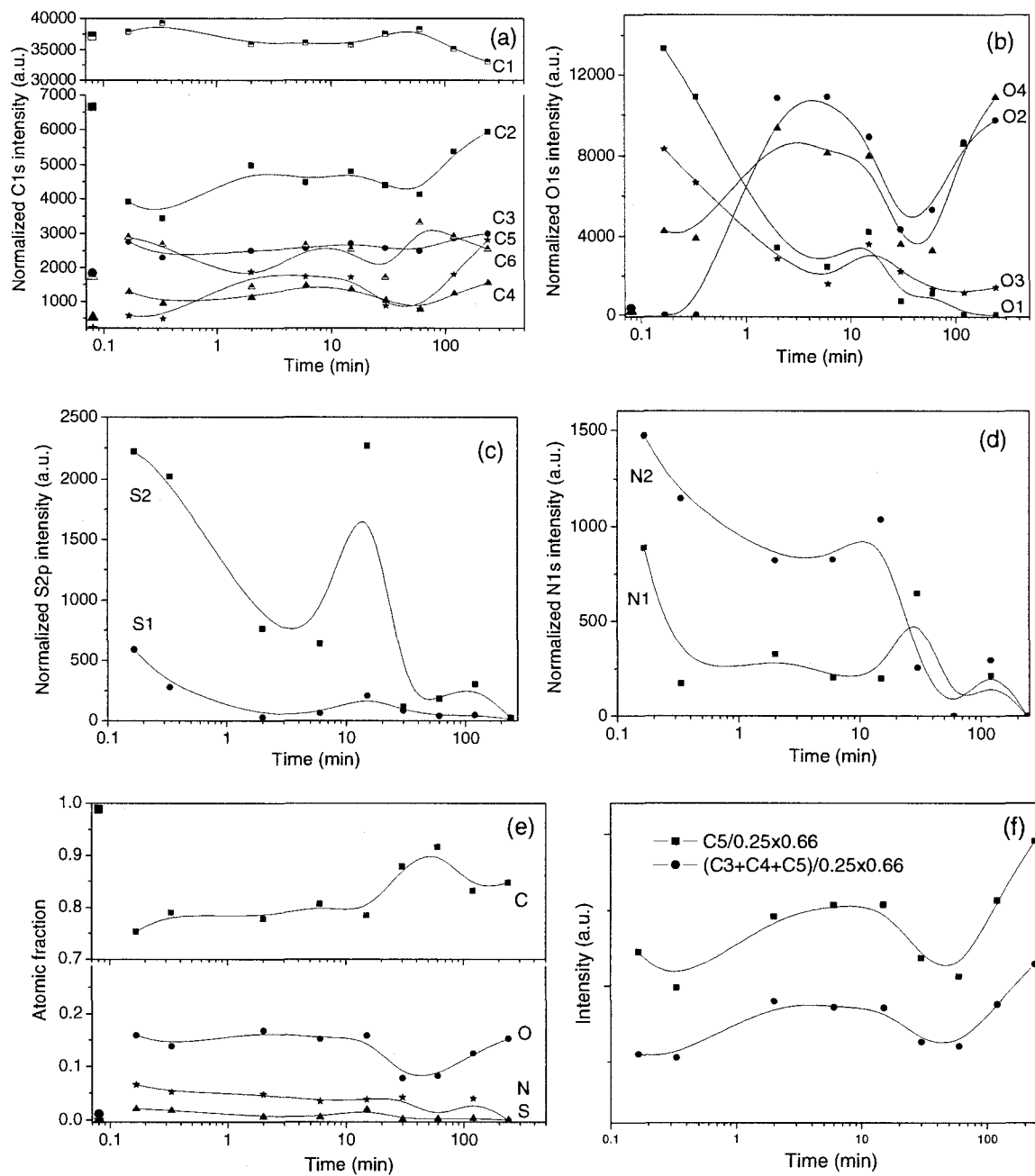
Figure 4.6. The variations of all the peak intensities of (a) C1s, (b) O1s, (c) S2p and (d) N1s; (e) the atomic percentages of the various elements; and (f) arbitrary O1s intensities divided by the C1s sensitivity factor and multiplying by the O1s sensitivity factor.

4.4.2 Raman Analysis

The D and D′ bands are attributed to defective graphene and disordered carbons, and may be used as diagnostics of disruption in the graphene structure. Figure 4.3c shows the variations of A_D/A_G and $A_{D'}/A_G$, where A indicates peak area, as a function of treatment time. A_D/A_G is very sensitive to the treatment while $A_{D'}/A_G$ is less so, confirming what some authors have reported [139]; this is due to the different Raman-allowed modes from which the D and D′ bands are generated, as already mentioned.

Figure 4.3d shows the Raman shift variations of the D, D′ and G bands with treatment time. The D′ band shift is much more sensitive to treatment than the others, and is the reason for the peak shape change in the 1500-1700 cm^{-1} region with treatment time. The width changes, in Figure 4.3e, show a maximum at ~ 15 minutes of treatment time, as do the N and S concentrations in Figures 4.6c and 4.6d; the opposing trends of the D (and D′) and G peaks implies that the former undergo a brief increase in disorder at the same time that the latter undergoes a brief decrease. This is clearly due to the short-lived formation of S- and N-containing species.

4.4.3 Oxidation Mechanism

In his explanation of the methyl group oxidation occurring in 2,4-dinitrotoluene, Yu [126] discussed the formation of •NO_2 and •NO free radicals, and their participation in the different transient structures formed. In addition to aromatic nitration, the methyl group is initially converted to aldehyde and alcohol, and the aldehyde subsequently forms COOH. The mechanism is reasonable, and in agreement with much that is known about reactions occurring in aromatic systems. Our comparison must be considered

within the limits of (1) the certain loss of nitrate and sulfate, imposed by our washing of the samples to terminate each treatment time, and (2) the fact that only the outer surface of the fiber is attacked, making any changes difficult to observe.

Several things are clear from our results:

· As seen in Figures 4.6c-e, both S and N are totally lost; that is, the expected aromatic nitration has not occurred.

· Both O2 and O4, in Figure 4.6b, evolve in similar fashions, especially toward the end of the treatment time, indicating the production of COOH. The similar evolution of C5, in Figure 4.6a, argues that COOH is the final product, in contradistinction to the Yu mechanism. As mentioned in section 4.1, there is evidence of the early formation of both –OH and –C=O.

· COOH formation occurs *subsequent to* the disappearance of both N and S, rather than simultaneously. This suggests that COOH formation is the rate-controlling step of the oxidation process, and uses sites *previously prepared* by the action of the H_2SO_4/HNO_3 sonication treatment, certainly promoted by the energy input of the sonication process [127].

Thus, while we cannot say what the effect, if any, of sulfate and nitrate production might be, and we do not yet know the precise identities of the transient $C-S-O_n$ and $C-N-O_n$ species seen in Figures 4.2b-d and 4.6b-d, there is a rapid, complex interplay of the concentrated H_2SO_4/HNO_3 mixture, presumably with the exposed aliphatic chains on the carbon fiber, whose result is to prepare sites for subsequent oxidation. This is supported by the Raman data in Figures 4.3c and 4.3e, where the increased disorder,

signaled by the D peak, ends with the loss of N and S, while the formation of COOH continues.

4.5. Conclusions

The oxidation of carbon fibers by concentrated H_2SO_4/HNO_3, has been studied using X-ray photoelectron, photoacoustic FTIR and Raman spectroscopies, and has revealed that previously offered mechanisms do not correspond to our findings. We have shown that aromatic nitration of the fibers does not occur. Following the production of S- and N-containing species that are eventually lost over the time of reaction, COOH is formed as the rate-controlling step; this indicates that the S- and N-containing species formed serve to prepare sites for subsequent COOH development. Raman spectroscopy indicates the increase and subsequent decrease of disorder during the oxidation process, as the S- and N-containing species form and disappear. While our understanding of the carbon fiber oxidation process remains incomplete, the complexity of the reaction, as revealed by the present study, offers a reason why. The mechanism of this treatment may be generally applicable to other graphene-containing materials, such as CNTs and HOPG, and with other H_2SO_4/HNO_3 ratios.

Chapter 5. Article 3: The structure and morphology of Co nanoparticles deposited onto highly oriented pyrolytic graphite

Gaixia Zhang, Dequan Yang, and Edward Sacher

Regroupement Québécois de Matériaux de Pointe, Département de Génie Physique, École Polytechnique, C.P. 6079, succursale Centre-Ville, Montréal, Québec H3C 3A7, Canada

Due to their unique structural, mechanical, and electrical properties, CNTs have recently been proposed to replace the carbon powder traditionally used in PEMFCs. However, the results, using loose CNTs, did not show advantages over carbon black because the Pt utilization within the PEMFC catalyst layer remained unaddressed. Growing CNTs directly on the carbon fiber paper, and subsequently electrodepositing the Pt selectively on the CNTs, promises to improve Pt utilization by securing the electronic route from the nanoparticles to the supporting electrode. The use of *in-situ* grown CNTs, and the resulting guaranteed electronic pathway it creates, eliminates the isolation of the carbon support from the Nafion-supported electrode. Since it is known that the size and the properties of the catalyst nanoparticles are directly related to the diameter of the CNTs, it is important to understand the interfacial interaction between the catalyst and their carbon fiber paper support, on which CNTs directly grow. To date, first transition series metal catalysts have been used, particularly inexpensive iron group metals, such as Co, Ni, as well as their alloys. Previously, our group had studied the properties of Ni nanoparticles. Here, we examined Co catalyst (see this chapter) and

Co-Ni (still being analyzed at the time of writing) alloy nanoparticles used to grow CNTs.

In this chapter, X-ray photoelectron spectroscopy (XPS) and atomic force microscopy (AFM) have been used to study Co nanoparticles evaporated onto freshly cleaved highly oriented pyrolytic graphite (HOPG) surfaces. XPS chemical characterization employed symmetrical lineshapes, and was carried out as functions of the amount of Co deposited, and of the time subsequent to deposition. The nominal amounts of evaporated Co ranged from 0.5 to 175 Å. On analyzing the relationships among the Co2p, C1s and O1s spectra, we found that evaporated Co reacts not only with HOPG surface defects (including oxidized carbon contaminant groups), but also with residual C- and O-containing species present in the vacuum chamber. Both carbide and oxide are produced as surface layers around each nanoparticle, stabilizing them and preventing further coalescence.

5.1. Introduction

The study of Co nanoparticles is very important because of their many applications, especially for data storage devices and sensors, where their use depends on their unexpected magnetic properties [140-142]; as well, they are efficient catalysts for the formation of carbon nanotubes (CNTs) [143-145]. Since the discovery of CNTs in 1991 [146], their unique properties [147,148] have made their synthesis and applications the subjects of many fundamental and applied studies.

Catalytic chemical vapor deposition has been widely used as a method for the synthesis of these CNTs, since it has the potential for low-cost, large-scale production, at lower temperatures and with less carbon impurities, when compared with arc discharge and laser ablation methods [149]. To date, First Transition Series metal catalysts have been used, particularly inexpensive iron group metals, such as Co and its alloys [150,151]. To obtain controlled or aligned CNTs using this method, it is necessary to manage the size and density of the deposited nanoparticle catalysts. To synthesize CNTs of a uniform diameter, it is crucial to distribute the catalyst uniformly across the substrate surface.

Highly oriented pyrolytic graphite (HOPG) has been widely used in the study of supported metal nanoparticles [12,152,153] because it has an inert, well defined, conducting surface, whose structure is well understood. In addition, its structure is similar to a number of novel carbon materials [154,155] that are widely used as substrates for growing CNTs [11,156-158].

Over the past several decades, work has been reported on Co deposited onto various substrates, such as Si, GaAs, Pt, Pd and HOPG [159-164], using low energy electron

diffraction (LEED), high resolution transmission electron microscopy (HRTEM), extended X-ray absorption fine structure (EXAFS), atomic force microscopy (AFM), Auger electron spectroscopy (AES) and X-ray photoelectron spectroscopy (XPS) techniques; it was found that Co nanoparticles react with some of these substrates. However, no reference has ever been made to the reaction of evaporated Co and residual gases. In the present work, we report our studies of Co nanoparticles evaporated onto freshly cleaved HOPG surfaces; we found that evaporated Co reacts not only with the substrate but also with residual gases, even in ultrahigh vacuum ($< 10^{-9}$ torr) and at room temperature.

We used XPS, a highly surface-specific technique with a probe depth of a few nanometers, which has been widely used in characterizing the chemical and electronic structural properties of metallic nanoparticles. Our resultant Co/HOPG spectra were analyzed using multicomponent symmetric peak separations for all the spectra (Co2p, C1s and O1s), which permitted us to identify interfacial interactions; we followed these peaks as a function of Co deposition, over a nominal range of 0.5-175 Å; they were also followed as a function of time subsequent to Co deposition. In addition, AFM was used for the morphological investigation of the deposited Co nanoparticles.

5.2. Experimental

HOPG, grade ZYA, 1 cm × 1 cm × 2 mm, was obtained from Advanced Ceramics, Inc. It was cleaved with adhesive tape immediately prior to each experiment and inserted into the X-ray photoelectron spectrometer.

Co evaporation used an ultra-pure Co rod purchased from SPI, Inc. It, too, was carried out in the preparation chamber, at a pressure of $< 3 \times 10^{-8}$ Torr, using a Quad-EVC

evaporator (Mantis Deposition, Ltd.), at a rate of ~ 0.15 nm/min. The thickness was monitored by a quartz crystal microbalance placed near the sample.

After transfer through a gate valve, without atmospheric exposure, XPS was performed in the analysis chamber of our VG ESCALAB 3 MARK II (Thermo VG Scientific), using a non-monochromated Al Kα X-ray source (1486.6 eV), at a base pressure of $< 2 \times 10^{-9}$ Torr. High resolution spectra were obtained at a perpendicular take-off angle, using a pass energy of 20 eV (step size: 0.05 eV; step dwell time: 200 ms). The instrument resolution was ~ 0.85 eV. After Shirley background removal, the component peaks were separated with the XPSPeak freeware [129], version 4.1, using mixed Gaussian-Lorentzian functions. The binding energy was calibrated by placing the principal C1s peak at 284.6 eV. The peak widths employed in the peak separations, given as full widths at half maxima (FWHM), were those previously found in our studies. In the cases of the C1s and O1s spectra, the same FWHM values were used for all the peaks in a given spectrum. In the case of the Co2p spectra, as described in the text, the FWHM of the Co^0 peak was somewhat narrower than those of the Co compounds formed, as is generally found for zerovalent metal nanocrystals.

The surface morphologies of Co deposited onto HOPG were obtained, *ex situ*, in contact mode, with a Si$_3$N$_4$ cantilever, using a Digital Instrument MultiMode Atomic Force Microscope (AFM). All the images collected were processed off-line using the WSxM 1.1 freeware [165].

5.3. Results

5.3.1. XPS spectra

5.3.1.1. The C1s spectra
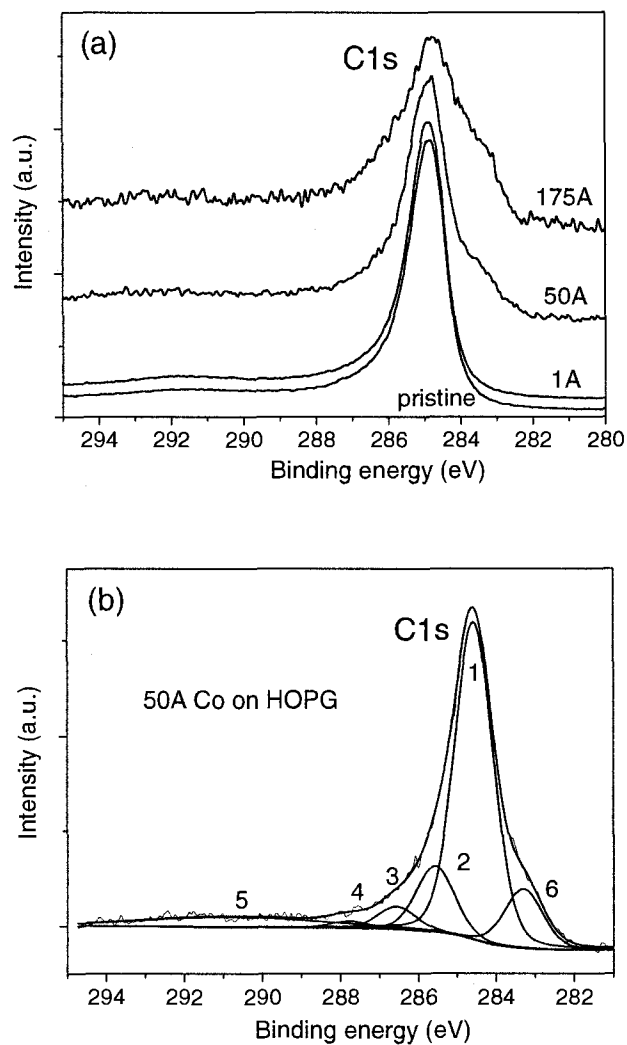
Figure 5.1. (a) The evolution of the C1s spectrum, as a function of nominal Co deposition onto HOPG surfaces, and (b) an example of XPS peak separation for 50 Å Co coverage.

Typical C1s XPS spectra, before and after Co deposition, are shown in Figure 5.1a. They are normalized to the same area as that in pristine HOPG. The spectral shape

obviously broadens with Co deposition, and a new peak appears in the 282-284 eV region, more clearly seen as the Co coverage increases, which signals carbide formation; this is quite different from what is found for many other metals deposited on HOPG surfaces [53,73,137]. Figure 5.1b shows an exemplary deconvolution of a C1s spectrum, with 50 Å Co coverage, where six symmetric components are needed, one more than the five used for pristine HOPG [53,73,137]. Except for the broader $\pi^* \leftarrow \pi$ shake-up peak, they all have the same FWHM; except for the additional peak, they are in the same positions as in pristine HOPG, where they have been attributed as follows [53,73,137]: $C1$ (284.6, undamaged alternant hydrocarbon structure), $C2$ (285.6, damaged alternant hydrocarbon structure), $C3$ (286.5, sp^3 free radical defects), $C4$ (287.8, the $C2$ $\pi^* \leftarrow \pi$ shake-up satellite), $C5$ (291.4, the $C1$ $\pi^* \leftarrow \pi$ shake-up satellite), and the new peak $C6$ (283.5 eV, carbide [166]). In the case of Co deposition, any additional peaks due to the presence of oxidized carbon species will superimpose on the original ($C1$-$C5$) peak range, and must be taken into account, as we previously reported [53,73,137] .

5.3.1.2 The O1s spectra

The O1s spectra for pristine HOPG, before and after Co deposition, are found in Figure 5.2a. Before Co deposition, the O1s spectrum exhibits a very small peak (elemental concentration, 0.3 %), with two identifiable components, at 532 eV ($O2$, double bonded oxidized carbon species, C=O) and 533.5 eV ($O3$, single bonded oxidized carbon species, C-OH). On Co deposition, a new peak appears at 530.5 eV ($O1$, in Figure 5.2b), attributed to the presence of a Co oxide [102].
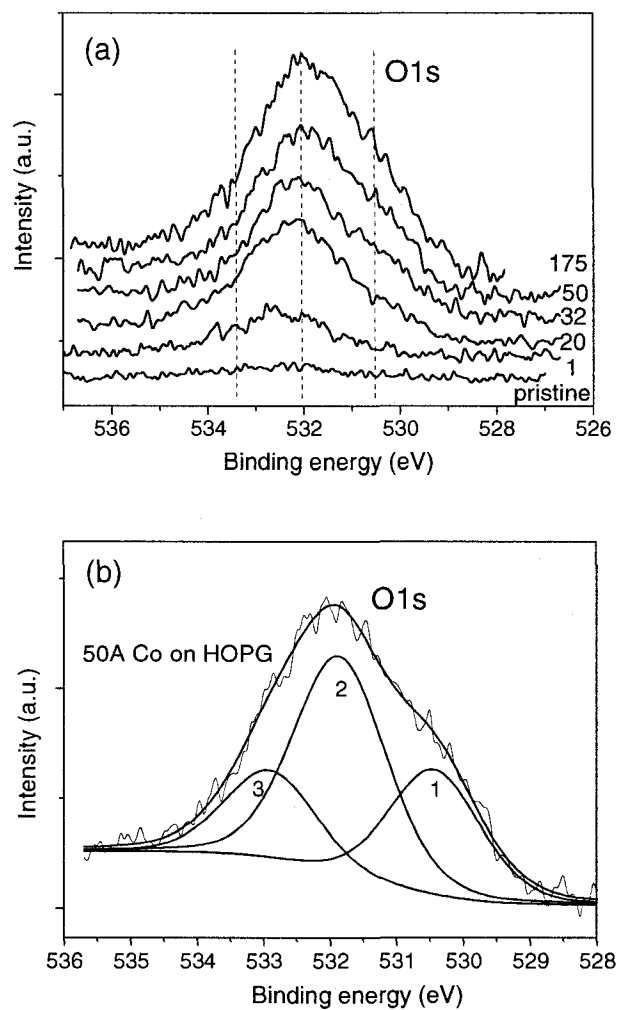
Figure 5.2. (a) The evolution of the O1s spectrum, as a function of nominal Co

deposition, and (b) an example of XPS peak separation for 50 Å Co coverage.

5.3.1.3 The Co2p spectra

Figure 5.3a shows the variation of the Co spectrum with coverage. The areal intensity

increases and the binding energy shifts to slightly lower energy with increasing Co

deposition; there is no obvious shape change. The techniques adopted for both

background removal and for obtaining the parameters used to separate the Co2p peaks were found to greatly influence the number, width and intensity of the peak components within the spectral envelopes. This is a major reason for inconsistencies in the number and positions of the component peaks, that have been found in the literature over the past three decades [167-170]. Here, we present the techniques used in the present case.
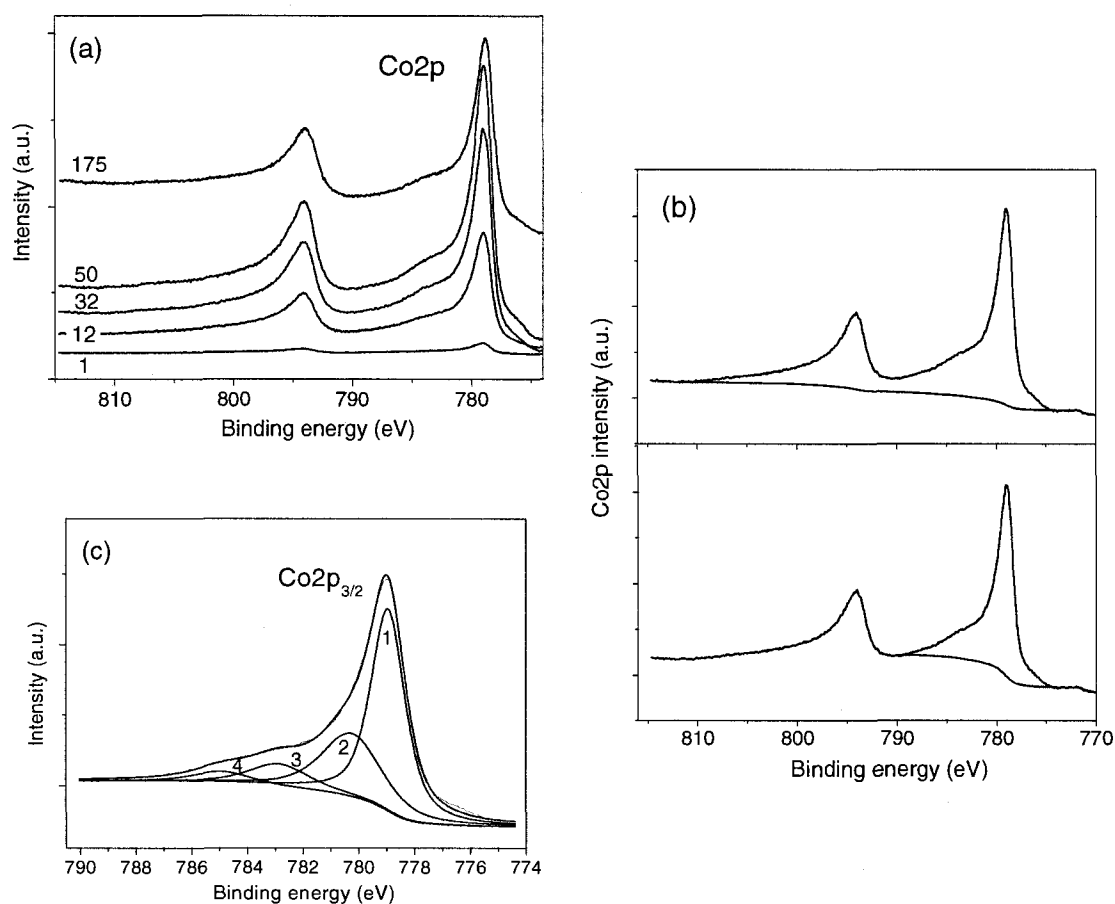
Figure 5.3. (a) The evolution of the Co2p spectrum, as a function of nominal Co deposition, (b) examples of background removal, and (c) an example of XPS peak separation for 50 Å Co coverage.

A. Background Removal

The accurate removal of the background contribution to a spectrum is a process that must be carried out with care since it may involve distortion of the data when incorrectly carried out. Any background removal will alter absolute peak intensities and will cause problems with any quantification model which must be defined with respect to clear background conditions. Generally, two approaches are discussed in literatures for non-linear backgrounds: the Shirley method and the Tougaard method. The first is commonly available on most data systems while the latter is much more recent and rarely used. There is no definite way to remove a background and the whole process is still controversial (see the detailed discussion in reference 16). In order to easily comparing our results to the results of other authors, we used the Shirley method, where the background intensity at any point is taken as proportional to the total peak area above the background, at that point

As the aforementioned papers all showed, the $2p_{3/2}$ and $2p_{1/2}$ doublets are well separated, by over 10 eV, far greater than any expected chemical shifts. This means that the energy values that delimit the range over which the background removal takes place may be confined to just one of the doublets, rather than taken over the entire $2p_{3/2}$-$2p_{1/2}$ energy range, as has often been done.

The importance of this distinction is seen in Figure 5.3b, in which Shirley backgrounds have been removed from a sample of 20 Å Co deposited onto pristine HOPG. In the upper plot, the whole Co2p doublet was used for the subtraction while, in the lower plot, only the $Co2p_{3/2}$ component was so used. It is clear that the use of the whole Co2p spectrum for background subtraction introduces a significant gap between the original spectrum and the baseline, which is then filled with peaks that may not exist.

Since all the previous researchers agreed that the peaks contributing to the $2p_{3/2}$ component spectrum did not overlap those of the $2p_{1/2}$ component, we have used only the $2p_{3/2}$ component for the background subtraction, as shown in the lower plot in Figure 5.3b.

B. Peak Separation

Considering the $2p_{3/2}$ component, the properties (intensity, FWHM, position) of the major constituent, at ~ 779 eV, are easily obtained to a good approximation, since it is the major contributor to the spectral envelope. The next constituent, the high energy shoulder, is then easily fit, and its FWHM is taken as suitable for all other Co (possible oxides, hydroxide) compounds; this shoulder is due to Co-C formation, as its intensity correlation with the *C6* carbide peak, which appears in the C1s spectrum on Co deposition, attests.

Co_3O_4 has two peaks in a 2:1 ratio (octahedral Co^{III} and tetrahedral Co^{II} [171], at the energy separation previously found for them. Once this doublet is added (Figure 5.3c), there is *nothing left over* for any possible CoO or $Co(OH)_2$ contributions posited by others, leading to the conclusion that, under our conditions, their concentrations are too small to measure. This method of peak separation was used on each of the Co2p spectra obtained, with identical results. Thus, each $Co2p_{3/2}$ spectrum was deconvoluted into four peaks, *Co1-Co4*; with increasing binding energy, they are attributed, respectively, to Co^0, Co-C, and Co_3O_4 (Co^{III} and Co^{II}).

5.3.2. The analysis of Co on HOPG as a function of thickness
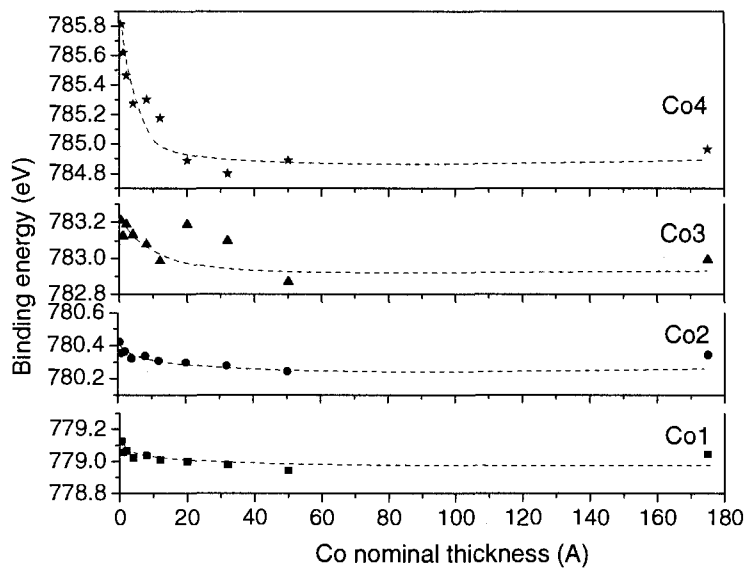
Figure 5.4. The evolution of the binding energies of the $Co2p_{3/2}$ component peaks, as a function of nominal Co deposition.
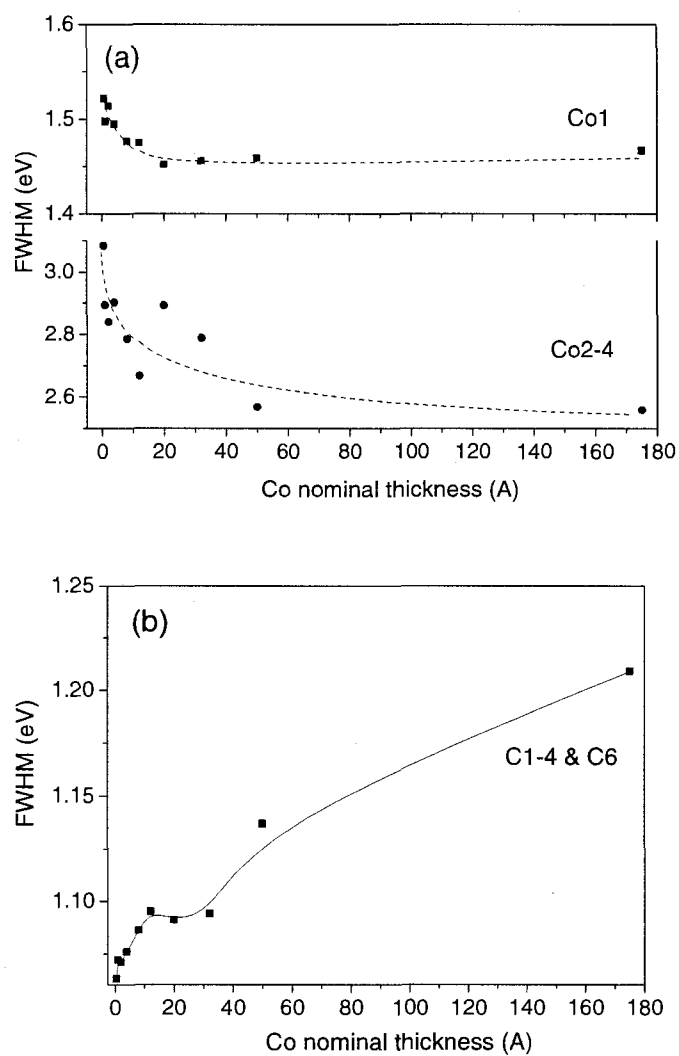
Figure 5.5. The FWHM changes of the component peaks of the (a) $Co2p_{3/2}$ and (b) $C1s$

spectra, as a function of nominal Co deposition.

Both the binding energies (Figure 5.4) and the FWHM values (Figure 5.5a) of the $Co2p_{3/2}$ components decrease with increasing Co coverage while the FWHM values of the $C1s$ components increase, but more rapidly, as shown in Figure 5.5b. The $Co2p$ and $C1s$ component fractions are plotted in Figure 5.6, where it is seen (Figure 5.6a) that *Co1* increases with increasing coverage, while the other component peaks decrease,
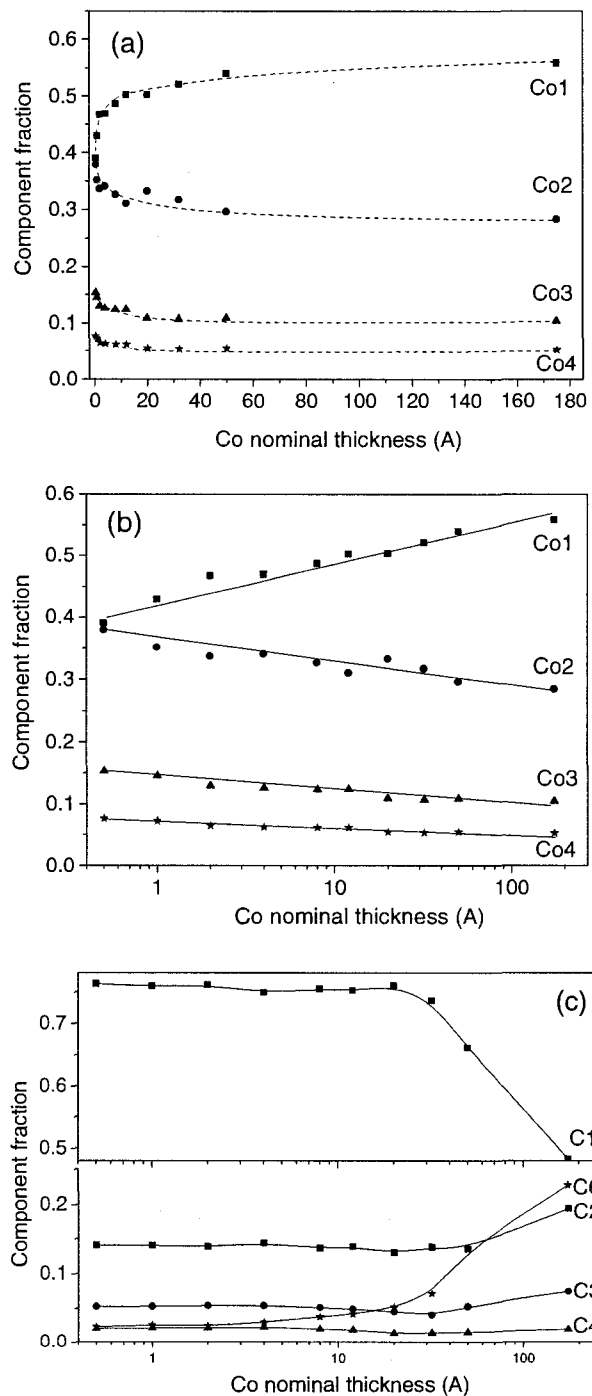
Figure 5.6. The $Co2p_{3/2}$ component fractions, plotted (a) linearly and (b) semi-logarithmically, as a function of nominal Co deposition; (c) the $C1s$ component fractions, plotted semi-logarithmically, as a function of nominal Co deposition.

before attaining a constant value at less than 20 Å Co coverage. When plotted semi-logarithmically, as in Figure 5.6b, these component fractions are seen to be approximately linear with Co deposition; the significance of this finding, if any, is not presently understood. The C1s component slope begins to change (Figure 5.6c) below 20 Å Co deposition, continuing linearly to 175 Å, indicating a change of the source of the C1s spectrum (the C1s probe depth is only ~ 45 Å [172]); this is also reflected in the FWHM evolution of the C1s components, as shown in Figure 5.5b.

The evolution of the elemental atomic concentrations, as determined from their peak areas and relative sensitivity factors, are plotted *vs* Co coverage in Figure 5.7. With increasing Co deposition, the Co and O fractions are seen to increase and the C fraction, to decrease.
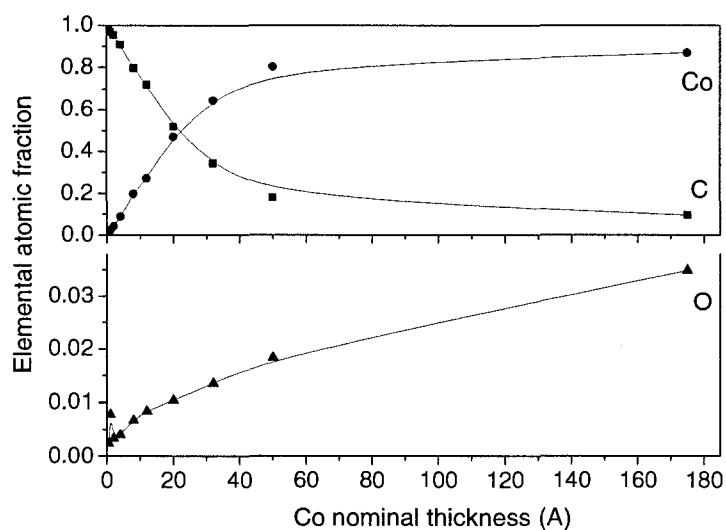
Figure 5.7. The evolution of the elemental atomic concentrations, as a function of nominal Co deposition.

5.3.3. The time-dependent stability of Co on HOPG

Dimensional stability was followed with time for three nominal Co depositions, 4, 12 and 175 Å. The $Co2p_{3/2}$ binding energies are found in Figure 5.8, and the $Co2p_{3/2}$ and C1s FWHM values are shown in Figure 5.9 (only the values for *Co1* and *C1* are shown here because all the other components have the same behavior). No significant change in Co binding energies or FWHM values were observed with time, indicating good temporal stability of the samples in ultrahigh vacuum; on the other hand, the FWHM value for the C1s component peaks (the same FWHM is used for all the components) increases with time, indicating facile carbon adsorption onto the Co nanoparticle surfaces. Here we note that, for the lower Co coverages, such as 4 and 12 Å, the increases of the FWHM due to adsorbed C are not easy seen because the signals are masked by the strong C1s intensity coming from the HOPG surface.
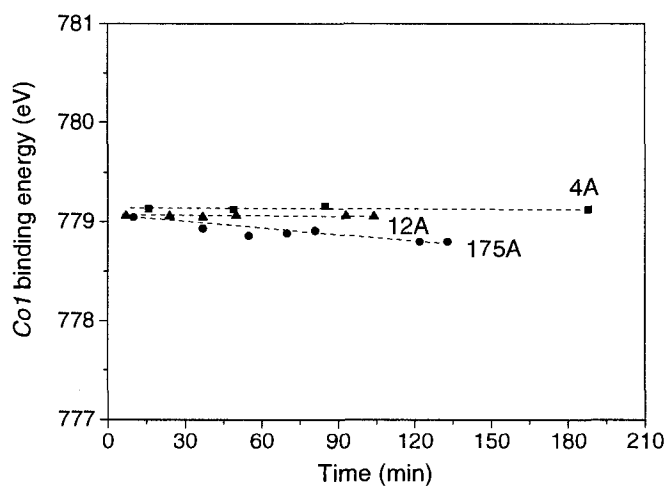
Figure 5.8. The binding energy evolutions of the *Co1* component peak, as a function of time subsequent to Co deposition.
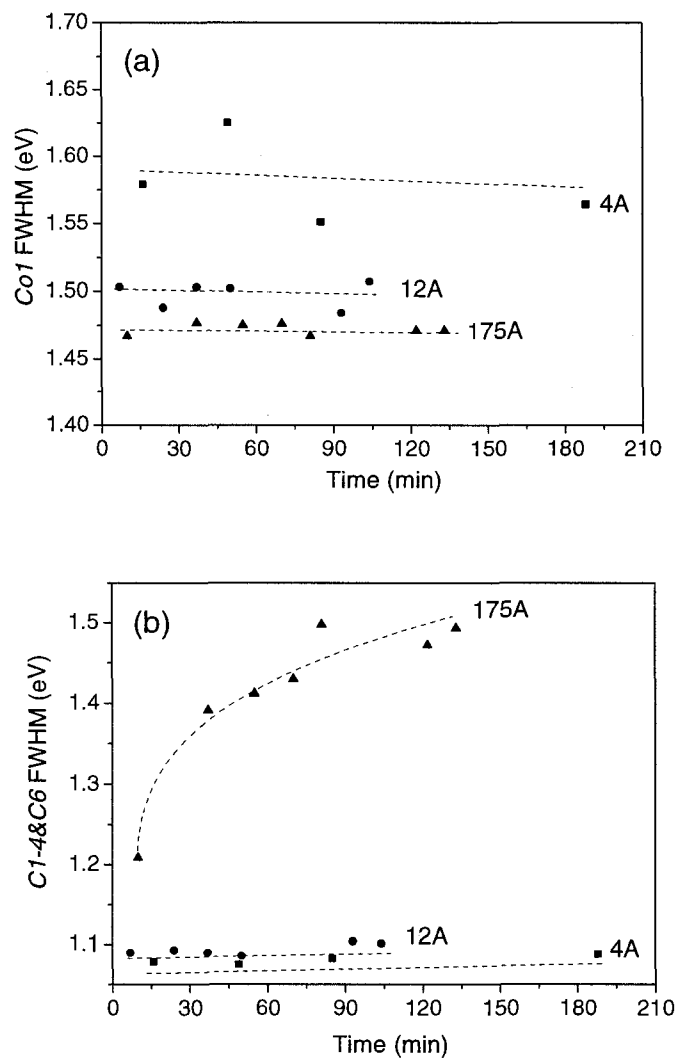
Figure 5.9. The FWHM evolutions of the (a) Co2p$_{3/2}$ and (b) C1s component peaks, as a function of time subsequent to Co deposition.

5.3.4. The morphology of Co on HOPG

Figure 5.10 presents planar and 3D AFM images and particle size distributions for 12 and 175 Å Co deposited onto pristine HOPG surfaces; all Co nanoparticles, over the entire surface, are uniform in size. They are dome-shaped, and remain similar in size

even for quite different Co coverages (compare the 12 and 175 Å data), with a height of ~ 2 nm and a diameter of 15-20 nm (aspect ratio ~ 0.12). However, we have found that with increasing Co deposition, the nanoparticle shapes appear become smoother and with the size distribution appears to narrow slightly. We believe that the increased smoothness with deposition is simply due to the increased amount of Co atoms that arrive at the surface, more of which condense onto the nanoparticles as the amount deposited increases, and the ratio of nanoparticles to exposed surface increases.
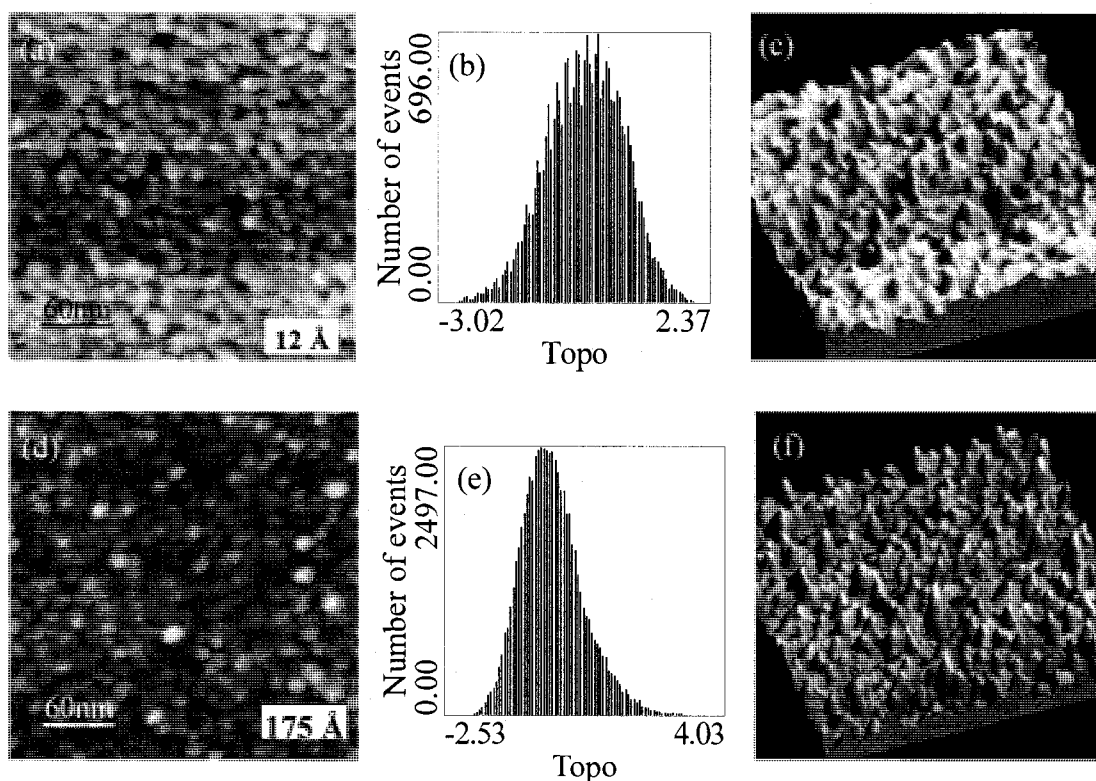
Figure 5.10. The surface morphologies of 12 and 175 Å Co evaporated onto HOPG surfaces. Because of tip/surface interactions, the distances in the figures are approximate.

5.4. Discussion

5.4.1. Interaction at the Co/HOPG interface

Our analysis of the $Co2p_{3/2}$, C1s and O1s spectra found that, in all cases over our 0.5 ~ 175 Å Co coverage range, Co carbide and oxide formed on the nanoparticle surfaces. Figure 5.6a presents the evolution of the Co component fractions with increasing Co deposition thickness. It reveals that there is a component order, always maintained, with *Co1* > *Co2* > *Co3* > *Co4*; for example, for 50 Å Co deposition, the component percentages are, respectively, 55, 30, 10 and 5%.

Since the attenuation lengths of Co2p, C1s and O1s photoelectrons are all ~ 15 Å, their probe depths are all about three times this value, ~ 45 Å. Therefore, in the case of thicker deposits, even considering the roughness of the surface, only the upper layers of the Co, rather than the HOPG substrate surface, are detected by XPS. Thus, the C1s signal (Figure 5.7), with its increased broadening (Figure 5.1a) and the obvious changes in the C1s component fractions (Figure 5.6c), cannot come from the HOPG surface but must come from C and O deposited from the surrounding vacuum. That is, Co nanoparticles appear to be surprisingly efficient getters. This is also attested to by the existence of the C1s shoulder, *C6*, at 283.5 eV, indicating carbide formation, and the O1s shoulder, *O1*, at 530.5 eV, indicating oxide formation. One notes that there is very little oxygen on the pristine HOPG surface, not nearly enough to give the O1s spectrum found, indicating that it must come from another source, such as the residual gases in the vacuum.

Because both carbide and oxide, from these residual gases, are present on the thicker Co deposits, there is no reason to believe that they did not also deposit onto the thinner

deposits. That is, the source of both carbide and oxide is by reaction with residual gases. However, the rapid changes for smaller Co thicknesses (less than 4 Å), as shown in Figure 5.6a, indicate the possible exception that the initially arriving Co atoms may have reacted with the free radical defects and oxidized carbon species initially present on the pristine HOPG; this interaction with the substrate is masked as the deposition thickness increases. That is, the evaporated Co nanoparticles react with both substrate and residual gases.

5.4.2. The Co nanoparticle shape and its growth mechanism on HOPG

The AFM analyses, in Figure 5.10, indicate some slight morphological differences of the nanoparticles as a function of the amount of Co deposited, such as smoother nanoparticles and narrower size distributions. It is interesting that all the Co nanoparticles have similar distributions, with heights of ~ 2 nm and diameters of 15-20 nm. This may well be due to the carbide/oxide surface layers, which limit further nanoparticle coalescence. This is also reflected by the small changes in Co binding energies (Figure 5.4) and FWHM values (Figure 5.5) with increasing deposition thickness.

In addition, these results furnish us with a reasonable explanation for the time-dependent stability of the Co nanoparticles found in Figure 5.9: the interfacial interaction is strong enough to bind the Co nanoparticles to the substrate, reducing the tendency for surface diffusion, and the surface layer on each of the nanoparticles, once formed, prevents the further coalescence of any nanoparticles that may ultimately come in contact. That is, the similarity of nanoparticle dimensions at all deposition thicknesses is governed by the rate of surface layer production; since this is due to the residual gases

present in the vacuum, and the rate of deposition is fixed at ~ 0.15 nm/min, the nanoparticle dimensions are essentially independent of the amount of Co deposited.

5.5. Conclusions

Co nanoparticles, evaporated onto freshly cleaved HOPG surfaces, have been studied using XPS and AFM. Nominal Co thicknesses ranged from 0.5 to 175 Å. Chemical characterization was carried out by using XPS, with multicomponent symmetric peaks for all the spectra. On analyzing the relationships among them, we found that the Co nanoparticles react not only with the defects on the HOPG surface but, also, with residual C- and O-containing gases in the high vacuum chamber of the XPS instrument, to form surface carbide and oxide. This surface layer prevents further nanoparticle coalescence and helps to stabilize them. AFM shows that the surface layer helps to maintain nanoparticle dimensions that are essentially independent of the amount deposited. Reaction with residual gases may take place in other active metal depositions, and should be considered in each case.

Chapter 6. General discussion, conclusions and future perspectives

Polymer electrolyte membrane (PEM) fuel cells with higher efficiency, low heat and noise signatures, fuel flexibility, clean, continuous operation, and modularity are an attractive choice over competitors such as batteries and internal combustion engines for portable and stand-alone power generation. As PEM fuel cells operate at a relatively low temperature (80 °C), they require the use of a catalyst to generate useful currents. All recent commercial and prototypical PEM fuel cells use Pt or Pt-based nanoparticles as catalysts, at both anode and cathode, because of their high surface area (high surface/volume ratio) and particle activity.

However, a serious problem for PEM fuel cells is the low reaction rate of the cathodic oxygen reduction reaction (ORR), for which one potentially effective solution is to use novel carbon materials as electrocatalyst supports, so as to help improve or increase the mass activity of the catalyst for the ORR [173]. In this regard, several novel carbon materials (including carbon black, carbon nanofibers and carbon nanotubes) have been tested. Unfortunately, even with the most advanced conventional electrodes, there is still a fraction of Pt that is isolated from the external circuit and/or the PEM, resulting in low Pt utilization.

The main objective of this project has been to investigate the interfacial interaction of Pt nanoparticles with their carbon supports and, then, to optimise the catalyst electrode and to increase its catalytic activity, thereby enhancing PEM fuel cell performance.

First, we studied the interfacial interaction (adhesion) of Pt nanoparticles evaporated onto untreated and Ar^+-treated highly oriented pyrolytic graphite surfaces, with, respectively, low and high surface defect densities. We found that those Pt nanoparticles

have very weak interactions with their pristine carbon material supports, with no evidence of compound formation between them. If this adhesion is not strong enough, the metal nanoparticles will diffuse on the support and coalesce into larger agglomerates, thereby decreasing both available catalytic surface and particle activity. According to our analysis, however, several properties (e.g., size, distribution, etc.) of those Pt nanoparticles are related to the defects appearing on the carbon substrate surfaces: using ion beams, plasmas, or other treatments to establish defects on the carbon substrate surface, the adhesion of Pt nanoparticles to their supports can be enhanced.

Further, by using multicomponent XPS analysis with symmetric lineshapes, we demonstrated a reasonable explanation for the changing shape of the Pt4f asymmetric envelope with nanoparticle size; that is, the asymmetry of the XPS lineshape is due to the existence of identifiable, overlapping component species having symmetric line-shapes. We have found that the previous attempt made to explain the asymmetry of the XPS lineshape, by Doniach and Šunjić [48], accepted for over 40 years, is inconsistent with our present results.

As we have already mentioned, Pt nanoparticles have very weak interfacial interactions with pristine carbon materials, resulting in surface diffusion of the nanoparticles, decreasing the surface area catalysis and the utilization of the Pt nanoparticles. It is only by the intentional chemical functionalization of these support materials that chemical groups are provided, to which the Pt nanoparticles adhere.

Using mixed H_2SO_4/HNO_3 acid treatments, we investigated several functionalization conditions, with and without sonication, at room and elevated temperatures, and obtained an efficient means of functionalizing carbon fibers. Using this efficient method, we have characterized the surface chemistry of functionalized carbon fiber paper by

combining infrared, Raman and X-ray photoelectron spectroscopies, to give new insights into the often-used oxidation of graphene-containing materials. We have, for the first time, demonstrated the presence of not only transient O-containing, but also transient N- and S-containing species during the oxidation process, as well as the fact that the intensities of those species varied unpredictably with treatment time, especially in the early stages, rather than constantly increasing with time. This study helps to better understand and control the functionalization of carbon materials so as to establish the strong adhesion of Pt nanoparticles, thereby enhancing fuel cell performance.

There are many advantages, for fuel cell applications, to growing CNTs directly on carbon fiber paper, followed by Pt deposition, since this ensures that all the deposited Pt nanoparticles are in electrical contact with the external electrical circuit, and also improves Pt utilization and could potentially decrease Pt usage. In order to synthesize controlled, uniform CNTs, it is necessary to manage the size and density of the deposited CNT growth catalyst. We have studied Co/Ni nanoparticles, where each was evaporated and studied separately, and co-evaporated (still being analyzed at the time of writing) onto carbon material supports, using XPS, ToF-SIMS, SEM and AFM. We have found that Co/Ni nanoparticles are quite reactive, not only with the carbon substrate but, also, with residual gas even in ultra high vacuum, to form surface carbides and oxides. This surface contaminant layer prevents further nanoparticle coalescence and helps to stabilize them. AFM shows that the surface layer helps to maintain Ni/Co nanoparticle dimensions that are essentially independent of the amount deposited. In addition, we have demonstrated that Co nanoparticles are more reactive than Ni. All this has helped better understand the role of the catalyst in the nucleation and growth of carbon nanotubes or carbon nanofibers, and will ultimately lead to control their growth.

In addition to enhancing the adhesion of the Pt nanoparticles to the carbon supports, the synthesis of specific platinum nanostructures has become an area of considerable interest, since catalytic efficiency and selectivity are highly dependent on the size and shape of the platinum material. To date, several methods have been reported to synthesize platinum nanostructures different from nanoparticles; however, the development of mild, template-free, surfactant-free routes for the production of pure single crystalline platinum nanowires remains a challenge. Here, we have demonstrated, for the first time, several routes to synthesize such nanostructures, such as 3D Pt nanoflowers (Appendix B) and the single-crystalline Pt NW–CNT heterojunctions (Appendix C), via simple chemical reduction reactions, at room temperature, without templates or surfactants. Electrodes modified with these novel Pt nanostructures exhibit good electrocatalytic activities, which may ultimately lead to their adoption in PEM fuel cells.

Further, we were the first to demonstrate the direct growth of single-crystalline Pt nanowires on carbon materials (Appendix C). We showed that the surface density of Pt NWs on the MWCNTs can be effectively controlled through the proper choice of the concentration ratio of MWCNTs and the Pt precursor; we can also obtain very high Pt loadings on CNTs, comparing to the Pt nanoparticles on CNTs. These heterojunction nanostructures hold much potential applications not only in electrocatalyst for fuel cells, but also in electronic, photonic, sensing nanodevices. We believe that our findings will have a significant impact in the fields susceptible to use Pt and CNT nanostructures.

In summary, the key contributions of this thesis are as follows:

(1) Studied the interaction between Pt nanoparticles and their carbon supports so as to achieve well-controlled Pt nanoparticle surface densities and sizes, as well as

long-time nanoparticle stability at the operating conditions of the fuel cell.

(2) Used symmetric XPS peak analysis to study the Pt4f spectrum. It was verified to contain three components, permitting the distinction of surface oxide, as well as of surface and bulk Pt^0; this new finding is in disagreement with the generally accepted explanation, proposed by Doniach and Šunjić, that the lineshape is naturally asymmetric.

(3) Demonstrated new insights into the mechanism of the often-used, but unexplained, sulfuric/nitric acid oxidation of graphene-containing materials, such as carbon fibers and carbon nanotubes, to better control the functionalization of the carbon materials, to which the Pt nanoparticles adhere.

(4) Characterized the properties of Co/Ni nanoparticles, which can be used as catalysts to grow carbon nanotubes, in order to control the diameter and surface density of the CNTs.

(5) Synthesized several novel specific Pt nanostructures with high surface area for great catalytic activity and utilization efficiency, which hold much potential for PEM fuel cell applications.

Thus, by analyzing the interfacial interaction between Pt and carbon materials, we found that Pt nanoparticles have very weak interactions with their pristine carbon supports. In order to have strong adhesion between them, there are two major techniques to optimize the catalyst electrodes. One technique is to functionalize the carbon supports by ion beams, plasmas, or chemical (e.g. H_2SO_4/HNO_3) treatments; the functionalities thus introduced are capable of forming strong covalent bonds to the deposited

nanoparticles. The other technique is to synthesize novel Pt nanoparticles having specific structures, such as Pt nanoflowers and Pt NW-CNT heterojunctions, with quite high surface-active areas and potentially high loading; once covalent bonds are formed to the substrate, the increased surface-active areas increase the electrocatalytic areas of the electrodes.

In addition, we studied Co/Ni as a catalyst for directly growing CNTs on carbon fiber paper, in which case the Pt/CNTs/CP composite guarantees an electronic pathway and eliminates the isolation of the carbon support from the Nafion-supported electrode, and improving Pt utilization.

We believe all these studies will have great impact on the catalyst electrodes for PEM fuel cell applications.

Future perspectives

These studies suggest three directions to extend the work, and further enhance the catalyst activity of the catalyst electrodes in future.

(1) To deposit Pt nanoparticles to the carbon nanotubes surfaces, functionalized by the sulfuric/nitric acid treatment of the present study, and by other functionalization studies developed in our laboratory [127,128], to study the extent of strong adhesion and high loading that may be obtained with the Pt nanoparticles.

(2) To study Pt-based metal nanoparticles, such as Pt_3Ni [174] and PtAu [175], since Pt_3Ni is reported to increase the catalytic activity of a platinum surface 90-fold over conventional cathode catalysts used today; as well, it is reported that adding tiny gold clusters to the outside of Pt cathode materials dramatically reduced the

tendency of platinum to dissolve over extended use. Our group has been carrying out an in-depth study on the adhesion of transition metal nanoparticles (Cu, Ni, Au, Pt, Co, CoNi, etc.) [12,137,176-179] for some years, and this prior experience will help us better understand the properties of these Pt-based nanoparticles.

(3) To synthesize shape-controlled, novel platinum nanostructures [180-183], such as nanotubes, nanorods, nano-multipods, and nanoporous Pt thin films, as well as tetrahexahedral Pt nanocrystals with high-index facets and high electro-oxidative activity; to characterize the Pt-carbon nanocomposites synthesized using these novel Pt nanostructures and the carbon materials found in fuel cell applications.

REFERENCES

1. Liu, J. H.; Jeon, M. K.; Woo, S. I. High-throughput screening of binary catalysts for oxygen electroreduction. *Appl. Surf. Sci.* **2006**, 252(7):2580–7.

2. Yim, S. D.; Park, G. G.; Yoon, Y. G.; Lee, W. Y.; Kim, C. S.; Seo, D. J.; Eguchi, K. Hydrogen production with integrated microchannel fuel processor for portable fuel cell systems. *J. Power Sources* **2005**, 145(2):702–6.

3. Cropper, M. A.; Geiger S.; Jollie, D. M. Fuel cells: a survey of current developments. *J. Power Sources* **2004**, 131(1–2):57–61.

4. Website of hydrogen, fuel cells & infrastructure technologies program: http://www1.eere.energy.gov/hydrogenandfuelcells/fuelcells/fc_types.html

5. Vishnyakov, V. M. Proton exchange membrane fuel cells. *Vacuum* **2006**, 80(10):1053–65.

6. Website of neutron imaging facility: http://physics.nist.gov/MajResFac/NIF/pemFuelCells.html.

7. Djilali, N. Computational modeling of polymer electrolyte membrane (PEM) fuel cells: Challenges and opportunities. *Energy* **2007**, 32(4):269-80.

8. Li, W. Z.; Liang, C. H.; Qiu, J. S.; Zhou, W. J.; Han, H. M.; Wei, Z. B.; Sun, G. Q.; Xin, Q. Carbon nanotubes as support for cathode catalyst of a direct methanol fuel cell. *Carbon* **2002**, 40(5):791-94.

9. Liu, Z. L.; Lin, X. H.; Lee, J. Y.; Zhang, W. D.; Han, M.; Gan, L. M. Preparation and characterization of platinum-based electrocatalysts on multiwalled carbon

nanotubes for proton exchange membrane fuel cells. *Langmuir* **2002**, 18(10):4054-60.

10. Wang, C.; Waje, M. M,; Wang, X.; Tang, J. M.; Haddon, R. C.; Yan, Y. S. Proton Exchange Membrane Fuel Cells with Carbon Nanotube Based Electrodes. *Nano. Lett.* **2004**, 4(2):345–48.

11. Sun, X. L.; Li, R. Y.; Villers, D.; Dodelet, J. P.; Désilets, S. Composite electrodes made of Pt nanoparticles deposited on carbon nanotubes grown on fuel cell backings. *Chem. Phys. Lett.* **2003**, 379(1–2):99–104.

12. Yang D.-Q.; Sacher, E. Interaction of evaporated nickel nanoparticles with highly oriented pyrolytic graphite: Back-bonding to surface defects, as studied by x-ray photoelectron spectroscopy. *J. Phys. Chem. B* **2005**, 109(41):19329-34.

13. Wang, R. M.; Chu, C. L.; Hu, T.; Dong, Y. S.; Guo, C.; Sheng, X. B.; Lin, P. H.; Chung, C. Y.; Chu, P. K. Surface XPS characterization of NiTi shape memory alloy after advanced oxidation processes in UV/H_2O_2 photocatalytic system. *Appl. Surf. Sci.* **2007**, 253(20):8507-12.

14. Jiang, Z. Q.; Zhang, W. H.; Jin, L.; Yang, X.; Xu, F. Q.; Zhu, J. F.; Huang, W. X. Direct XPS evidence for charge transfer from a reduced rutile TiO_2 (110) surface to Au clusters. *J. Phys. Chem. C* **2007**, 111(33):12434-39.

15. Zhou, J. H.; Sui, Z. J.; Zhu, J.; Li, P.; Chen, D.; Dai, Y. C.; Yuan, W. K. Characterization of surface oxygen complexes on carbon nanofibers by TPD, XPS and FT-IR. *Carbon* **2007**, 45(4):785-96.

16. Briggs, D. Surface analysis of polymer by XPS and static SIMS. 1st Edition, Cambridge university press, 1998, chapter 2.

17. Tao, Y. Sulfur passivation of InP(100) surfaces. PhD thesis, École Polytechnique De Montréal, Montréal, 1993.

18. Website of Keck Interdisciplinary Surface Science (Keck-II) Center: http://www.nuance.northwestern.edu/KeckII/.

19. Website of lecture notes on surface science by Philip Hofmann: http://whome.phys.au.dk/~philip/q1_05/surflec/node11.html

20. Siegbahn, K.; Nordling, C.; Fahlman, A.; Nordberg, K.; Harmrin, K.; Hedman, J.; Johansson, G.; Bergmark, T.; Karlsson, S. E.; Lindgren, I.; Lindberg, B. ESCA: Atomic, molecular and solid state structure by means of electron spectroscopy. Almqvist and Wiksells, Uppsala, 1967.

21. Website of geochemical instrumentation and analysis: http://serc.carleton.edu/research_education/geochemsheets/techniques/ToFSIMS.html

22. Website of introduction to IR spectra: http://www.chem.ucla.edu/~webspectra/irintro.html

23. Banwell, C. N.; McCash, E. M. Fundamentals of molecular spectroscopy. 4th edition, Mcgraw-Hill College, London, 1994.

24. Website of Raman spectroscopy: http://www.andor.com/chemistry/?app=64.

25. Website of welcome to the world of scanning electron microscopy by Lowa state university: http://mse.iastate.edu/microscopy/path2.html

26. Ohring, M. Materials Science of Thin Films: Deposition and Structure. 2nd Edition, Academic Press, USA, 2002, chapter 10.

27. Website of the transmission electron microscope:

    http://nobelprize.org/educational_games/physics/microscopes/tem/index.html

28. Website of atomic force microscope:

    http://en.wikipedia.org/wiki/Atomic_force_microscope.

29. Yan, Y. D.; Sun, T.; Dong, S. Study on effects of tip geometry on AFM nanoscratching tests. *Wear* **2007**, 262(3-4):477-83.

30. Tranchida, D.; Piccarolo, S.; Deblieck, R. A. C. Some experimental issues of AFM tip blind estimation: the effect of noise and resolution. *Meas. Sci. Technol.* **2006**, 17(10):2630-2636.

31. Sasaki, N.; Tsukada, M. Theory for the effect of the tip–surface interaction potential on atomic resolution in forced vibration system of noncontact AFM. *Appl. Surf. Sci.* **1999**, 140(3-4):399-43.

32. Matsumoto, T.; Komatsu, T.; Nakano, H.; Arai, K.; Nagashima, Y.; Yoo, E.; Yamazaki, T.; Kijima, M.; Shimizu, H.; Takasawa, Y.; Nakamura, J. Efficient usage of highly dispersed Pt on carbon nanotubes for electrode catalysts of polymer electrolyte fuel cells. *Catal. Today* **2004**, 90(3-4):277-81.

33. Tang, H.; Chen, J. H.; Huang, Z. P.; Wang, D. Z.; Ren, Z. F.; Nie, L. H.; Kuang, Y. F.; Yao, S. Z. High dispersion and electrocatalytic properties of platinum on well-aligned carbon nanotube arrays. *Carbon* **2004**, 42(1):191-7.

34. Li, W. Z.; Liang, C. H.; Zhou, W. J.; Qiu, J. S.; Li, H. Q.; Sun, G. Q.; Xin, Q. Homogeneous and controllable Pt particles deposited on multi-wall carbon nanotubes as cathode catalyst for direct methanol fuel cells. *Carbon* **2004**, 42(2):436-39.

35. Antolini, E. Formation, microstructural characteristics and stability of carbon supported platinum catalysts for low temperature fuel cells. *J. Mater. Sci.* **2003**, 38(14):2995-3005.

36. Cheung, T. T. P. X-ray photoemission of small platinum and palladium clusters. *Surf. Sci.* **1984**, 140(1):151-64.

37. Yang, D.-Q.; Sacher, E. Argon ion treatment of the Dow Cyclotene 3022 surface and its effect on the adhesion of evaporated copper. *Appl. Surf. Sci.* **2001**, 173(1-2):30-39.

38. Boyen, H.-G.; Ethirajan, A.; Kästle, G.; Weigl, F.; Ziemann, P. Alloy formation of supported gold nanoparticles at their transition from clusters to solids: Does size matter? *Phys. Rev. Lett.* **2005**, 94(1):016804, 1-4.

39. Lim, D. C.; Lopez-Salido, I.; Dietsche, R.; Bubek, M.; Kim, Y. D. Oxidation of Au nanoparticles on HOPG using atomic oxygen. *Surf. Sci.* **2006**, 600(3):507-13.

40. Yang, D.-Q.; Martinu, L.; Sacher, E.; Sadough-Vanini, A. Nitrogen plasma treatment of the dow Cyclotene 3022 surface and its reaction with evaporated copper. *Appl. Surf. Sci.* **2001**, 177(1-2):85-95.

41. Liu, Y.; Chen, T. P.; Fu, Y. Q.; Tse, M. S.; Hsieh, J. H.; Ho, P. F.; Liu, Y. C. A study on Si nanocrystal formation in Si-implanted SiO_2 films by x-ray photoelectron spectroscopy. *J. Phys. D: Appl. Phys.* **2003**, 36(19):L97-100.

42. Morant, C.; Andrey, J.; Prieto, P.; Mendiola, D.; Sanz, J. M.; Elizalde, E. XPS characterization of nitrogen-doped carbon nanotubes. *Phys. Stat. Sol.* **2006**, 203(6):1069-75.

43. Cheung, T. T. P. Lineshape studies of the X-ray photoemission of small metal clusters. *Surf. Sci.* **1983**, 127:L129-34.

44. Cheung, T. T. P. X-ray photoemission-studies of reactions of arsine with platinum, palladium, and nickel metals and metal-oxides. *J. Phys. Chem.* **1990**, 68(11):5827-34.

45. Hughes, H. P.; Scarfe, J. A. Lineshapes in core-level photoemission from metals .1. Theory and computational analysis. *J. Phys.: Condens. Matt.* **1996**, 8(10):1421-38.

46. Mahan, G. D. Excitation in metals: infinite hole mass. *Phys. Rev.* **1967**, 163(3):612-17.

47. Nozières, P.; de Domenicis, C. T. Singularities in the x-ray absorption and emission of metals. III. One-body theory exact solution. *Phys. Rev.* **1969**, 178(3):1097-107.

48. Doniach, S.; Šunjić, M. Many-electron singularity in x-ray photoemission and x-ray line spectra from metals. *J. Phys. C: Solid State Phys.* **1970**, 3:285-291.

49. Citrin, P. H.; Wertheim, G. K.; Baer, Y. Many-electron effects in core-level x-ray and electron spectroscopies from Na, Mg, and Al. *Phys. Rev. Lett.* **1975**, 35(13):885-88.

50. Gadzuk, J. W.; Šunjić, M. Excitation energy of core-level x-ray-photoemission-spectra line shapes in metals. *Phys. Rev. B* **1975**, 12(2):524-30.

51. Minnhagen, P. On the quantitative evaluation of XPS lineshape asymmetries for free-electron-like metals. *J. Phys. F: Metal Phys.* **1977**, 7(11):2441-50.

52. Cheung, T. T. P. X-ray photoemission of carbon: lineshape analysis and application to studies of coals. *J. Phys. Chem.* **1982**, 53(10):6857-62.

53. Yang, D.-Q.; Sacher, E. s-p hybridization in highly oriented pyrolytic graphite and its change on surface modification, as studied by X-ray photoelectron and Raman spectroscopies. *Surf. Sci.* **2002**, 504(1-3):125-37.

54. Yang, D.-Q.; Sacher, E. Interaction of evaporated nickel nanoparticles with highly oriented pyrolytic graphite: Back-bonding to surface defects, as studied by x-ray photoelectron spectroscopy. *J. Phys. Chem. B* **2005**, 109(41):19329-34.

55. Kim, K. S.; Winogard, N.; Davis, R. E. Electron spectroscopy of platinum-oxygen surfaces and application to electrochemical studies. *J. Am. Chem. Soc.* **1971**, 93(23):6296-97.

56. Smith, R. A. P.; Armstrong, C. W.; Smith, G. C.; Weightman, P. Observation of a surface chemical shift in carbon 1s core-level photoemission from highly oriented pyrolytic graphite. *Phys. Rev. B* **2002**, 66(24):245409, 1-6.

57. Sette, F.; Wertheim, G. K.; Ma, Y.; Meigs, G.; Modesti, S.; Chen, C. T. Lifetime and screening of the c1s photoemission in graphite. *Phys. Rev. B* **1990**, 41(14):9766-70.

58. Yang, D.-Q.; Rochette, J.-F.; Sacher, E. Controlled chemical functionalization of multiwalled carbon nanotubes by kiloelectronvolt argon ion treatment and air exposure. *Langmuir* **2005**, 21(18):8539-45.

59. Yang, D.-Q.; Sacher, E. Carbon 1s X-ray photoemission line shape analysis of highly oriented pyrolytic graphite: The influence of structural damage on peak asymmetry. *Langmuir* **2006**, 22(3):860-62.

60. Delgass, W. N.; Hughes, T. R.; Fadley, C. S. "shake-up" electron spectrum associated with the. Ni(2p) lines. *Catal. Rev.* **1970**, 4(2):179.

61. Wang, G. Q.; Lin, Y.; Xiao, X. R.; Li, X. P.; Wang, W. B. X-ray photoelectron spectroscopy analysis of the stability of platinized catalytic electrodes in dye-sensitized solar cells. *Surf. Interface Anal.* **2004**, 36(11):1437-40.

62. Yang, D.-Q.; Zhang, G.-X.; Sacher, E.; José-Yacamán, M.; Elizondo, N. Evidence of the interaction of evaporated Pt nanoparticles with variously treated surfaces of highly oriented pyrolytic graphite. *J. Phys. Chem. B* **2006**, 110(16):8348-56.

63. Mason, M. G.; Lee, S.-T.; Apai, G.; Davis, R. F.; Shirley, D. A.; Franciosi, A.; Weaver, J. H. Particle-size-induced valence changes in samarium clusters. *Phys. Rev. Lett.* **1981**, 47(10):730-33.

64. Yang, D.-Q.; Poulin, S.; Sacher, E.; Hyett, C. The surface structure of Dow Cyclotene 3022, as determined by photoacoustic FTIR, confocal Raman and photoelectron spectroscopies. *Appl. Surf. Sci.* **2000**, 165(1):116-22.

65. Hinnen, C.; Imbert, D.; Siffre J. M.; Marcus, P. An in-situ XPS study of sputter-deposited aluminum thin-films on graphite. *Appl. Surf. Sci.* **1994**, 78(3):219-31.

66. Engelhard, M.; Baer, D. Third row transition metals by x-ray photoelectron spectroscopy. *Surf. Sci. Spectra* **2000**, 7(1-4):1-68.

67. Murgai, V.; Raaen, S.; Strongin, M.; Garrett, R. F. Core-level and valence-band photoemission study of granular platinum films. *Phys. Rev. B* **1986**, 33:4345-48.

68. Eberhardt, W.; Fayet, P.; Cox, D. M.; Fu, Z.; Kaldor, A.; Sherwood, R.; Sondericker, D. Photoemission from mass-selected monodispersed Pt clusters. *Phys. Rev. Lett.* **1990**, 64(7):780-84.

69. Howells, A.; Harris, T.; Sashikata, K.; Chottiner, G. S.; Scherson, D. A. Model systems in electrocatalysis: Electronic and structural characterization of vapor deposited platinum on the basal plane of highly oriented pyrolytic graphite. *Solid State Ion.* **1997**, 94(1-4):115-21.

70. Gloaguen, F.; Leger, J. M.; Lamy, C.; Marmann, A.; Stimming, U.; Vogel, R. *Electrochim. Acta.* Platinum electrodeposition on graphite: electrochemical study and STM imaging. **1999**, 44(11):1805-16.

71. Fauth, K.; Hebler, M.; Batchelor, D.; Schutz, G. Strong influence of defects on the electronic structure of Pt adatoms and clusters on graphite. *Surf. Sci.* **2003**, 529(3):397-402.

72. Shen, P.; Chi, N.; Chan, K. Y.; Philips, D. L. Platinum nanoparticles spontaneously formed on HOPG. *Appl. Surf. Sci.* **2001**, 172(1-2):159-66.

73. Yang, D.-Q.; Sacher, E. Ar$^+$-induced surface defects on HOPG and their effect on the nucleation, coalescence and growth of evaporated copper. *Surf. Sci.* **2002**, 516(1-2):43-55.

74. Yang, D.-Q.; Sacher, E. Platinum nanoparticle interaction with chemically modified highly oriented pyrolytic graphite surfaces. *Chem. Mater.* **2006**, 18(7):1811-16.

75. Parkinson, C. R.; Walker, A.; McConville, C. F. Reaction of atomic oxygen with a Pt (111) surface: chemical and structural determination using XPS, CAICISS and LEED. *Surf. Sci.* **2003**, 545(1-2):19-33.

76. Marcus, P.; Hinnen, C. XPS study of the early stages of deposition of Ni, Cu and Pt on HOPG. *Surf. Sci.* **1997**, 392(1-3):134-42.

77. Derry, G. N.; Ross, P. N. High coverage states of oxygen adsorbed on Pt(100) and Pt(111) surfaces. *Surf. Sci.* **1984**, 140:165-80.

78. US Atomic Energy Commission Report ANL-5750, as found in the CRC Handbook of Chemistry and Physics, CRC Press, Cleveland, OH, 54th edition (1973-74), p. D-56.

79. Huheey, J. E. "Inorganic Chemistry", Harper & Row, 3rd Edition. 1983, p. A-37.

80. Binns, C.; Baker, S. H.; Demangeat, C.; Parlebas, J. C. Growth, electronic, magnetic and spectroscopic properties of transition metals on graphite. *Surf. Sci. Rept.* **1999**, 34(4-5):107-70.

81. http://www.phy.cuhk.edu.hk/~surface/XPSPEAK/.

82. http://escalab.snu.ac.kr/~berd/Fitt/fitt.html.

83. Briggs, D.; Gibson, V. A. Direct observation of multiplet splitting in 2P photoelectron peaks of cobalt complexes. *Chem. Phys. Lett.* **1974**, 25(4):493-96.

84. Piyakis, K. N.; Yang, D.-Q.; Sacher, E. The applicability of angle-resolved XPS to the characterization of clusters on surfaces. *Surf. Sci.* **2003**, 536(1-3):139-44.

85. Yang, D.-Q.; Meunier, M.; Sacher, E. Room temperature air oxidation of nanostructured Si thin films with varying porosities as studied by x-ray photoelectron spectroscopy. *J. Appl. Phys.* **2006**, 99(8):084315, 1-6.

86. Yang, D.-Q.; Gillet, J.-N.; Meunier, M.; Sacher, E. Room temperature oxidation kinetics of Si nanoparticles in air, determined by x-ray photoelectron spectroscopy. *J. Appl. Phys.* **2005**, 97(2):024303, 1-6.

87. Mason, M. G.; Gerenser, L. J.; Lee, S.-T. Electronic structure of catalytic metal clusters studied by x-ray photoemission spectroscopy. *Phys. Rev. Lett.* **1977**, 39(5):288-91.

88. Mason, M. G. Electronic structure of supported small metal clusters. *Phys. Rev. B* **1983**, 27(2):748-62.

89. Tsai, M.-H. The electronic configuration of platinum (110) surface atoms with the least coordination number. *Chinese J. Phys.* **1981**, 19(1):22-26.

90. Lübcke, M.; Sonntag, B. Size-dependent valance change in small Pr, Nd, and Sm clusters isolated in solid Ar. *Phys. Rev. B* **1986**, 34(6):5184-90.

91. Xu, W. X.; Schierbaum, K. D.; Goepel, W. Ab initio study of electronic structures of Pt-n clusters (n=2-12). *Internat. J. Quant. Chem.* **1997**, 62(4):427-36.

92. Yang, S. H.; Drabold, D. A.; Adams, J. B.; Ordejón, P.; Glassford, K. Density functional studies of small platinum clusters. *J. Phys.: Condens. Matt.* **1997**, 9(5):L39-45.

93. Kua, J.; Goddard III, W. A. Chemisorption of organics on platinum. 1. The interstitial electron model. *J. Phys. Chem. B* **1998**, 102(47):9481-91.

94. Xiao, L.; Wang, L. C. Structures of platinum clusters: Planar or spherical? *J. Phys. Chem. A* **2004**, 108(41):8605-14.

95. Puglia, C.; Nilsson, A.; Hernnäs, B.; Karis, O.; Bennich, P.; Mårtensson, N. Physisorbed, chemisorbed and dissociated O_2 on Pt(111) studied by different core-level spectroscopy methods. *Surf. Sci.* **1995**, 342(1-3):119-33.

96. Saliba, N. A.; Tsai, Y.-L.; Panja, C.; Koel, B. E. Oxidation of Pt(111) by ozone (O_3) under UHV conditions. *Surf. Sci.* **1999**, 419(2-3):79-88.

97. Gambardella, P.; Šljivančanin, Ž.; Hammer, B.; Blanc, M.; Kuhnke, K.; Kern, K. Oxygen dissociation at Pt steps. *Phys. Rev. Lett.* **2001**, 87(5):056103. 1-4.

98. Petrovykh, D. Y.; Kimura-Suda, H.; Opdahl, A.; Richter, L. J.; Tarlov, M. J.; Whitman, L. J. Alkanethiols on platinum: Multicomponent self-assembled monolayer. *Langmuir* **2006**, 22(6):2578-87.

99. Gouérec, P.; Denis, M. C.; Guay, D.; Dodelet, J. P.; Schulz, R. High energy ballmilled Pt-Mo catalysts for polymer electrolyte fuel cells and their tolerance to CO. *J. Electrochem. Soc.* **2000**, 147(11):3989-96.

100. Hull, R. V.; Li, L.; Xing, Y. C.; Chusuei, C. C. Pt nanoparticle binding on functionalized multiwalled carbon nanotubes. *Chem. Mater.* **2006**, 18(7):1780-88.

101. Wertheim, G. K.; Dicenzo, S. B. Cluster growth and core-electron binding energies in supported metal clusters. *Phys. Rev. B* **1988**, 37(2):844-47.

102. http://srdata.nist.gov/xps/.

103. Tang, H.; Chen, J. H.; Huang, Z. P.; Wang, D. Z.; Ren, Z. F.; Nie, L. H.; Kuang, Y. F.; Yao, S. Z. High dispersion and electrocatalytic properties of platinum on well-aligned carbon nanotube arrays. *Carbon* **2004**, 42(1):191-7.

104. Antolini, E. Formation of carbon-supported PtM alloys for low temperature fuel cells: A review. *Mater. Chem. Phys.* **2003**, 78(3):563–73.

105. Wang, M. H.; Woo, K. D.; Kim, D. K. Preparation of Pt nanoparticles on carbon nanotubes by hydrothermal method. *Ener. Conv. Manag.* **2006**, 47(18–19):3235–40.

106. Mu, Y. Y.; Liang, H. P.; Hu, J. S.; Jiang, L.; Wan, L. J. Controllable Pt nanoparticle deposition on carbon nanotubes as an anode catalyst for direct methanol fuel cells. *J. Phys. Chem. B* **2005**, 109(47):22212–16.

107. Tsai, M. C.; Yeh, T. K.; Tsai, C. H. An improved electrodeposition technique for preparing platinum and platinum-ruthenium nanoparticles on carbon nanotubes directly grown on carbon cloth for methanol oxidation. *Electrochem. Commun.* **2006**, 8(9):1445–52.

108. Li, L.; Wu, G.; Xu, B. Q. Electro-catalytic oxidation of CO on Pt catalyst supported on carbon nanotubes pretreated with oxidative acids. *Carbon* **2006**, 44(14):2973–83.

109. Dicks, A. L. The role of carbon in fuel cells. *J. Power Sources* **2006**, 156(2):128–41.

110. Chen, L. H.; AuBuchon, J. F.; Chen, I. C.; Daraio, C.; Ye, X. R.; Gapin, A.; Jin, S.; Wang, M. C. Growth of aligned carbon nanotubes on carbon microfibers by dc plasma-enhanced chemical vapor deposition. *Appl. Phys. Lett.* **2006**, 88(3):033103, 1–3.

111. Waje, M. M.; Wang, X.; Li, W. Z.; Yan, Y. S. Deposition of platinum nanoparticles on organic functionalized carbon nanotubes grown in situ on carbon paper for fuel cells. *Nanotechnol.* **2005**, 16(7):S395–400.

112. Tzeng, S. S.; Hung, K. H.; Ko, T. H. Growth of carbon nanofibers on activated carbon fiber fabrics. *Carbon* **2006**, 44(5):859–65.

113. Golovko, V. B.; Hofmann, S.; Williams, D. R.; Ducati, C.; Geng, J.; Boskovic, B. O.; Kleinsorge, B.; Jefferson, D. A.; Ferrari, A. C.; Johnson, B. F. G.; Robertson, J. Wet catalyst assisted growth of carbon nanofibers on complex three-dimensional substrates. *Diamond Relat. Mater.* **2005**, 14(3–7):733–8.

114. Chen, C. C.; Chen, C. F.; Hsu, C. H.; Li, I. H. Growth and characteristics of carbon nanotubes on carbon cloth as electrodes. *Diamond Relat. Mater.* **2005**, 14(3–7):770–3.

115. Buckley, J. D.; Edie, D. D. *Carbon-Carbon Materials and Composites*; Noyes: New Jersey, 1993; Chapter 2 and 3.

116. Morgan, P. *Carbon Fibers and their Composites*; Taylor and Francis: Boca Raton, 2005; Chapter 2-7.

117. Wang, Y.-Q.; Zhang, F.-Q.; Sherwood, P. M. A. X-ray photoelectron spectroscopic study of carbon fiber surfaces. 23. Interfacial interactions between polyvinyl alcohol and carbon fibers electrochemically oxidized in nitric acid solution. *Chem. Mater.* **1999**, 11(9):2573–83.

118. Zhang, J.; Zou, H. L.; Qing, Q.; Yang, Y. L.; Li, Q. W.; Liu, Z. F.; Guo, X. Y.; Du, Z. L. Effect of chemical oxidation on the structure of single-walled carbon nanotubes. *J. Phys. Chem. B* **2003**, 107(16):3712–18.

119. Xing, Y. C. Synthesis and electrochemical characterization of uniformly-dispersed high loading Pt nanoparticles on sonochemically-treated carbon nanotubes. *J. Phys. Chem. B* **2004**, 108(50):19255–9.

120. Wang, Y. B.; Iqbal, Z.; Mitra, S. Rapidly functionalized, water-dispersed carbon nanotubes at high concentration. *J. Am. Chem. Soc.* **2006**, 128(1):95–9.

121. Hull, R. V.; Li, L.; Xing, Y. C.; Chusuei, C. C. Pt nanoparticle binding on functionalized multiwalled carbon nanotubes. *Chem. Mater.* **2006**, 18(7):1780–8.

122. Xu, C. L.; Chen, J. F.; Cui, Y.; Han, Q. Y.; Choo, H.; Liaw, P. K.; Wu, D. H. Influence of the surface treatment on the deposition of platinum nanoparticles on the carbon nanotubes. *Advan. Eng. Mater.* **2006**, 8(1–2):73–7

123. Xing, Y. C.; Li, L.; Chusuei, C. C.; Hull, R. V. Sonochemical oxidation of multiwalled carbon nanotubes. *Langmuir*, **2005**, 21(9):4185–90.

124. Yu, R. Q.; Chen, L. W.; Liu, Q. P.; Lin, J. Y.; Tan, K. L.; Ng, S. C.; Chan, H. S. O.; Xu, G. Q.; Andy Hor, T. S. Platinum deposition on carbon nanotubes via chemical modification. *Chem. Mater.* **1998**, 10(3):718–22.

125. Queiroz, J. F.; Carneiro, J. W. M.; Sabino, A. A.; Sparrapan, R.; Eberlin, M. N.; Esteves, P. M. Electrophilic aromatic nitration: Understanding its mechanism and substituent effects. *J. Org. Chem.* **2006**, 71(16):6192–203

126. Yu, Q. Z. Discussion on TNT oxidation mechanism in nitric-sulfuric acid mixture. *Ind. Eng. Chem. Prod. Res. Dev.* **1982**, 21(3):356–359.

127. Yang, D.-Q.; Rochette, J.-F. ; Sacher, E. Functionalization of multiwalled carbon nanotubes by mild aqueous sonication. *J. Phys. Chem. B* **2005**, 109(16):7788–94.

128. Yang, D.-Q.; Sacher, E. Platinum nanoparticle interaction with chemically modified highly oriented pyrolytic graphite surfaces. *Chem. Mater.* **2006**, 18(7):1811–16.

129. http://www.phy.cuhk.edu.hk/~surface/XPSPEAK/.

130. See, e.g., http://srdata.nist.gov/xps/.

131. Chollon, G.; Takahashi, J. Raman microspectroscopy study of a C/C composite. *Composites: Part A* **1999**, 30(4):507–13.

132. Murphy, H. Papakonstantinou, P.; T Okapalugo, T. I. Raman study of multiwalled carbon nanotubes functionalized with oxygen groups. *J. Vac. Sci. Technol. B* **2006**, 24(2):715–20.

133. Endo, M.; Kim, C.; Karaki, T.; Tamaki, T.; Nishinura, Y.; Matthews, M. J.; Brown, S. D. M. Structural analysis of the B-doped mesophase pitch-based graphite fibers by Raman spectroscopy. *Phys. Rev. B* **1988**, 58(14):8991–96.

134. Peng, Y.; Liu, H. W. Effects of oxidation by hydrogen peroxide on the structures of multiwalled carbon nanotubes. *Ind. Eng. Chem. Res.* **2006**, 45(19):6483–88.

135. Yang, D.-Q.; Rochette, J.-F.; Sacher, E. Spectroscopic evidence for π–π interaction between poly(diallyl dimethylammonium) chloride and multiwalled carbon nanotubes. *J. Phys. Chem. B* **2005**, 109(10):4481–84.

136. Bellamy, L. J. *The Infra-red Spectra of Complex Molecules*; John Wiley & Sons: New York, 1958; Chapter 5 and 22.

137. Zhang, G.-X.; Yang, D.-Q.; Sacher, E. X-ray photoelectron spectroscopic analysis of Pt nanoparticles on highly oriented pyrolytic graphite, using symmetric component line shapes. *J. Phys. Chem. C* **2007**, 111(2):565–70.

138. Yang, D.-Q.; Rochette, J.-F.; Sacher, E. Controlled chemical functionalization of multiwalled carbon nanotubes by kiloelectronvolt argon ion treatment and air exposure. *Langmuir* **2005**, 21(18):8539–45.

139. Antunes, E. F.; Lobo, A. O.; Corat, E. J.; Trava-Airoldi, V. J.; Martin, A. A.; Veríssimo, C. Comparative study of first- and second-order Raman spectra of MWCNT at visible and infrared laser excitation. *Carbon* **2006**, 44(11):2202–11.

140. Qiang, Y.; Sabiryanov, R. F.; Jaswal, S. S.; Liu, Y.; Haberland, H.; Sellmyer, D. J. Magnetism of Co nanocluster films. *Phys. Rev. B* **2002**, 66(6):064404, 1-4.

141. Petit, C.; Russier, V.; Pileni, M. P. Effect of the structure of cobalt nanocrystal organization on the collective magnetic properties. *J. Phys. Chem. B* **2003**, 107(38):10333-6.

142. Klebanoff, L. E.; Vancampen, D. G.; Pouliot, R. J. Spin-resolved and high-energy-resolution XPS studies of cobalt metal and a cobalt magnetic glass. *Phys. Rev. B* **1994**, 49(57):2047-57.

143. Zhang, W. D.; Thong, J. T. C.; Tjiu, W. C.; Gan, L. M. Fabrication of vertically aligned carbon nanotubes patterns by chemical vapor deposition for field emitters. *Diam. Relat. Mater.* **2002**, 11(9):1638-42.

144. Lee, C. J.; Park, J. Growth and structure of carbon nanotubes produced by thermal chemical vapor deposition. *Carbon* **2001**, 39(12):1891-96.

145. Terrado, E.; Redrado, M.; Muñoz, E.; Maser, W. K.; Benito, A. M.; Martínez, M. T. Carbon nanotube growth on cobalt-sprayed substrates by thermal CVD. *Materials Science and Engineering C* **2006**, 26(5-7):1185-88.

146. Iijima, S. Helical microtubules of graphitic carbon. *Nature* **1991**, 354(6348):56-58.

147. Carrillo, A.; Swartz, J. A.; Gamba, J. M.; Kane, R. S.; Chakrapani, N.; Wei, B. Q.; Ajayan, P. M. Noncovalent functionalization of graphite and carbon nanotubes with polymer multilayers and gold nanoparticles. *Nano. Lett.* **2003**, 3(10):1437-40.

148. Jiang, K. Y.; Eitan, A.; Schadler, L. S.; Ajayan, P. M.; Siegel, R. W. Selective attachment of gold nanoparticies to nitrogen-doped carbon nanotubes. *Nano. Lett.* **2003**, 3(3):275-77.

149. Li, W. Z.; Wen, J. G.; Ren, Z. F. Effect of gas pressure on the growth and structure of carbon nanotubes by chemical vapor deposition. *Appl. Phys. A* **2001**, 73(2):259-64.

150. Huh, Y.; Green, M. L. H.; Kim, Y. H.; Lee, J. Y.; Lee, C. J. Control of carbon nanotube growth using cobalt nanoparticles as catalyst. *Appl. Surf. Sci.* **2005**, 249(1-4):145-50.

151. Coquay, P. ; Peigney, A.; Grave, E. D. ; Flahaut, E. ; Vandenberghe, R. E. ; Laurent, C. Fe/Co alloys for the catalytic chemical vapor deposition synthesis of single- and double-walled carbon nanotubes (CNTs). 1. The CNT-Fe/Co-MgO system. *J. Phys. Chem. B* **2005**, 109(38):17813-24.

152. Lim, D. C.; Lopez-Salido, I.; Dietsche, R.; Bubek, M.; Kim, Y. D. Oxidation of Au nanoparticles on HOPG using atomic oxygen. *Surf. Sci.* **2006**, 600(3):507-13.

153. Marcus, P.; Hinnen, C. XPS study of the early stages of deposition of Ni, Cu and Pt on HOPG. *Surf. Sci.* **1997**, 392(1-3):134-42.

154. Buckley, J. D.; Edie, D. D. *Carbon-Carbon Materials and Composites*; Noyes: New Jersey, 1993.

155. Morgan, P. *Carbon Fibers and their Composites*; Taylor and Francis: Boca Raton, 2005.

156. Wang, C.; Waje, M. M.; Wang, X.; Tang, J. M.; Haddon, R. C.; Yan, Y. S. Proton exchange membrane fuel cells with carbon nanotube based electrodes. *Nano. Lett.* **2004**, 4(2):345-48.

157. Waje, M. M.; Wang, X.; Li, W. Z.; Yan, Y. S. Deposition of platinum nanoparticles on organic functionalized carbon nanotubes grown *in situ* on carbon paper for fuel cells. *Nanotechnol.* **2005**, 16(7):S395-400.

158. Chen, C. C.; Chen, C. F.; Hsu, C. H.; Li, I. H. Growth and characteristics of carbon nanotubes on carbon cloth as electrodes. *Diamond Relat. Mater.* **2005**, 14(3-7):770-73.

159. Derrien, J.; Crescenzi, M. D.; Chainet, E.; d'Anterroches, C. Co/Si(111) interface formation at room temperature. *Phys. Rev. B* **1987**, 36(12):668184.

160. Pan, J. S.; Liu, R. S.; Zhang, Z.; Poon, S. W.; Ong, W. J.; Tok, E. S. Co growth on Si(001) and Si(111) surfaces: Interfacial interaction and growth dynamics. *Surf. Sci.* **2006**, 600(6):1308-18.

161. García-Méndez, M.; Castillón, F. F.; Hirata, G. A.; Farías, M. H.; Beamson, G. XPS and HRTEM characterization of cobalt-nickel silicide thin films. *Appl. Surf. Sci.* **2000**, 161(1-2):61-73.

162. Chembers, S. A.; Boscherini, F.; Anderson, S. B.; Joyce, J. J.; Chen, H. W.; Ruckman, M. W.; Weaver, J. H. Summary abstract: reaction and epitaxy at the Co/Si(111) interface. *J. Vac. Sci. Technol. A* **1987**, 5(4):2142-43.

163. Monchesky, T. L.; Unguris, J. Magnetic properties of Co/GaAs(110). *Phys. Rev. B* **2006**, 74(24):24130(R), 1-4.

164. Poon, S. W.; Pan, J. S.; Tok, E. S. Nucleation and growth of cobalt nanostructures on highly oriented pyrolytic graphite. *Phys. Chem. Chem. Phys.* **2006**, 8(28):3326-34.

165. http://www.nanotec.es/.

166. Brundle, C. R.; Chuang, T. J.; Rice, D. W. X-ray photoemission study of the interaction of oxygen and air with clean cobalt surfaces. *Surf. Sci.***1976**, 60:286-300.

167. McIntyre, N. S.; Cook, M. G. X-ray photoelectron studies on some oxides and hydroxides of cobalt, nickel, and copper. *Analytical chemistry* **1975**, 47(13):2208-13.

168. Bonnelle, J. P.; Grimblot, J.; D'huysser, A. Influence de la polarisation des liaisons sur les spectres ESCA des oxydes de cobalt. *Journal of Electron Spectroscopy and Related Phenomena* **1975**, 7:151-62.

169. Boscherini, F.; Joyce, J. J.; Ruckman, M. W.; Weaver, J. H. High-resolution photoemission study of Co/Si(111) interface formation. *Phys. Rev. B* **1987**, 35(9):4216-20.

170. Fu, L.; Liu, Z. M.; Liu, Y. Q.; Han, B. X.; Hu, P. G.; Cao, L. C.; Zhu, D. B. Beaded cobalt oxide nanoparticles along carbon nanotubes: Towards more highly integrated electronic devices. *Adv. Mater.* **2005**, 17(2):217-21.

171. Chuang, T. J.; Brundle, C. R.; Rice, D. Interpretation of the x-ray photoemission spectra of cobalt oxides and cobalt oxide surfaces. W. *Surf. Sci.***1976**, 59:413-29.

172. Ke, R.; Haasch, T.; Finnegan, N.; Dottl, L. E.; Alkire, R. C.; Farrell, H. H. Chemical and matrix effects on sensitivity factors in electron spectroscopies. I. C and Si containing materials. *J. Vac. Sci. Technol. A* **1996**, 14(1):80-88.

173. Li, W. Z.; Liang, C. H.; Zhou, W. J.; Qiu, J. S.; Zhou, Z. H.; Sun, G. Q.; Xin, Q. Preparation and characterization of multiwalled carbon nanotube-supported platinum for cathode catalysts of direct methanol fuel cells. *J. Phys. Chem. B* **2003**, 107(26):6292-99.

174. Sramenkovic, V. R.; Fowler, B.; Mun, B. S.; Wang, G. F.; Ross, P. N.; Lucas, C. A.; Marković, N. M. Improved oxygen reduction activity on Pt₃Ni(111) via increased surface site availability. *Science* 2007, 315(5809):493-97.

175. Zhang, J.; Sasaki, K.; Sutter, E.; Adzic, R. R. Stabilization of platinum oxygen-reduction electrocatalysts using gold clusters. *Science* 2007, 315(5809):220-222.

176. Zhang, G. X., Yang, D. Q., Sacher, E. The structure and morphology of Co nanoparticles deposited onto highly oriented pyrolytic graphite. *J. Phys. Chem. C*, in course of publication.

177. Yang, D.-Q.; Sacher, E. Coalescence kinetics of copper clusters on highly oriented pyrolytic graphite and Dow Cyclotene, as determined by x-ray photoelectron spectroscopy. *J. Appl. Phys.* **2001**, 90(9):4768-71.

178. Yang, D.-Q.; Sacher, E. Initial- and final-state effects on metal cluster/substrate interactions, as determined by XPS: copper clusters on Dow Cyclotene and highly oriented pyrolytic graphite. *Appl. Surf. Sci.* **2002**, 195(1-4):187-95.

179. Yang, D.-Q.; Sacher, E.; Meunier, M. Excimer laser manipulation and pattering of gold nanoparticles on the SiO_2/Si surface. *J. Appl. Phys.* **2004**, 95(9):5023-5026

180. Tian, N.; Zhou, Z. Y.; Sun, S. G.; Ding, Y.; Wang, Z. L. Synthesis of tetrahexahedral platinum nanocrystals with high-index facets and high electro-oxidation activity. Science 2007, 316 (5825):732-35.

181. Kijima, T.; Yoshimura, T.; Uota, M.; Ikeda, T.; Fujikawa, D.; Mouri, S. Noble-metal nanotubes (Pt, Pd, Ag) from lyotropic mixed-surfactant liquid-crystal templates. *Angew. Chem. Int. Ed.* **2004**, 43(2):228-32.

182. Song, Y.; Steen, W. A.; Pena, D.; Jiang, Y. B.; Medforth, C. J.; Huo, Q.; Pincus, J. L.; Qiu, Y.; Sasaki, D. Y.; Miller, J. E.; Shelnutt, J. A. *Chem. Mater.* **2006**, *18*, 2335.

183. Teng, X.; Yang, H. Synthesis of platinum multipods: an induced anisotropic growth. *Nano Lett.* **2005**, 5(5):885-91.

APPENDICES

Appendix A

As already mentioned in chapter 3, where the interfacial interaction of Pt nanoparticles and HOPG surfaces was discussed, we used *asymmetric* XPS lineshape analysis: the C1s and $Pt4f_{7/2}$ peaks were each considered to be composed of one asymmetric peak, and changes in their asymmetry parameters were used to study their interfacial interactions (details are discussed in this appendix). Further, using *symmetric* XPS lineshape analysis, we demonstrated that the lineshape asymmetry is due to the existence of identifiable, overlapping symmetric component species (details were shown in chapter 3). We used the varying intensities of these symmetric component peaks, as a function of deposited Pt, to explain the changing shape of the Pt4f asymmetric envelope with nanoparticle size. Both methods demonstrated that the asymmetry of Pt lineshape increases with Pt nanoparticle size.

In this following paper, the interactions of Pt nanoparticles, deposited by evaporation onto highly oriented pyrolytic graphite (HOPG) surfaces modified by keV Ar^+ beam treatment, have been studied by XPS core-level line shape analysis. The C1s and $Pt4f_{7/2}$ peaks were each considered to be composed of one asymmetric peak, and changes in their asymmetry parameters were used to study their interfacial interactions. In addition to these changes, strong signal intensity changes with time were found for both the C1s and Pt4f peaks, indicating an initial crystalline orientational instability of the Pt nanoparticles, which is supported by time-dependent high resolution electron microscope studies at elevated temperatures.

Evidence of the Interaction of Evaporated Pt Nanoparticles with Variously Treated Surfaces of Highly Oriented Pyrolytic Graphite

D-Q. Yang, G.-X. Zhang and E. Sacher

Regroupement Québécois de Matériaux de Pointe, Département de Génie Physique, École Polytechnique, C.P. 6079, succursale Centre-Ville, Montréal, Québec H3C 3A7, Canada

M. José-Yacamán and N. Elizondo

Center for Nano and Molecular Technology, Texas Materials Institute, Department of Chemical Engineering, The University of Texas at Austin, Austin, Texas 78712, U.S.A.

Introduction

The interaction between metal nanoparticles and substrate surfaces has long attracted attention[1-3]. This is because of underlying interests in understanding (1) the behavioral transition from atomic to bulk-like properties, as a function of nanoparticle size, (2) the effect of size-dependent electronic structures in heterogeneous catalysis, (3) the dimensionally controlled fabrication of supported nanoparticles, (4) thin film deposition onto heterogeneous surfaces[4], and (5) the adhesion associated with interfacial interactions.

Pt nanoparticles, one of the most important catalysts in the petroleum reforming and petrochemical industries, as well as in fuel cells, are of considerable interest, especially when supported on carbonaceous materials, such as amorphous carbon and graphite [1,5-17]. Studies have indicated that the evaporation, sputter and electrochemical depositions of Pt all lead to particle formation on such substrates, due to both a lack of substrate wetting and relatively weak interfacial interactions [10,13].

X-ray photoelectron spectroscopy (XPS) is a major tool in the characterization of the chemical and electronic structural properties of nanoparticles, and has been extensively used to characterize Pt nanoparticles supported on highly oriented pyrolytic graphite (HOPG) or amorphous carbon (a-C) [5-17]. The main conclusions of these studies were that (1) the core level Pt4f spectrum shifts to high binding energy with decreasing particle size [7-17], (2) the full width at half maximum (FWHM) of the core level decreases with increasing particles size [7,8,12], similar to the behaviors of other supported nanoparticles, e.g., Cu on HOPG [18,19], and (3) the asymmetries of both the Pt4f$_{7/2}$ and Pt4f$_{5/2}$ components increase with increasing nanoparticles size [7,8,12,20], to a maximum for bulk Pt. We emphasize that this is opposite to the behaviors of First Transition Series metals, e.g., Ni, Mn, Cr, V, Cu etc.[2, 21].

In disagreement, a recent study, by Fauth et al.[15,16], suggested that the Pt XPS shift is a result of interfacial interaction between Pt and defects on the graphite surface, consistent with Pt clusters supported on a Ag surface [22], rather than from any Pt particle size effects. In their view, the size-dependent behavior of Pt nanoparticles may not play an important role in the core level binding energy shift.

The treatment of asymmetric XPS peaks as single asymmetric peaks, rather than as an asymmetric composite of several symmetric peaks, has a long history. In 1967, Mahan

[23] proposed that the conduction electron scattering amplitude, for interband absorption or emission at the metal Fermi level, is a singularity. Subsequently, in the third of a series of papers on singularities in metals, Nozières and de Domenicis [24] showed that this singularity arose because of the competition between the scattering resonance and deep level broadening. Doniach and Šunjić [25] and, later, Gadzuk and Šunjić [26] demonstrated that, when the Mahan proposal was applied to photoelectron emission from metals, an asymmetry was expected in the metal core level electron emission peak, extending to the lower kinetic (i. e., higher binding) energy side. The reason for this is a potential created between the hole formed by the photoemission and the remaining electrons; this permits the promotion of electrons near the Fermi level to empty states just above it. As in a shake-up process, this promotion occurs simultaneously with photoemission and, indeed, Gadzuk and Šunjić [26] referred to this as the Mahan shake-up structure. The equation that Doniach and Šunjić [25] derived for the photoemission line shape intensity, I, is

$$I(\varepsilon) = \frac{\Gamma(1-\alpha)}{(\varepsilon^2 + \gamma^2)^{(1-\alpha)/2}} \left[\frac{\cos \pi \alpha}{2} + (1-\alpha) \tan^{-1} \frac{\varepsilon}{\gamma} \right], \tag{1}$$

where Γ is the Gamma function, ε is the energy relative to that at the peak height of the unbroadened line, γ is the lifetime width of the hole, and α is the Anderson asymmetry parameter [27], given as

$$\alpha = 2\sum_l (2l+1) \left[\frac{\delta_l}{\pi} \right]^2. \tag{2}$$

Here, δ_l is the Fermi level phase shift of the lth partial wave. Because the calculation of α is formidable, the practice has been to turn the problem around, and evaluate α from the asymmetry. Confirmation has, thus, been based on consistency (e. g., between spin-orbit components) and interlaboratory reproducibility. The end result is the following: despite inconsistencies of α values for spin-orbit components [28,29], and experimental data that have been used both pro [30] and con [31], there is a general concurrence that both experiment [32-39] and theory [40] support the Mahan singularity as the source of the asymmetry.

Because of this, it has since been generally assumed that any asymmetric XPS core emission peak, particularly for metals, is due to the Mahan shake-up process. However, we have recently shown [18,19] that the asymmetry in the C1s peak of HOPG is due, instead, to the existence of identifiable carbon species. Further, in an as yet unpublished study [41], a Co film was found to initially display symmetric 2p spin-orbit components, which became increasingly asymmetric with time under vacuum; simultaneously, a peak appeared at 283 eV in the C1s spectrum, indicative of carbide formation [42], which increased in magnitude with increasing Co2p asymmetry.

We have considered the applicability of the Mahan theory to the metal nanoparticles we have been studying. In a recent examination of Ni nanoparticle deposition onto HOPG [21], we found that the asymmetry of the Ni2p spin-orbit components decreased with increasing nanoparticle size. This was found to be due to the presence of two overlapping symmetric peaks, the first being due to the presence of Ni^0. The second, at a binding energy slightly higher than that of the Ni^0 peak, was due to those Ni atoms in the nanoparticle directly bonded to surface defects on the HOPG. The asymmetry decreased with increasing nanoparticle size because the deposited Ni atoms added to the existing

nanoparticles in the absence of further surface defects, raising the intensity of the Ni^0 peak, alone. Similar results have been obtained for Cu nanoparticles supported on both HOPG and low permittivity polymers [43].

Further, in a recent paper on peak deconvolution techniques [44], comparing (1) one single asymmetric peak and (2) several overlapping symmetric peak components, we demonstrated that the single peak asymmetry of the C1s spectrum of HOPG is due to the increase in intensity of that symmetric peak component signaling structural damage.

Here, we consider Pt nanoparticles evaporated onto three different HOPG surfaces: one of very low defect density (untreated), one having a high defect density surface (Ar^+-treated), and one having a surface containing a high defect density of oxidized C structures (Ar^+ treatment, followed by air exposure). We use XPS peak shape analysis to explore the interactions between the Pt nanoparticles and the HOPG surface, concentrating our attention on the asymmetry changes of the C1s and $Pt4f_{7/2}$ spectra induced by Pt deposition.

Experimental

HOPG, grade ZYA, 1 cm $\times$ 1 cm $\times$ 2 mm, was obtained from Advanced Ceramics. Inc. It was cleaved with adhesive tape just prior to each experiment and immediately inserted into the X-ray photoelectron spectrometer. Sample surface treatments and Pt deposition were carried out in the UHV preparation chamber of the XPS instrument, which was connected to the analysis chamber by a gate valve. The Ar^+ treatment of HOPG was performed using a 3 keV Ar^+ beam having a flux of $\sim 1\times10^{13}$ ions/cm^2/sec, for 4 min, at an angle of $\sim 60°$ between the surface normal and the beam. This condition provides a uniform, repeatable surface defect density, as previously shown [18,19]. For surface

oxidation, the HOPG was first treated with Ar^+ for 4 min, followed by exposure to air (40% RH at room temperature) for at least 2 h. This exposure has been shown to be sufficient for the free radicals produced at the HOPG surface to react with components in air (O_2, H_2O), to produce oxidation products (-C-OH, -C=O, -COOH).

Pt evaporation was carried out, at room temperature, in the preparation chamber, using a Quad-EVC evaporator (Mantis Deposition, Ltd.) at a rate of ~ 0.15 nm/min. The thickness was monitored by a quartz crystal microbalance placed near the sample.

XPS was performed in a VG ESCALAB, using non-monochromated Mg K_α radiation, at 300 W. High resolution spectra were obtained at a perpendicular take-off angle, using a pass energy of 20 eV and 0.05 eV steps. The instrument resolution was ~ 0.75 eV. After Shirley background subtraction, the peaks were fit using the freely available XPSPeak 4.1 program [45] for asymmetric peak line shapes, which gives the asymmetry in terms of the TS peak shape asymmetry and the TL tail extension asymmetry indices; we have recently shown [44] that an increase in TS reflects any reduced delocalization of electrons in the C1s HOPG π-orbital system, and an increase in TL reflects any subsequent oxidation occurring on air exposure. As shown in our previous paper [44], α asymmetry indices, calculated from half widths at half heights, vary in a fashion identical to that of the XPSPeak TS values, and may be used interchangeably; the use of α is preferred by most workers. We give examples of the use of both.

High resolution transmission microscopy studies were carried out on a JEOL 2010 FEG, outfitted with a JEOL drift-controlled heating stage, and having an information limit of 0.14 nm. Samples were evaporated onto thin graphene layers that were stripped by adhesive tape from freshly cleaved HOPG and transported to the electron microscope in capsules, under argon; these samples, thin enough to be directly observed in the

microscope, were observed at the optimum defocus condition. Experiments were carried out at 450°C, on the stabilized heating stage; sequential exposures were obtained at 5 s intervals, using a CCD camera.

Results

The C1s spectral envelopes of the samples considered here are asymmetric; they were previously separated into five symmetric components [18,19], comprising peaks attributed to extensive (undamaged) and localized (damaged) electron delocalization (called C1 and C2, respectively), their $\pi^* \leftarrow \pi$ shake-up satellites (C4 and C5, respectively) and sp^3 defects (C3). It has been found that the C1s spectra do not change significantly on the deposition of many metals [18,19,46,47], and no new peaks, which would signify carbide formation, appear in the 282-284 eV region. Thus, it is clear that the C1s line shape is insensitive to the presence (i.e., interfacial interaction) of numerous metals. Many researchers [48-53] have found that the asymmetric C1s spectral line shape is well described by the Doniach-Šunjić equation [25]. Based on this, it has generally been supposed that the C1s line shape of HOPG is determined by an excitonic state near the Fermi level (π-electron band) in the hole-state density of states [48], due to many-electron effects, although an alternative view, using attributable, quantifiable, overlapping symmetric peak components, exists [44].

All C1s and Pt4f$_{7/2}$ spectra could be fit with asymmetry line shapes having appropriate asymmetry parameters. Typical C1s and Pt4f spectra, and their asymmetric peak fits are seen in Fig. 1, subsequent to Shirley background subtraction. The peak binding energies are seen in Figure 2, as a function of Pt thickness, as are the FWHMs in Figure 3, and the TS and TL asymmetry indices in Figure 4. As previously indicated [44], the α

asymmetry index varies linearly with the TS asymmetry index; this is confirmed in the present work, where, as shown in Fig. 5, this relationship holds, regardless of HOPG surface treatment and Pt particle size.
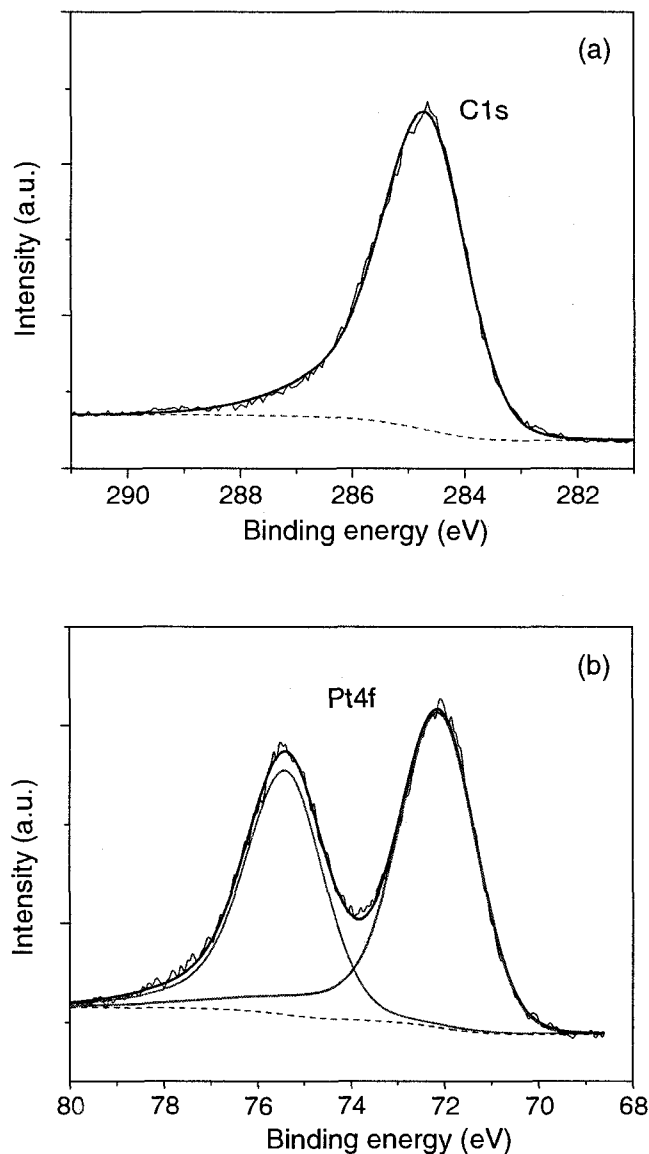

Figure 1. XPS spectra of 0.2 nm Pt evaporated onto the Ar^{+}-treated HOPG surface: (a) C1s and (b) Pt 4f.
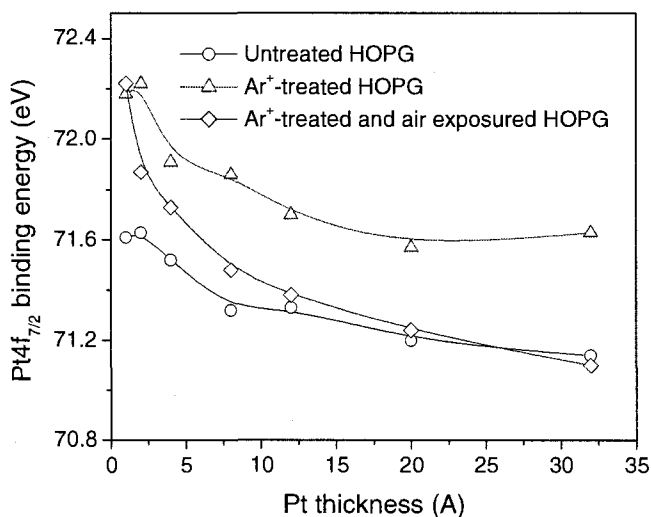
Figure 2. Binding energy shifts of the Pt4f$_{7/2}$ spectra as a function of Pt deposition onto variously treated HOPG surfaces.

We also found that each of the asymmetric Pt4f spin-orbit components may be fit with several symmetric peaks. While this was previously observed for Pt nanoparticles on SiO$_2$ [9], it was attributed there to many-electron effects, due to the particles being non-metallic. We will report on our use of symmetric Pt peak components in a later paper.

The α asymmetry index of the C1s spectrum is seen to decrease (Figure 4), and its FWHM to increase (Figure 3), with increasing Pt thickness, while those of Pt change in the opposite directions. These changes are accompanied by (1) an increase in C1s intensity (Figure 6) over the first 0.5 nm of Pt deposition, before decreasing with further deposition, and (2) a slight increase in C1s binding energy (not shown) over the same first 0.5 nm of Pt thickness.
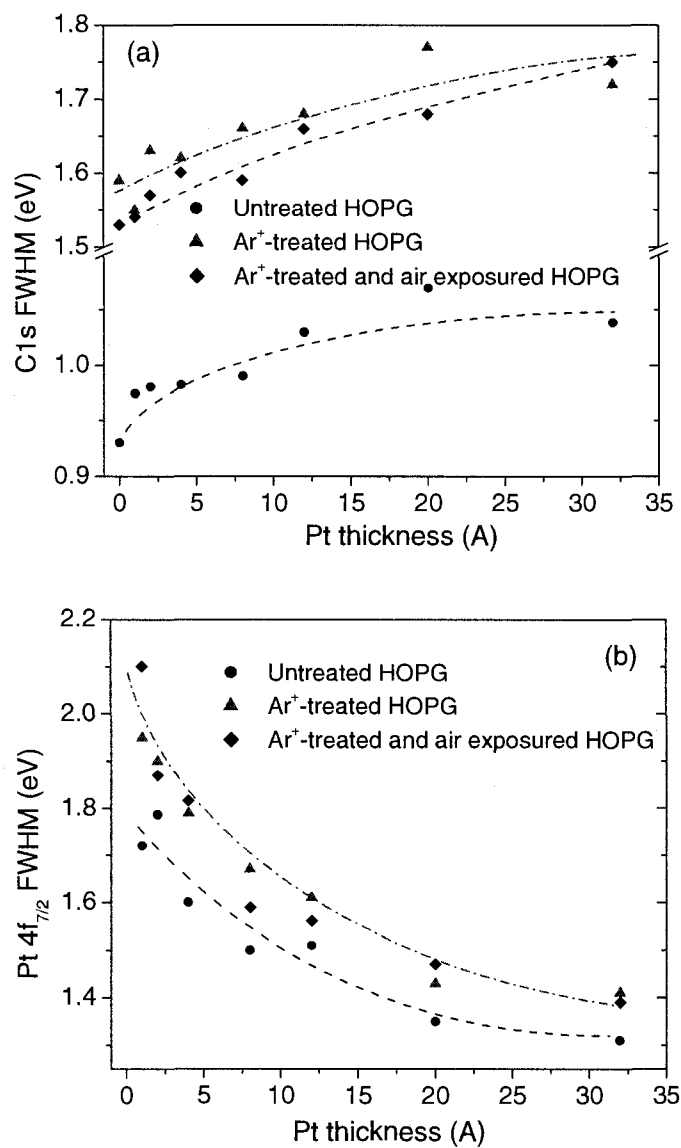
Figure 3. FWHM changes of the (a) C1s and (b) Pt4f$_{7/2}$ spectra as a function of Pt

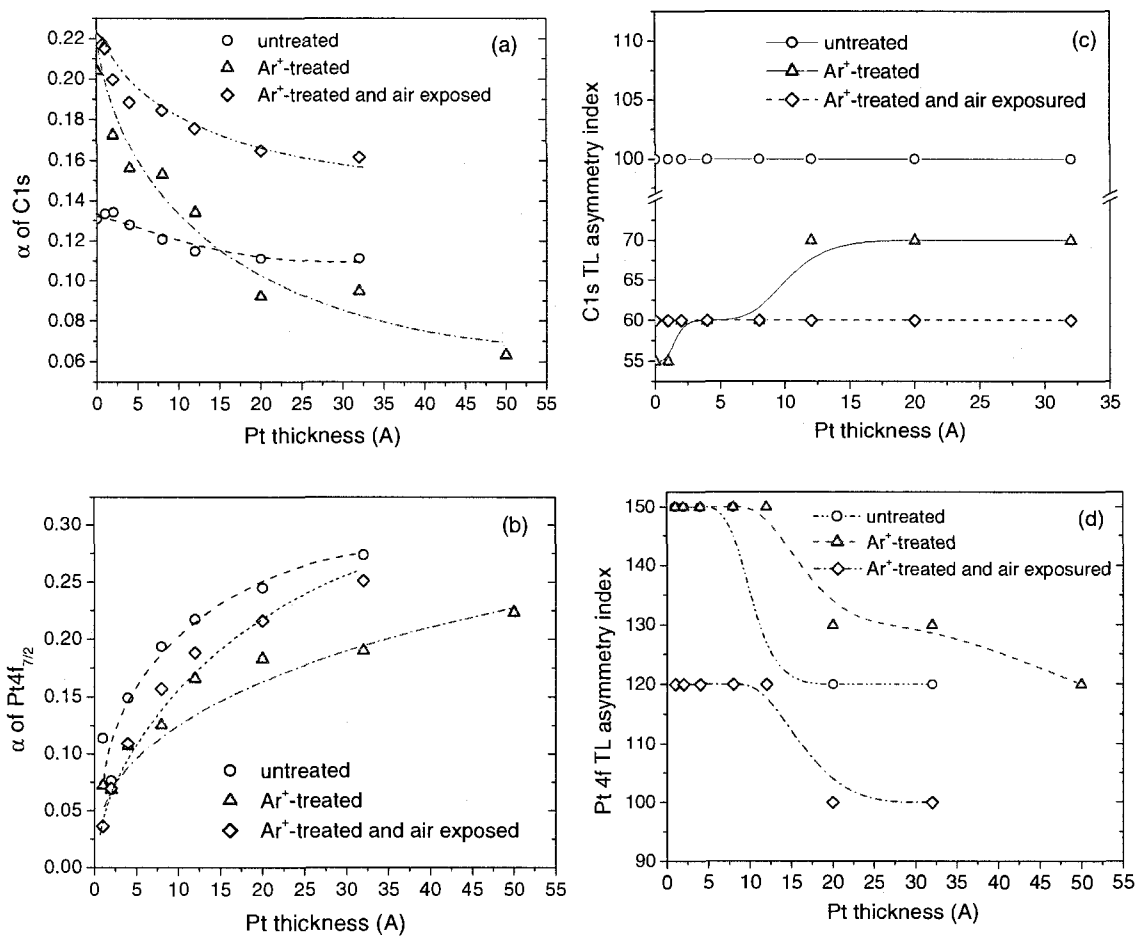deposition onto variously treated HOPG surfaces.

Figure 4. Asymmetry indices as a function of Pt deposition onto variously treated HOPG surfaces: α indices for (a) C1s, (b) Pt4f$_{7/2}$, (c) TL indices for C1s and (d) TL indices for Pt4f$_{7/2}$.
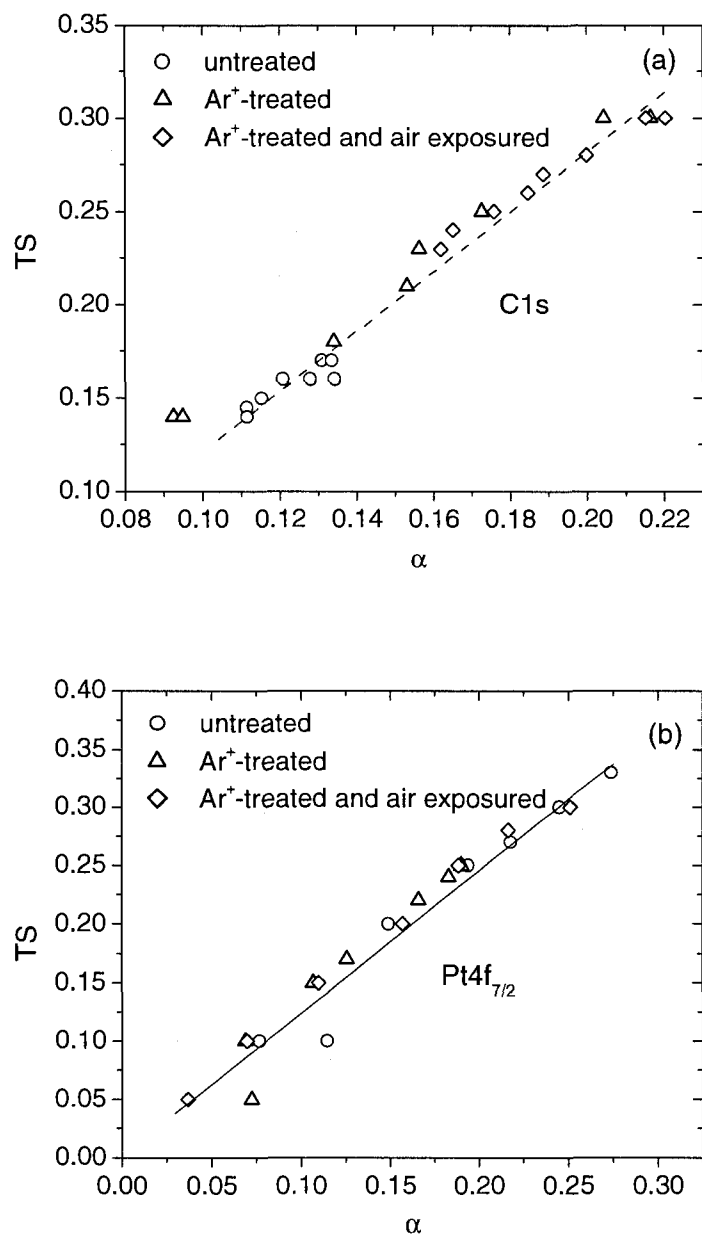
Figure 5. TS asymmetry indices as a function of α, (a) C1s, (b) Pt4f$_{7/2}$.
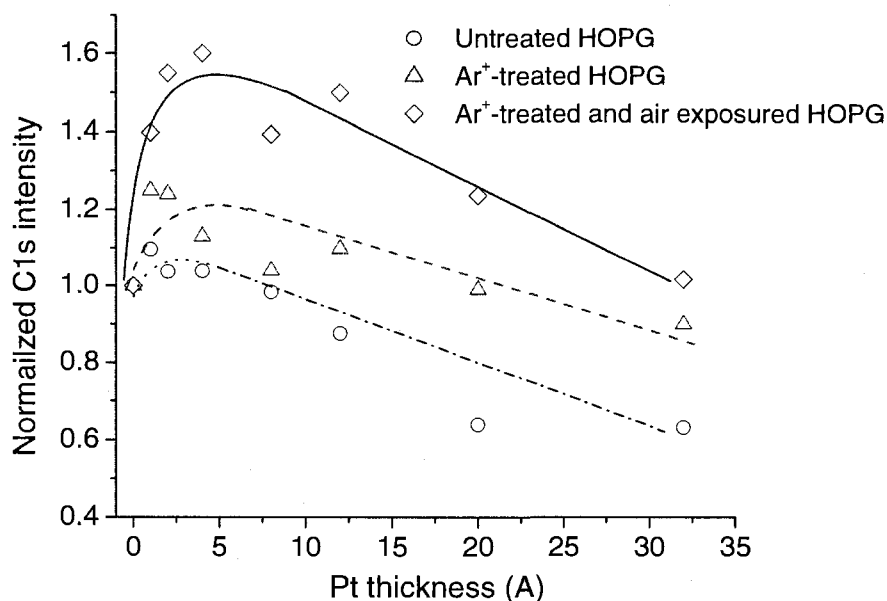
Figure 6. Normalized C1s peak intensity as a function of Pt deposition onto variously treated HOPG surfaces.

The TL indices for untreated and for air-exposed Ar^+-treated HOPG do not seem to change with Pt deposition, although those for Ar^+-treated (not air-exposed) HOPG increase. As we previously showed [18], this latter treatment produces stable free radicals in this spectral region, which are shown by the TL values and their effect on the C1s peak asymmetry.

The changes in the TL indices for Pt, under all conditions, are clearly size-related. They may be associated with the dimensions of the Kubo gap, which is the average energy of the gap between quantum levels at the Fermi energy: while normally much less than kT for a metal, the gap increases in size as the particle dimension decreases, eventually becoming greater than kT. At this point, the particle becomes non-metallic. This occurs in the 1-2 nm range [54].

Thus, the asymmetry parameters, peak positions (particularly that of $Pt4f_{7/2}$), peak widths and the C1s peak intensity are all dependent on the nominal thickness of deposited Pt. The changes in the $Pt4f_{7/2}$ spectrum, with increasing Pt deposition thickness, are due to contributions from nanoparticle/substrate interactions [15,16] and size-dependent final-state effects [9], without the formation of Pt-C covalent bonds (no carbide formation).

The FWHM values for both the $Pt4f_{7/2}$ and C1s spectra (Figure 3) manifest different developments with deposition: $Pt4f_{7/2}$ shows a continued decrease and C1s, a continued increase. Although the $Pt4f_{7/2}$ spectrum contains contributions from both the nanoparticle size and its interaction with the substrate, which are difficult to separate, this does not apply to the C1s spectrum. The increase of the C1s FWHM (Fig. 3a), due to phonon broadening, indicates that there is *some* interaction between Pt and HOPG surface, whether or not the surface is treated. Added to the decrease seen in the C1s asymmetry index, these suggest that the charge transfer from Pt particle to HOPG surface, or localized surface electron states, are partly compensated (perturbed) by the Pt particles. This is more clearly seen for a more localized surface, such as that for Ar^+-treated HOPG, in Fig. 4a, due the increased interaction between Pt and HOPG.

The normalized C1s peak area, as a function of Pt deposition (Fig. 6), varies in a manner similar to that of Ni nanoparticles on HOPG [21], with the enhanced photoemission from the substrate attributed to the forward scattering of photoelectron diffraction through the Pt [55]: the forward scattering of the photoelectrons aligns as the initial nanoparticle size increases and the crystallinity and orientation are perfected [55-57]; again, this indicates interfacial interaction insofar as the ability to orient the

direction of crystalline perfection with respect to the plane of the substrate. Eventually, orientational order is lost with increasing size, and scattering increases.

Decreases of the C1s asymmetry indices with Pt deposition, especially for Ar^+-treated HOPG, with simultaneous increases of the $Pt4f_{7/2}$ asymmetry indices, also indicate interfacial interaction. All these change patterns in our C1s and $Pt4f_{7/2}$ spectral features, occurring upon Pt deposition, are similar to those in an early report on Pt deposited onto carbon foil[7], although they were attributed to another source.

While the free radicals, created at the HOPG surface on Ar^+ treatment, react readily with O_2 and H_2O on air exposure, which can lead to a significant increase in the relative concentration of incorporated oxygen, this causes a minor change in the C1s α peak asymmetry index, from 0.206 on Ar^+ treatment to 0.214 (Table 1). The O1s evolution on Pt deposition onto an air exposed Ar^+-treated HOPG surface is seen in Fig. 7. Although there is a slight broadening of the line width, there is a lack of any firm evidence of the formation of a Pt-O bond (a new component would be expected in the 530-531 eV range, and might be difficult to see because of the weak signal).

Table 1. C1s asymmetry parameter analysis from the variously treated HOPG surfaces.

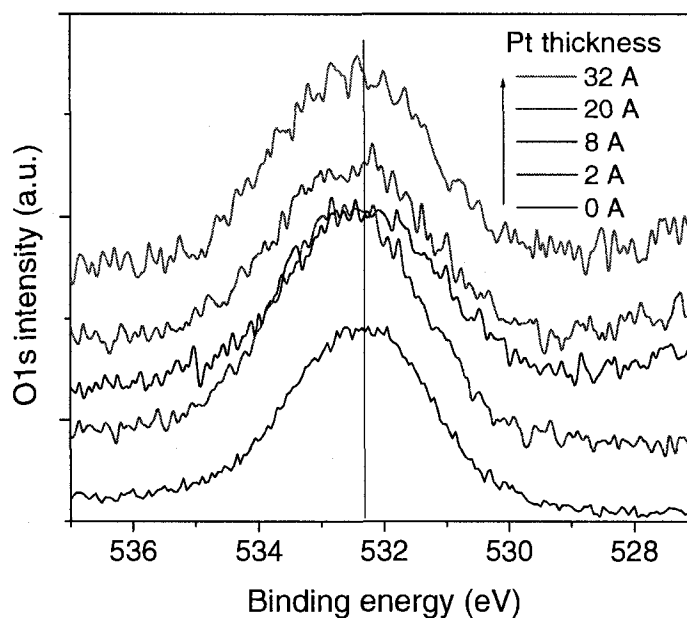| Surface	FWHM (eV)	TS asymmetry index	α asymmetry index	Oxygen Concentration (atomic %)
untreated	0.93	0.17	0.135	<1
Ar^+-treated	1.59	0.30	0.206	0
Ar^+-treated and air exposed	1.53	0.30	0.214	~10

Figure 7. O1s spectral evolution on the Ar$^+$-treated and air exposed HOPG surface as a function of Pt deposition.

The time-dependent stabilities of the C1s and Pt4f$_{7/2}$ spectra offer insights into nanoparticle/interface interactions. Figure 8a shows the time dependence of the C1s peak area intensity of a nominal one monolayer of Pt deposited onto variously treated HOPG substrates, and Figure 8b shows the corresponding Pt4f$_{7/2}$ dependence. In all cases, the C1s spectra are characterized by an initial decrease in intensity over the first moments subsequent to deposition, followed by an increase over the initial 10 minutes; this is followed by a slower decrease over the next two hours. As the Pt4f$_{7/2}$: C1s ratio in Figure 9 shows, there is no change, as a function of time, beyond the first few minutes of nanocrystal reorganization, indicating an absence of coalescence; that is, the nanoparticles are fixed to the surface.
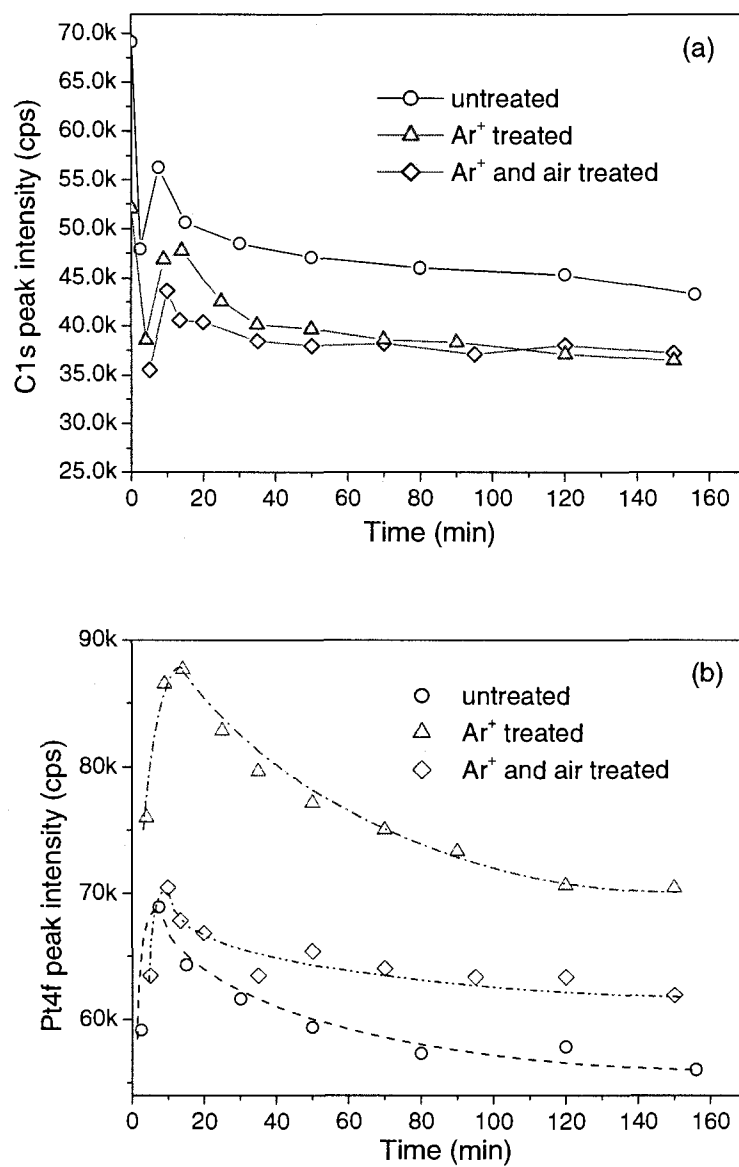
Figure 8. Peak intensity changes of the (a) C1s and (b) Pt4f$_{7/2}$ spectra as a function of time for 0.3 nm Pt deposited onto variously treated HOPG surfaces.
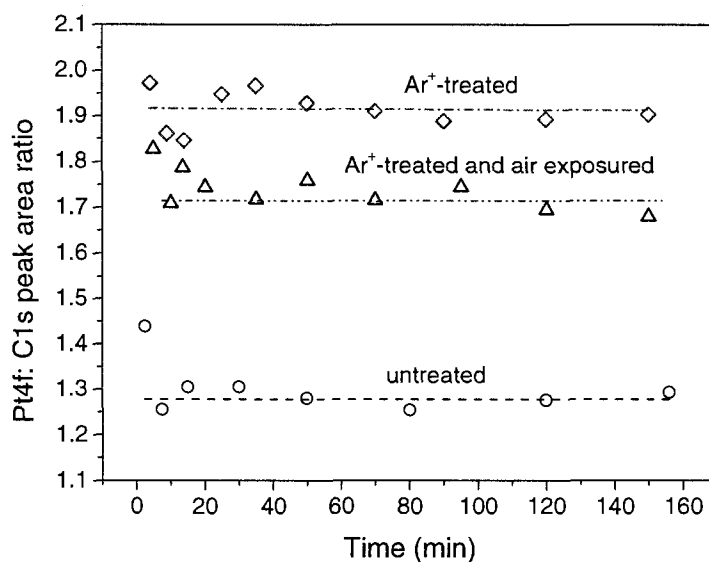
Figure 9. The Pt4f$_{7/2}$: C1s intensity ratio as a function of time for 0.3 nm Pt deposited onto variously treated HOPG surfaces.

The Pt4f$_{7/2}$ spectra do not show the initial decrease in intensity seen in the C1s spectra but mirror the increase and the subsequent decrease. Similar behavior characterizes the α asymmetry indices in Figure 10, although with more scatter. The initial decrease in the C1s spectra implies a time-dependent interfacial alignment in the Pt nanoparticle (chemical reactions would be expected to occur far more quickly), and coalescence is ruled out because of strong adhesion [58]; once this occurs, the time-dependent behaviors of both spectra are quite similar, indicating an increased forward scattering due to Pt nanocrystalline alignment, followed by a crystalline reorganization.

Figure 10. Time-dependent α asymmetry indices of (a) C1s and (b) Pt4f$_{7/2}$ spectra for 0.3 nm Pt deposited onto variously treated HOPG surfaces. As indicated in the text, the α indices vary in a manner identical to that of the TS indices, and may be used interchangeably.
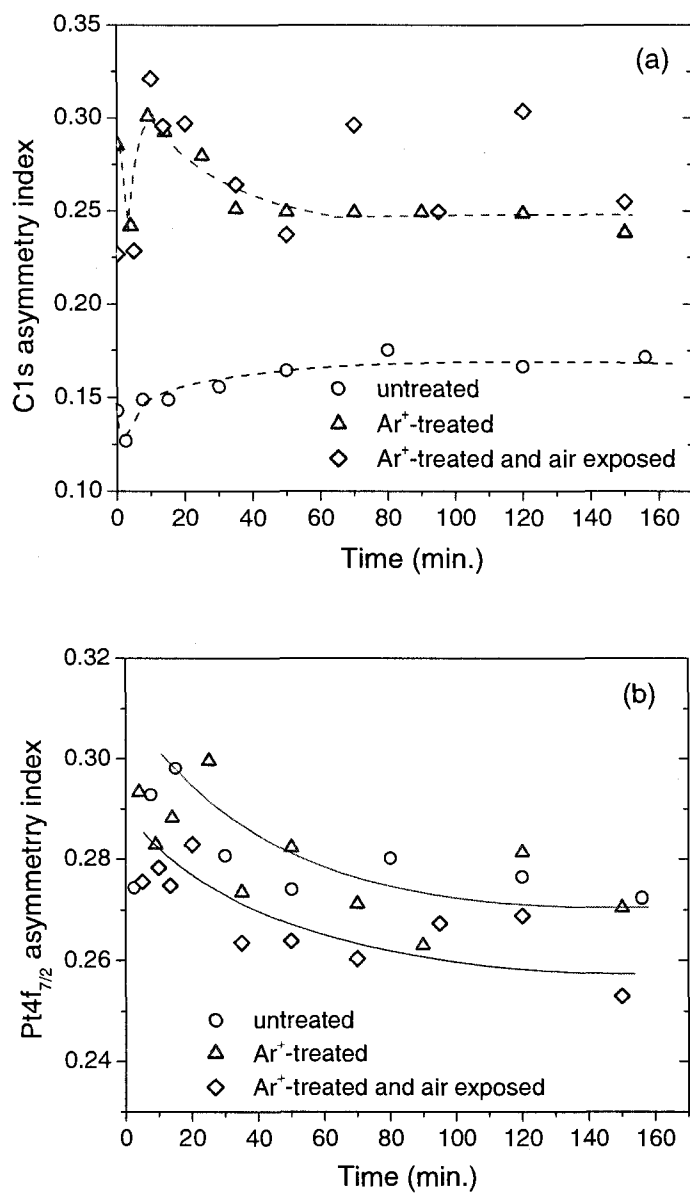
Figure 11. Time-dependent α asymmetry indices of (a) C1s and (b) Pt4f$_{7/2}$ spectra for 0.3 nm Pt deposited onto variously treated HOPG surfaces. As indicated in the text, the α indices vary in a manner identical to that of the TS indices, and may be used interchangeably.
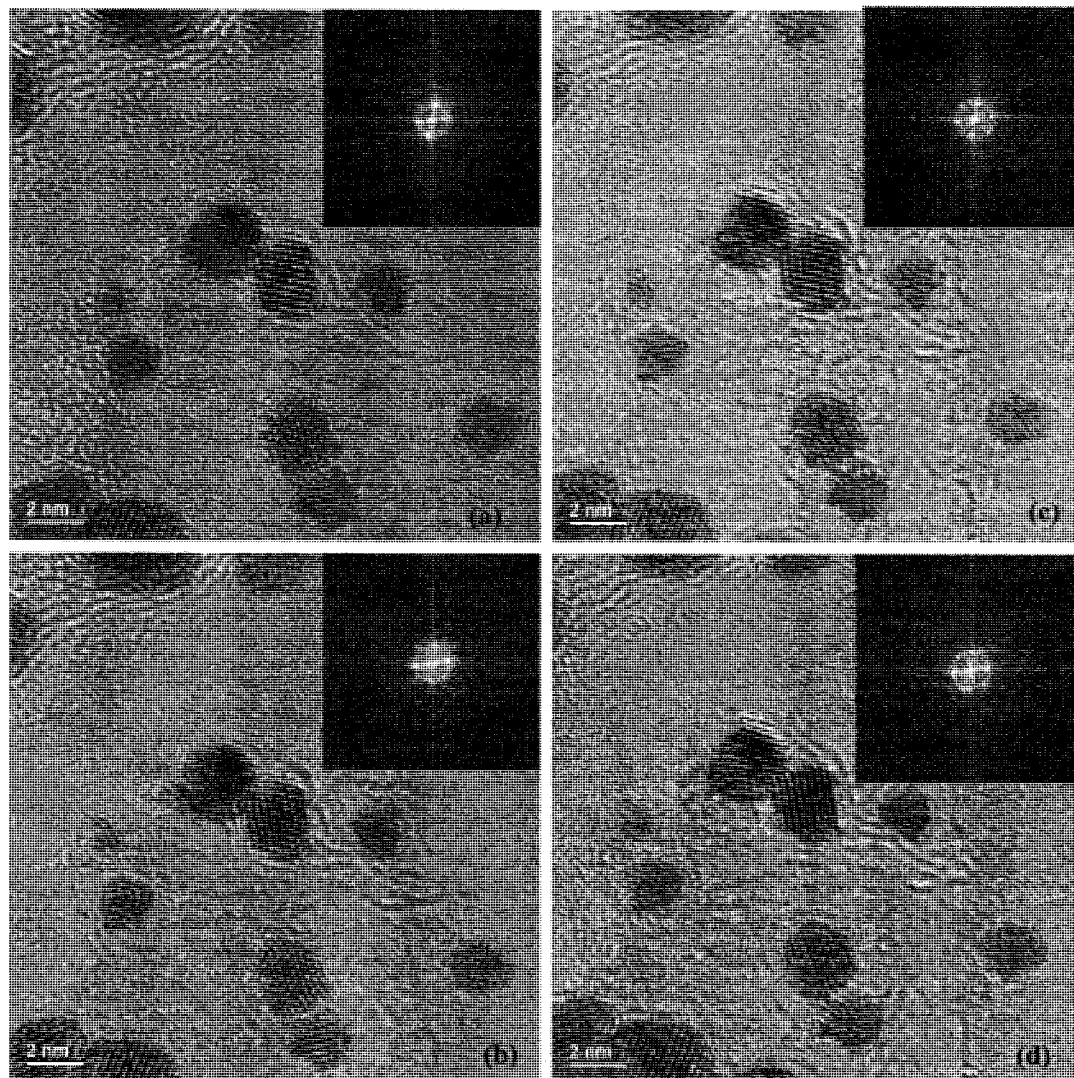
Such a reorganization is demonstrated by the high resolution electron microscope sequence seen in Figure 11. It is but one sequence coming from nominal 0.1 nm thick samples of Pt, evaporated onto freshly cleaved HOPG, and held at 450°C, a temperature essential to supply the energy necessary for the reorganization to be seen over a longer period of time; there are about 5 seconds between each frame. The evolution is characterized by (1) a Pt particle size distribution from ~ 1-2.5 nm, with well-defined, oriented crystals after the initial stage of nucleation and growth, (2) a lack of motion across the HOPG surface, even at 450°C, obviating coalescence, in agreement with the XPS data, as well as (3) changes in the crystalline structure, as demonstrated by the continually changing fast Fourier transforms, inserted as the corresponding electron diffraction patterns.

Discussion

A. Interaction of Pt nanoparticles with the HOPG surface

For the three treatments used here, the $Pt4f_{7/2}$ peak shifts to lower binding energy (Figure 2b) and its FWHM narrows (Figure 3b) with increasing Pt deposition, consistent with the behavior of Pt nanoparticles supported on SiO_2 [9]. This can be attributed to nanoparticle size-dependent (final-state) effects and phonon broadening, as well as broadening induced by inhomogeneities in the nanoparticles. This behavior is similar to that of many other deposited nanoparticles. Judging from the binding energy shifts, their known relationship to nanoparticle sizes, and the known relationship of nanoparticle size to nanoparticle/substrate interaction, we conclude that the interaction of Pt nanoparticles with the substrates used here is in the order: Ar^+-treated > Ar^+-treated and air exposed > untreated. The increase of the C1s FWHM (Figure 3a), and the decrease of the α and

TS asymmetry indices, with increasing Pt deposition indicate phonon broadening and charge transfer from Pt particles to HOPG surface induced by interfacial reaction.

The α asymmetry index, (which we have shown [44] to behave identically to the TS asymmetry index; see also Figure 5), is generally associated with the Pt nanoparticle size [7,9]. The behavior of the TS indices, in Figure 4b, indicates that the Pt nanoparticles deposited onto our samples have the size order: Ar^+-treated < Ar^+-treated and air exposed < untreated, consistent with the conclusions previously drawn from the binding energy shifts.

The C1s line shape undergoes significant changes induced by Pt deposition. The FWHM increases (Figure 3a), and the asymmetry index decreases (Figure 4a), with increasing Pt deposition. The decrease of the asymmetry index is a result of a decrease in the C2 component of the C1s spectrum [44], due to localized (damaged) electron delocalization, and signals that the presence of Pt nanoparticles at these defects heals the previously localized electron delocalization, probably through interfacial interaction. The increase of FWHM with Pt deposition is most probably due to phonon broadening, due to this interfacial interaction. The order of TS asymmetry index values (Figure 4a) implies that the ability to mend the damaged HOPG surface structure is in the order: Ar^+-treated and air exposed > Ar^+-treated > untreated, while the order of the FWHM values (Figure 3a) is that previously found for Pt: Ar^+-treated > Ar^+-treated and air exposed > untreated.

The electronic configuration of zerovalent Pt is $[Xe]\ d^{10}$, with no unpaired electrons. Its interaction with HOPG would then be expected to be similar to that of Ni, which forms back-bonds to defects in the HOPG surface [21]. Indeed, as STM data [14] show, Pt initially nucleates along steps of the untreated HOPG surface, which contain defects,

and does not diffuse laterally [58]; this is similar to the behavior of Ni [21]. The introduction of defects by Ar^{+} treatment increases the surface density of bonding sites, resulting in a higher density of smaller Pt nanoparticles [58]. The reaction of Pt nanoparticles with an Ar^{+}-treated surface that has been exposed to air has previously been shown [58] to be chemical in nature, with hydrogen bonds formed between the oxidized HOPG surface and the surface-oxidized Pt nanoparticle. The unexpected order of Pt nanoparticle interaction with the treated HOPG substrates (i.e., Ar^{+}-treated > Ar^{+}-treated and air exposed, as revealed by our studies), reflects the stronger bonds formed on Pt back-bonding to HOPG free radical defects, introduced on Ar^{+} treatment, than their reaction with the chemical species subsequently introduced on air exposure. These results are consistent with very recent SEM results [59] for Au nanoparticles evaporated onto Ar^{+}-treated HOPG and amorphous carbon (which is similar to Ar^{+}-treatment followed by air exposure): the Au nanoparticle size on Ar^{+}-treated HOPG was found to be smaller than that on amorphous carbon when similar thicknesses were deposited at room temperature.

B. Reorganization of Pt nanoparticle crystallinity on the HOPG surface

The variation of the C1s peak intensity with deposition thickness (Figure 6) and with time (Figure 8a), as well as that of the $Pt4f_{7/2}$ peak with time (Figure 8b), point to changes in the crystalline structure of the Pt nanoparticles while remaining fixed to the substrate. Figure 11 demonstrates such crystallinity changes in Pt nanoparticles. The conditions used were different than those for our XPS observations, in that thermal energy was continually supplied; this was made necessary so as to permit HREM observations over the longer time scale necessitated by sample preparation and insertion into the electron microscope.

We believe that the reorganization is simply the particle shape oscillations we spoke of in our previous paper [60], described by the Frank-Read slip mechanism, here modified by the nanoparticle/substrate interaction already identified in the present work. The energy for this derives from the condensation energy of the Pt nanoparticle (~ 565 kJ/mole), which, until it dissipates into the surroundings, serves to orient the entire nanoparticle; the dissipation time found here is of the same order of magnitude as the time previously found for energy dissipation from Cu nanoparticles subsequent to low energy ion bombardment [61]. Once dissipated, the thermal background permits the Frank-Read mechanism to produce sufficient distortions to randomize the crystalline orientation with respect to the surface.
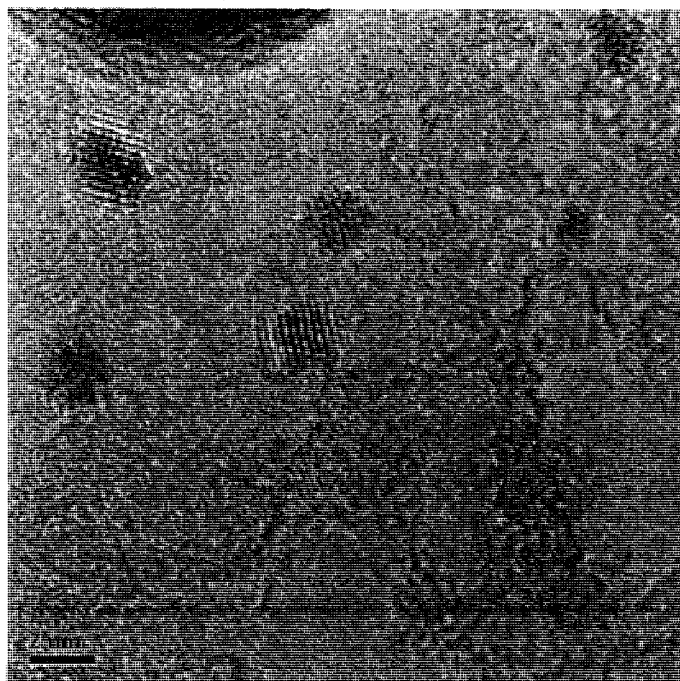

Figure 12. A HREM photomicrograph of a HOPG surface containing Pt nanoparticles, subsequent to 2 h of C^+ perpendicular irradiation at 2 MeV. The nanoparticles have

moved on irradiation, their shapes have been modified and the presence of a moiré pattern gives evidence for graphene layer damage and rotation

The concept of crystalline orientation through energy dissipation is supported by our recent study of the irradiation of Pt nanoparticles in a 2 MeV Pelletron accelerator, using a perpendicular C^+ beam at a flux of 3×10^{15} ions/cm^2/sec; the beam energy is transferred to the Pt nanoparticles through electron stopping. This energy was used to affect motion and crystalline modifications in the nanoparticles, causing noticeable damage to the substrate, before being transferred to the HOPG. By contrast, we have found that the identical irradiation of clean HOPG has little effect, even after 2 h. The presence of Pt nanoparticles is thus the intermediary for the production of substantial changes: (1) the nanoparticles move during irradiation, as energy from the beam is transferred to the Pt and dissipated to the substrate in movement, as previously found [60]; (2) such energy transfer to the substrate leads to damage and rotation in the outer layers of the HOPG, as evidenced by the moiré patterns that appear. Figure 12 shows the results of 2 h of C^+ irradiation; a more detailed account will be published elsewhere.

Conclusions

A systematic XPS core level asymmetry index analysis has been used to characterize Pt nanoparticles on variously treated HOPG surfaces. Our analysis, based on both the size-dependent Pt4f$_{7/2}$ and size-independent C1s spectral features (binding energy shift, FWHM and asymmetry indices), indicates that Pt nanoparticles interact most extensively with the Ar$^+$-treated HOPG surface, and least extensively with the untreated HOPG surface. In all cases, the reaction is sufficiently extensive to bind the Pt nanoparticles and to permit the observation of a crystalline reorganization during the dissipation of the heat of condensation into the surroundings.

Acknowledgments

References and Notes

[1]   Henry, C. R. *Surf. Sci.* **1998**, *31*, 231.

[2]   Binns, C.; Baker, S. H.; Demangeat, C.; Parlebas, J. C. *Surf. Sci.* **1999**, *34*, 105.

[3]   Freund, H.-J. *Surf. Sci.* **2002**, *500*, 271.

[4]   Gates, B. C. *J. Mol. Catal. A* **2000**, *163*, 55.

[5]   Antolini, C. *J. Mater. Sci.* **2003**, *38*, 2995.

[6]   Mason, M. G.; Gerenser, L. J.; Lee, S. T. *Phys. Rev. Lett.* **1977**, *39*, 28.

[7]   Cheung, T. T. *Surf. Sci.* **1984**, *140*, 151.

[8]   Murgai, V.; Raaen, S.; Strongin, M.; Garrett, R. F. *Phys. Rev. B* **1986**, *33*, 4345.

[9]   Eberhardt, W.; Fayet, P. *Phys. Rev. Lett.* **1990**, *64*, 780.

[10] Steve, C.; Chottiner, G. S.; Scherson, D. A.; Pruett, G. *Langmuir* **1990**, *6*, 1316.

[11] Schmidt, A. A.; Eggers, H.; Herwig, K.; Anton, R. *Surf. Sci.* **1996**, *349*, 301

[12] Marcus, P.; Hinnen, C. *Surf. Sci.* **1997**, *392*, 134.

[13] Zoval, J. V.; Lee, J.; Gorer, S.; Penner, R. M. *J. Phys. Chem. B* **1998**, *102*, 1166.

[14] Howells, A. R.; Hung, L.; Chottiner, G. S.; Scherson, D. A. *Solid State Ionics* **2002**, *150*, 53.

[15] Fauth, K.; Hessler, M.; Batchelor, D.; Schütz, G. *Surf. Sci.* **2003**, *529*, 397.

[16] Fauth, K.; Schneider, N.; Hessler, M.; Schütz, G. *Eur. Phys. J. D* **2004**, *29*, 57.

[17] Rheaume, J. M.; Müller, B.; Schulze, M. *J. Power Sources* **1998**, *76*, 60.

[18] Yang, D.-Q.; Sacher, E. *Surf. Sci.* **2002**, *504*, 125.

[19] Yang, D.-Q.; Sacher, E. *Surf. Sci.* **2002**, *516*, 43.

[20] Engelhard, M.; Baer, D. *Surf. Sci. Spectra* **2000**, *7*, 1.

[21] Yang, D.-Q.; Sacher, E. *J. Phys. Chem. B* **2005**, *109*, 19329.

[22] Roy, H.-V.; Fayet, P.; Patthey, F.; Schneider, W.-D.; Delley, B.; Massobrio, C. *Phys. Rev. B* **1994**, *49*, 5611.

[23] Mahan, G. D. *Phys. Rev.* **1967**, *163*, 612.

[24] Nozie`res, P.; de Domenicis, C. T. *Phys. Rev.* **1969**, *178*, 1097.

[25] Doniach, Sÿunjic, M. *J. Phys. C: Solid State Phys.* **1970**, *3*, 285.

[26] Gadzuk, W.; Sÿunjic, M. *Phys. Rev. B* **1975**, *12*, 524.

[27] Anderson, P. W. *Phys. Rev. Lett.* **1967**, *18*, 1049.

[28] Hüfner, S.; Wertheim, G. K. *Phys. Rev. B* **1975**, *11*, 678.

[29] Chiang, S.; Wertheim, G. K.; Di Salvo, F. J. *Solid State Commun.* **1976**, *19*, 75.

[30] Shevchik, N. J. *Phys. Rev. Lett.* **1974**, *33*, 1336.

[31] Dow, J. D.; Franceschetti, D. R. *Phys. Rev. Lett.* **1975**, *34*, 1320. This reference also contains a substantial list of previously published papers challenging the validity of the Mahan process and its application to XPS.

[32] Citrin, P. H. *Phys. Rev. B* **1973**, *8*, 5545.

[33] Hüfner, S.; Wertheim, G. K.; Buchanan, D. N. E. *Chem. Phys. Lett.* **1974**, *24*, 527.

[34] Hüfner, S.; Wertheim, G. K. *Phys. Lett. A* **1975**, *51*, 301

[35] Hüfner, S.; Wertheim, G. K.; Wernick, J. H. *Solid State Commun.* **1975**, *17*, 417.

[36] Wertheim, G. K.; Hüfner, S. *Phys. Rev. Lett.* **1975**, *35*, 53.

[37] Citrin, P. H.; Wertheim, G. K.; Baer, Y. *Phys. Rev. Lett.* **1975**, *35,* 885.

[38] Wertheim, G. K.; Walker, L. R. *J. Phys. F: Met. Phys.* **1976**, *6*, 2297.

[39] Wertheim, G. K. *Phys. Rev. B* **1982**, *25*, 1987.

[40] Minnhagen, P. *Phys. Lett. A* **1976**, *56*, 327.

[41] McManus, M. K.; Cochrane, R. W.; Sacher, E. Unpublished results.

[42] *Gmelin's Handbuch der Anorganischen Chemie*, Kobalt, Teil A Ergäzungsband, Achte Auflage; System-Nummer 58; Verlag Chemie: Weinheim, Germany, 1961; p 34.

[43] Yang, D.-Q.; Sacher, E. Unpublished results.

[44] Yang, D.-Q.; Sacher, E. *Langmuir* **2006**, *22*, 860.

[45] http://www.phy.cuhk.edu.hk/_surface/XPSPEAK/.

[46] Yang, D.-Q.; Poulin, S.; Sacher, E.; Hyett, C. *Appl. Surf. Sci.* **2000**, *165*, 116.

[47] Yang, D.-Q.; Sacher, E. *Appl. Surf. Sci.* **2001**, *173*, 30.

[48] P. M. Th. M. van Attekum, Wertheim, G. K. *Phys. Rev. Lett.* **1979**, *43*, 1896.

[49] Cheung, T. T. P. *J. Appl. Phys.* **1982**, *53*, 6857;

[50] Cheung, T. T. P. *J. Appl. Phys.* **1984**, *55*, 1388

[51] Prince, K. C.; Ulrych, I.; Peloi, M.; Ressel, B.; Cháb, V.; Crotti, C.; Comicioli, C. *Phys. Rev.B* **2000**, *62*, 6866.

[52] Sette, F.; Wertheim, G. K.; Ma, Y.; Meigs, G.; Modesti, S.; Chen, C. T. *Phys. Rev. B* **1990**, *41*, 9766.

[53] Smith, R. A.; Armstrong, C. W.; Smith, G. C.; Weightman, P. *Phys. Rev. B* **2002**, *66*, 245409.

[54] Rao, C. N. R.; Kulkarni, G. U.; Thomas, P. J.; Edwards, P. P. *Chem. Eur. J.* **2002**, *8*, 28.

[55] Egelhoff, W. F., Jr. *Phys. Rev. B* **1982**, *30*, 1052; *J. Vac. Sci. Technol., A* **1985**, *3*, 1511.

[56] Armstrong, R. A.; Egelhoff, W. F.; Jr. *Surf. Sci.* **1985**, *154*, L225.

[57] Yang, D.-Q.; Sun, Y.; Da, D. A. *Appl. Surf. Sci.* **1999**, *144-145*, 451.

[58] Yang, D.-Q.; Sacher, E. *Chem. Mater.* **2006**, *18*, 1181.

[59] Büttner, M.; Oelhafen, P. *Surf. Sci.* **2006**, *600*, 1170.

[60] José-Yacamán, M.; Gutierrez-Wing, C.; Miki, M.; Yang, D.-Q.; Piyakis, K. N.; Sacher, E. *J. Phys. Chem. B* **2005**, *109*, 9703.

[61] Yang, D.-Q.; Sacher, E. *Surf. Sci.* **2003**, *536*, 67.

Appendix B

It is generally acknowledged that both catalytic efficiency and selectivity are highly dependent on the size and shape of the PEMFC catalyst material (e.g. Pt). Therefore, the synthesis of platinum with specific nanostructures has become an area of considerable interest. To date, a range of techniques has been developed for preparing nanostructured Pt. Most of these studies have been limited to nanoparticles obtained by using a variety of chemical procedures that involve the presence of organic surfactants at elevated temperatures. Therefore, with respect to the procedures and materials used, the production of Pt catalysts with high surface area for great catalytic performance and utilization efficiency is still costly and far from being trivial.

Here, we demonstrate a facile, efficient, and economical route for the large-scale synthesis of 3D flower-like Pt nanostructures via a simple chemical reduction reaction, at room temperature, using neither template nor surfactant. The synthesized Pt nanoflowers consist of large quantities of single-crystal nanowires. Moreover, the nanoflowers could be assembled *in-situ* onto carbon fiber paper during the reduction process, where carbon paper was used as the fuel cell charge-collecting electrode. Electrodes modified with these Pt nanoflowers exhibit good electrocatalytic activities implying potential adoption in PEM fuel cells.

Template-free, Surfactant-free Room Temperature Synthesis of Self-Assembled 3D Pt Nanoflowers from Single-Crystal Nanowires

Shuhui Sun,[a] Dequan Yang,[b] Dominique Villers,[a] Gaixia Zhang,[b] Edward Sacher,[b] and Jean-Pol Dodelet[a]

[a] INRS, Énergie, Matériaux et Télécommunications, Varennes, QC J3X 1S2, Canada

[b] Département de Génie Physique, École Polytechnique, Montréal, QC H3C 3A7,

Canada

Platinum has stimulated extensive research due to its unusual physical and chemical properties; this has led to many technological applications, such as chemical sensors [1,2] and biosensors [3], as catalysts in the production of hydrogen from methane [4] and in the reduction of pollutant gases emitted from automobiles [5] and, particularly, as electrocatalysts in polymer electrolyte membrane (PEM) fuel cells [6,7]. It is generally accepted that both catalytic efficiency and selectivity are highly dependent on the size and shape of the platinum material. Therefore, the synthesis of platinum with specific nanostructure has become an area of considerable interest [8-10].

To date, a range of techniques has been developed for preparing nanostructured platinum. Most of these studies have been limited to nanoparticles that could be obtained by using a variety of chemical procedures [11-13]. In general, such methods involve the reduction of platinum salts in the presence of organic surfactants or polymeric stabilizers at elevated temperature. The channels of porous materials [14], self-assembled structures of surfactant [15], as well as Se nanowires [16], have been used as templates to synthesize platinum nanowires or nanotubes. Template-based methods are technically complicated, due to requirements for template removal to obtain pure products. This limits their applications, to some extent [17]. Recently, Xia and co-workers have demonstrated the synthesis of single crystalline platinum nanowires by a polyol process, combined with the introduction of a trace amount of Fe^{2+} or Fe^{3+}; poly(vinyl pyrrolidone) (PVP) was used as a surfactant, and the reaction was carried out at 110 °C

[18]. Despite this, the development of mild, template-free, surfactant-free routes for the production of single crystalline platinum nanowires remains a challenge.

Here, we demonstrate a facile, efficient, and economical route for the large-scale synthesis of 3D flower-like platinum nanostructures via a simple chemical reduction of hexachloroplatinic acid, commonly used for this purpose, with formic acid, at room temperature, using neither template nor surfactant. Reduction took place by the following chemical reaction:

$$H_2PtCl_6 + 2HCOOH \longrightarrow Pt + 6Cl^- + 6H^+ + 2CO_2 \uparrow$$
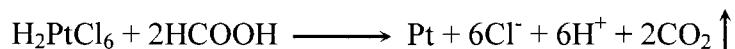
Briefly, H_2PtCl_6 is mixed with HCOOH in aqueous solution at room temperature and atmospheric pressure, and the mixture is then stored under the same conditions for periods up to 16 h, which permits Pt nanoflowers to form. The synthesized Pt nanoflowers consist of large quantities of single-crystal nanowires. Moreover, the nanoflowers could be assembled *in-situ* onto carbon paper during the reduction process, and used as fuel cell charge-collecting electrodes. Assembly takes place through a self-organization process, without surface functionalization of the carbon support. Electrodes modified with these Pt nanoflowers exhibit good electrochemical activities implying potential adoption in PEM fuel cells.

The structure and morphology of these Pt nanoflowers were investigated by scanning electron microscopy (SEM). Figure 1a shows the overall morphology of the sample, which indicates that the product obtained consists of large quantities of flower-like structures with diameters in the range of 150–400 nm. The enlarged SEM image shown in Figure 1b reveals that numerous nanowires, with lengths of 100–200 nm, assemble into 3D flower-like superstructures. Platinum nanoflowers can further assemble, forming
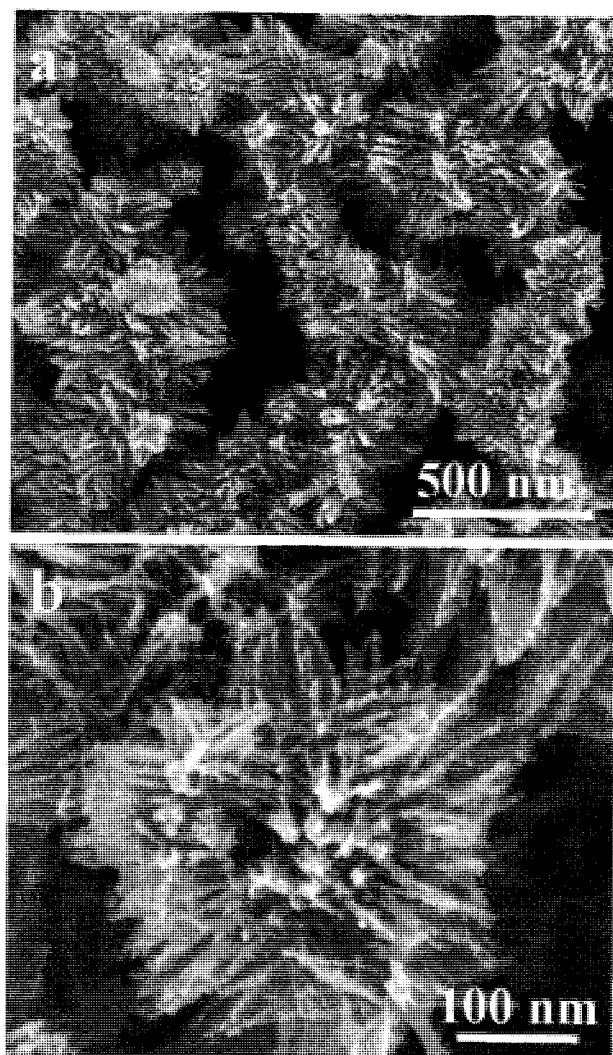
Figure 1. SEM photomicrographs of Pt nanoflowers composed of nanowires.

more complex hierarchical nanostructures, as shown in Figure 1a. Both EDS and XPS characterizations established that the flower-like nanostructures are composed of metallic platinum (see Figures S1 in the Supporting Information). High resolution Pt4f spectra were deconvoluted into one asymmetric doublet (Figure S1b), as has been

reported [19]. The asymmetry indices (TS=0.4 and TL=130) obtained using the public domain XPSPeak program, to be described in the Experimental section, are consistent with those for evaporated Pt nanoparticles on HOPG, in ultrahigh vacuum [19a]. The Pt4f$_{7/2}$,4f$_{5/2}$ binding energies are 71.4 and 74.7 eV, which are in good agreement with those of pure bulk platinum [20]. In addition, no obvious shoulders at higher binding energies, representing Pt^{2+} and Pt^{4+}, were found, and no trace of chlorine from the Pt precursor could be detected by XPS (Figure S1c). Based on these analyses, we believe that the Pt nanoflowers are composed of metallic Pt nanowires.

The nanoflowers were further characterized by transmission electron microscopy (TEM). Figure 2a shows a typical example of nanoflower morphology, which confirms the SEM results. Figure 2b shows an enlarged image of the portion indicated by the white square in Figure 2a. It is clear that the basic Pt nanowires have relatively uniform diameters along their lengths, except for slightly larger tips, with an averaged length of about 120 nm. Selected-area electron diffraction (SAED) patterns for the Pt nanowires reveal several bright concentric rings (Figure 2c), which are attributable to {111}, {200}, {220} and {311} Pt face-centered-cube (fcc) crystal diffractions. This confirms that the platinum nanowires synthesized by this method are crystallized in a phase similar to bulk Pt [18]. This conclusion is also supported by the XRD pattern (Figure S2, Supporting information), which was taken from the Pt nanowires deposited on carbon fiber support. Figure 2d shows the HRTEM image of a single Pt nanowire with a diameter of about 4 nm. The nanowire has grown along the <111> direction, and the distance between the {111} planes is 0.225 nm, which is in agreement with that found for bulk Pt crystals.
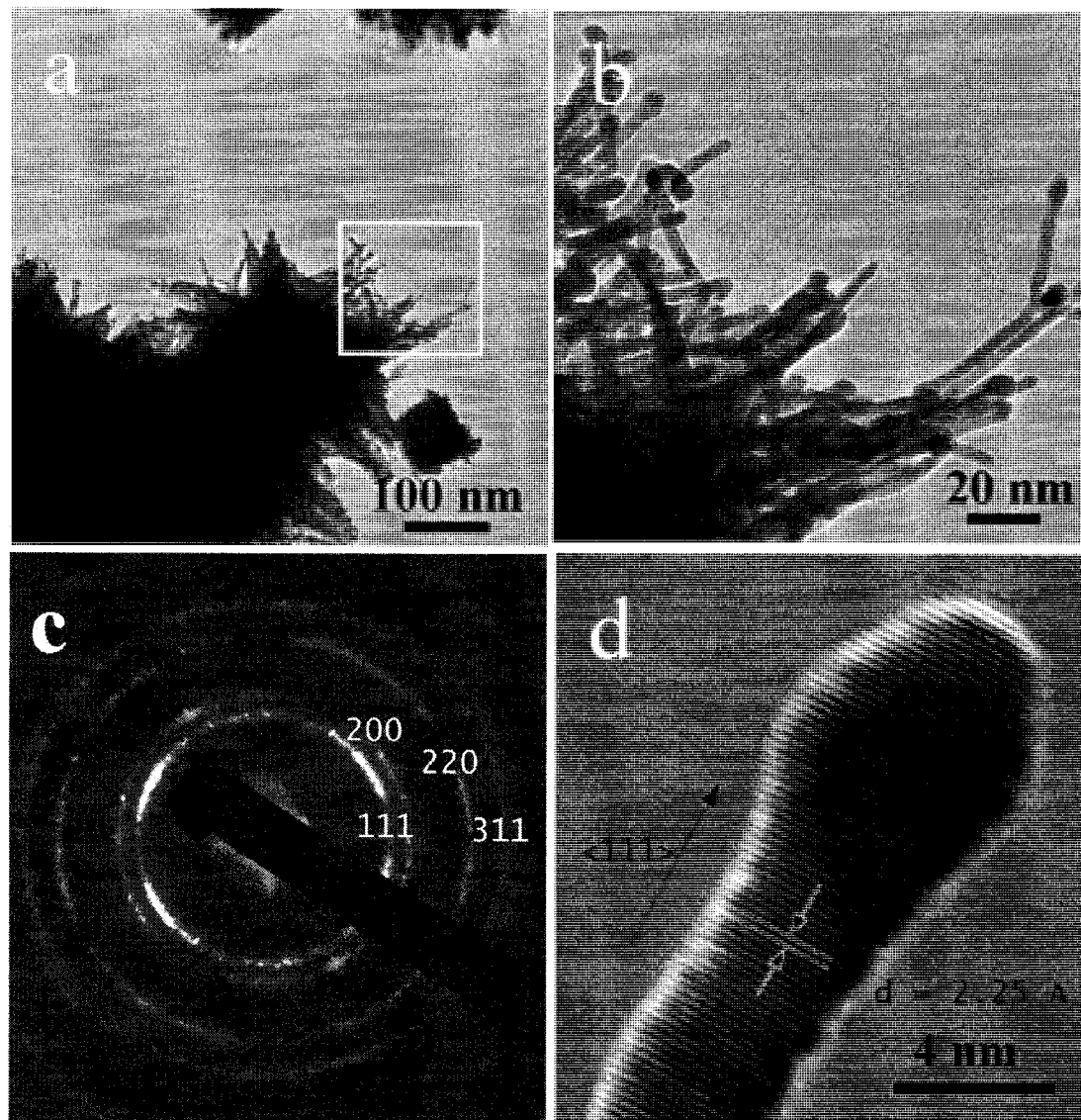
Figure 2. a) Low-magnification TEM photomicrograph of Pt nanoflower structure; b) enlarged TEM photomicrograph of the edge of a nanoflower; c) selected-area electron diffraction patterns of nanowires; d) HRTEM photomicrograph of the tip of an individual Pt nanowires, indicating that it to be a single crystal, with its growth direction along the <111> axis.

We investigated the effect of reaction temperature on the morphology of the nanostructures. When the synthesis was performed at 80 °C, the reduction was much faster than at room temperature, with the reacting system turning black within 15 min, and only individual nanoparticles forming. Figure 3 shows a representative TEM image of the nanoparticles, which reveals that they are very uniform in diameter, with a mean size of about 4 nm; some particles appear to have coalesced to form aggregates. No nanowires were formed, even when the solution was heated at 80 °C for several hours. The same results were also obtained at 50 °C. These observations indicate that a more rapidly reduction at higher temperature favors the formation of nanoparticles, suppressing the growth of nanowires.
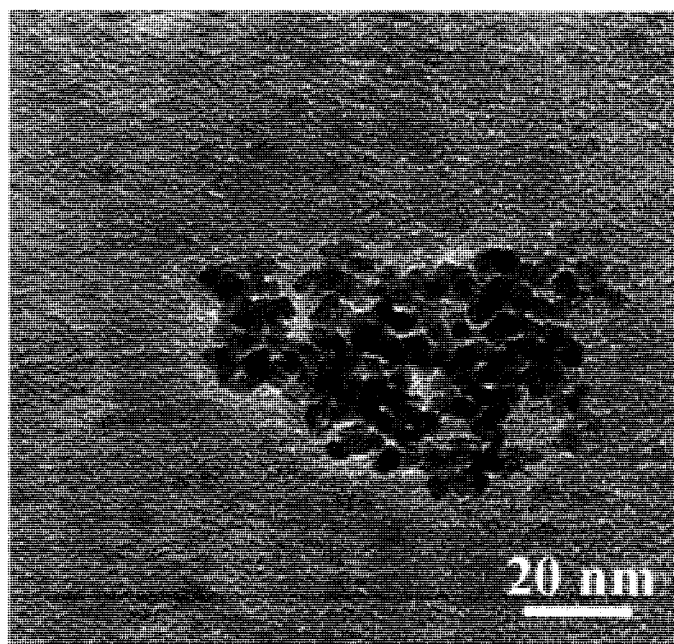

Figure 3. TEM photomicrograph of Pt nanoparticles obtained in solution at 80 °C.
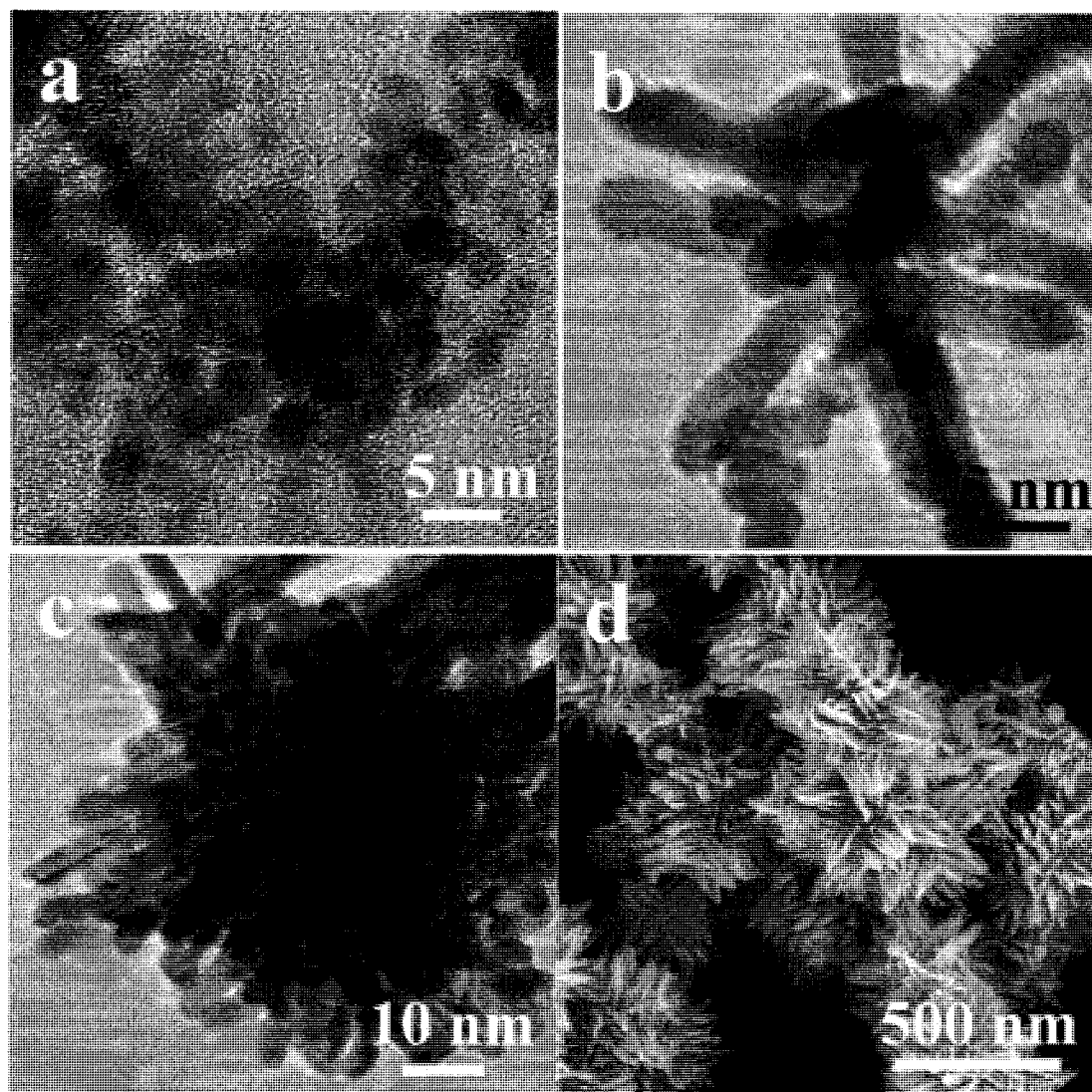
Figure 4. TEM and SEM photomicrographs of Pt nanoflowers collected at various times after mixing the two solutions: a) 4, b) 8, c) 12, and d) 16 h.

For a complete view of the nanoflower formation process and their growth mechanism, a morphological evolution study was conducted over an extended period of time at room temperature. Products were collected from the reaction solution as a function of time,

and their morphologies were evaluated by TEM and SEM. As shown in Figure 4, when a sample is collected after 4 h of reaction, the product is composed of Pt nanoparticles about 3 nm in size, which begin to aggregate (Figure 4a); after 8 hours, short nanowires (mean length, 10 nm) are formed (Figure 4b); after 12 h, the Pt nanowires grow longer (up to 30 nm) and begin to form small nanoflowers (Figure 4c). Finally, after 16 h, contiguous nanoflowers, composed of nanowires up to 100–200 nm in length, form the structures shown in Figure 4d.

A schematic illustration for the evolution of Pt nanostructures, based on the SEM and TEM results, is presented in Figure 5. First, Pt nanonuclei are formed in solution through the reduction of H_2PtCl_6. The freshly formed nuclei are thermodynamically unstable, because of their high surface energy, and they tend to aggregate, driven by the minimization of interfacial energy [21]. As the reaction is conducted at room temperature, the reduction rate is very slow, and anisotropic growth is favored because, for fcc structures, the order of surface energies is (111) < (100) < (110) [22]. Therefore, according to the Lowest Energy principle, the growth rate along the closed-packed <111> direction is enhanced. The key to synthesize the Pt nanowires is to reduce the rate of Pt ion reduction, favoring the growth of {111} planes, and leading to the formation of 1D nanowires [14b]. The short nanowires agglomerate and continue to grow, forming the flower-like nanostructures that are found. These nanoflowers can agglomerate further, forming more complex hierarchical architectures. On the other hand, when the reaction is carried out at 80 °C, the reduction proceeds much quickly, and large amounts of Pt nuclei are formed simultaneously. Under these conditions, only isotropic Pt nanoparticles are produced [23].
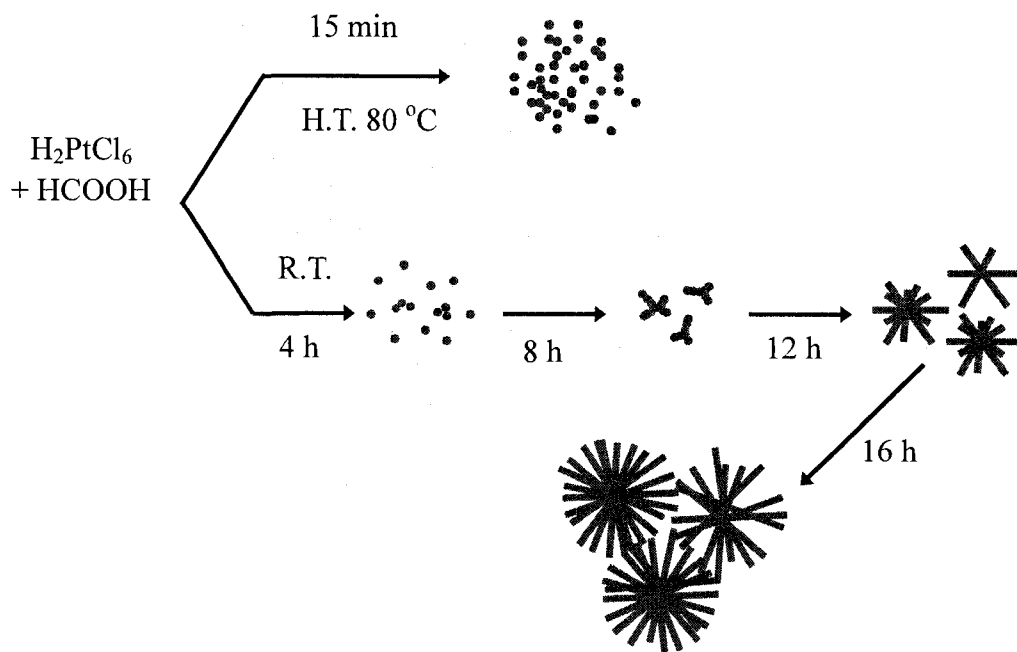
Figure 5. Schematic illustration of the formation and shape evolution of Pt nanostructures.

The Pt nanowires may be deposited onto carbon paper, which can be used in fuel cells as the charge-collecting electrode. On deposition, they form 3D nanoflowers through a self-organization process, without any functionalization of the carbon paper support. Figure 6a shows a low-magnification SEM image of porous carbon paper loaded with Pt. The carbon paper is seen to be composed of fibers with diameters of about 5 μm. A medium-magnification SEM image (Figure 6b) indicates that a large number of nanoflowers, with sizes similar to those synthesized directly in solution, densely cover the whole surface of the carbon fiber. A high-magnification SEM image (Figure 6c) shows that the nanoflowers assemble along the carbon fiber, forming 3D Pt nanostructures, similar to what was obtained without a carbon support (Figure 1).
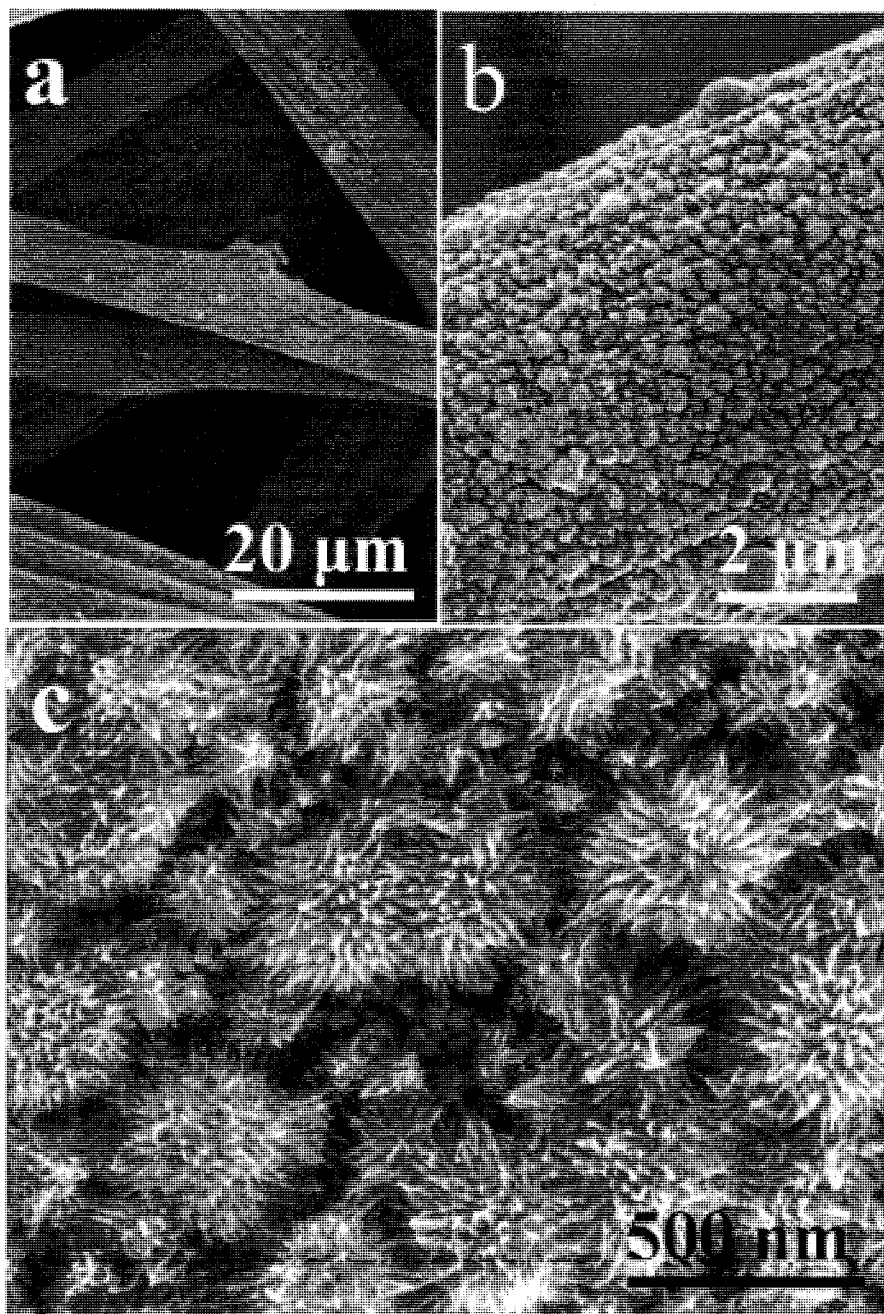
Figure 6. SEM photomicrographs of Pt nanoflowers deposited *in-situ* onto carbon paper.

Electrochemical responses were obtained, in deaerated H_2SO_4 solution, for both a Pt nanoflower-grafted carbon paper electrode and, for comparison, pristine carbon paper. As can be seen from the cyclic voltammograms in Figure 7, the pristine carbon paper electrode shows a current due only to carbon capacitance, whereas the Pt nanoflower-grafted carbon paper electrode shows strong peaks characteristic of hydrogen electrosorption below 0 V, and both typical Pt oxide formation and its reduction above it. Multiple peaks for hydrogen adsorption and desorption, rather than a single broad peak, are indicative of multiple exposed crystallographic planes. The charge value (Q_H) measured under the electroadsorption curve for hydrogen is 34.5 mC/cm^2. Neutron activation analysis reveals that the Pt nanoflower loading is 0.166 mg/cm^2, giving 207.9 mC/mg Pt. This is to be compared with a typical commercial product, a 0.40 mg Pt/cm^2 $ELAT^®$ commercial electrode, giving a Q_H value of 82 mC/cm^2 and 205 mC/mg Pt. Using the Q_H value and Pt loading, it is possible to calculate the electrochemical active surface of Pt on carbon paper, as:

$$S_{EL} = Q_H / (Q_{ref} \times Pt \ Loading)$$

S_{EL} is obtained in cm^2/mg when the Pt loading is in mg/cm^2; Q_{ref} = 0.21 mC/cm^2, corresponding to a surface density of 1.3×10^{15} Pt atoms per cm^2, is generally accepted for polycrystalline Pt electrodes [24].

A value of S_{EL} = 99 m^2/g is obtained for Pt nanoflowers on carbon paper, while S_{EL} = 97.6 m^2/g for the $ELAT^®$ commercial product. This indicates that more Pt is available electrochemically at the Pt nanoflowers/carbon paper surface than at the surface of the commercial electrode. These results indicate the promising potential of using Pt nanoflower-modified carbon paper as efficient electrodes in PEM fuel cells and, perhaps, in other electrochemical systems.
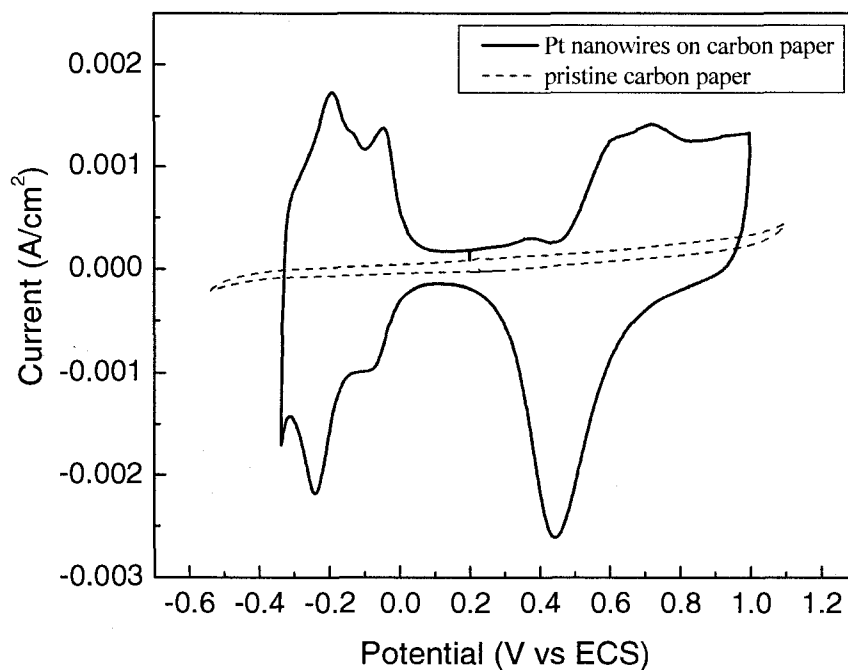
Figure 7. Cyclic voltammetry of Pt nanoflowers deposited onto carbon paper (solid line) and pristine carbon paper (dash line), measured at a scan rate of 10 mV/s, in deaerated H_2SO_4, at pH 1.

In summary, we have developed a facile procedure to synthesize 3D Pt superstructures, in which the large-scale assembly of nanoflowers, composed of single-crystal nanowires, occurs at room temperature, without surfactant or template. The nanoflowers adhere to carbon paper, exhibiting an enlarged electroactive surface area comparable to that of a commercial Pt/C electrode. More detailed electrochemical evaluations of the Pt nanoflowers are in progress, with the aim of optimizing the use of these electrodes in PEM fuel cells and in other electrochemical applications.

Experimental

In a typical synthesis, 0.032 g Hexachloroplatinic acid ($H_2PtCl_6 \cdot 6H_2O$, Aldrich) and 1 ml formic acid (HCOOH, Aldrich) were added simultaneously to 20 ml H_2O at room temperature. All aqueous solutions were prepared with ultrapure water from a Barnstead Nanopure water system. The reactions were conducted at room temperature up to 16 h and at 80 °C for 15 min, the solutions turning from golden orange to dark brown. For the Pt self-attachment to carbon fibers, a piece of carbon paper (E-TEK, 0.17 mm thick, 81% porosity) was immersed in the solution at room temperature.

The morphology and structure of the hierarchical nanostructures synthesized were characterized by field emission scanning electron microscopy (FESEM, Hitachi S-4700, operating at 5 kV), and by transmission electron microscopy (TEM, JEOL 2100F, operating at 200 kV). For SEM observations, a drop of the nanoflower dispersion was placed on a silicon wafer and dried under ambient conditions. For TEM observations, a drop of dispersion taken from different reaction stages was placed on a carbon film-coated copper grid, followed by solvent evaporation under ambient conditions. XRD patterns were recorded on a Bruker D8 Advance diffractometer equipped with a Cu-Kα radiation source. X-ray photoelectron spectroscopic (XPS) analysis was carried out in a VG ESCALAB 220iXL, using monochromated Al Kα source (1486.6 eV), at a base pressure of 2×10^{-9} mbar. High resolution spectra were obtained at a perpendicular take-off angle, using a pass energy of 20 eV and steps of 0.05 eV. All the binding energies were calibrated by placing the C1s line of adventitious hydrocarbon at 284.8 eV [25]. After Shirley background removal, the component peaks were separated using the public domain XPSPeak program version 4.1[26].

The electrochemical properties of the Pt/carbon paper composite were investigated by cyclic voltammetry in a standard three-electrode cell at room temperature. A Pt foil served as the counter electrode, with a saturated calomel electrode (SCE) as the reference. Cyclic voltammetry measurements were carried out on a 273A EGG Potentiostat, using a 10 mV/s sweep rate. A H_2SO_4 solution, at pH 1, purged with N_2, was used to perform the voltammetry on the Pt/carbon paper. The amount of Pt in contact with the electrolyte was measured by integration of the charge related to the H-adsorption in the cyclic voltammogram recorded at 10 mV/s.

Acknowledgments

References

[1] R. F. Service, *Science* **1999**, *285*, 682.

[2] K. V. Kordesch, G. R. Simader, *Chem. Rev.* **1995**, *95*, 191.

[3] S. Hrapovic, Y. L. Liu, K. B. Male, J. H. T. Luong, *Anal. Chem.* **2004**, *76*, 1083.

[4] A. T. Bell, *Science* **2003**, *299*, 1688.

[5] A. Rouxoux, J. Schulz, H. Patin, *Chem. Rev.* **2002**, *102*, 3757.

[6] E. Antolini, Mater. *Chem. Phys.* **2003**, *78*, 563.

[7] D. R. Rolison, *Science* **2003**, *299*, 1698.

[8] Y. J. Song, W. A. Steen, D. Pena, Y. B. Jiang, C. J. Medforth, Q. S. Huo, J. L. Pincus, Y. Qiu, D. Y. Sasaki, J. E. Miller, J. A. Shelnutt, *J. Am. Chem. Soc.* **2004**, *126*, 635.

[9] R. Narayanan, M. A. El-Sayed, *J. Phys. Chem. B* **2004**, *108*, 5726.

[10] R. Narayanan, M. A. El-Sayed, *J. Am. Chem. Soc.* **2004**, *126*, 7194.

[11] F.Mirkhalaf, J. Paprotny, D. J. Schiffrin, *J. Am. Chem. Soc.* **2006**, *128*, 7400.

[12] T. S. Ahmadi, Z. L. Wang, T. C. Greem, A. Heglein, M. A. El-Sayed, *Science* **1996**, *272*, 1924.

[13] H. Bönnemann, K. S. Nagabhushana, *J. New.Mat. Electrochem.Systems.* **2004**, *7*, 93.

[14] a)Y. Han, J. Kim, G. D. Stucky, *Chem. Mater,* **2000**, *12*, 2068; b) Y. Sakamoto, A. Fukuoka, T. Higuchi, N. Shimomura, S. Inagaki, M. Ichikawa, *J. Phys. Chem. B* **2004**, *108*, 853; c) Z. Liu, Y. Sakamoto, T. Ohsuna, K. Hiraga, O. Terasaki, C. H. Ko, H. J. Shin, R. Ryoo, *Angew. Chem. Int. Ed.* **2000**, *39*, 3107; d) A. Husain, J. Hone, H. W. C. Postma, X. M. H. Huang, T. Drake, M. Barbic, *Appl. Phys. Lett.* **2003**, *83*, 1240.

[15] T. Kijima, T. Yoshimura, M. Uota, T. Ikeda, D. Fujikawa, S. Mouri, *Angew. Chem. Int. Ed.* **2004**, *43*, 228.

[16] B. Mayers, X. Jiang, D. Sunderland, B. Cattle, Y. Xia, *J. Am. Chem. Soc.* **2003**, *125*, 13364.

[17] H. P. Liang, H. M. Zhang, J. S. Hu, Y. G. Guo, L. J. Wan, C. L. Bai, *Angew. Chem. Int. Ed.* **2004**, *43*, 1540.

[18] J. Y. Chen, T. Herricks, M. Geissler, Y. N. Xia, *J. Am. Chem. Soc.* **2004**, *126*, 10854.

[19] a) D. Q, Yang, G. X. Zhang, E. Sacher, *J. Phys. Chem. B* **2006**, *110*, 8348; b) P. Gouérec, M. C. Denis, D. Guay, J. P. Dodelet, R. Schulz, *J. Electrochem. Soc.* **2000**, *147*, 3989.

[20] P. Marcus, C. Hinnen, *Surf. Sci.* **1997**, *392*, 134.

[21] C. Z. Wu, Y. Xie, L. Y. Lei, S. Q. Hu, Z. Z. Ouyang, *Adv. Mater.* **2006**, *18*, 1727.

[22] J. D. Hoefelmeyer, K. Niesz, G. A. Somorjai, T. D. Tilley, *Nano Lett.* **2005**, 5, 435.

[23] T. Teranishi, M. Hosoe, T. Tanaka, M. Miyake, *J. Phys. Chem. B* **1999**, *103*, 3818.

[24] R. Woods, *J. Electrochem. Soc.* **1976**, *9*, 1.

[25] Moulder, J. F.; Stickle, W. F.; Sobol, P. E.; Bomben, K. D. in *Handbook of X-ray Photoelectron Spectroscopy* (Ed: J. Chastain), PERKIN-ELMER CORP., MN, **1992.**

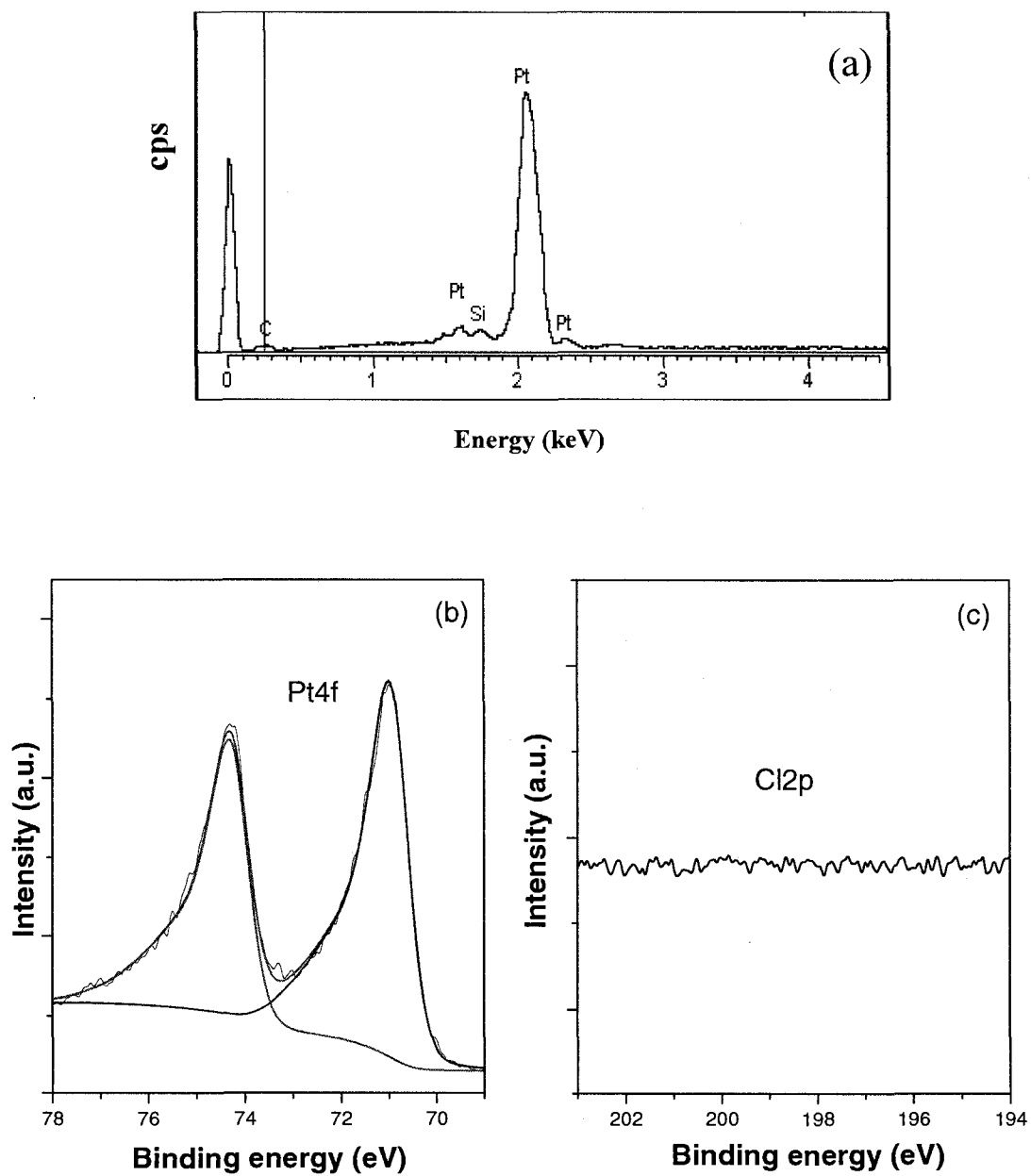[26] http://www.phy.cuhk.edu.hk/~surface/XPSPEAK/

Supporting Figures

Figure S1. a) EDS, and b) Pt 4f and c) Cl 2p XPS spectra of Pt nanoflowers.
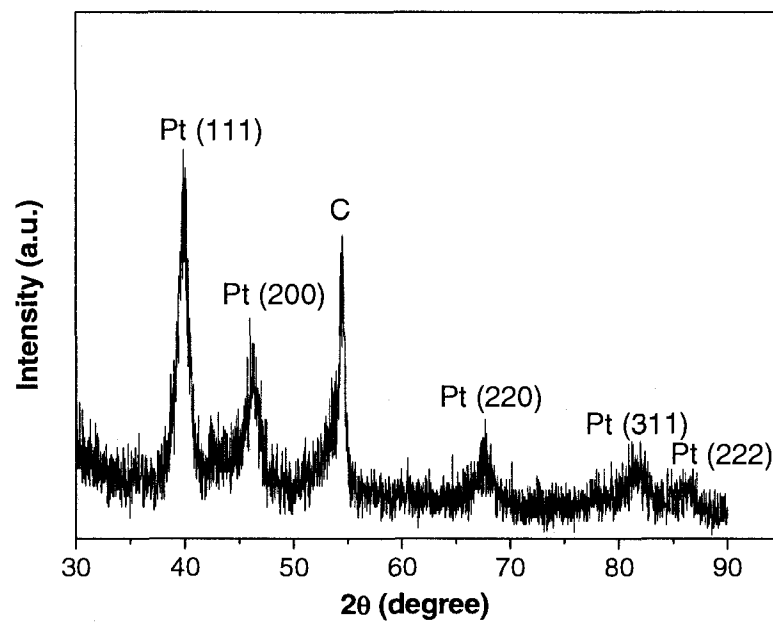
Figure S2. A typical X-ray diffraction pattern of the Pt nanoflowers grown on carbon paper, showing characteristic crystalline faces of Pt. The C peak is from the carbon fiber.

Appendix C

Carbon nanotubes (CNTs) are of particular interest because of their unique geometric morphologies (high aspect ratios and surface areas), as well as the remarkable electronic, thermal, and the mechanical properties intrinsically associated with CNTs. The synthesis of heterojunctions of Pt nanostructures with CNTs is anticipated to extend the possibilities of both nanostructures for potential applications. Although the growth of Pt nanoparticles on CNT has been studied extensively, the direct growth of single-crystalline Pt nanowire–CNT (NW–CNT) heterojunctions remains a big challenge.

Here, as a continuing part of our research effort, we demonstrate a cost-effective procedure for growing single-crystalline Pt NWs on high-surface-area pristine MWCNTs, which are commonly used as electrocatalyst supports in fuel cells, at room temperature in aqueous solution, forming Pt NW–CNT heterojunctions. Moreover, the surface density of Pt NWs on the MWCNTs can be effectively controlled through the proper choice of the concentration ratio of MWCNTs and the Pt precursor; we can obtain very high Pt loadings on CNTs, comparing to evaporated Pt nanoparticles on CNTs. These heterojunction nanostructures promise potential applications, not only in electrocatalyst for fuel cells, but also in electronic, photonic, and sensing nanodevices. We believe that our findings will have a significant impact in the fields susceptible to use Pt and CNT nanostructures.

Synthesis and Characterization of Carbon Nanotube–Platinum Nanowire Heterostructures

Shuhui Sun,[a] Dequan Yang,[b] Gaixia Zhang,[b] Edward Sacher,[b] and Jean-Pol Dodelet[a]

[a] INRS, Énergie, Matériaux et Télécommunications, Varennes, QC J3X 1S2, Canada

[b] Département de Génie Physique, École Polytechnique, Montréal, QC H3C 3A7, Canada

Composite nanostructures are important to both an understanding of scientific fundamentals in nanoscience and to potential applications in nanoscale systems, because of their many desirable properties, which can be tailored by fine-tuning the composition, morphology, size, and organization patterns of the primary nanobuilding blocks [1]. Accordingly, considerable effort has been made, in recently years, to fabricate nanocomposites with core–shell [2], coaxial nanocable [3], and one- and two-dimensional (1D and 2D) heterojunction structures [4]. In particular, the assembly of 1D nanostructures containing different materials is important for many electronic, optoelectronic, and sensing applications [5-11]. Various 1D heterostructures have been reported; examples include the synthesis of hierarchical $ZnO-In_2O_3$ nanostructures using an evaporation method [5], aligned ZnO heterojunction arrays on GaN, $Al_{0.5}Ga_{0.5}N$, and AlN substrates by a vapor–liquid–solid (VLS) process [6], $Si-SiO_2$ hierarchical heterostructures by using self-assembly and VLS methods [7], hierarchical W nanothorn arrays on WO_3 nanowhiskers by a two-step evaporation process [8], MWCNT–ZnS

heterojunctions by a combination of ultrasonic and heat treatment [9], CNT–Si nanowire heterojunctions by a VLS process [4a], a-CNT–Ag nanowire heterojunctions by a combination of electrochemical deposition and chemical vapor deposition (CVD) [10], and SWCNT–Au nanorod 1D heterojunctions through the selective solution growth of Au nanorods on SWCNT [11]. Among them, CNT-based heterostructures are of particular interest because of their unique geometric morphologies (high aspect ratios and surface areas), as well as the remarkable electronic, thermal, and the mechanical properties intrinsically associated with CNTs [12]. Pt nanostructures are shown to possess novel physical and chemical properties useful in chemical sensors [13] and biosensors [14], catalytic applications [15] and, particularly, as electrocatalysts in polymer electrolyte membrane (PEM) fuel cells [16]. The large-scale formation of heterojunctions of Pt with other nanomaterials (particularly CNTs) is anticipated to extend the possibilities of Pt nanostructures for potential applications. Although a variety of Pt nanostructures, including particles [17], tubes [18], wires [19], dendritic structures [20], and multipods [21], have been studied extensively, the formation of single-crystal Pt nanowires (Pt NWs) has been the subject of fewer studies [19a,c]. In particular, the direct growth of single-crystalline Pt NW–CNT heterojunctions remains a big challenge.

In this communication, we describe a cost-effective and efficient approach for the large-scale synthesis heterojunctions between single-crystalline Pt nanowires (Pt NWs) and multiwalled CNTs (MWCNTs), through their contact in the absence of prior CNT functionalization. Our work represents a new type of heterostructure with many benefits. First, the procedure is very simple and can be performed at room temperature, using commercially availably reagents, without the need for templates or potentiostats. Second, no CNT functionalization process, in which harsh oxidizing acids are used to produce

carboxylic acid sites on the surface, is required, thus preserving the electronic structure of the CNTs. Third, Pt NWs are grown directly onto the surfaces of the CNTs, without using any ligands or protecting groups; this both simplifies the synthesis and permits good mixing, with better interfacing between the two nanophases. Fourth, the process is carried out in an environmentally benign aqueous solution. Fifth, the surface density of Pt NWs on the MWCNTs can be effectively controlled through the proper choice of the concentration ratio of MWCNTs, serving as cores, and the Pt precursor. Sixth, there are many potential applications for these structures; for example, Pt NWs will serve as tiny, reproducible, electrical contacts for integrating MWCNTs in electronic, photonic, and sensing nanodevices, while metal nanostructures of various shapes, supported on MWCNTs, will be useful in both electrocatalysis and electrochemical sensing applications.

Scanning electron microscopy (SEM) was employed to characterize the morphologies of the products. A typical photomicrograph of the nanostructures is shown in Figure 1a; it reveals that many nanowires, shaped like thorns, have grown on the CNT stems. The powder X-ray diffraction (XRD) pattern, shown in Figure 1b, reveals that the Pt NWs crystallized in a face-centered cubic (fcc) structure similar to bulk Pt.

Transmission electron microscopy (TEM) was used to determine further details of the hetero-nanostructures. Numerous Pt NWs, with lengths in the 10–30 nm range, were found to have grown over the entire carbon nanotube surface, forming well-ordered heterostructures (Figure 2a). Some Pt nanowires have assembled into 3D flower-like superstructures on carbon nanotubes. An enlarged section of the image, shown in Figure 2b, indicates that the nanowires grew radially, on the surface of MWCNTs, with diameters of 3–4 nm. Selected-area electron diffraction (SAED) patterns reveal several
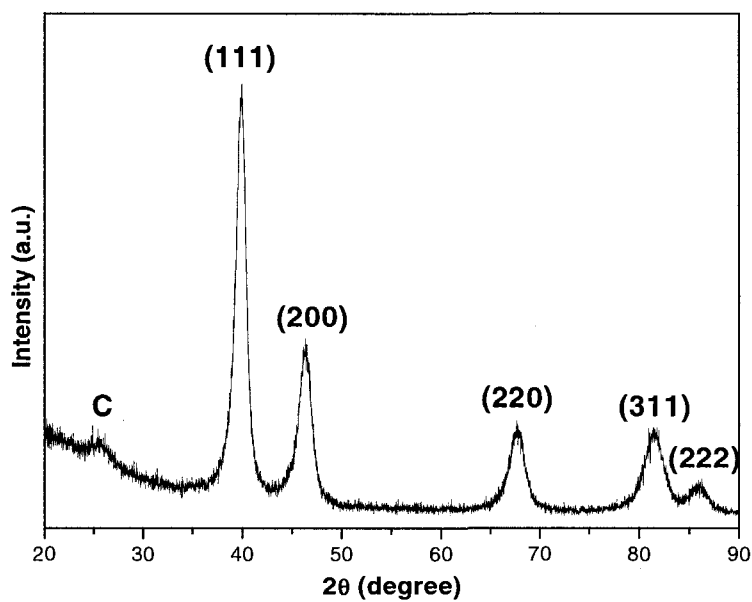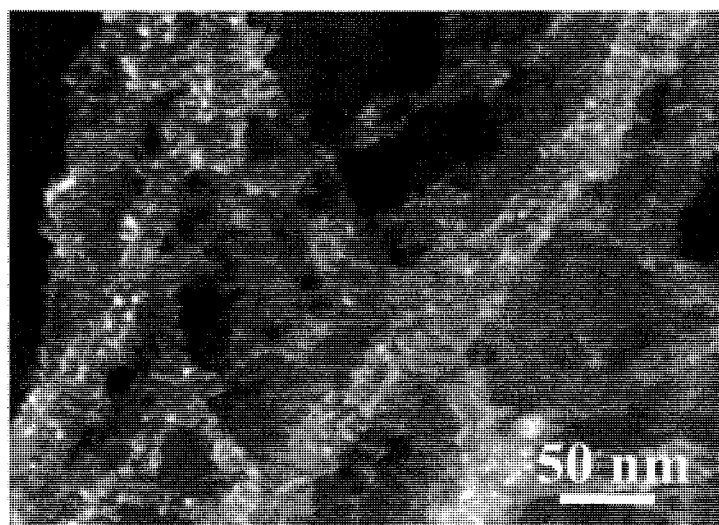
Figure 1. (a) SEM image of Pt NW–MWCNT heteronanostructures. (b) XRD pattern of the Pt nanowires grown on carbon nanotubes. The C peak is from the MWCNTs.
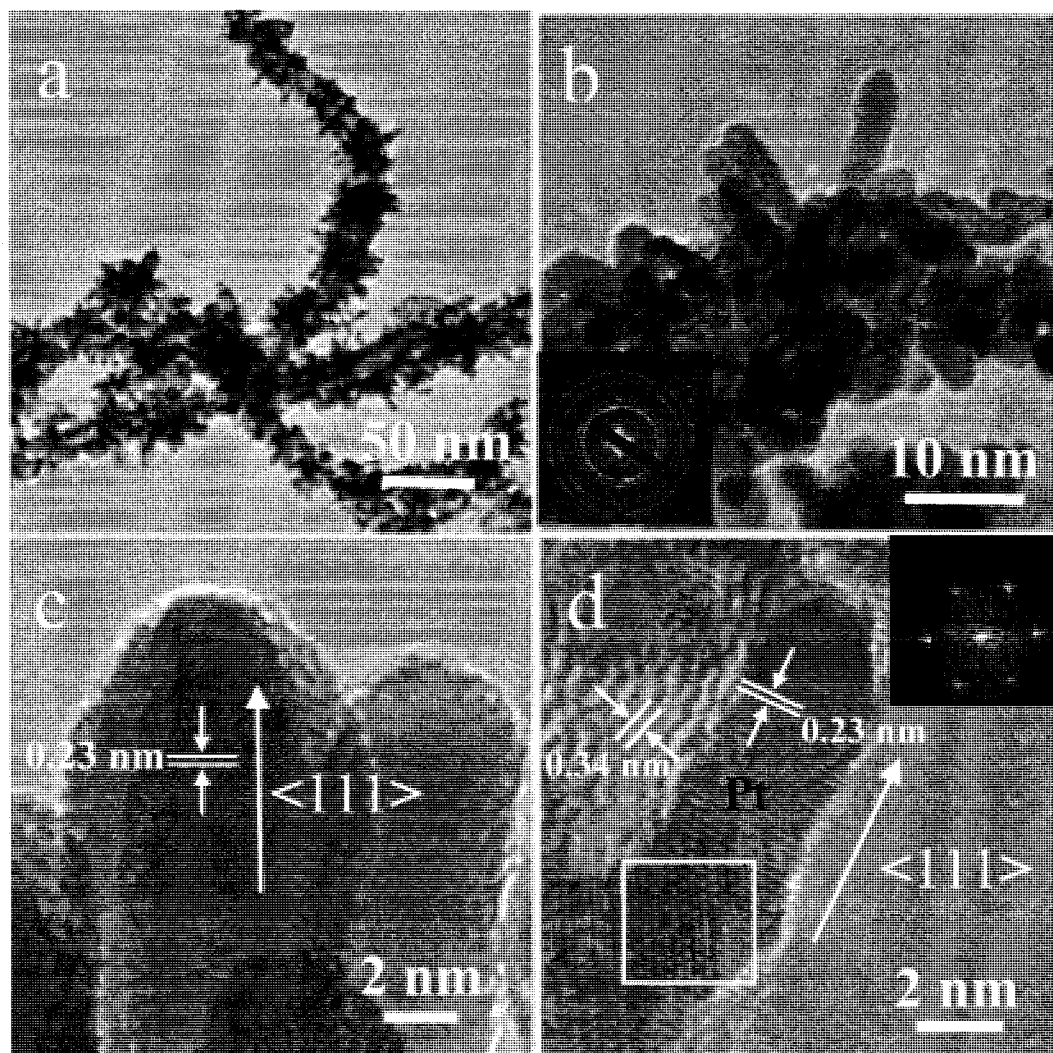
Figure 2. Typical TEM images of Pt NW–MWCNT heteronanostructures: (a) a low-magnification TEM image; (b) a medium-magnification TEM image, inset shows the SEAD pattern obtained from the heteronanostructures; (c) an HRTEM image of the Pt nanowire array; (d) an HRTEM image of the interface of Pt nanowire and MWCNT stem; the FFT in the inset, corresponding to the square area of the photomicrograph.

bright concentric rings (inset to Figure 2b), attributable to the {111}, {200}, {220} and {311} crystal planes of a fcc Pt crystal. This confirms that the platinum nanowires, synthesized by this method, crystallize in a phase similar to bulk Pt [19a]. The crystallographic orientation of the Pt nanowires was investigated by high-resolution (HR) TEM, as shown in Figure 2c and d. The closely packed nanowire arrays contain single-crystal atomic structures (Figure 2c), growing along the <111> direction, with a lattice spacing, between the {111} planes, of 0.23 nm, in agreement with the value in a bulk Pt crystal. Figure 2d displays the interfacial region between a Pt NW and the CNT on which it lies. The intact MWCNT structure and the crystalline Pt NW fringes are clearly observed. From the figure, the spacing between adjacent MWCNT walls has been determined to be 0.34 nm, similar to that in graphite. The nanowire lying on the nanotube has grown along the <111> direction, with a lattice spacing of 0.23 nm. The fast Fourier transform (FFT) of the atomic lattice fringing, in the inset to Figure 2d, corresponding to the zone in the square, further demonstrates the crystallinity of the nanowire.

Figure 3 shows the schematic diagrams (3a-d), and corresponding TEM images (3a'-d'), that illustrate the growth process we propose for our heterostructure formation. The entire process is composed of three steps. First, the pristine MWCNTs (15–30 nm in diameter) are used as supports in the synthesis of the hetero-nanostructures (step 1, Figure 3a and a'). At room temperature, the chemical reduction of H_2PtCl_6 by HCOOH produces Pt nuclei. The as-formed nuclei deposit on selected carbon nanotube sites, and act as sites for further nucleation, through the absorption of Pt^{4+} ions, leading to the formation of clustered particles. With the reduction of H_2PtCl_6, a high density of nuclei forms on the surfaces of MWCNTs. Pt, continuously supplied from solution, is deposited on the Pt nuclei, resulting in short Pt "nanosprouts" (step 2). The length of the
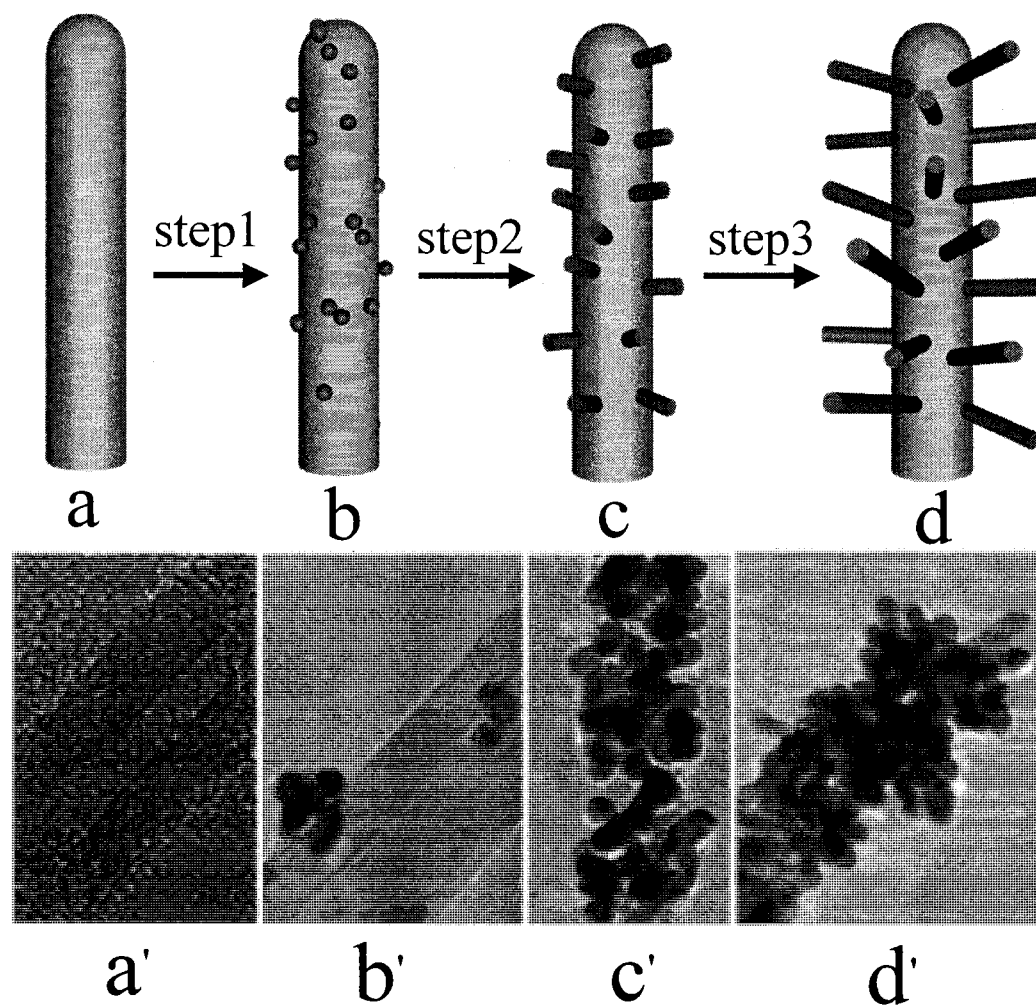
Figure 3. Schematic illustrations of the formation and shape evolution of Pt NW–MWCNT heteronanostructures. (a)–(d): schematic illustrations of the growth steps of the heteronanostructures; (a')–(d') TEM photomicrographs corresponding to (a)–(d), respectively.
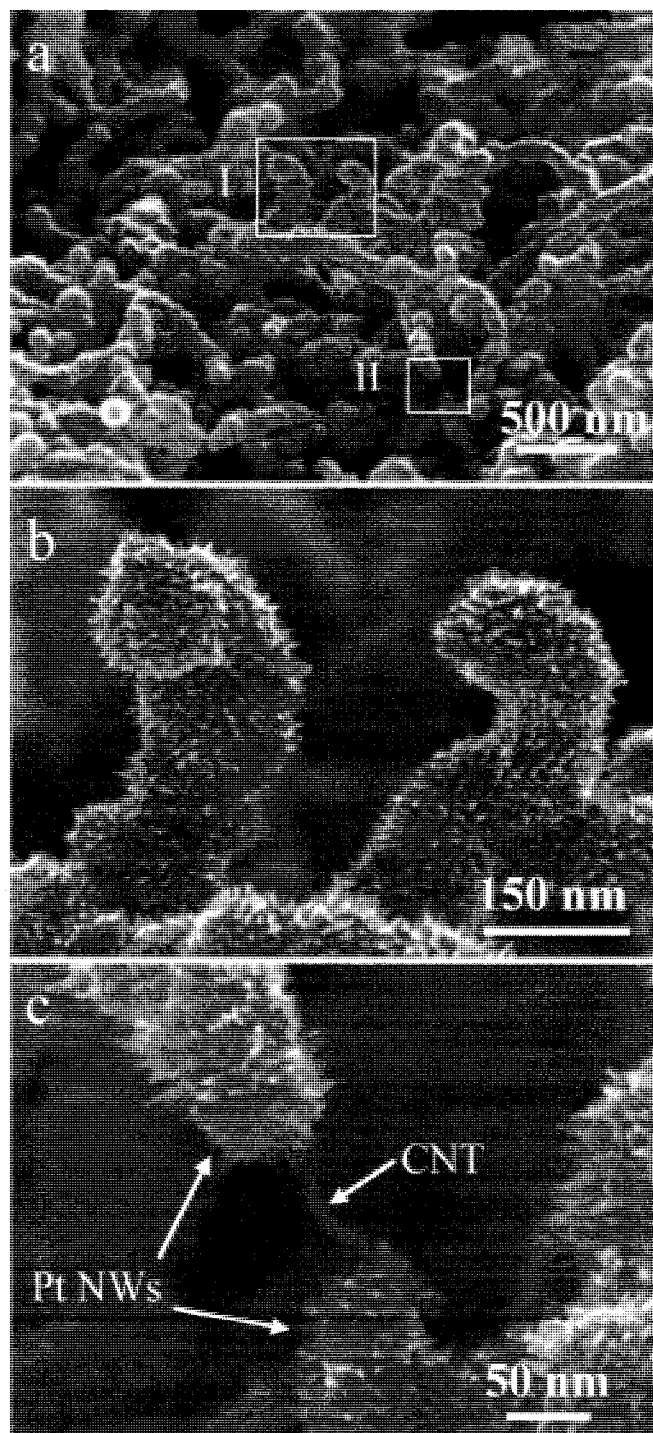
Figure 4. SEM images, at three magnifications, of the product when a large amount of H_2PtCl_6 precursor (Pt:C = 4:1) was used.

sprouts increases, producing Pt nanothorns (step 3). The resulting high density of Pt NWs on MWCNT is shown in Figure 3d and d'. The seed-mediated growth mechanism is not fully understood, but it is believed that anisotropic growth, preferentially in the <111> direction, is promoted by the very slow reduction rate and the Lowest Energy principle [22].

Interestingly, the Pt NW growth density on MWCNTs can be effectively modulated by controlling the weight ratio of CNTs to Pt precursor, while keeping other parameters constant to ensure nanowire growth. Figure 4 shows SEM photomicrographs, at three magnifications, of the product when a large amount of H_2PtCl_6 precursor (Pt:C = 4:1) was used at room temperature. We can see that entire surfaces are covered with a high density of Pt nanowires. From Figure 4b, the enlarged SEM image of zone I in Figure 4a, we see that increasing the Pt precursor concentration has increased the Pt nanowire surface density. A more detailed image of the nanostructure (Figure 4c, an enlarged image of zone II in Figure 4a) reveals many Pt nanowires, self-assembled at an angle to the MWCNT core, forming nanowire arrays with multiple junctions to the CNT. The Pt nanowires were confirmed to have diameters of ca. 4 nm and lengths of several tens of nanometers.

In summary, Pt NW arrays were self-assembled onto the surfaces of MWCNTs by a facile solution method at room temperature, forming Pt NW–MWCNT heterojunction nanostructures. The Pt nanowire surface density on carbon nanotubes could be easily controlled by manipulating the Pt precursor: MWCNT weight ratio. These new nanostructures are scientifically interesting, and have great potential in sensors, nanoelectronics, as electrocatalysts in fuel cells and other electrochemical applications.

Acknowledgments

References

[1] (a) Yang, H. G.; Zeng, H. C. *J. Am. Chem. Soc.* 2005, 127. 270. (b) Zhang, D. F.; Sun, L. D.; Jia, C. J.; Yan, Z. G.; You, L. P.; Yan, C. H. J. *Am. Chem. Soc.* **2005**, *127*, 13492.

[2] (a) Yong, L.; Chim, W. K. *J. Am. Chem. Soc.* **2005**, *127*, 1487. (b) Gu, H. W.; Zheng, R. K.; Zhang, X. X.; Xu, B. *J. Am. Chem. Soc.* **2004**, *126*, 5664. (c) Hayden, O.; Greytak, A. B.; Bell, D. C. *Adv. Mater.* **2005**, *12*, 701.

[3] (a) Zhang, Y. ; Suenaga, K.; Colliex, C.; Iijima, S. *Science* **1998**, *281*, 973. (b) Shi, W. S.; Peng, H. Y.; Xu, L.; Wang, N.; Tang, Y. H.; Lee, S. T. *Adv. Mater.* **2000**, *12*, 1927.

[4] (a) Hu, J.; Ouyang, M.; Yang, P. D.; Lieber, C. M. *Nature* **1999**, *399*, 48. (b) Hu, J.; Bando, Y.; Zhan, J.; Golberg, D. *Adv. Mater.* 2005, 17, 1964. (c) Luo, J.; Zhang, L.; Zhu, J. *Adv. Mater.* **2003**, *15*, 579.

[5] Lao, J. U.; Wen, J. G.; Ren, Z. F. *Nano. Lett.* **2002**, *2*, 1287.

[6] Wang, X. D.; Song, J. H.; Li. P.; Ryou, J. H.; Dupuis, R. D.; Summers, C. J.; Wang, Z. L. *J. Am. Chem. Soc.* **2005**, *127*, 7920.

[7] (a) Ye, C.; Zhang, L.; Fang, X.; Wang, Y.; Yan. P.; Zhao, L. *Adv. Mater.* **2004**, *16*,

1019. (b) Hu, J.; Bando, Y.; Zhan, J.; Yuan, X.; Sekiguchi, T.; Golberg, D. *Adv. Mater.* **2005**, *17*, 971.

[8] Baek, Y.; Song, Y.; Yong, K. *Adv. Mater.* **2006**, *18*, 3105.

[9] Du, J.; Fu, L.; Liu, Z.; Han, B.; Li, Z.; Liu, Y.; Sun, Z.; Zhu, D. *J. Phys. Chem. B* **2005**, *109*, 12772.

[10] Luo, J.; Huang, Z.; Zhao, Y.; Zhang, L.; Zhu, J. *Adv. Mater.* **2004**, *16*, 1512.

[11] Mieszawska, A. J.; Jalilian, R.; Sumanasekera, G. U.; Zamborini, F. P. *J. Am. Chem. Soc.* **2005**, *127*, 10822.

[12] (a) Ajayan, P. M.; Zhou, O. Z. *Top. Appl. Phys.* **2001**, *80*, 391. (b) Odom, T. W.; Huang, J. L.; Kim, P.; Lieber, C. M. *Nature* **1998**, *391*, 62. (c) Baughman, R. H.; Zakhidov, A. A.; de Heer, W. A. *Science* **2002**, *297*, 787.

[13] (a) Service, R. F. *Science* **1999**, *285*, 682. (b) Kordesch, K. V.; Simader, G. R. *Chem. Rev.* **1995**, *95*, 191.

[14] S. Hrapovic, Y. L. Liu, K. B. Male, J. H. T. Luong, *Anal. Chem.* **2004**, *76*, 1083.

[15] (a) Bell, A. T. *Science* **2003**, *299*, 1688. (b) Rouxoux, A.; Schulz, J.; Patin, H. *Chem. Rev.* **2002**, *102*, 3757.

[16] (a) Antolini, E. Mater. *Chem. Phys.* **2003**, *78*, 563. (b) Rolison, D. R. *Science* **2003**, *299*, 1698.

[17] (a) Ahmadi, T. S.; Wang, Z. L.; Henglein, A.; El-Sayed, M. A. *Chem. Mater.* **1996**, *8*, 1161. (b) Song, H.; Kim, F.; Connor, S.; Somorjai, G. A.; Yang, P. *J. Phys. Chem. B* **2005**, *109*, 188.

[18] (a) Mayers, B.; Jiang, X.; Sunderland, D.; Cattle, B.; Xia, Y. *J. Am. Chem. Soc.*

2003, *125*, 13364.(b) Kijima, T.; Yoshimura, T.; Uota, M.; Ikeda,T.; Fujikawa, D.; Mouri, S.; Uoyama. S. *Angew. Chem. Int. Ed.* **2004**, *43*, 228.

[19](a) Chen, J. Y.; Herricks, T.; Geissler, M.; Xia, Y. N. *J. Am. Chem. Soc.* **2004**, *126*, 10854. (b) Fu, X.; Wang, Y.; Wu, N.; Gui, L.; Tang, Y. *J. Mater. Chem.* **2003**, *13*, 1192.(c) Shen, Z.; Yamada, M.; Miyake, M. *Chem. Commun.* **2007**, *3*, 245. (d) Fukuoka, A.; Sakamoto, Y.; Higuchi, T.; Shimomura, N.; Ichikawa, M. *J. Porous Mater.* **2006**, *13*, 231.

[20](a) Song, Y.; Steen, W. A.; Pena, D.; Jiang, Y. B.; Medforth, C. J.; Huo, Q.; Pincus, J. L.; Qiu, Y.; Sasaki, D. Y.; Miller, J. E.; Shelnutt, J. A. *Chem. Mater.* **2006**, *18*, 2335. (b) Teng, X.; Liang, X.; Maksimuk, S.; Yang, H. *Smal*, **2006**, *2*, 249. (c) Ullah, M. H.; Chung, W. S.; Kim, Il.; Ha, C. S. *Small* **2006**, *2*, 870.

[21]Teng, X.; Yang, H. *Nano Lett.* **2005**, *2*, 249.

[22]Hoefelmeyer, J. D.; Niesz, K.; Somorjai, G. A.; Tilley, T. D. *Nano Lett.* **2005**, *5*, 435.